FACULTY OF ENGINEERING AND ARCHITECTURE

Experimental Characterisation of Short Fibre Reinforced Thermoplastic Materials for the Use in Heat Exchangers: Development of Test Setups and Methodology for Subcomponents, Coupons and Embedded Single Fibres

Joanna Schalnat

Doctoral dissertation submitted to obtain the academic degree of
Doctor of Electromechanical Engineering Technology

Supervisors

Prof. Wim Van Paepegem, PhD - Prof. Lode Daelemans, PhD

Department of Materials, Textiles and Chemical Engineering
Faculty of Engineering and Architecture, Ghent University

February 2022

GHENT UNIVERSITY

FACULTY OF ENGINEERING AND ARCHITECTURE

Experimental Characterisation of Short Fibre Reinforced Thermoplastic Materials for the Use in Heat Exchangers: Development of Test Setups and Methodology for Subcomponents, Coupons and Embedded Single Fibres

Joanna Schalnat

Doctoral dissertation submitted to obtain the academic degree of
Doctor of Electromechanical Engineering Technology

Supervisors
Prof. Wim Van Paepegem, PhD - Prof. Lode Daelemans, PhD

Department of Materials, Textiles and Chemical Engineering
Faculty of Engineering and Architecture, Ghent University

February 2022

GHENT UNIVERSITY

ISBN 978-94-6355-568-5
NUR 928
Wettelijk depot: D/2022/10.500/9

Members of the Examination Board

Chair

Honorary Prof. Ronny Verhoeven, PhD, Ghent University

Other members entitled to vote

Prof. Ludwig Cardon, PhD, Ghent University
Prof. Michel De Paepe, PhD, Ghent University
Prof. Guy Van Assche, PhD, Vrije Universiteit Brussel
Prof. Danny Van Hemelrijck, PhD, Vrije Universiteit Brussel
Tom Wieme, PhD, Ghent University

Supervisors

Prof. Wim Van Paepegem, PhD, Ghent University
Prof. Lode Daelemans, PhD, Ghent University

Summary

The recovery of waste energy holds economic and environmental benefits. For that reason, heat exchangers are widely spread in all areas of life and industry. However, the price for classic industrial heat exchanger materials like copper is rising, which makes the investment in heat exchangers less attractive. The solution is the transition to another cheaper material, but suited alternatives are rare. Heat exchangers are often placed in aggressive environments with high pressure and temperature or acidic fluids. Metals can endure the temperature and pressure but typically do not withstand acidity. Therefore, research on polymers arose. Polymers have the advantage of good chemical resistance but are typically not thermally conductive. Fillers, which form with the polymer matrix a composite, can be added to improve the heat conductivity. To investigate the potential of composite heat exchangers, the Compohex project was proposed. Its goal was to (i) find suitable material combinations, (ii) adapt the design of classical metal heat exchangers to the possibilities thermoplastics are offering and (iii) to classify the strength and stiffness of the material. Thereby, not only short-term tests are relevant, but especially the long-term performance is of interest since a heat exchanger has a life expectancy of up to 20 years. This proves quite a challenge, as for the long-term analysis, the performance needs to be estimated based on a shorter testing time than the real-life application. In addition, circumstances like environment and loading mode are often difficult to replicate.

In the frame of this experimental PhD, different test methods for the short- and long-term study on the performance of heat exchanger composite materials were performed. Since many new material combinations were produced in-house, a routine to ensure the quality of the material was developed. With microscopy, also filler-orientation and distribution could be measured, allowing for an accurate simulation of the material. The simulation was performed by colleagues within the project and was used to estimate the behaviour of a structured heat exchanger wall under temperature and pressure.

To verify the simulations experimentally, a new setup had to be developed. This device allowed the testing of a unit cell of 10x10 cm^2, wherein two heat exchanger walls can be layered. On the outside and between the layers, fluid with different heat and pressure can be circulated, representing the environment of a heat exchanger. Deformations and stress concentrations of the heat exchanger wall were measured optically with digital image correlation (DIC) through a glass window and the fluid. It served the evaluation of the material in a specific structure in a realistic environment. As such, this method can be considered as a subcomponent test setup.

To compare different materials, this prototype setup is less suited, since the geometry influences the result and the occurring stresses cannot be measured directly. For that purpose, coupon tests in quasi-static tension and creep were chosen. In addition to the standard test, a heat chamber was added to study the behaviour of the potential wall

material under the influence of elevated temperature. Temperature is especially relevant when working with composites based on thermoplastics, since their mechanical behaviour, including strength and stiffness changes with temperature. Also here, digital image correlation was used through a glass window to measure strain accurately. Exact measurements were needed since extrapolated long-term predictions are based on these test results. Every uncertainty in the experimental result intensifies in the prediction. The prediction is done numerically and by the Time-Temperature-Superposition principle (TTSP), assuming that the influence of time and temperature is the same. Therefore, experiments are accelerated by increasing the temperature stepwise.

However, the reaction of the standard coupon is thermally relatively slow since the heat chamber is big and the sample relatively thick. Therefore, dynamic mechanical analysis (DMA) was considered as a faster adapting system. The coupons and heat chamber are a lot smaller and the thermal stability is significantly better. Since the device is typically used for thermal measurements for which the absolute mechanical properties do not matter, the accuracy and repeatability was lacking for mechanical characterisation when following the standard guidelines. An extensive parameter study was performed to improve the quality of the test results significantly. With the improved quality, long-term predictions are possible using TTSP. A comparison of static versus dynamic measurements as the origin for the long-term behaviour was performed. Both methods deliver the same result for a mid-term prediction. For long-term predictions, the method closest to the real-life application needs to be chosen.

Valid simulations of the long-term behaviour require a good material model. Next to the filler orientation and distribution, the interface between filler and polymer matrix needs to be known. Measuring the interfacial strength of a single fibre with typically a few micrometres in diameter is hardly possible and the results are often unreliable. In addition, literature on the interface of short fibres in the thermoplastic matrix is scarce. To obtain a better understanding of the debonding behaviour, a short single fibre was embedded between polymer films and loaded in an in-house developed miniature tensile stage. The debonding was visualised with polarised light using a light microscope. The same test was also performed on three parallel fibres to study the influences of the fibres on each other. The developed setup shows the potential to study interfacial debonding on a microscopic level.

Samenvatting (Dutch summary)

De recuperatie van energie is interessant, zowel voor de economie als het milieu. Daarom zijn warmtewisselaars terug te vinden in alle delen van de industrie en in het dagdagelijkse leven. De prijs van klassieke warmtewisselaar materialen zoals koper is echter aan het stijgen, wat de investering in warmtewisselaars minder interessant maakt. Een oplossing is de transitie naar goedkopere materialen, maar er zijn niet veel opties. Warmtewisselaars worden typisch gebruikt in toepassingen met hoge druk en/of temperaturen, al dan niet in combinatie met corrosieve vloeistoffen. Aangezien metalen niet allemaal evengoed bestand zijn tegen deze corrosieve omstandigheden, werd het mogelijke gebruik van polymeren onderzocht. Polymeren beschikken immers vaak over een goede chemische weerstand, maar zij vertonen echter een lage thermische geleidbaarheid. Het Compohex project werd gelanceerd om het potentieel van warmtewisselaars vervaardigd uit vezelversterkte kunstoffen te evalueren. Het doel was (i) het vinden van geschikte materiaal combinaties, (ii) het aanpassen van het design van een klassieke warmtewisselaars om de voordelen van thermoplastische kunststoffen zoveel mogelijk te benutten en (iii) het bepalen van de mechanische eigenschappen, meer bepaald de stijfheid en sterkte van deze materialen. Dit blijkt een grote uitdaging te zijn, aangezien de verwachte levensduur van warmtewisselaars twintig jaar is. Bijgevolg zijn de korte-duur testresultaten heel belangrijk, aangezien de inschatting van de prestatie op de lange termijn op basis van deze korte-duur testen moet gebeuren. Bovendien is het niet evident om exact dezelfde omstandigheden qua type belasting en omgeving te creëren.

In het kader van dit experimentele doctoraat zijn verschillende test methoden onderzocht voor zowel korte- als lange-termijn studies om de prestatie van warmtewisselaars uit vezelversterkte kunststof te evalueren. Aangezien er veel verschillende materiaalcombinaties gecreëerd zijn binnen dit project, is er in eerste instantie een routine ontwikkeld om de kwaliteit van alle verschillende materialen verifiëren. Met behulp van microscopie werd de oriëntatie en distributie van de vulstoffen in kaart gebracht. Dit kon vervolgens gebruikt worden in de numerieke simulaties van het materiaal, uitgevoerd door collega's binnen het project, om het gedrag van warmtewisselaar elementen te onderzoeken bij verschillende drukken en temperaturen.

Deze simulaties moesten echter experimenteel gevalideerd worden, en hiervoor werd een nieuwe setup ontwikkeld en gebouwd. Met deze opstelling kon een eenheidscel van 10x10cm^2, geschikt voor twee wanden uit een warmtewisselaar, getest worden. Zowel aan de binnen- als aan de buitenzijde kon vloeistof op verschillende druk en temperatuur worden gecirculeerd, om zo de effectieve omstandigheden in een warmtewisselaar te genereren.

De vervormingen en spanningsconcentraties konden optisch worden opgevolgd met behulp van 'Digital Image Correlation' ofte DIC, waarbij deze techniek moest worden

toegepast doorheen de gebruikte vloeistof en de glaswand omheen de opstelling. Deze metingen dienden als rechtstreekse evaluatie van het materiaal in realistische omstandigheden op schaal van een klein prototype.

Echter, om verschillende materialen goed met elkaar te kunnen vergelijken, was deze setup minder geschikt aangezien de geometrie van de wanden het eindresultaat kan beïnvloeden en de effectief optredende spanningen in het materiaal niet kunnen worden gemeten.

Bijgevolg is in een volgende fase overgeschakeld op de standaard proefstukgeometrie voor quasi-statische trekproeven en kruipproeven. Bovendien werd een klimaatkast gebruikt, om het gedrag van het potentiele wandmateriaal te studeren onder de invloed van temperatuur. Dit is immers relevant voor vezelversterkte thermoplastische kunststof, aangezien de mechanische eigenschappen zoals stijfheid en sterkte veranderen in functie van de temperatuur. Opnieuw werd gebruikt gemaakt van DIC doorheen de glazen wand van de klimaatkast om het rekveld zo nauwkeurig mogelijk in kaart te brengen. Zeer nauwkeurige metingen zijn immers vereist, aangezien de geëxtrapoleerde voorstellingen op deze metingen gebaseerd zijn. Dergelijk voorspellingen kunnen numeriek worden gedaan met behulp van het tijd-temperatuur superpositie principe (TTSP), ervan uitgaande dat de invloed van tijd en temperatuur hetzelfde zijn. Mede hierdoor kunnen de experimenten versneld worden uitgevoerd door het stapsgewijs verhogen van de temperatuur.
Een mogelijk nadeel aan deze methode is echter dat een standaard trekproefstuk relatief groot en massief is en bijgevolg thermisch nogal traag reageert. Bovendien heeft de klimaatkast ook een zeker thermische traagheid.

Om een thermisch sneller reagerend systeem te realiseren, werd overgeschakeld op dynamic mechanical analysis (DMA). De proefstukgeometrie en de thermische kamer zijn bij dit systeem immers merkelijk kleiner en de temperatuur is nauwkeuriger instelbaar en blijft constanter. Dergelijke opstelling wordt echter in hoofdzaak gebruikt voor thermische analyses en minder voor mechanische karakterisatie, en bijgevolg was de nauwkeurigheid en herhaalbaarheid op mechanisch vlak in eerste instantie niet voldoende. Om dit te verhelpen, is er een uitgebreide parametrische studie uitgevoerd met positief resultaat. Hierdoor was het nu mogelijk om de lange-duurvoorspelling te doen met behulp van TTSP. Een vergelijkende studie tussen statische en dynamische metingen als basis voor lange-termijn voorspellingen is vervolgens uitgevoerd en beide methoden blijken een goed resultaat te geven voor de middellange-tijd. Voor de lange-termijn voorspelling is de methode die meest gelijkaardig is aan de werkelijke applicatie de beste oplossing.

Om nauwkeurige numerieke simulaties te kunnen uitvoeren voor lange-termijn voorspellingen is een goed materiaalmodel nodig. Hiervoor zijn niet enkel de eerder vermelde oriëntatie en vullingsgraad van belang, ook het gedrag van de interface tussen het matrixmateriaal en de vulstof moet goed gekend zijn.

Experimenten om de hechting van een enkel vezel van typisch een paar micrometer in diameter te onderzoeken zijn echter zeer moeilijk en het resultaat is vaak niet reproduceerbaar. Ook in de literatuur is er tot heden niet veel terug te vinden over het gedrag van de interface van korte vezels in thermoplastische kunststof matrices.

Om het 'de-bonding' proces toch beter te begrijpen, werd een procedure ontwikkeld waarbij één korte vezel ingebed wordt tussen twee polymeerfilms en vervolgens in trek wordt belast op een zelf ontwikkelde miniatuur trekbank. Het 'de-bonding' proces kon worden gevisualiseerd met gepolariseerd licht met behulp van een microscoop. Vervolgens werd een gelijkaardige test ook herhaald, maar op een proefstuk met drie ingebedde vezels, dit om te invloed van naburige vezels op elkaar te bestuderen. De ontwikkelde setup vertoont veel potentieel om dit gedrag op microscopisch niveau te leren begrijpen.

I wish cake flew by instead of time.

Anonymous

Acknowledgement

When people ask you “what is your PhD about?”, you have several choices to answer. I typically simplify to “I destroy things to know how strong they were” and most people were very satisfied with this answer. Another option, you can give a long explanation ideally with pictures for clarification, which gives you satisfaction when you managed to keep the attention of the other. Lastly, you could tell the story of what is all behind a PhD, that only a small fraction of it is science and that a big part is about friendship, support, and cake.

I would therefore like to fill this part of the book with all the people that are not named as author, but the reason that this journey did not end in year 3, but continued to this point and beyond.

First, I would like to thank my favourite professor of all times, baking guru and promoter Wim Van Paepegem. Thank you Wim for all the talks we had, for all the advice I got, for all the challenges you gave me. The sentence “not scientific enough” was my biggest obstacle, but also the reason this book reached the level it is at. You were always there when I needed you and had advice far beyond the academic aspect of a PhD. Also, a big thank you to Lode for all the patience with my DMA questions, for the help with the papers and the nice visit to the cafe in Antwerp.

And on a rainy day, when work does not go smooth and it is coffee break time, and you are not sure, if you should go at all, because you don’t feel like talking, but you go anyways. Then there is Ives, just talkative, open and infectious with it. Thank you for all the mood-lifting breaks, for all the spontaneous help when Murphy was hanging out a bit too much in the lab and for all the reading work you did in the last year. 

Outside of work, my biggest smile and biggest hugs go to my closest family. Mathijs, thanks to you I ate healthy when I was just craving pizza, was leaving the couch for a walk, even though it seemed so exhausting and had a social life without putting effort. Thank you for sticking it out with me through the bad times and the good and for always having a partner to laugh with. 
Und danke an euch, MamPa, dass ich/wir immer willkommen sind. Unsere schönen Skypetelefonate und die Besuche mit Rundumversorgung muntern mich stets auf und ich freue mich schon auf das nächste Mal mit den besten Pfannkuchen und echtem Barista-Kaffee. 

Erik and Ruben, thank you for all our fun times, for the help with work, especially to Erik with LabView and my whining. Thank you for the great boardgame evenings and New Year’s gatherings. Also, I am certainly grateful for the plenty cat-petting-opportunities and your very healthy, regular craving for cake and coffee 

Vielen lieben Dank auch an meine Freunde, die mich aus der Ferne unterstützen, speziell Laura, Birgit, Anke und Judith. Ihr gebt mir immer einen guten Grund zum Reisen, mit reichlich Fikas und Zebradielenbesuchen. Ich wüsste gar nicht, wo ich ohne euren Lebensbeistand wäre. Besonders großes Danke an Laura, um mich daran zu erinnerin, dass die Welt nicht nur aus promovierenden Ingenieuren besteht  

Sweet, sweeter, sweetest. Inge, I like our healthy baking trends, but even more the unhealthy ones. If technical challenge during lockdown or designs in 3D, one day we will make it to bake-off, I am sure. :-D Thank you for making baking our great hobby and taking my mind off work with it. 

In the weekend, there is time for trips, relaxation, and joy. Larissa and Paula, it was such a coincidence to get to know you both at the same PhD meeting and unforgettable since. Thank you for all the girls talk and cosiness, we had together, especially Larissa for the cool trips and Paula for the delicious tortillas. 

I still owe a few cakes here and there, but especially to Tom and Olivier. I cannot count how often you explained DSC results to me, had an open ear or more advices than I was expecting to get before casually stopping by your offices. 

As equal partners in the struggle of a PhD and temporary office mates: Herthog, for the bad jokes and good talks, Lotte for the fun and craziness, Arada for the kindness and joy, and Daniele for the successfully passed quizzes. Thank you for the time together and for the opportunity to learn from the decisions of the others about the possibilities in life. Sometimes, it really just helps to see data chaos on a different screen than your own. 

As well thank you Ilse for all the good book suggestions throughout the years and the nice talks. Thank you for keeping the cultural side inside me alive. 

Furthermore, I would like thank all the other people who were helping me on a professional level. Many thanks to my master students with special thanks to Roy, to all project partners and to the jury members.

And last but not least, a thank and smile to all others not named, but still very important to form a network of fun, creativity and community.

About the author

Joanna Schalnat was born on September 13th, 1990 in Hannover, Germany. From there, she moved to Dresden, Germany to study process engineering with a focus on wood and fibre material technology at the technical university of Dresden. As a student job aside, she took the opportunity to work for several PhD students. Her main task was characterising strength and stiffness on wood and wooden composites, which motivated her to search for more opportunities for mechanical testing. In internships at Danzer in Kesselsdorf, Germany and at SP in Borås, Sweden, she could extend her knowledge on the production and testing of laminates as well as composites and successfully achieved her engineering diploma in 2016.

Without ever having been to Belgium before, she decided enthusiastically to join the research group Mechanics of Materials and Structures at Ghent University. Funded by the Compohex project and the Relicario project, she has spent a great time in the mechanical lab to learn about testing, composites, test-setups and the importance of teamwork. The results are presented in this dissertation.

During her studies, she contributed to scientific publications and participated in several international conferences. An overview of her publications is given below.

Publications

Publications in peer reviewed journals (A1)

J. Schalnat, D. G. Gómez, L. Daelemans, I. De Baere, K. De Clerck, and W. Van Paepegem, "Influencing parameters on measurement accuracy in dynamic mechanical analysis of thermoplastic polymers and their composites," Polymer Testing, vol. 91, p. 106799, 2020.

J. Schalnat, L. Daelemans, I. De Baere, K. De Clerck, and W. Van Paepegem, "Long-term stiffness prediction of particle filled polymers by dynamic mechanical analysis: Frequency sweep versus creep method," Polymer Testing, p. 107368, 2021.

A. Krairi, I. Doghri, J. Schalnat, G. Robert, and W. Van Paepegem, "Thermo-mechanical coupling of a viscoelastic-viscoplastic model for thermoplastic polymers: Thermodynamical derivation and experimental assessment," International Journal of Plasticity, vol. 115, pp. 154–177, 2019.

C.-M. Popescu, D. Jones, J. Schalnat, K. Segerholm, M. Henriksson, and M. Westin, "Structural characterization and mechanical properties of wet-processed fibreboard based on chemo-thermomechanical pulp, furanic resin and cellulose nanocrystals," International journal of biological macromolecules, vol. 145, pp. 586–593, 2020.

Publications in international conferences (C1)

J. Schalnat, A. Krairi, T. Wieme, and W. V. Paepegem, "Experimental Characterization of Thermoplastics for Use in Heat Exchangers," in Multidisciplinary Digital Publishing Institute Proceedings, 2018, vol. 2, no. 8, p. 375.

J. Jermer, B.-L. Andersson, and J. Schalnat, "Corrosion of fasteners in furfurylated wood: final report after 9 years exposure outdoors," in IRG48 Scientific Conference on Wood Protection, 2017.

A. Krairi, J. Schalnat, and W. Van Paepegem, "Thermo-mechanical constitutive behaviour models for unfilled and short fibre reinforced polymers for application in heat exchangers," in 18th European Conference on Composite Materials, Abstracts, 2018.

A. Krairi, X. Wang, J. Schalnat, and W. Van Paepegem, "Thermo-mechanical analysis of short fibre reinforced polymers for application in composite heat exchangers," in 18th European Conference on Composite Materials (ECCM 18), 2018.

Other presentations at conferences

J. Schalnat, D. Garoz Gómez, L. Daelemans, W. Van Paepegem, "Experimental and Numerical sensitivity study of sources of scatter in quantitative mechanical characterisation of polymers using DMA equipment" JTACC+V4, 2nd Journal of Thermal Analysis and Calorimetry Conference and 7th V4 Thermo-analytical Conference, 2019

J. Schalnat, D. Garoz Gómez, L. Daelemans, W. Van Paepegem, "Experimental and Numerical sensitivity study of sources of scatter in quantitative mechanical characterisation of polymers using DMA equipment" in TAWN Users Meeting, 2019

Table of Content

List of acronyms

μCT	Microcomputed tomography
ABS	Acrylonitrile-butadiene-styrene
ASTM	American Society for Testing and Materials
ATHT	Applied Thermodynamics and Heat Transfer, research group at Ghent University under, Michel De Paepe
a_T	Shift factor
BN	Boron nitride
CAD	Computer-aided design
CCD	Charge-coupled device
CF	Carbon fibre
CFD	Computational Fluid Dynamics
CNT	Carbon nano tubes
CPMT	Centre for Polymer and Material Technologies, research group at Ghent University under Ludwig Cardon
Cr	Creep
CT	Computed tomography
DAQ	Data acquisition
DC	Direct current
DIC	Digital image correlation
DIN	German Institute for Standardisation
DMA	Dynamic mechanical analysis
DSC	Differential scanning calorimetry
EN	European standard
FE	Finite element
FEM	Finite element method
FFT	Fast Fourier transformation
FS	Frequency sweep
GF	Graphite flakes
GL	Glass fibre
HDPE	High density polyethylene
HSV	Hue-Saturation-Value
IFSS	Interfacial shear strength
ISO	International Organisation for Standardisation
LC	Load cell
LDPE	Low-density polyethylene
LED	Light-emitting diode

LVE	Linear viscoelastic region
MMS	Mechanics of Materials and Structures, research group at Ghent University under Wim Van Paepegem
PA 6	Polyamide 6
PC	Polycarbonate
PE	Polyethylene
PEEK	Polyether ether ketone
PESU	Polyethersulfone
PET	Polyethylene terephthalate
pH	Potential hydrogen
PLA	Polylactic acid
PP	Polypropylene
PPS	Polyphenylene sulphide
PS	Polystyrene
RPM	Revolutions per minute
SBO	Strategic Basic Research
SEM	Scanning electron microscope
SIM	Stepped isothermal method
STDEV	Standard deviation
ST-ratio	Span length to thickness ratio
TSS	Total sum of squares
TTSP	Time temperature superposition principle
UGent	Ghent university
UTS	Ultimate tensile strength
UV	Ultra violet
vol%	volume percent
VRO	Variable ray origin
wt%	weight percent

Chapter 1

Introduction

Abstract: The demand for cost-efficient heat exchangers for economics and the protection of the climate is rising. To address the problem, the Strategic Basic Research (SBO)-project "Compohex" on composite heat exchangers is introduced. The replacement of the heat exchanger material opens new possibilities, but also poses new challenges with regard to material testing. Accurate tests for strength and stiffness as well as lifetime predictions on a structural and material level are missing. This PhD takes an important step to fill that gap. In this chapter, an introduction on heat exchangers is given and the need for appropriate testing methods on different scales is highlighted together with the general outline of the PhD.

1.1 Introduction to heat exchangers

Heat exchangers are found in every area of life where heat is transferred. Examples are radiators, where hot water is used to warm-up the living room, in a refrigerator where the refrigerant is cooling stored food or in industry (Figure 1-1), where heat from exhaust gas is regenerated to save energy for the process [1].

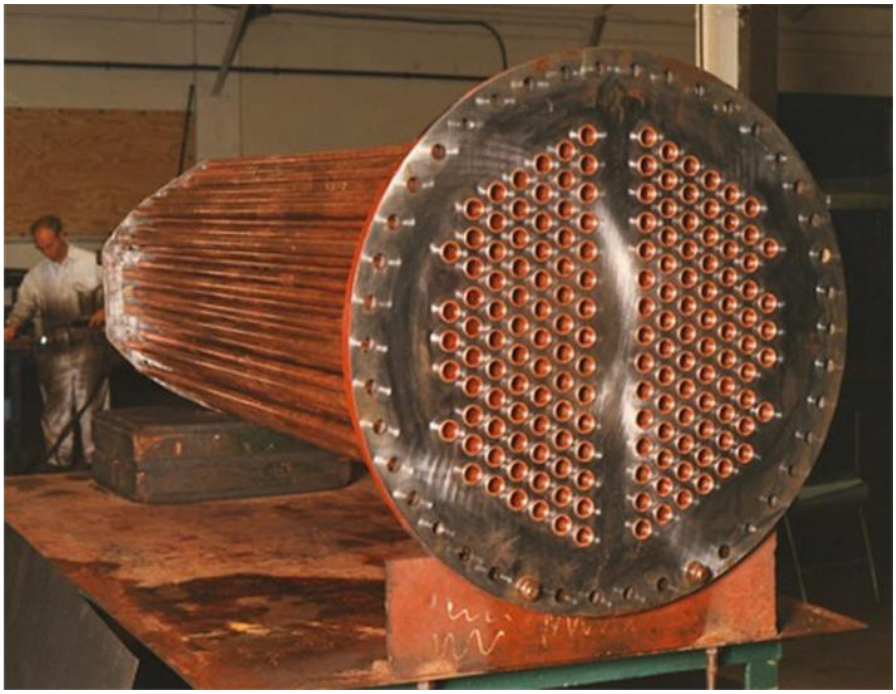

Figure 1-1: Copper heat exchanger used for example in offshore, pharmaceutical or petrochemical processes

The efficiency of a heat exchanger is determined by the amount of heat transferred. Therefore, the thermal conductivity of the heat exchanger material and the heat transfer coefficient to the fluid are crucial properties that influence the efficiency. Due to their suited properties (Table 1-1), metals like steel, titanium or copper alloys have established themselves as main material in industries with high energy requirements such as power plants, petrochemical plants and desalination plants [2,3]. Their high pressure resistance allows the wall thickness to be low, which leads to little importance of the thermal resistance of the wall. However, industries are facing a problem: The price of the materials is rising. On the example of copper, the price is quadrupling in the last years, as Figure 1-2 illustrates. In addition, the production, assembly and transportation costs are high compared to some other materials like for example polymers.

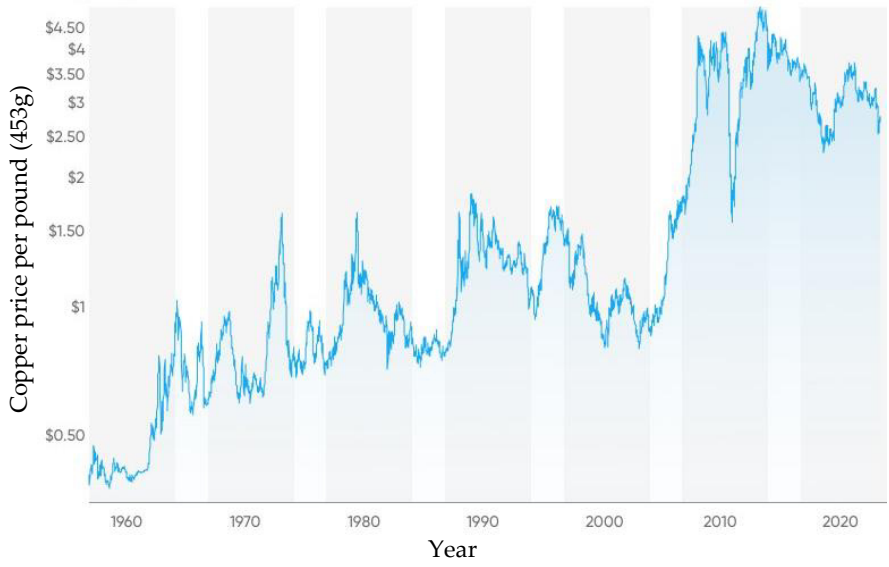

Figure 1-2: Development of the copper price over the last 60 years in US-dollar/pound [4]

As such, on one hand, the payback time of a heat exchanger is growing and the investment is less attractive. On the other hand, the climate measures are tightened and energy becomes more and more precious, which increases the demand for energy saving as for example by using heat exchangers. Therefore, the demand of heat exchangers is predicted to grow in Europe 7.21% within the next 4 years [5]. To increase the growth, it is worth to look into alternative materials heat exchangers could be made from.

Next to the initial investment, also the required stopping times for maintenance and the overall life-time have an important impact on the cost. Typical problems during the life-time are corrosion and clogging caused by fouling, which is the accumulation of contamination on solid surfaces, both illustrated in Figure 1-3.

Due to the heat transfer, fluids can evaporate or condense in the heat exchanger [6], which can change their pH-level, which might affect the wall material. Although corrosion does not necessarily lead to failure, the heat transfer can be reduced due to corroded surfaces as in case of copper. The risk of fouling and thereby the frequency of cleaning maintenance can be limited by using heat exchanger materials with a low surface roughness. The lifetime expectancy of a heat exchanger is between 10 years [7,8] and 20 years [9].

Figure 1-3: Reduction of efficiency and life-expectancy of a heat exchanger due to (a) corrosion and (b) fouling

As an alternative, heat exchangers based on polymers are being developed. They have the advantage over metals to be more light weight, which is an interesting aspect if the heat exchanger is used in vehicles such as cars [10]. In addition, polymers are corrosion resistant and their smooth surface and surface chemistry can have an anti-fouling effect [11]. Also, the assembly cost could be reduced compared to a traditional metal heat exchanger, because of fewer required welding connections. However, polymers have several disadvantages as low thermal conductivity, sensitivity to certain fluids and low strength, resulting in creep. The low heat conductivity and low strength of polymers can be increased by adding heat conductive fillers [12]. Filled polymers are a composite material. For comparison, several heat-exchanger-relevant properties are given in Table 1-1 for copper, stainless steel, the high temperature resistant polymer polyphenylene sulphide (PPS) and its graphite filled composite. The comparison shows, that the properties differ substantially and make a simple material replacement impossible. Specific material knowledge is needed to compensate for weaknesses and make efficient use of the strength of the individual material. Due to the potentially lower material and production costs as well as lower maintenance, composite heat exchangers could be financially interesting compared to metal heat exchangers.

Table 1-1: Overview of properties of different materials

	Copper [13]	Stainless Steel [14]	Polymer [15]*	Composite [16]**
Density [g/cm^3]	8.93	8	1.35	1.78
Thermal conductivity [W/mK]	385	16.2	0.29-0.32	14
Melting temperature [°C]	1083	1450	280	>200
Tensile strength [MPa]	210	520-720	33-90	47.9
Roughness [17] [µm]	1.5	15	1.5	-

* Example of PPS

** Example of PPS highly filled with graphite

However, metal heat exchangers are established and industries are reluctant invest in new types of heat exchanger. This is also, because the behaviour of composites under temperature and pressure as common in heat exchangers is not studied well, yet [18]. In addition, the requirements are beyond standardised mechanical testing, resulting in a lack of well-defined testing methods. Not only the short-term qualification of the material is insufficient, also a lifetime prediction is required, since creep is the main reason for failure of polymer heat exchangers. Creep test results are needed to gain the trust of the industry in composite materials [19]. Existing standardised tests are also here not sufficient to provide accurate test results. The improvement of the testing methods is of highest priority to have knowledge about lifetime expectancy under the specific environmental conditions. Only with trustworthy results on the lifetime stability, a broad change in industry to composite heat exchangers is possible. However, this change can benefit the economy with its lower price and make it more attractive to invest in heat exchangers, which reduces the overall energy consumption and therewith benefits the environment.

1.2 Working principles of a heat exchanger

All heat exchangers work in the same way: heat is transferred from one fluid to another as Figure 1-4 shows. Fluids can be different media like air, water, refrigerants, or chemicals in gaseous or liquid form. Thereby, either the fluids mix in direct contact with each other and the heat exchanger provides only the space for the mixing, or heat is transferred through the wall of a heat exchanger. In both cases, the heat exchanger needs to withstand the temperature and pressure of the fluids.

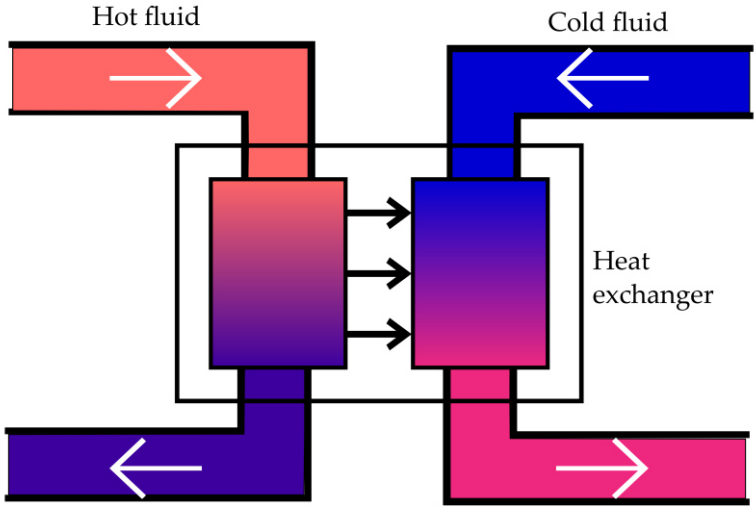

Figure 1-4: Basic principle of a heat exchanger, heat is transferred from hot fluid to cold fluid

Many different geometries, flows, and materials are possible for heat exchangers. The main geometrical difference are plate and tubular heat exchangers, possibly in combination with enhanced surfaces that improve the turbulence and therewith the heat transfer. Common wall geometries are displayed in Figure 1-5.

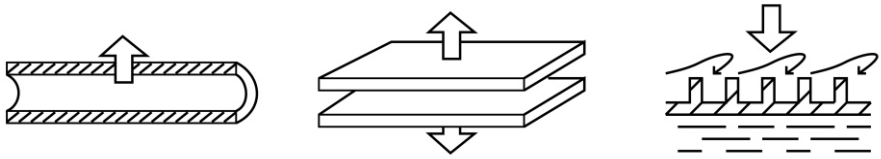

(a) Tubes (b) Plates (c) Enhanced surfaces

Figure 1-5: Wall geometries of heat exchangers [3]

Different directions of flow have an impact on the heat transfer and can be chosen according to the requirements. The three available directions are parallel, counter and cross flow, visualised in Figure 1-6.

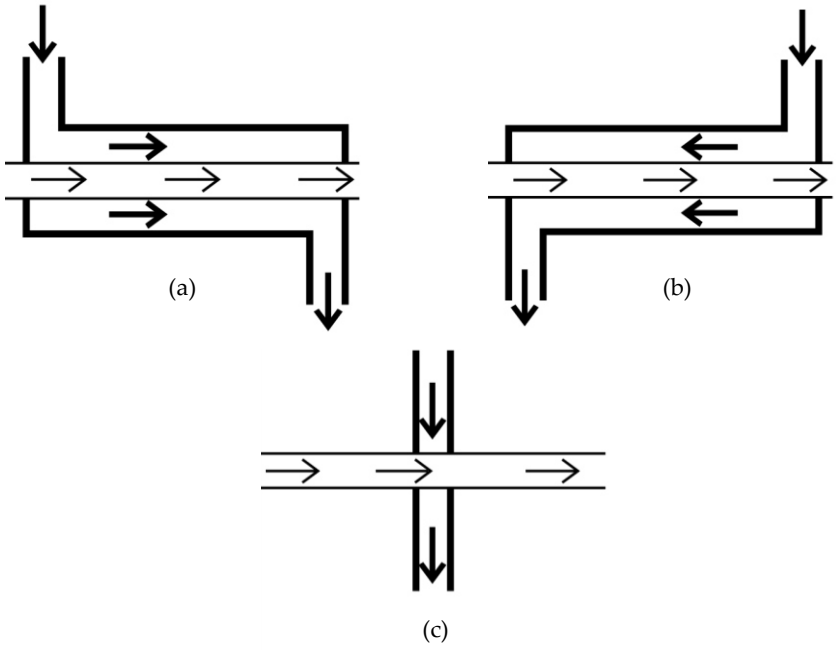

Figure 1-6: Flow directions in heat exchangers, (a) parallel flow, (b) counter flow, (c) cross flow [3]

An example of a heat exchanger can be seen in Figure 1-7. It has enhanced surfaces and the flow direction is counterflow. The thin sheets, the enhanced turbulence, and the heat conductive material (here aluminium) provide a good heat transfer between the two fluids.

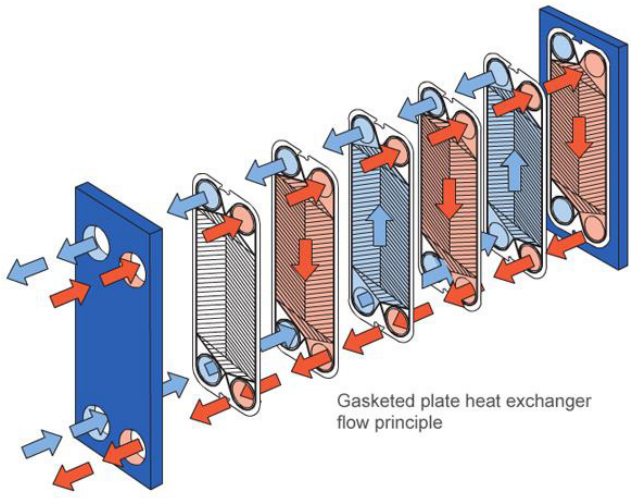

Figure 1-7: Example of an enhanced plate heat exchanger [6]

The geometrical design possibilities of a heat exchanger are endless and the best solution strongly depends on the application. Next to the material, the geometry has an important influence on the heat flux and the resulting thermal performance of the heat exchanger.

In a classical metal heat exchanger, the thermal conductivity is relatively good for all possible materials. The same applies for the thermal stability and the mechanical stiffness. Requirements that are more relevant are the type of fluid and a long maintenance interval. Corrosion caused by the type of fluid and fouling can shorten the interval and are therefore important factors to consider. For metal heat exchangers, the most critical parameters are:

- Type of fluid
- Fouling resistance
- Costs

1.3 Polymer heat exchangers

In a polymer-based heat exchanger, the design requirements are not entirely the same as for metal, which complicates the direct exchange of these two materials. Polymers are inherently corrosion resistant in the classical sense, though some are sensitive to certain solvents. The broad range of polymers with different sensitivities to different solvents often enables to find an appropriate polymer material for the heat exchanger and its specific fluid type (solvent). However, the biggest difference between some

polymers, namely thermoplastics, and metals is the dependency on temperature. Thermoplastics are sensitive and behave different at different temperatures, especially their stiffness decreases. In addition, a good heat transfer is not naturally given but can be improved as shown in Equation (1-1), where Q is the heat transfer, κ the thermal conductivity, A the surface area, ΔT the temperature difference between hot and cold side and d the thickness of the wall. By adding heat conductive fillers, the heat conductivity of the polymer increases, but also the cost. By lowering the wall thickness, the stiffness is compromised.

$$Q = \frac{\kappa \, A \, \Delta T}{d} \tag{1-1}$$

Besides, factors like increased ductility due to the temperature or embrittlement due to radiations like UV need to be considered, which can shorten the in-service time. The most critical design parameters are therefore:

- Temperature
- Pressure
- Thermal conductivity
- Lifetime
- Costs

Historically, polymer heat exchangers are found first in the 60s [20] and got further developed since [19,20–23]. As an example, an air-to-air heat exchanger for barns is shown in Figure 1-8. Heat transfer takes place through the material of the air channel profiles. The efficiency is sufficient for the purpose of a low performance heat exchanger. Polymer is here used over metal, due to the advantage of easy cleaning, since the dust-rich barn air causes clogging and fouling.

Figure 1-8: Polypropylene air-to-air heat exchanger in barn [24]

For more demanding application areas, polymer heat exchangers are still lacking in performance [19,23]. One issue is that they soften at elevated temperatures. To solve this issue, a hybrid heat exchanger can be considered. It uses polymers in corrosion sensitive areas and steel in the high temperature applications. A pre-heater of air is shown in Figure 1-9. Air is pre-heated for combustion or drying air by recovering the waste heat of exhaust gas (flue gas). Flue gas condenses below its dew point to a metal corroding acid. Therefore, a conventional heat exchanger needs to be built fully from expensive stainless steel or titanium, which increases the total cost of the heat exchanger and makes the cost of heat recovery less attractive. The used polymer can withstand the acidity. It is inserted here in form of bundles of polymer tubes, in which the flue gas condenses.

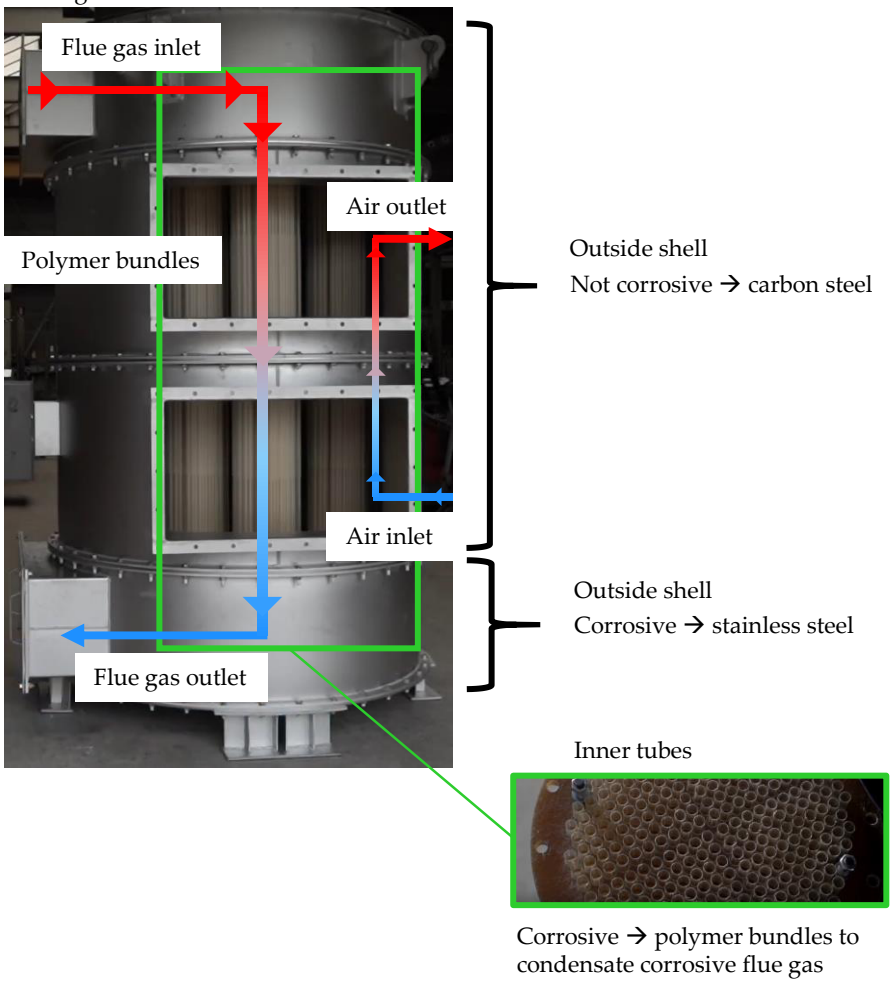

Figure 1-9: Hybrid polymer air pre-heater. Flue gas condenses when cooling down and would cause corrosion on metals due to its acidity [25]

Another weak characteristic of polymer heat exchangers is the low thermal conductivity [23]. To enhance the heat flux, two options are available as can be derived from Equation (1-1). The first option is to reduce the wall thickness, making the conductivity of the wall material less critical. However, this poses a challenge for the structural integrity of the heat exchanger. Nevertheless, heat exchangers with ultra-thin walls (<100 μm) exist as shown in Figure 1-10. Their mechanical stability is low, but sufficient for low-pressure cases. The second option is to improve the thermal conductivity of the wall material so that a sufficient thickness can be maintained that serves higher pressure. On this second option, the Compohex project was based.

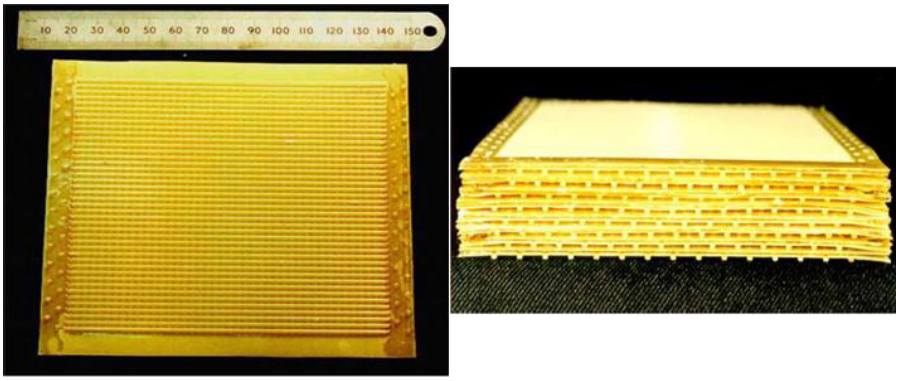

Figure 1-10: Thin wall polymer heat exchanger from polyetheretherketone (PEEK) with wall thickness of 100 μm [26]

1.4 The Compohex project

To improve the conductivity of a polymer, conductive fillers as graphite or short carbon fibres can be included, which form together with the polymer matrix a composite. To make composite heat exchangers more accessible and validated, the Strategic Basic Research (SBO)-project "Compohex" [27,28], standing for composite heat exchangers, was granted. The objective of the project was to explore the potential of composites for heat exchangers in concern of low- and high-levels for temperature and pressure. Traditional metal-based heat exchangers are facing corrosion and scarcity of the material. Composite heat exchangers could offer an alternative if they are developed further and if the features of the material are incorporated. Together with project partners from material supply like Bekaert [29], manufacturers of subcomponents as Parker [30] and heat exchangers as Vyncke [31] as well as with end-users like Daikin [32], Atlas Copco [33] or Vito [34], the potential was evaluated.

It showed that end users are interested in polymeric heat exchangers, because of the additional benefits as corrosion and fouling resistance, weight reduction, and costs. Despite polymer and composite heat exchangers being on the market, the end users

have not broadly switched to polymers, yet. Main reasons are limits in temperature and pressure as well as concerns of lifetime performance.

The switching of metal by polymer-based composites is not evident. Existing alternative heat exchangers often mimic metal heat exchangers. Thereby, the different thermo-fluidic and thermo-mechanical characteristics are not considered sufficiently, the design possibilities due to the different production method are not taken advantage of, yet. For example, the listed polymer heat exchangers on the market are to the author's opinion not fully optimised. With higher heat conductivity the size of the exchanger could be reduced, higher material strength would allow for more pressure, or an improved geometry for enhanced turbulence and therewith higher heat transfer are imaginable.

The Compohex project had the goal to combine experts from heat exchanger design, fluid dynamics, material production, and performance testing to look at composite heat exchangers from different angles. Although thermosets could offer advantages in terms of thermal and mechanical stability compared to thermoplastics, thermoplastics reinforced with short fibres offer a simpler production route and more design possibilities due to their ability to be thermoformed. Therefore, only thermoplastic polymers are considered in this work. The mechanical validation of the material as well as the geometrical structure was one of the key elements. The Compohex project included industrial partners providing material, advice, and expertise as well as three different academic working groups. The tasks of the latter are visualised in Figure 1-11. Each research group focussed on experimental and numerical studies in parallel. In the design & flow group (Applied Thermodynamics and Heat Transfer, ATHT [35], prof. Michel De Paepe), the wall design of heat exchangers was simulated for an enhanced heat transfer and experimentally tested in a flow setup. The material choice & production group (Centre for Polymer and Material Technologies, CPMT [36], prof. Ludwig Cardon) focussed on the selection of materials with enhanced properties and simulated the injection moulding of potential parts. In the group strength & stiffness (Mechanics of Materials and Structures, MMS [37], prof. Wim Van Paepegem), load was numerically simulated and experimentally applied to validate design and material choice. This PhD describes the experimental methods used to evaluate the thermomechanical performance of materials for the use in heat exchangers. Furthermore, results served as input and validation for the development of temperature-dependent material models [38].

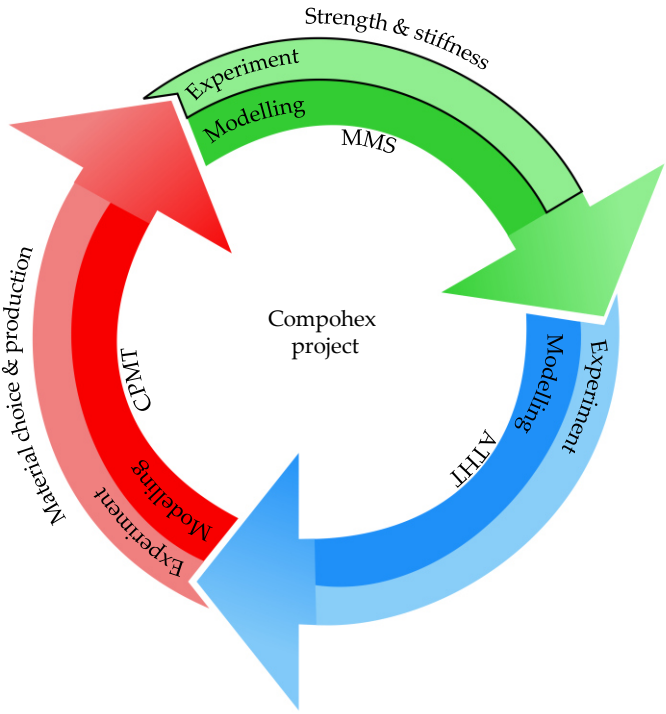

Figure 1-11: Overview of the different working groups in the Compohex project

1.5 Standardised test methods for heat exchanger materials

To determine the strength, stiffness, and creep resistance of a polymer or composite for heat exchangers, not much data is available. Reasons are the very specific conditions as high temperature, pressure load and the influence of fluid. To the author's knowledge, no test method is available that mimics the conditions well while measuring the strength precisely. However, different standardised tests are available that can help to identify potential heat exchanger materials [1,8]:

- relative thermal index [39]
- absorption of fluid [40]
- glass transition temperature [41,42]
- heat deflection temperature [43,44]
- tensile strength [45]
- flexural modulus [46]
- creep tests [47]

The following paragraphs shortly describe the different test methods:

Relative thermal index
The relative thermal index describes the ageing of material and the related degradation over time due to temperature. Samples are stored in an oven and a slow temperature cycle with four temperatures over seven weeks is performed. These cycles are repeated typically 20 times and specimens are tested in between in a relevant mechanical test, for example a tensile test. This results to a testing time of 2.7 years and requires about 90 samples (10 samples per batch, one batch tested every other cycle). From the mechanical values, the degradation in that specific property can be determined and an end-of-life approximated [39].

Absorption of fluid
If plastics are exposed over a large period of time to hot water, the material can degrade and turn brittle, swell or soften. This degradation is caused by water penetrating and reacting with the polymer. If the water absorption is minimal, the risk for long-term degradation is small. A test on water absorption according to ASTM D570 [40] indicates the severity of absorption in a test at room temperature over 24 h.

Glass transition temperature
The glass transition temperature is a specific characteristic for polymer-based materials. It describes the temperature when the amorphous regions transition from a solid, glassy state to a soft, rubbery state. Typical methods to find this temperature are differential scanning calorimetry (DSC) and dynamic mechanical analysis (DMA). Both methods are standardised as ASTM D7028 [41,42].

Heat deflection temperature
The test on heat deflection (ASTM D648 or DIN EN IS 75-1) serves the evaluation of material stiffness at elevated temperature [43,44]. A sample is placed in a bending setup, immersed in a bath of high heat transfer liquid like silicon oil. A specific load is applied and the temperature stepwise increased. The temperature when the sample deflects 0.25 mm is taken as heat deflection temperature and gives an indication of the maximal service temperature.

Tensile strength
Tensile strength can be measured by applying tensile force on a sample according to ASTM D638 [45]. The sample is typically in a rectangular or dogbone shape. During the tensile test, force and displacement are measured. From the resulting curve, important information about the material behaviour can be extracted. The tensile strength describes the ultimate strength the sample can hold before failure.

Flexural modulus
The flexural modulus can be determined in a 3-point bending test according to ASTM D790 [46]. The information is extracted equivalent to the ones of a tensile test.

Creep tests
Creep tests describe the time-dependent behaviour of a material under a constant load. Thereby, different loading types are possible like tension, 3-point bending or compression [47]. A typical real-time creep test lasts at least 1000 h (42 days). For tensile mode, an accelerated method is standardised as ASTM D6992 to provide data within 60 000 s (17 h) [48].

Raman et al. used this information to evaluate the suitability of a polymer as a heat exchanger. As a guiding value, the maximal humidity uptake is for example limited to 1% [8]. The tensile strength is seen as defining value for the pressure holding capacity, the flexural modulus as capability of bending of a coil, if required for the geometrical design [8]. The combination of these tests gives a good indication of the suitability of a material for a heat exchanger, but long-term performance will only show in service. In addition, the sample geometry and loading mode between the listed tests and a heat exchanger wall are different. Next to the standardised coupon tests, tests on a sample with the correct geometrical structure are needed.

Furthermore, all tests are lacking the correct conditions like the temperature gradient over the material, the correct fluid and the limited lifetime prediction compared to the lifetime expectancy of a heat exchanger. Wu [49] used a valid superposition principle on simple creep tests to predict the behaviour of polymers used in a tubular solar boiler for up to 10 years. This principle allows to make a life-time prediction from short testing times. However, a solar boiler is a very low-pressure heat exchanger and the correct loading is less relevant. For higher pressure applications (above 3 bar [50]), the existing tests are not sufficiently demonstrating the load. Furthermore, to predict long-term behaviour accurately, the measurement of the deformation needs to be accurate. This is not given in the current setups. Better test methods for the specific use of composites in the environment of a heat exchangers are needed.

Beyond the experimental testing, the Compohex project foresees a numerical analysis of strength and stiffness. It serves the prediction of material behaviour. Experimentally generated material properties can be used as an input. However, failure cannot be accurately predicted, since the failure mechanism in thermoplastic, short-fibre composite is not studied well.

The goal of this experimental PhD is therefore to examine the following points:

- Testing methods on different scales
  - subcomponent-scale
  - coupon-scale
  - small coupon-scale
  - interface-scale
- Components representative for heat exchanger wall
- Testing conditions representative for heat exchanger climate
- Instrumentation to extract relevant properties
- Provide accurate material properties for input into material models and long-term prediction

1.6 Objectives and outline of this dissertation

The state-of-the-art provides insufficient information and test methods for the use of thermoplastic composites in heat exchangers. It is therefore required to develop new testing methods. Thereby, the focus should lay on realistic conditions and the accurate measurement of strength and stiffness. As test methods, prototype testing and long-term studies seem indispensable to proof the performance of heat exchangers. On closer examination, lack of material knowledge exists on different levels of material testing, namely:

(i) on a subcomponent-scale where the geometry of heat exchanger walls is examined,

(ii) on a coupon-scale where the strength of the material is quantitatively determined and,

(iii) on a microscopic-scale that studies the interface between fibre and matrix to give input for a precise material model.

An overview of the different setups developed and/or used to measure on the different scales can be seen in Figure 1-12.

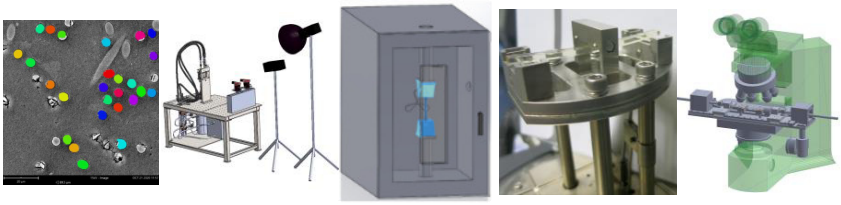

Figure 1-12: Different scales of test setups used to study potential heat exchanger materials

Before any analysis, it should be ensured that the material quality is sufficient to produce representative tests. Afterwards, different mechanical tests can be performed.

(i) For the in-service prediction of a heat exchanger, the test setup should be as similar as possible to the real-life application. This means, next to the material strength and stiffness, the performance of the geometry is to be considered. The sample has to be produced in the correct geometry of the heat exchanger wall as a representative subcomponent. Therefore, this testing is suited for a small selection of potential materials in combination with accurate geometry.

(ii) To test the pure material strength for a material evaluation, the influence of a specific geometry should be avoided. Standardised tests under in-service conditions are a convenient choice and allow for long-term predictions. Many different materials can be compared that way. Next to the classically used electromechanical test benches, dynamic mechanical analysis (DMA) can be used. Both methods complement each other. Electromechanical benches are rather suited for high loads in the range of 1 kN and upwards with a precision of around 0.2 N. DMA measures on the other hand are very precisely with a resolution of 0.00001 N, but are typically limited to less than 50 N. Long-term predictions are already well known on the electromechanical benches and can be directly applied. On DMA, the reproducibility is lacking, if the precision the machine is able to measure is not represented in the accuracy of the sample production and execution of the test and post-processing.

(iii) Even more precision is required, when not the full material, but the interaction between a single fibre and the matrix is studied. This adhesion determines the microscopic behaviour, which is part of the macroscopic strength and influences, together with the geometry, the performance of a full heat exchanger.

These examinations from subcomponent setup down to debonding of a single fibre from the matrix is considered in this PhD. In the following, the summary of each chapter is given and the key innovative aspects are highlighted. The state-of-the-art will be described per chapter, since the current level of knowledge differs per test method.

Chapter 2: Material quality inspection

Before mechanical tests are executed, the material should be inspected qualitatively. Flaws like voids or fibre clusters can be identified with microscopy and lead to material rejection before testing. In case of good composite quality, fibre content, orientation, and visual adhesion between fibres and matrix give important information for experimental testing and numerical simulation. Measurements of the thermal history and the moisture help to evaluate the later results from mechanical testing. **A routine was developed to do quality inspection systematically.**

Chapter 3: Subcomponent testing under temperature and pressure

After the material quality is ensured, the development of a new in-service product requires relevant tests. However, the build of a full heat exchanger is too expensive for classifying a new material. For this purpose, a prototyping **subcomponent setup was built** that allows for testing and evaluating of composite samples in the later geometrical structure and under the given conditions in a heat exchanger, namely temperature and pressure. **Optical strain measurements with digital image correlation allow for a detailed view of the strain distribution through glass and water.**

Chapter 4: Coupon testing at elevated temperature with digital image correlation

To compare many materials in short time, standardised tests offer great potential; however, composites with thermoplastic matrix are not sufficiently classified by a single test result. Temperature and speed determine the material behaviour significantly. Therefore, it is relevant to measure at different temperatures and strain rates. Thereby, the strain measurement should not lack in quality compared to tests at room temperature. **A test setup was assembled that combines DIC and a heat chamber of an electromechanical test bench**. **In tensile and creep studies, short and long-term behaviour was analysed.** The results of these tests led to the journal paper "Thermo-mechanical coupling of a viscoelastic-viscoplastic model for thermoplastic polymers: Thermodynamically derivation and experimental assessment" by A. Krairi et al. [38].

Chapter 5: Small coupon test with dynamic mechanical analysis

Dynamic mechanical analysis (DMA) is a method of mechanical material characterisation with the advantage of precise measurement under small loads, small samples and therewith a fast response to thermal changes. Before the method could deliver reliable results, analysis on the method itself was needed. It was found that the

DMA measurement accuracy and repeatability is strongly influenced by (i) the testing fixture and corresponding loading mode and (ii) the sample preparation. In combination with finite element simulations and in-situ strain measurements by digital image correlation (DIC), **the main influences on measurement accuracy of 3-point bending DMA were identified and subsequently used to determine measurement guidelines**. Using these guidelines, DMA measurements allow quantitative assessment of the viscoelastic response for rigid polymer and composite materials. This chapter is based on the publication "Influencing parameters on measurement accuracy in dynamic mechanical analysis of thermoplastic polymers and their composites" [51].

Chapter 6: Long-term predictions of small coupon tests

Based on reliable test results, achieved with dynamic mechanical analysis (DMA), long-term predictions can be made. To make predictions, a method called stepped isothermal method (SIM) can be used. Therefore, the same test is repeated at different temperatures and the results post-processed. Two different tests methods are available to obtain SIM data: (i) static creep tests and (ii) dynamic frequency sweeps. In this chapter, both methods are compared. It was found, that **both SIM methods in DMA deliver the same long-term predictions up to a decade and the predictions are reproducible.** Thereby, care needs to be taken in the reproducibility of the experimental raw data and the TTSP optimization using shift factors. This study is published as "Long-term stiffness prediction of particle filled polymers by dynamic mechanical analysis: frequency sweep versus creep method" [52].

Chapter 7: Interface study on debonding of a single fibre from the polymer matrix

Mechanical failure of composite materials does not only occur on a macroscopic level, but also on a microscopic level. The main failure mechanism there is the debonding between matrix and fibres. However, the debonding mechanism is not well explored yet in literature. Especially the combination of short fibres in thermoplastic matrix is hardly assessed. Based on existing experimental approaches described in literature, **a test method was developed and the equipment, a small-scale tensile stage that can be used under a microscope, was designed.** Preliminary experimental results on fully embedded short fibres were obtained and can form the basis for future experiments.

Chapter 8: Conclusions and outlook

In this final chapter, the work of this **PhD is positioned with respect to the state-of-the-art** of testing methods for composite heat exchangers. Improvements on measuring accuracy and the appropriate conditions are highlighted. Furthermore**, future research** possibilities based on the developed setups are discussed.

References

[1] C. Thibaud-Erkey and A. Alahyari, "Final Report for Project titled High Thermal Conductivity Polymer Composites for Low-Cost Heat Exchangers," 2016.

[2] W. Faes, S. Lecompte, Z.Y. Ahmed, J. Van Bael, R. Salenbien, K. Verbeken, and M. De Paepe, "Corrosion and corrosion prevention in heat exchangers," *Corrosion reviews*, vol. 37, 2019, pp. 131–155.

[3] S. Kakaç, H. Liu, and A. Pramuanjaroenkij, *Heat exchangers: selection, rating, and thermal design*, CRC press, 2012.

[4] "Copper price history, online: https://capital.com/copper-price-history," 2021.

[5] "Europe Heat Exchanger Market - Growth, Trends, COVID-19 Impact, and Forecasts (2021 - 2026) [online: https://www.mordorintelligence.com/industry-reports/europe-heat-exchanger-market]," 2020.

[6] "Alfa Laval, Types of gasketed plate heat exchangers, https://www.alfalaval.com/microsites/gphe/types/," 2020.

[7] C. Wu, S.C. Mantell, and J.H. Davidson, "A method for measuring the creep behavior of pressurized polymer tubing," *Experimental mechanics*, vol. 41, 2001, pp. 368–374.

[8] R. Raman, S. Mantell, J. Davidson, C. Wu, and G. Jorgensen, "A review of polymer materials for solar water heating systems," *J. Sol. Energy Eng.*, vol. 122, 2000, pp. 92–100.

[9] Toshiba, "Air to air heat exchangers," 2017.

[10] J.P. Shuster and A.J. Cesaroni, "Heat exchanger fabricated from polymer compositions," 1990.

[11] I. Darawsheh, P. Rodgers, V. Eveloy, S. Bojanampati, A. Diana, and F. Al Maskari, "Thermal and Mechanical Performance Assessment of Polymer Composite Materials for Heat Exchanger Applications," 2016.

[12] T. Wieme, "Designing the formulation variables and processing conditions for controlling thermal conductivity of thermoplastic composites," Ghent University, 2020.

[13] "Copper properties [online: http://matweb.com/search/DataSheet.aspx?MatGUID=9aebe83845c04c1db5126fada6f76f7e&ckck=1, 09/2021]."

[14] "Thyssenkrupp Materials (UK) Ltd, Material data sheet: Stainless Steel 1.4301 - 304," 2018.

[15] "Polymer Database PPS, [online: http://polymerdatabase.com/Commercial%20Polymers/PPS.html, 09/2021]."

[16] J. Caprano, *Technoform Heat transfer solutions*, Technoform Kunststoffprofile GmbH, 2019.

[17] "Surface roughness [online: https://www.enggcyclopedia.com/2011/09/absolute-roughness/, 09/2021]."

[18] D.M. Zarkadas and K.K. Sirkar, "Polymeric hollow fiber heat exchangers: An alternative for lower temperature applications," *Industrial & engineering chemistry research*, vol. 43, 2004, pp. 8093–8106.

[19] C. T'Joen, Y. Park, Q. Wang, A. Sommers, X. Han, and A. Jacobi, "A review on polymer heat exchangers for HVAC&R applications," *International journal of refrigeration*, vol. 32, 2009, pp. 763–779.

[20] J.G. Cevallos, A.E. Bergles, A. Bar-Cohen, P. Rodgers, and S.K. Gupta, "Polymer heat exchangers—history, opportunities, and challenges," *Heat Transfer Engineering*, vol. 33, 2012, pp. 1075–1093.

[21] X. Chen, Y. Su, D. Reay, and S. Riffat, "Recent research developments in polymer heat exchangers–A review," *Renewable and Sustainable Energy Reviews*, vol. 60, 2016, pp. 1367–1386.

[22] X. Chen, Y. Su, D. Reay, and S. Riffat, "225: A review of polymer heat exchanger," *Sustainable Energy*, 2015, p. 604.

[23] A.R.J. Hussain, A.A. Alahyari, S.A. Eastman, C. Thibaud-Erkey, S. Johnston, and M.J. Sobkowicz, "Review of polymers for heat exchanger applications: Factors concerning thermal conductivity," *Applied thermal engineering*, vol. 113, 2017, pp. 1118–1127.

[24] "CB group, https://www.cbgroep.be/," 2018.

[25] R. Sakko, "Waste heat recovery from flue gsaes using polymer heat exchangers," *https://heatmatrixgroup.com/*, Heat Matrix, 2019.

[26] L. Zaheed and R. Jachuck, "Review of polymer compact heat exchangers, with special emphasis on a polymer film unit," *Applied thermal engineering*, vol. 24, 2004, pp. 2323–2358.

[27] M. De Paepe, L. Cardon, W. Van Paepegem, and et al., "SBO Project proposal, IWT Vlaanderen - Composite Heat Exchangers (COMPOHEX)," 2015.

[28] M. De Paepe, L. Cardon, W. Van Paepegem, and et al., "SBO Project Endreport, SBO project no.150013 - Composite Heat Exchangers (COMPOHEX)," 2020.

[29] "Bekaert better together, company website: https://www.bekaert.com/," 2021.

[30] "Parker Hannifin, company website: www.parker.com," 2021.

[31] "Vyncke clean energy technology, company website: https://www.vyncke.com/," 2021.

[32] "Daikin, company website: www.daikin.be," 2021.

[33] "Atlas Copco, company website: www.atlascopco.com," 2021.

[34] "VITO, company website: www.vito.be," 2021.

[35] "UGent, Research group applied thermodynamics & heat transfer, website: https://www.ugent.be/ea/eemmecs/en/research/stfes/thermo," 2021.

[36] "UGent, Research group Centre for polymer and material technologies CPMT, website: https://www.ugent.be/ea/match/cpmt/en," 2021.

[37] "UGent, Research group Mechanics of materials and structures MMS, website: https://www.ugent.be/ea/match/mms/en," 2021.

[38] A. Krairi, I. Doghri, J. Schalnat, G. Robert, and W. Van Paepegem, "Thermo-mechanical coupling of a viscoelastic-viscoplastic model for thermoplastic polymers: Thermodynamical derivation and experimental assessment," *International Journal of Plasticity*, vol. 115, 2019, pp. 154–177.

[39] UL746B, "Polymeric Materials—Long Term Property Evaluations," 1998.

[40] A.S. D0570, *Standard Test Method for Water Absorption of Plastics*, 1998.

[41] *ASTM D7028-15: Glass Transition Temperature (DMA Tg) of Polymer Matrix Composites by Dynamic Mechanical Analysis (DMA)*, ASTM International, 2015.

[42] *ASTM D3418 - 15: Standard Test Method for Transition Temperatures and Enthalpies of Fusion and Crystallization of Polymers by Differential Scanning Calorimetry*, ASTM International, .

[43] *ASTM D648-07: Standard Test Method for Deflection Temperature of Plastics Under Flexural Load in the Edgewise Position*, ASTM International, 2007.

[44] *DIN EN ISO 75-1: Kunststoffe - Bestimmung der Wärmeformbeständigkeitstemperature - Teil 1: Allgemeines Prüfverfahren*, DIN Deutsches Institut für Normen e.V., .

[45] *ASTM D638 Standard Test Method for Tensile Properties of Plastics*, ASTM International, 2014.

[46] *ASTM D790-10 Standard Test Methods for Flexural Properties of Unreinforced and Reinforced Plastics and Electrical Insulating Materials*, ASTM international, 2010.

[47] *ASTM D2990 Standard test method for tensile, compressive, and flexural creep and creep-rupture of plastics, 2009*, ASTM International, .

[48] *ASTMD6992-03: Accelerated Tensile Creep and Creep-Rupture of Geosynthetic Materials Based on Time-Temperature Superposition Using the Stepped Isothermal Method*, ASTM International, 2015.

[49] C. Wu, S.C. Mantell, and J. Davidson, "Polymers for solar domestic hot water: long-term performance of PB and nylon 6, 6 tubing in hot water," *J. Sol. Energy Eng.*, vol. 126, 2004, pp. 581–586.

[50] "Pressure in solar domestic hot water system [online: http://www.ecohisolar.co.uk/solar-thermal/how-do-solar-thermal-systems-work/, 2021]."

[51] J. Schalnat, D.G. Gómez, L. Daelemans, I. De Baere, K. De Clerck, and W. Van Paepegem, "Influencing parameters on measurement accuracy in dynamic mechanical analysis of thermoplastic polymers and their composites," *Polymer Testing*, vol. 91, 2020, p. 106799.

[52] J. Schalnat, L. Daelemans, I. De Baere, K. De Clerck, and W. Van Paepegem, "Long-term stiffness prediction of particle filled polymers by dynamic mechanical analysis: Frequency sweep versus creep method," *Polymer Testing*, 2021, p. 107368.

Chapter 2

Material quality inspection

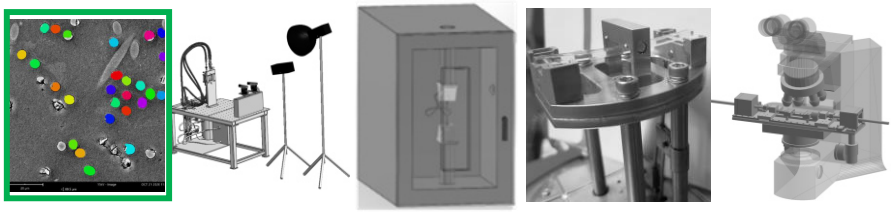

Quality check

Abstract: In this chapter, the sample production and material quality control for mechanical testing is described. Thereby, especially optical methods were used to control for voids or inclusions in the matrix as well as the condition of the fillers before and after mechanical testing. Bad quality can be identified before time-consuming mechanical tests are executed and in case of good quality, knowledge about fibre content, orientation, and visual adhesion between fibres and matrix give important information for experimental testing and numerical simulation. Measurements of the thermal history and the moisture help to evaluate the later results from mechanical testing. A routine for systematic quality inspection was developed.

2.1 Material selection

Quality control is of high importance for any material. In a heat exchanger, the quality in-service can only be controlled by opening the heat exchanger, requiring shutting down the heat exchanger and any possible production lines that depend on it. The more at risk the material of the heat exchanger is, the more often the material needs to be controlled. As an example, the aftercooler for chloride gas [1] is in constant contact with acids that are leading to corrosion. Also in less dangerous cases, like the air-to-air heat exchanger from dusty areas like farms, can lead to a quick fouling and therefore clogging of the channels and requires regular cleaning [2]. Maintenance frequency can be reduced by using material that is of good quality and therewith durable and little affected by corrosion, little prone to fouling and easy to clean.

Polymers are fulfilling these requirements; they do not corrode in the classic sense of an electromechanical reaction and their smooth surface prevents material from sticking to it easily. Nonetheless, the material needs to be chosen carefully and the initial material quality needs to be verified. Due to an increasing demand for recyclability from industry and advantages in production possibilities, thermoplastic polymers were in focus of this study. Next to their ability to be re-molten, they also offer the potential to be thermoformed after sheet production. Other methods like injection moulding or 3D printing could be used, but are less suited for the production of sheet materials in large quantities. The ability of the materials to be formed increases the opportunities in structural design. However, pure plastics do not conduct heat well; they are in fact rather insulating. To improve the heat conductivity, fillers like carbon fibres or graphite flakes can be used. For the thermoforming, short fibres or particles are preferred, since they can more easily be shaped. They also allow for a material production in extrusion or injection process. In addition, their orientation in the material can be influenced [3] to increase heat transfer through the material. Nevertheless, the re-shaping and the adding of fillers results in more factors in the material production that can influence the quality of the final material.

For the Compohex project, material combinations were produced in-house by the project partner Centre for Polymer and Material Technologies CPMT or purchased from industry. An overview can be found in Table 2-1 and Table 2-2 and their abbreviations are explained below the second table. Reason for the high amount of material combinations is the parallel work on the flow design, the material choice, and the strength. Primary concerns were the improvement of the thermal conductivity κ and the strength. Each research group improved material properties over time, which led to a big variety of composites. Throughout this PhD, several of these materials are considered in different experiments.

Table 2-1: Overview of materials provided

Material	Material supplier	Sample supplier	Why considered?
PA6	Solvay	CPMT	Low density, no compatibiliser needed, high κ
PA6_2	Leartiker	Leartiker	Low density, no compatibiliser needed, high κ
PA6-CF_1	Leartiker/Astar	Leartiker	High tensile strength
PA6-CF_2	Leartiker/Safran	Leartiker	High tensile strength
PA6-GF	Solvay/Asbury	CPMT	High κ
PC	Bayer	Conrad.be	High temperature
PC-CF	Trinseo/Timrex	CPMT	High temperature
PESU	Solvay	Solvay	High temperature
PESU-GL	Solvay	Solvay	High strength
PP	Sabic	CPMT	Low price
PP-GF-CNT	Sabic/Asubury/Nanocyl	CPMT	High tensile strength
PP-GF	Technoform	Technoform	High κ
PPS-GF	Technoform	Technoform	High κ
PS	KVS	Conrad.be	Low price

Table 2-2: Trials to enhance thermal conductivity by optimising material combination and filler orientation [3,4] produced by CPMT

Material	Material supplier
ABS	LG chem.
ABS-GF	LG chem./Asbury
HDPE	Sabic
HDPE-GF	Sabic /Asbury
PC-GF	Trinseo/Asbury
PET-GF	Eastman/Asbury
PLA	Natureworks
PLA-GF	Natureworks/Asbury
PP-BN	Sabic/HeBoFill
PP-BN-CNT	Sabic/HeBoFill/Nanocyl
PP-CF	Sabic/Asbury
PP-CF-CNT	Sabic/Asbury/Nanocyl
PP-GF	Sabic/Asbury
PP-GF-CF	Braskem/Asbury/Asbury
PP-GF-CNT	Sabic/Asbury/Nanocyl
PP-talc	Sabic/Finntalc
PP-talc-CNT	Sabic/Finntalc/Nanocyl
PS	Styrolution
PS-GF	Styroltution/Asbury

ABS	**Acrylonitrile-butadiene-styrene**	**LG-Chem, HI-121**
BN	**boron nitride**	**HeBoFill 490**
CF	**carbon fibre**	**Astar Zoltek px35 50K carbon fibre/ Safran Hexcel 12k Carbon fibre / Timrex AGM94MF0159**
CNT	**carbon nano tubes**	**Nanocyl PP WMCTN20% masterbatch**
GF	**Graphite flakes**	**Asbury, 3806 size 19µm**
GL	**glass fibre**	**Solvay, Veradel AG330 PESU GL**
HDPE	**High density polyethylene**	**Dow, 25055E**
PC	**polycarbonate**	**Bayer Makrolon GP** **Trinseo, Calibre 201**
PESU	**polyethersulfone**	**Solvay, Veradel A301**
PET	**Polyethylene terephthalate**	**Eastman GP001**
PLA	**Polylactic acid**	**Natureworks, 3100HP**
PA 6	**Polyamide 6**	**Solvay Technyl C230 Natural** **Leartiker PA6**
PP	**Polypropylene**	**Sabic, 575P** **Braskem PP DR115**
PS	**Polystyrene**	**KVS Polystyrolplaat Reely** **Styrolution Ineos 165N and 124N**
talc	**hydrated magnesium silicate**	**Finntalc M05N**

Due to the amount of different materials, time-intensive testing series should only be performed on materials with a good quality. A procedure was developed to detect flaws as early on in the process as possible. To understand the procedure, the production process is explained first, since it is the biggest potential origin for quality issues. Afterwards, the individual components of the material as well as their interaction and history are controlled in concern of their quality using microscopy and differential scanning calorimetry (DSC).

Materials were controlled on their quality according to this protocol. The materials that passed are listed in Table 2-3. Every material has an outstanding characteristic that makes the material worth considering for the use in heat exchangers are underlined in the table. All these materials were tested at least in tensile or DMA testing.

Table 2-3: Mechanical characteristics of materials that passed the quality check. Their best properties are underlined

Material	E [MPa]	UTS [MPa]	ε [%]	HDT [°C]	€/kg	κ [W/mK]	ϱ [g/cm³]
PA6_2	3200	60	>20	75	2.02	0.26	1.12
PA6-CF_1	16200	197	2.19	-	-	-	1.2
PA6-CF_2	17300	210	3.8	-	-	-	1.2
PC	2400	60	6	127	3.12	0.2	1.2
PESU	2690	89	6.5	200	6.92	0.13	1.37
PP	1950	22	-	54	1.38	0.24	0.91
PP-GF	7836	29	0.47	157	-	14	1.58
PPS-GF	16523	48	0.30	-	-	14	1.78

E **Tensile modulus [MPa]**
UTS **Ultimate tensile strength [MPa]**
ε **Elongation at break [%]**
HDT **Heat deflection temperature (1.82 MPa) [°C]**
κ **Thermal conductivity [W/mK]**
ϱ **Density [g/cm³]**

With good quality ensured, different mechanical tests were performed to measure strength and stiffness of the material. Then, fracture surfaces were optically analysed to evaluate the failure behaviour of the materials. This is relevant, since composites from thermoplastic matrix and short carbon fibres under a specific loading and environmental condition are less studied in literature than for example glass-epoxy composites [5]. This leads to a lack in knowledge about the debonding mechanism and well calibrated material models. As a first step, visual inspection can help to understand the failure mechanism better. This chapter shows techniques of quality

control, primarily based on optical methods. The results also provide information about the composite composition like fibre orientation and fibre length, serving as a basis for numerical analysis for the following chapters.

2.2 Injection moulding

To understand the origin of potential lacks in quality, the production procedure of short fibre composites is summarised. Injection moulding is a common way to produce parts in industry, but also for the production of mechanical testing samples, it is a standard procedure. For this purpose, fillers and matrix are compounded with a twin screw extruder first, forming a filament with a die. A water bath cools and therewith solidifies the material. To be able to feed the extruded filament into the injection machine, the material is chopped into pellet size. The full procedure is visualised in Figure 2-1a.

The production of material requires a lot of experience, since many parameters are flexible and need to be adjusted depending on the polymer and filler type. Before processing, the material needs to dry to avoid water vapour inside the material. Different temperatures or temperature profiles have to be set as well as pressures and speeds. These settings ensure the overall processibility, the melting of the polymer without degrading it, the crystallinity when cooling and the dispersion of the fibres. The speed of the production as well as the chopping into pellet size is crucial to maintain the desired filler size. After the extrusion, the pellets need to be dried again. Dry pellets can be used to injection mould material into shapes, for example dogbones according to ISO 527-1 [27]. Again, pressure, temperature, and speed need to be optimised for the process. In Figure 2-1b, the injection process of standard dogbones is displayed.

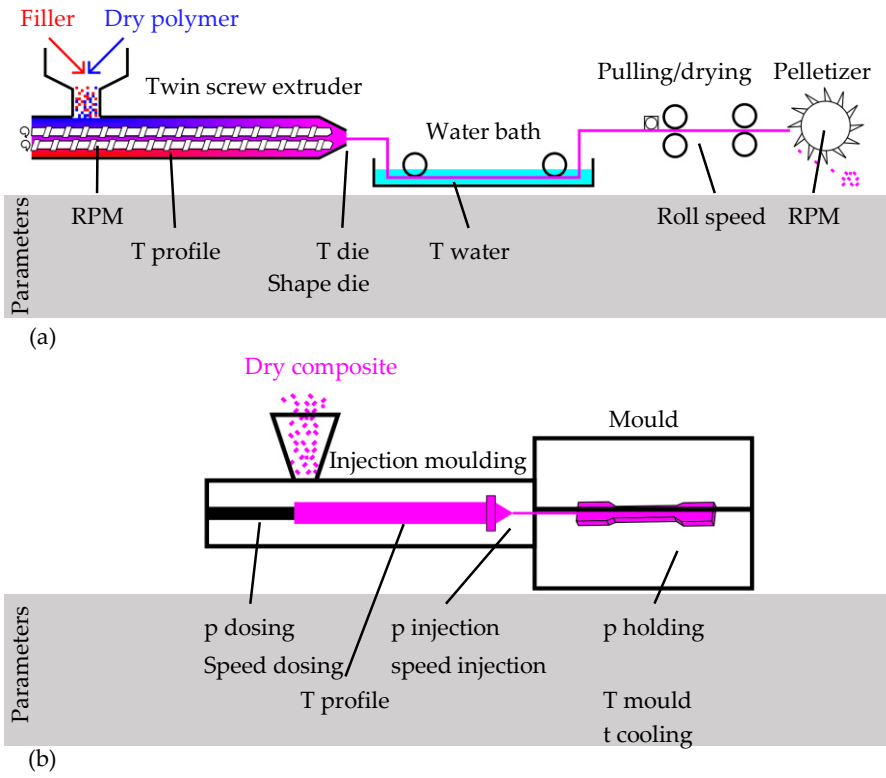

Figure 2-1: Schematic of (a) extrusion of pellets and (b) injection moulding of dogbones. Parameters RPM= revolutions per minute, p=pressure, T=Temperature, t= time highlighted for both processes [6]

2.3 Quality control

In a short fibre composite, different quality issues can occur. Goal of a quality control is to discover imperfections. The following areas are considered for inspection:

- Polymer (matrix) for voids or unwanted inclusions
- Fibre for equal length, orientation and distribution
- Fibre-matrix-interface for good adhesion

In addition, the thermal history and conditioning of the materials are also taken into account.

2.3.1 Polymer (matrix)

The quality of the raw components is crucial. Standards for the quality control of matrix material mainly exist for thermoset resin, since they are used for decades in

industries like aerospace for safety-relevant structures. Standardised tests exist for the gel-time and viscosity [7,8]. However, these parameters are irrelevant for thermoplastic resins. There the age and thermal history are determining the quality of the matrix and can be assessed by differential scanning calorimetry (DSC). The procedure is described in the section 2.3.4 Thermal history. Next to the pure quality of the resin, voids and unwanted inclusions introduced by the production process are critical [9]. Typically, voids are not visual on the surface of the sample, but occur in the middle of the sample. Voids can arise from wet polymer, chemical gases, air or wrong pressure; inclusions from contamination of the pellets or residuals in the machine [10]. Different methods exist to detect flaws in the matrix, which classify into non-destructive and destructive methods [10]. The main techniques and their advantages and disadvantages are listed in Table 2-4.

Table 2-4: Advantages and disadvantages of the main techniques used for void characterisation [10]

Test method	Measurable characteristics	Advantages	Disadvantages
Ultrasonic testing	• Void content • Planar size • Planar distribution	• Precise • Non-destructive	• Needs coupling agent • Flat, smooth surface needed
Micro-CT	• Void content • Size • 3D shape • Distribution	• Relatively accurate • 3D analysis • (Non-destructive)	• Needs small samples for high resolution • Location-biased • Time consuming • Costly • Carbon fibres hard to detect
Density determination	• Void content	• Easy and inexpensive • Relatively quick	• Accuracy uncertain • Destructive • Needs density input
Microscopy	• Void content • Size • 2D shape • Distribution	• Easy and inexpensive • Relatively quick • 2D analysis	• Section-biased • Location-biased • Needs multiple analysis • Destructive

Non-destructive methods are for example ultrasound or CT-scan, but also laser vibrometry and infrared thermography are known [11]. Voids can be detected with all methods, but the time-investment and equipment make the methods more expensive than common destructive techniques. Furthermore, the resolution is typically limited to the range of millimetres which leaves the amount and shape of the voids uncertain. CT-scans can reveal voids as a 3D-image and also show fibre orientations, if the

contrast between matrix and filler is high. However, the typical sample size for a high resolution CT-scan is a cubical of a few millimetres [12], since as a rule of thumb, the resolution is 1/1000 of the sample size. In case of bigger samples, the high-resolution CT-scan method is destructive, since the sample needs to be cut and the information is local, similarly to the observation in a microscope. Due to the higher costs and time of CT-scan compared to microscopy, the method is less interesting.

Density determination is a way to compare the measured density of the material with the theoretical one without voids. If the values differ, a quality issue can be assumed. This method is fairly easy, but gives no information about void size and distribution.

Microscopy and visual inspection is likely the most flexible and precise method for a 2D location. Voids are typically located in the inside of the sample. In a first step, the relevant layer is revealed in a destructive manner. Depending on how critical voids are, the observation method can be adapted from naked eye over light microscopy to scanning electron microscope (SEM). Shape, size and distribution of voids can be detected. Optical counting and area fraction are useful methods to determine the severity in the observed location [11,13]. Thereby, fracture surfaces can be observed as well as polished surfaces.

In Figure 2-2 different inclusions and voids are shown from 3.3 mm down to 0.5 μm diameter observed in different magnifications. A 300 μm big inclusion can be seen on the fracture surface of a pigmented PA6 sample after tensile test (Figure 2-2a). It was to spot by naked eye and magnified with a light microscope for the picture. Also the void in Figure 2-2b in the centre of a PA6 sample could be seen by naked eye after the sample was cut in half and roughly polished. With the help of a light microscope, smaller voids can be detected. On the example of polished carbon fibre filled PC (Figure 2-2c) the void distribution is shown. Next to the voids, also the fibre orientation is visible. Smaller voids are only visible with an electron microscope as in Figure 2-2d on the example of a fracture surface of graphite filled PA6. A single void in that size has no noticeable impact on the composite strength, but a cluster of voids can lead to severe weaknesses. Therefore, a good executed microscopic examination is relevant and considered in this research.

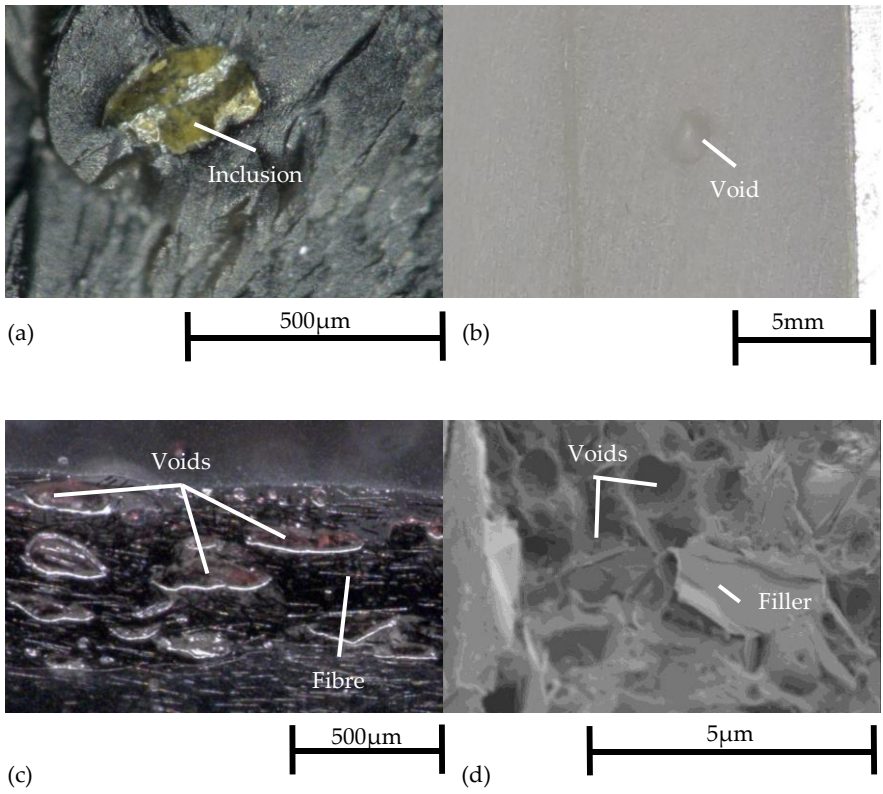

Figure 2-2: (a) Inclusion in PA6_2 and (b-d) voids in different injected polymers and composites (PA6, PC-CF, PA6-GF). Detection method varies from size of void from (b) visual detection to (c) light microscope or (d) electron microscope

The effect and severity of inclusions, voids or surface quality cannot be given as a general rule. Rather, the application, the material thickness, the material type and the production process are giving boundaries for every situation. In fact, inclusions and voids should always be kept to a minimum and the surface roughness depends on the filler-matrix combination and application.

2.3.2 Fibres

To produce a composite of high quality, the quality of the fibres needs to be high. The higher the tensile stiffness of the individual fibres is the stiffer the composite can be. A tensile stage for individual fibres (for example Favimat [14]) can be used [15]. This test is only applicable if the fibre length is at least 15 mm.

Next to the strength of the fibre, the surface quality determines the later adhesion with the matrix. Thereby, knowledge about the surface structure as well as the shape of the fibre end is important to predict the bonding ability to the matrix. Scanning electron

microscopy (SEM) with high magnification on the fibres before processing allows seeing the structure and measuring the fibre diameter, as shown in Figure 2-3.

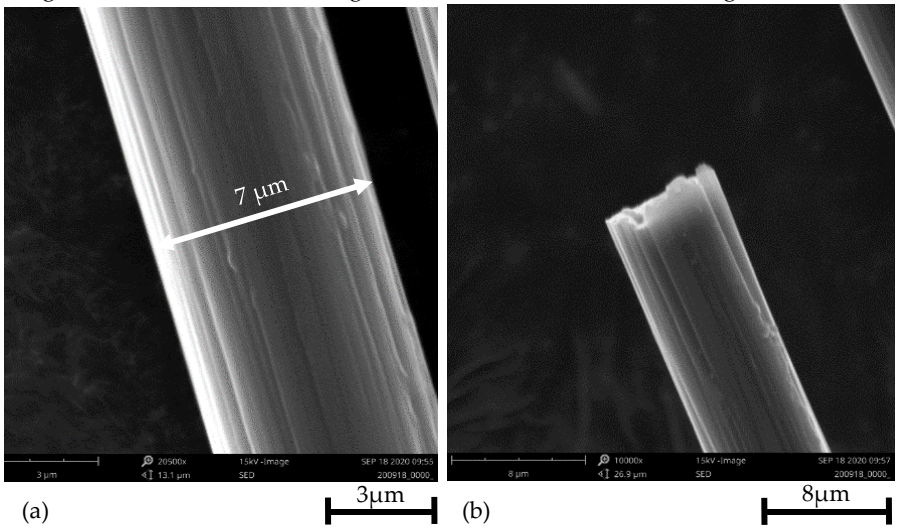

Figure 2-3: Quality of fibre surface under SEM: (a) fibre surface and diameter, (b) fibre end, relevant for simulation

Furthermore, parameters like fibre orientation and distribution in the matrix determine the strength of the composite [16]. To measure them, the material needs to be polished and for SEM imaging gold sputtered in case of low electric conductivity [11]. A high polishing quality is of importance for an overall sharp image without scratches or pulled out particles. For composites with PA6 matrix and carbon or graphite fillers, the routine in Table 2-5 was developed and optimised to showed successful results. Since the material is abrasive, relatively short polishing times, low pressure (5 N) and low rotation speed (150 rpm) suffice and prevent damage of the composite surface. In the last steps, a water-based diamond paste is used as a polishing compound. It was shown that longer polishing time leads to more diamond particles pushed into the matrix and falsify the image, as shown in Figure 2-4.

Table 2-5: Polishing steps for fibre analysis in PA6

Grit	Polishing time [s]	Lubricant
320	15	water
800	45	water
1200	120	water
2000	210	water
mol	210	diamond paste 3 µm
nap	300	diamond paste 1 µm

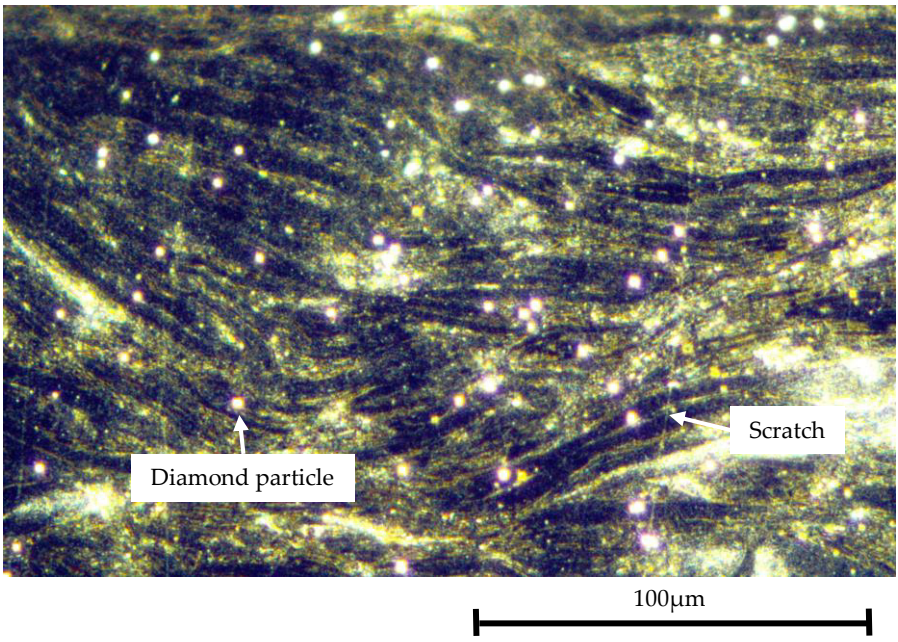

Figure 2-4: Badly polished sample with scratches due to too short polishing times at lower grits and diamond particles due to too long polishing times at higher grit

A polished sample can be observed under the microscope to analyse the length and distribution of the fibres. The dimensions of the fibres can be taken before embedding them in the polymer matrix, but the processing, especially in the twin screw extruder and pelletizing, can be abrasive to the fibre and change their dimensions. The fibre length is difficult to measure in a single polished layer of the composite, because a slight misalignment of the fibre makes the fibre appear shorter. For that reason, burning tests are used. Under heat, the matrix degrades and only the fibre is left. Microscopic imaging then makes it possible to measure the length of the exposed fibres. By weighing the composite before and after the burning step, also the fibre weight fraction can be controlled.

To measure the diameter after processing, polishing perpendicular to the fibre suffices. Depending on the fibre diameter, optical microscopy or SEM is needed. For carbon fibres, the fibre analysing tool of the electron microscope Phenom Pro Suite – ParticleMetric [17] was used to detect the fibres and measure their diameters as in Figure 2-5. The individual fibres are highlighted in random colour for visual separation.

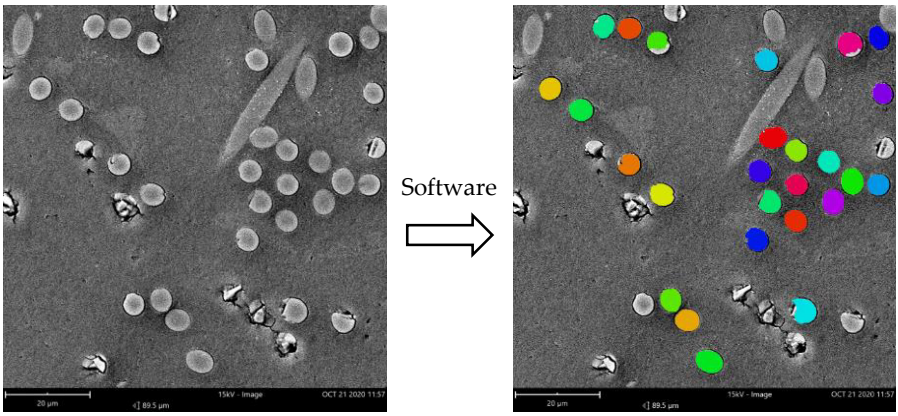

Figure 2-5: SEM-Detection of fibre cross-sections to measure their diameter

The production process also influences the orientation of the fibres. In the injection moulding, a skin and a core layer form, illustrated in Figure 2-6a. In the skin layer, the flowing speed and therewith the flow velocity is lower than in the core because of friction, allowing the fibres to orient in parallel to the moulding edge. In the core layer, the polymer flows faster and the particles are rather oriented perpendicular to the flow [16].

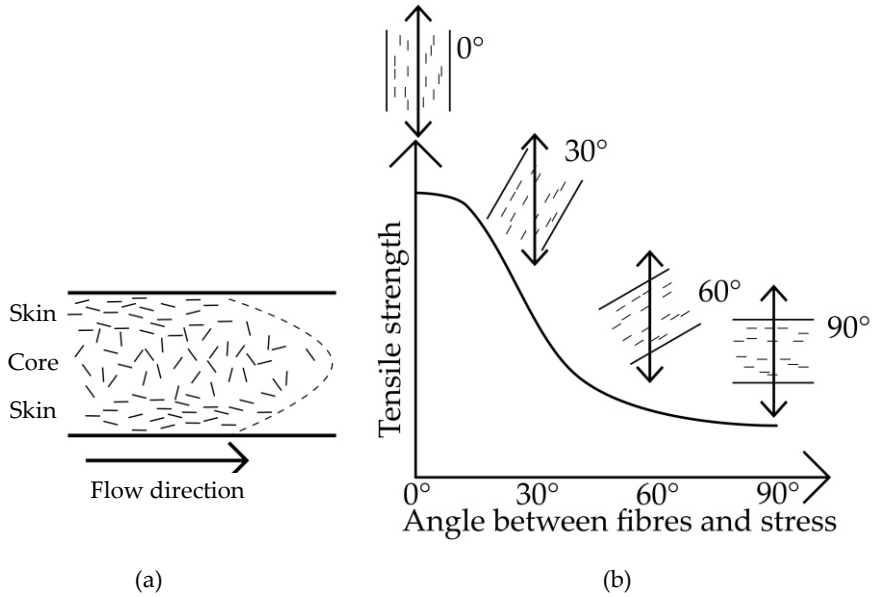

Figure 2-6: Fibre orientation (a) depending on the flow direction and (b) its influence on the tensile strength [18]

Knowledge about the thickness of the different layers can help to estimate the strength of the composite, since skin and core layer contribute in an unequal manner to the

strength of the composite due to the different fibre orientations (Figure 2-6b). Experimentally, different layers and orientations can be revealed from inside the polymer by polishing as to see in Figure 2-7. The skin and core layer are well visible in the cross section as well as in different depth throughout the thickness.

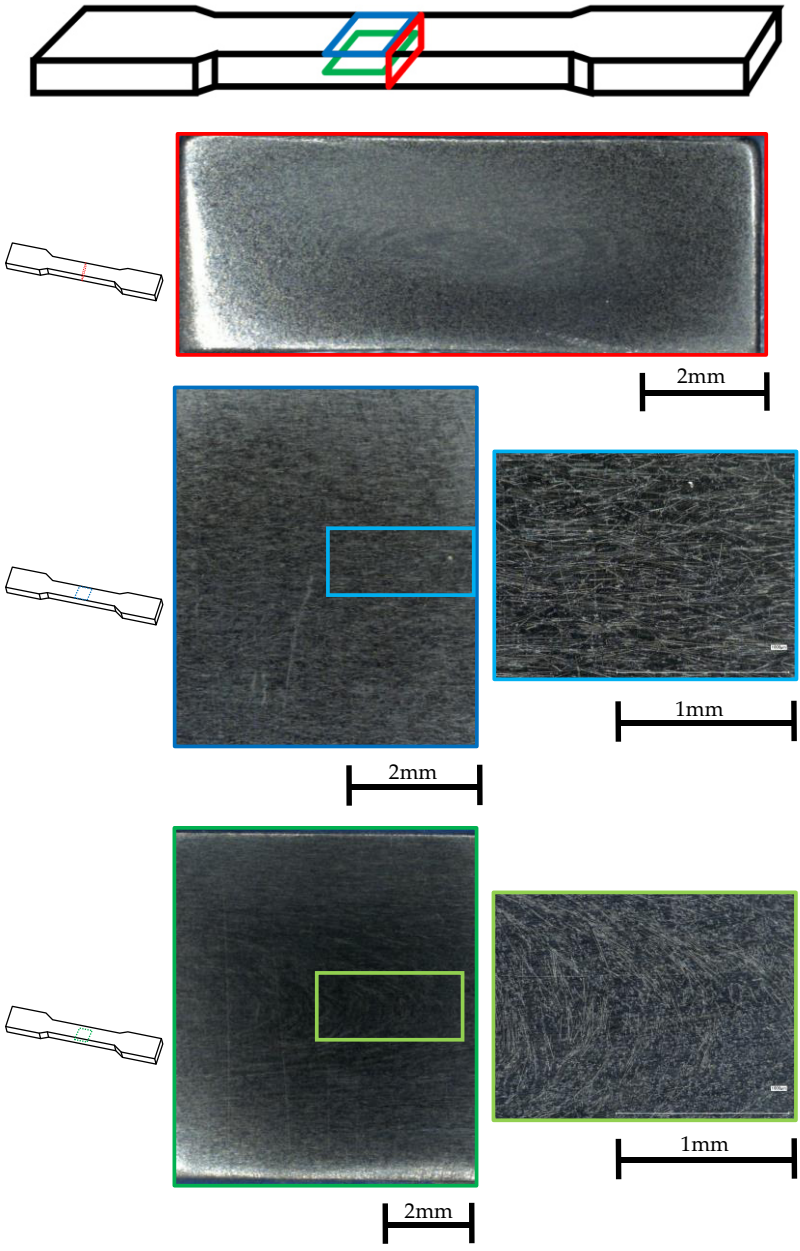

Figure 2-7: Cross section (red), skin layer (blue) and core layer (green) of injection moulded carbon fibre reinforced PA6 sample

2.3.3 Fibre-matrix-interface

The interfacial strength between fibre and matrix is of high interest, since it determines the eventual strength of the full composite. However, this measurement is impossible in a conventional test on an injected dogbone, since the value of the interfacial strength overlaps with effects like fibre length, orientation and distribution. Instead, tested samples from a conventional mechanical test like tensile test can be taken and the fracture surface qualitatively observed under the SEM. The image gives an idea about the adhesion. An example for a good adhesion is shown in Figure 2-8a and b on the example of PA6 with carbon fibres from this project. Even after a tensile test, the matrix still covers the fibre at least at the ends and the matrix around the pulled fibres widened instead of the interface just failing in a simple pull-out of the fibre. In case of bad adhesion, as in the examples from literature c and d, the fibres are detached from the matrix without residuals on the fibre surface. In Figure 2-8c, the fibres are not even covered by the matrix, but just surrounded.

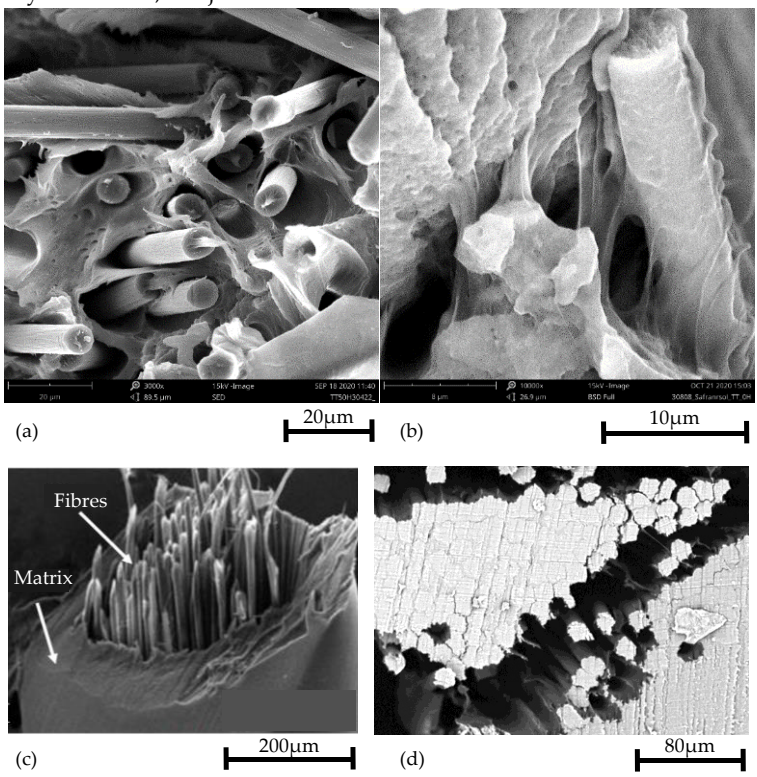

Figure 2-8: Examples of good adhesion are (a) tensile load did not pull-out the fibres immediately (b) matrix covers detached fibre (PA6-CF_2). Examples of bad adhesion are (c) lack of matrix penetration in fibre bundle and (d) fibre detaching under perpendicular tensile load (PET with aramid fibres [19])

2.3.4 Thermal history

For semi-crystalline polymers, the degree of crystallinity and amorphous phases depends on the speed of cooling [20,21]. For injection moulding, it is therefore relevant to control the cooling speed of the mould and determine the temperature at which the mould can be opened. The standardised heat deflection test gives information at which temperature the material is form stable [22,23]. In composites, the crystallinity is also strongly influenced by the fillers, since they work as nucleating agents. The resulting degree of crystallinity can be verified using differential scanning calorimetry (DSC). The crystallinity is considered to have a significant impact on the mechanical behaviour, but has not been investigated further in the current work. Overall, the DSC scan can be used to determine relevant phase transitions of the material, as for example the glass transition temperature Tg [24]. In Figure 2-9 an example DSC scan of polypropylene with a graphite filler content of 75 wt% (50 vol%) (PP-GF) is shown. No Tg is visible, since the scan started only at 25°C and the expected Tg is below room temperature. In addition, polypropylene does not show a very distinct Tg and the high filler content can make transitions less visible, since the actual mass of the polymer is very small compared to the full sample mass. In this first heating cycle, the thermal history of the production is visible. A first melting point at 165°C and a second melting peak at about 180°C occur, indicating that the matrix contained two different crystalline structures. The knowledge of the main melting temperature is crucial for mechanical tests to know the upper temperature limit for the sample stability during mechanical tests.

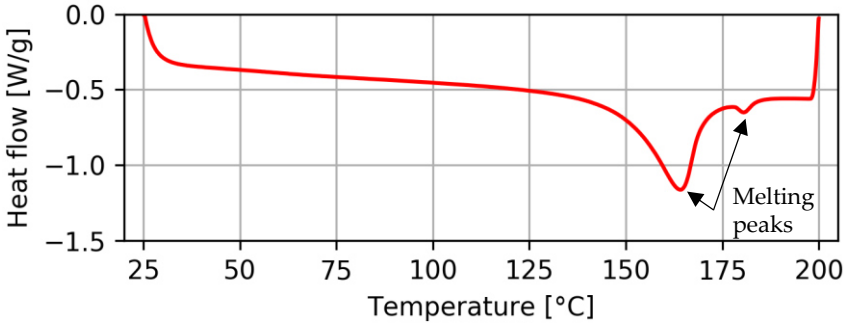

Figure 2-9: DSC scan to find transition zones and information about crystallinity

2.3.5 Conditioning

Some thermoplastics are very sensitive to moisture. It is therefore not only relevant to control the moisture content before injection moulding, but also before mechanical testing. The moisture content can be calculated by weighing the wet and dried material [25]. To condition the sample at a specific humidity, different protocols are

available. The air around the sample is typically set to a specific humidity by either using an electric climate chamber with humidity control or an oven in combination with an aqueous solution [26]. The achievable relative humidity lays between 0 and 99%. In case of permeable polymers, the humidity reaches to the centre of the specimen. To test material for the application in heat exchangers, material should be conditioned to the environment in service. In low-pressure heat exchangers, humidity containing air or water are possible fluids and the conditioning is possible according to standard procedures. If another fluid is used or the pressures are high, the sample should be stored under those circumstances prior testing. For this purpose, the project partner ATHT built the pressure vessel in Figure 2-10. In a volume of 2 L test samples can be placed. The chamber can be filled with different, commonly used refrigerants like R22 or R134a and can be pressurised up to 45 bar at 80°C. The soaked samples can be taken out for mechanical testing, which allows studying the influence on the mechanical performance of conditioning with pressurised refrigerant.

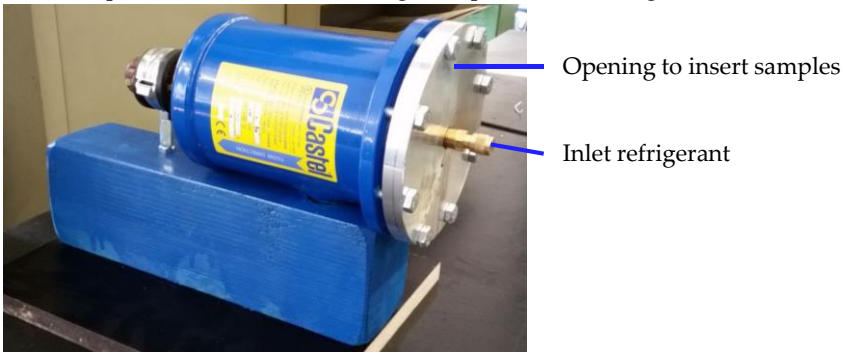

Figure 2-10: Pressure vessel to condition test samples for mechanical testing

In rare cases, as in Figure 2-11, a visual inspection of the material is sufficient to evaluate the impact of the fluid. PA6 degraded in water 21 days respectively 50 days at 50°C, leading to a discolouring and a brittle, cracked surface, which is indicating a general embrittlement of the material.

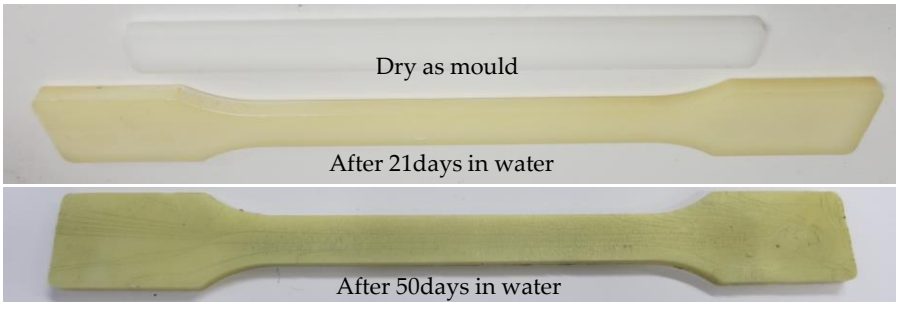

Figure 2-11: PA6 degraded in 50°C warm water over time. Discolouring and embrittlement due to humidity and temperature

2.3.6 Developed protocol for material quality check

Material controls during the full production and testing campaign help to assure material quality or to identify problems. In Figure 2-12, a procedure is suggested that ensures valid results of mechanical testing or that identifies quality issues early on in the procedure to avoid time-intensive testing campaigns on a low quality material. The production of samples starts with the quality assurance of the raw materials by microscopic inspection of a batch sample. That includes the assessment of clean matrix material to avoid impurities as well as the microscopic examination of fillers to ensure high quality. In a second step, the raw materials, especially the matrix should be dried to avoid vapour-voids in the injected material. To assess the quality after the injection moulding process, a visual inspection by eye, followed by a microscopic analysis is recommended. Thereby, not only voids in the core can be detected, but also the filler content, distribution, and orientation studied in the different layers of the material. A DSC scan can determine the phase transitions.

If the material passed until this point, the samples should be conditioned for mechanical testing. The weighing of dry and conditioned samples is used to determine the moisture content (or other fluid content) and thereby to ensure the correct conditioning. After mechanical testing at different levels of humidity, a microscopic analysis of the fracture surface can reveal overlooked impurities or give valuable information of the fibre-matrix interface.

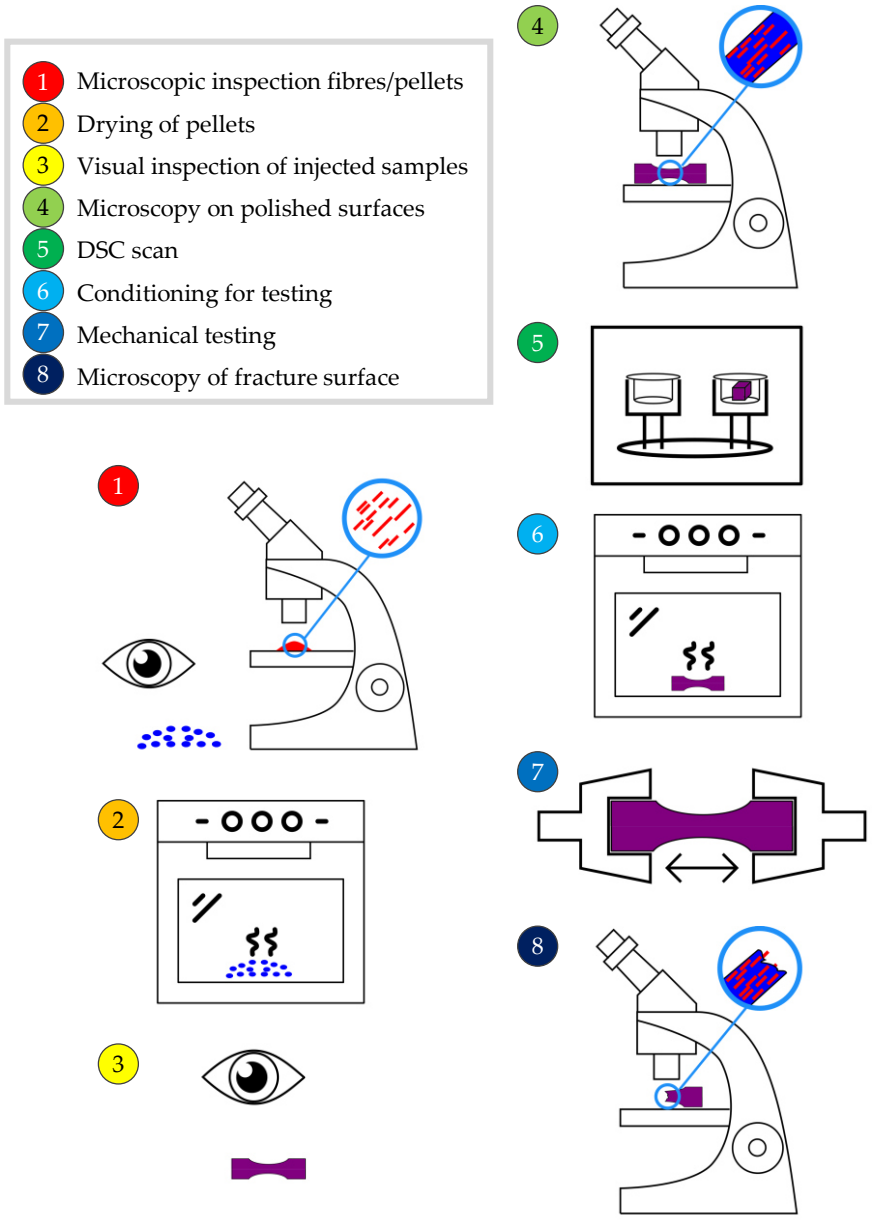

Figure 2-12: Procedure for quality control of thermoplastic composites, from raw materials to fracture surface

2.4 Conclusion of the material selection

In this chapter, the opportunities of basic methods of material inspection are described. As visualisation method, microscopy was chosen over other, partially non-destructive

methods due to the precise result, the speed of the method, the relatively low financial investment and the opportunity to do different quality controls on the same device. Microscopic imaging is used to reveal unwanted voids or inclusions, can ensure surface quality of the fillers and can in addition be used to perform measurements on the fillers. These measurements include the dimension of the filler before and after processing as well as their distribution and orientation in the matrix and show the matrix-filler interface after mechanical testing. In addition to microscopy, thermal history and moisture content measured before testing can help to interpret test results or pinpoint improvements for the production. All listed methods serve a qualitative evaluation purpose and can help to give a first estimation of the expected strength and stiffness. In case of visually insufficient material quality for the chosen application, an inspection can save testing time by rejecting the material immediately.

Furthermore, to condition samples in refrigerants under pressure a pressure vessel was designed by ATHT. This allows for mechanical testing under similar environmental conditions as given in a heat exchanger. The quality of the soaking can be determined by weighing samples before and after treatment.

References

[1] R. Sakko, "Waste heat recovery from flue gsaes using polymer heat exchangers," *https://heatmatrixgroup.com/*, Heat Matrix, 2019.

[2] "CB group, https://www.cbgroep.be/," 2018.

[3] T. Wieme, B. Augustyns, L. Duan, and L. Cardon, "Increased through-plane thermal conductivity of injection moulded thermoplastic composites by manipulation of filler orientation," *Plastics, rubber and composites*, 2020, p. 8.

[4] T. Wieme, D. Tang, L. Delva, D.R. D'hooge, and L. Cardon, "The relevance of material and processing parameters on the thermal conductivity of thermoplastic composites," *Polymer Engineering & Science*, vol. 58, 2018, pp. 466–474.

[5] J. Thomason and L. Yang, "Temperature dependence of the interfacial shear strength in glass–fibre epoxy composites," *Composites science and technology*, vol. 96, 2014, pp. 7–12.

[6] T. Wieme, "Designing the formulation variables and processing conditions for controlling thermal conductivity of thermoplastic composites," Ghent University, 2020.

[7] *ASTM D3532 / D3532M - 19: Standard Test Method for Gel Time of Carbon Fiber-Epoxy Prepreg*, ASTM International, West Conshohocken, PA,, 2019.

[8] *ASTM D1725 - 12: Standard Practice for Preparing Resin Solutions for Viscosity Measurement by Bubble Time Method*, ASTM International, West Conshohocken, PA, 2019.

[9] A. Buchman and A. Isayev, "Quality assurance of various thermoplastic composites," *SAMPE Journal*, vol. 27, 1991, pp. 19–27.

[10] M. Mehdikhani, L. Gorbatikh, I. Verpoest, and S.V. Lomov, "Voids in fiber-reinforced polymer composites: A review on their formation, characteristics,

and effects on mechanical performance," *Journal of Composite Materials*, vol. 53, 2019, pp. 1579–1669.

[11] Z. Fawaz, "Quality control and testing methods for advanced composite materials in aerospace engineering," *Advanced composite materials for aerospace engineering*, Elsevier, 2016, pp. 429–451.

[12] P. Parlanti, V. Cappello, F. Brun, G. Tromba, R. Rigolio, I. Tonazzini, M. Cecchini, V. Piazza, and M. Gemmi, "Size and specimen-dependent strategy for x-ray micro-ct and tem correlative analysis of nervous system samples," *Scientific reports*, vol. 7, 2017, pp. 1–12.

[13] D.K. Hsu and K.M. Uhl, "A morphological study of porosity defects in graphite-epoxy composites," *Review of progress in quantitative nondestructive evaluation*, Springer, 1987, pp. 1175–1184.

[14] *Favimat+ Automatic Single-Fibre Tester*, TexTechno, 2015.

[15] *ISO 11566:1996: Carbon fibre — Determination of the tensile properties of single-filament specimens*, International Organization for Standardization, 1996.

[16] S.-Y. Fu, B. Lauke, and Y.-W. Mai, *Science and engineering of short fibre reinforced polymer composites*, Elsevier, 2009.

[17] "Phenom XL G2 Desktop SEM, Thermofisher," 2020.

[18] S. Bagherpour, *Fibre reinforced polyester composites*, InTech London, 2012.

[19] W. van P. Lode Daelemans Ludwig Cardon Matthieu N. Boone Sander Rijckaert and K.D. Clerck, "Continuous fiber reinforced aramid/PETG 3D printed composites with high fiber loadings through low-cost Fused Deposition Modelling," *Unpublished*, 2021.

[20] H. Zuidema, G. Peters, and H. Meijer, "Influence of cooling rate on pVT-data of semicrystalline polymers," *Journal of Applied Polymer Science*, vol. 82, 2001, pp. 1170–1186.

[21] M. Boutaous, N. Brahmia, and P. Bourgin, "Parametric study of the crystallization kinetics of a semi-crystalline polymer during cooling," *Comptes rendus mecanique*, vol. 338, 2010, pp. 78–84.

[22] *DIN EN ISO 75-1: Kunststoffe - Bestimmung der Wärmeformbeständigkeitstemperature - Teil 1: Allgemeines Prüfverfahren*, DIN Deutsches Institut für Normen e.V., .

[23] *ASTM D648-07: Standard Test Method for Deflection Temperature of Plastics Under Flexural Load in the Edgewise Position*, ASTM International, 2007.

[24] *ASTM D3418 - 15: Standard Test Method for Transition Temperatures and Enthalpies of Fusion and Crystallization of Polymers by Differential Scanning Calorimetry*, ASTM International, .

[25] A.S. D5229, *Standard Test Method for Moisture Absorption Properties and Equilibrium Conditioning of Polymer Matrix Composite Materials*, 2014.

[26] "ISO 483 Plastics — Small enclosures for conditioning and testing using aqueous solutions to maintain the humidity at a constant value," *International Organization for Standardization*, 2005.

[27] *DIN EN ISO 527-1: Bestimmung der Zugeigenschaften Teil 1; Allgemeine Grundsätze*, DIN Deutsches Institut für Normung e.V., 2012.

Chapter 3

Subcomponent testing under temperature and pressure

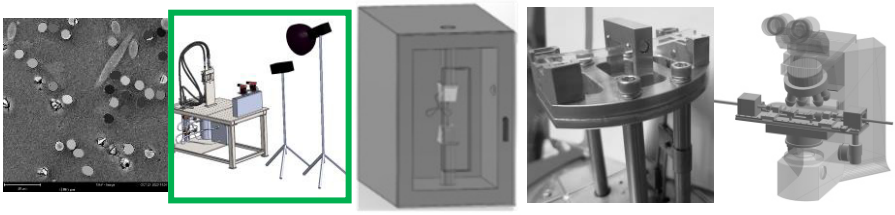

Subcomponent scale

Abstract: After material quality is ensured, the development of a new in-service product requires relevant tests. However, the build of a full heat exchanger is too expensive for classifying a new material. For this purpose, a prototyping subcomponent setup was built that allows for testing and evaluating of composite samples in the later geometrical structure and under the given conditions in a heat exchanger, namely temperature and pressure. Optical strain measurements with digital image correlation allows for a detailed view of the strain distribution through glass and water.

3.1 Introduction to subcomponent testing

Composite heat exchangers offer many new design possibilities compared to full metal heat exchangers [1–3]. The shape of the walls can be entirely different due to the possibilities of injection moulding or thermoforming, thereby increasing the efficiency while consuming less space [2]. The individual components can be loose or connected using a mechanical or adhesive joint or welded connection. However, these design capabilities also pose challenges, because components and connections need to be verified and optimised, ideally without building a full prototype. Accurate modelling has proved difficult, especially for glued or welded connections between two surfaces, since the connection points are not uniform due to the manual production process [4]. In addition, the experimental verification of the simulated results is missing. Since common heat exchangers are large, the idea emerged to test only a small representative section of a heat exchanger that simulates temperature and pressure accurately on the composite walls. This representative fraction will hereafter be called unit cell. In literature, such unit cells are typically built and tested for heat exchangers in respect to the heat transfer and flow simulation [5–8]. In respect to strength and stiffness, no experimental analysis on the structure or the connections could be found. Authors compare values to the tensile or bending strength and simulate the behaviour numerically [9].

Due to the lack of an existing structural analysis, a setup needed to be build that is able to (i) clamp the unit cell, apply (ii) temperature and (iii) pressure differences over the wall of the heat exchanger and (iv) offers the possibility for strain measurement on the unit cell. Test results can enable long-term predictions for structure and material under realistic conditions.

3.2 Simulation of subcomponents

Aside from experimental analysis, also a numerical simulation can be used to calculate the behaviour of the material under load. While this was done in previous research, it was never experimentally validated. To show the importance of the experimental analysis, the workflow of the numerical model made by a colleague is briefly explained.

The model is based on the structural shape of the composite walls represented in a unit cell. To accurately describe the material, the fibre orientation in a short fibre composite is essential. For this purpose, the fibre orientation was confirmed with microscopy of the material cross-section. To calculate the stiffness numerically, the distribution of temperature and pressure over the composite walls also needs to be given accurately. For the model on stiffness, this information has to be combined. In the Compohex project, team members of the MMS group established a simulation workflow

(Figure 3-1) to connect the data of the material with the load of the fluid on the example of a tubular heat exchanger.

(1) In Moldex3D [10] the flow of an injection process can be simulated, which creates a map showing the fibre orientation in the matrix. For extruded pieces, the fibres are assumed to be in the flow direction, oriented along a spline that follows the thermoformed shape of the material.
(2) Digimat [11] subsequently translates the data from Moldex3D to Abaqus.
(3) In addition, the fluid parameters, namely temperature and pressure, calculated by computational fluid dynamics (CFD) simulation by Ansys Fluent [12] are transferred to Abaqus.
(4) Abaqus [13] is the software to perform the structural analysis. Based on the data from steps 1-3, it can calculate the strength and stiffness of the structure at specific environmental conditions.

An experimental validation to verify the accuracy of model has to be added.

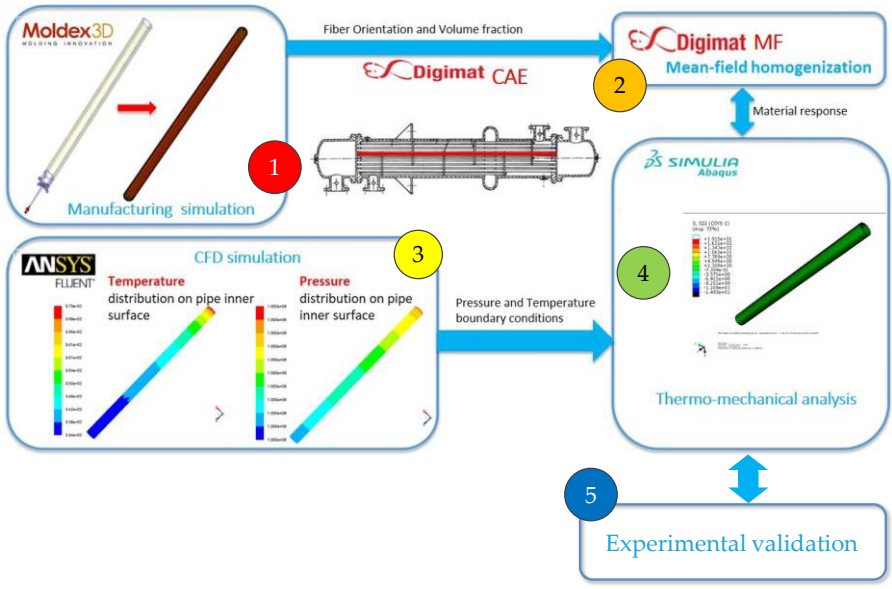

Figure 3-1: Schematic overview of the workflow of numerical simulation of the efficiency of a heat exchanger [14]

The simulation (step 1-4) can be performed for any sample shape. In a linear elastic simulation in Figure 3-2, sinusoidal polycarbonate (PC) plates were simulated with 7 bar and 70°C on the hot side, and 1 bar and 20°C on the cold side. The contact points were assumed to be perfectly shaped, rigid spot welded connections. Experimentally, those connections should be evaluated, since an entangling of the polymer chains and therewith an assumed physical and chemical connection cannot be expected. The tensile stresses are the most critical stresses in this design, showing maximum concentrations at the contact points between the plates (Figure 3-2b). The highest stress

concentration in this design under the given loading conditions was 44.2 MPa in tension. At 70°C, PC has a maximum tensile strength of 53 MPa, which is slightly higher. However, weld quality, cyclic loading causing fatigue and creep would cause the material to fail in practice.

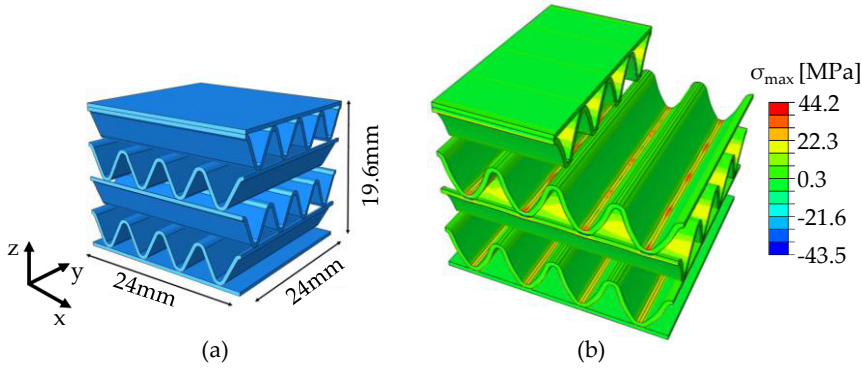

Figure 3-2: Model of unit cell with 4 layers: (a) Crosswise oriented sinusoidal samples, (b) contour plot showing the distribution of maximal tensile stresses in the material at Δp=6 bar and ΔT=50°C

Experimental work is missing to validate the accuracy of this simulation. Especially, the welding points, which have the highest stress concentration are an uncertainty in the simulation, since they are assumed as perfect spot welds, which is not necessarily representative for a real sample. Out of the need of experimental validation, this chapter focuses on the design and build of a setup to test structured plates under temperature and pressure to supply the numerical work with enough information to validate their approach.

3.3 Requirements for subcomponent testing

In terms of a sample, the unit cell, a fraction of the heat exchanger, is chosen. The unit cell needs to fully represent the geometry of the composite walls, which can be repeated to create the full size heat exchanger. Likewise, the connections between walls has to be representative for the full structure. On this unit cell, the strain should be measured to know the weak points in material and structural design. Therefore, a method that captures the full sample surface is required.

The test setup itself needs to be able to set pressure and temperature as in a real heat exchanger. This means, accurately keeping the pressure and temperature differences constant over the composite wall. It was decided to not measure the heat flow and transfer in this setup, since there is a specific setup available for that purpose with a partner of the project.

Requirements for the testing range were chosen based on existing applications for heat exchangers and are listed in Table 3-1. The design process was split into two stages.

Stage 1 It serves the proof of concept to ensure pressure and temperature can be applied and strain measured. The chosen conditions are realistic for an air-to-air heat exchanger for example for indoor air ventilation [15] or for drying compressed air in an aftercooler [16].

Stage 2 A more advanced heat exchanger with more challenging atmosphere was planned. However, due to budget constraints this second stage was never put into action and remains theoretical. The conditions of the second scenario are realistic for a pre-heater or after cooler for flue gas from refining or petro-chemical plants [17]. Flue gas turns highly corrosive when it liquefies due to cooling. Corrosion resistant composites are an alternative to the commonly used, expensive titanium.

Table 3-1: Requirements for the test setup in two stages

	Stage 1	**Stage 2**
Temperature [°C]	80	220
Maximum pressure [bar]	7	8
Flow [L/min]	6	45
Typical application	Aftercooler	Flue gas cooling

To achieve these conditions, different components are needed. For the temperature control, heating and cooling elements are elementary. The pressure has to be built up, using a combination of valves and pumps, which also regulates the flow. The parameters should be kept constant during a test. For this purpose, temperature, pressure and flow have to be extracted at different positions inside the setup to measure the conditions over the unit cell. The values from the sensors are used to keep the parameters constant by controlling the components with an automated feedback loop.

Since no off-the-shelf setup that fulfils all these requirements could be found, a novel in-house design was developed. The chosen design of a unit cell is based on the design of a typical cross flow plate heat exchanger [18]. In such a heat exchanger, a hot, pressurised fluid is circulated between two plates, transferring energy through the walls to the colder fluid on both outer sides (Figure 3-3). To create a unit cell of such a heat exchanger, two sinusoidal shaped plates were stacked cross-wise, assuming the hot side is in between the two plates and the cold side outside.

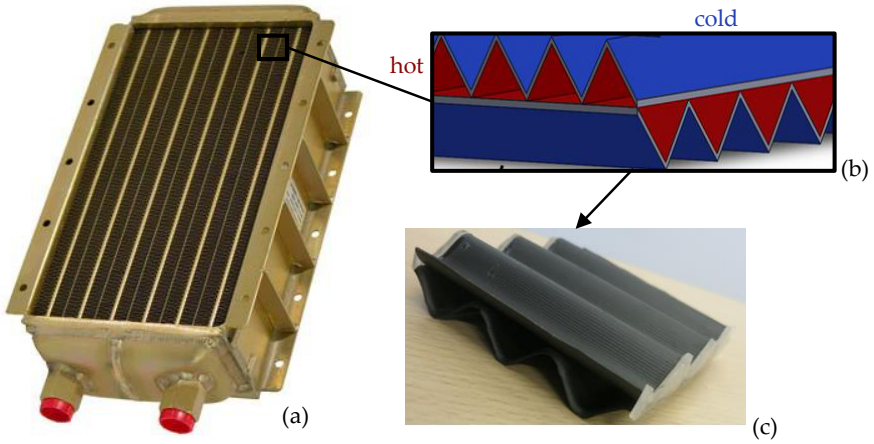

Figure 3-3: Plate fin heat exchanger (a) existing design from metal [19] serving as inspiration for a composite heat exchanger, (b) schematic distribution of hot and cold fluid in a unit cell, (c) unit cell realised in composite (PC-CF)

3.4 Development of a test setup for subcomponent testing

A test setup was designed in-house. Its components are introduced in Figure 3-4. Briefly, the setup consists of:

(1) the hydraulic system for the fluid and its control unit, providing the pressure and temperature to the specimen,
(2) the overall mechanical layout including the clamping unit,
(3) the software of the system and,
(4) the optical measurement of the deformation

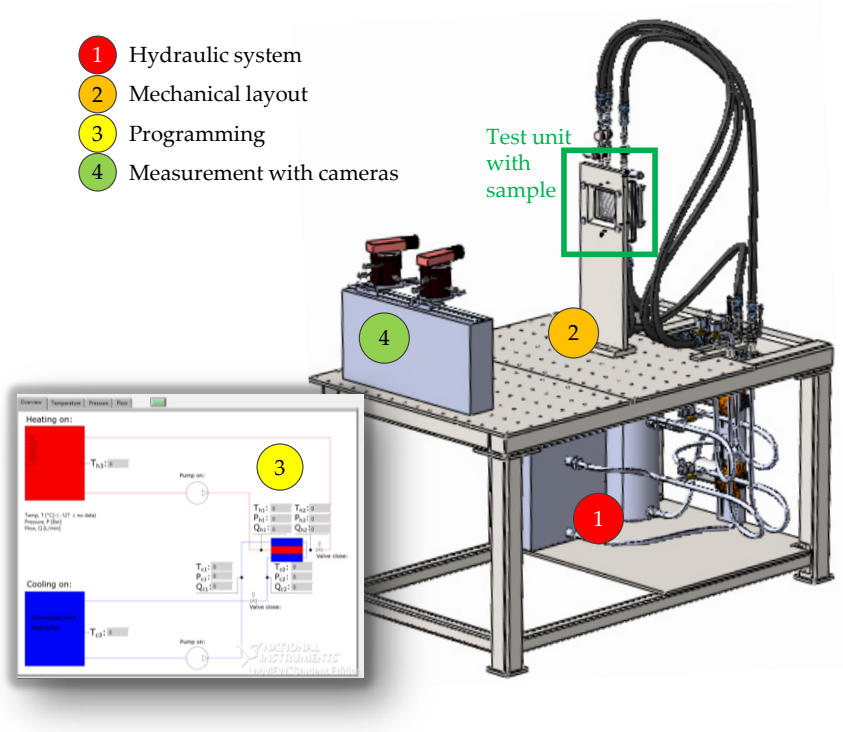

Figure 3-4: Overview of the developed unit cell test setup drawn in Solidworks [20] and screen shot of the control software

3.4.1 Unit-cell specimen

The clamping of the specimens is one of the main requirements. However, the clamping of the complex shaped samples is not evident. The walls of plate heat exchangers are typically not flat, but shaped to create turbulence, which enhances the heat exchange. Some possible shapes are presented in Figure 3-5. These shapes are all very different from the perspective of clamping. For this reason, samples were homogenised by using a square segment of the structure with an added all-around flat edge. The shape of the full chosen sample is to see in Figure 3-5d. The square testing area was decided to be 100 mm wide, the clamping edge additional 25 mm. The chosen pattern for the experiments was a sinusoidal sample with an apex angle of 90° and a tip diameter of 10 mm. With the chosen dimensions, the pattern repeats itself three times, which makes it possible to measure the effect of neighbouring repetitions of the same pattern. The width of the clamping edge was determined after different trials.

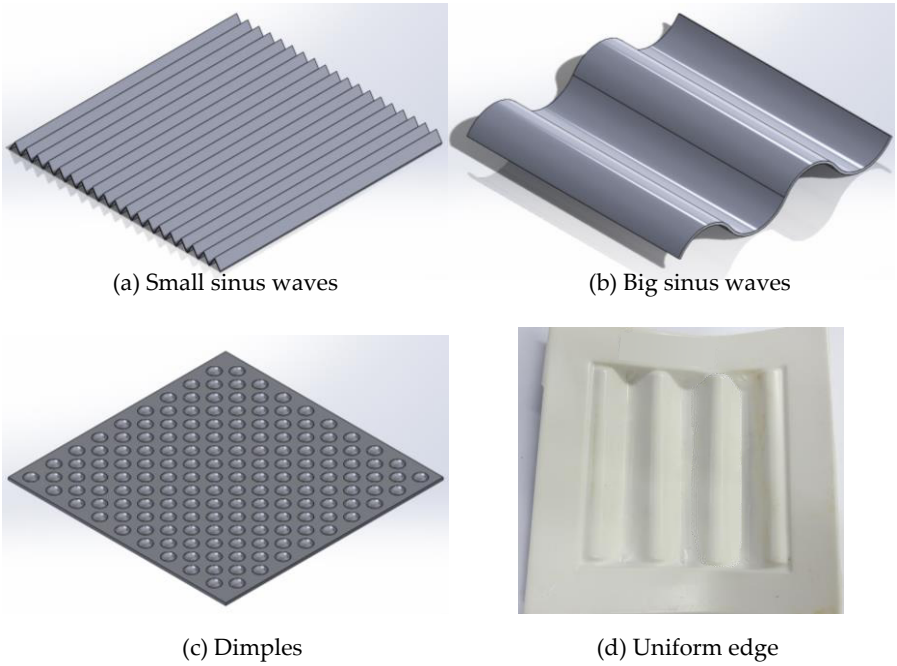

(a) Small sinus waves (b) Big sinus waves

(c) Dimples (d) Uniform edge

Figure 3-5: (a-c) Different possible shapes of heat exchanger walls, (d) unified clamping area on big sinus sample made from HDPE

Heat exchanger walls can also be welded together to create a stronger unit. To find out, which welding connection would be best for the wall material, dogbones were injection moulded from polycarbonate (PC) with 5 wt% short carbon fibres. Afterwards, the dogbones were cut in half and reconnected with different glues. The connection was tested in a tensile test. From the same material, flat sheets were also produced in extrusion, but did not pass the quality control. To test the subcomponent setup of this chapter, commercially available layered sheets from high density polyethylene (HDPE) coated with acrylonitrile butadiene styrene (ABS) were used instead. 0.9 mm thick plates were thermoformed to the chosen sinusoidal shape using vacuum forming machine (Formech 508FS). For the proof of concept, sample pairs were produced without spot welding. Also, flat plates were prepared for testing.

3.4.2 Hydraulic system

The key decision for the hydraulic system was, if the system should be closed or half-open. In a closed system, all fluid is heated and pressurised and then circulated without air contact. This bears the danger of overheating and overpressure, since no excess fluid is present to dissipate heat or pressure. On the upside, higher pressures are possible and less fluid is needed than in a half-open system.

A half-open system on the other hand, contains a reservoir with air contact. The fluid is pressurised when entering the closed system, the reservoir itself stays unpressurised. The fluid is circulated through the open reservoir. This system is safer, since the open reservoir can dissipate heat or pressure. In addition, the components are also less expensive and the maintenance is easier. Due to the cost benefits, it was decided to design an open system with reservoirs for the hot and cold fluid. Figure 3-6 provides a schematic overview of the hydraulics of the setup.

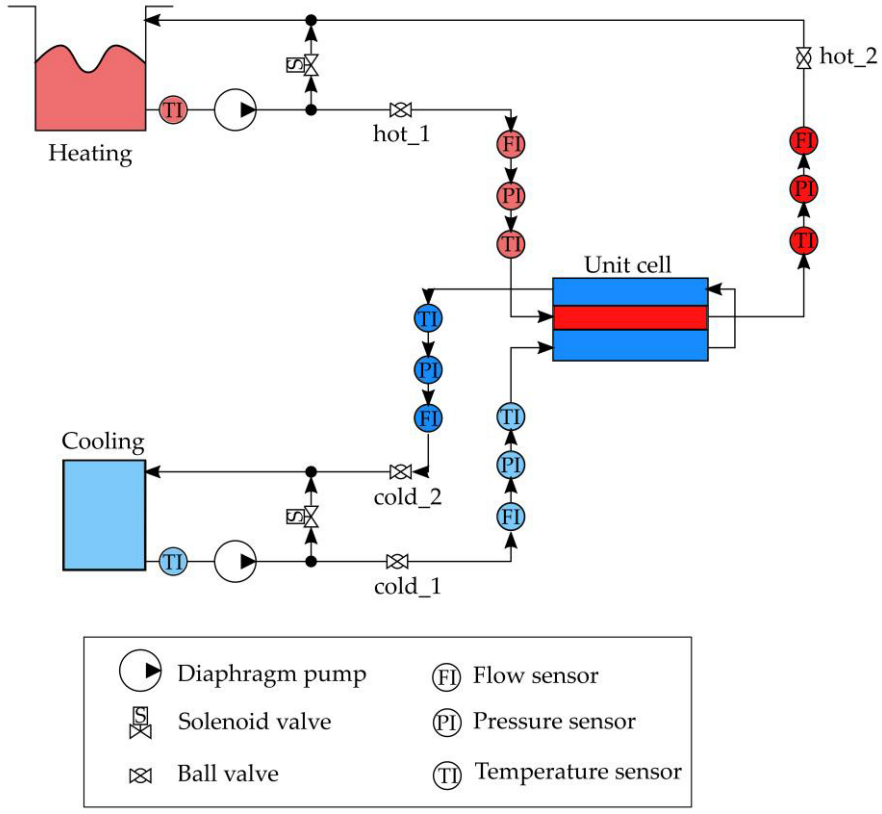

Figure 3-6: Fluid schematics of the test setup for stage 1

In the reservoir, the *Fluid*s are not pressurised, but heated, allowing for thermal expansion and an exchange with fresh fluid through an inlet. The rest of the system is a closed loop of *Tubing* and the testing chamber. The fluids are being pressurised using a combination of *Pumps* and *Valves*. A safety valve can open in case of overpressure and releases the water back into the tanks. *Sensors* for temperature, pressure and flow are placed before and after the unit cell. They give feedback to the temperature control units for *Temperature regulation*.

An overview of all the purchased off-shelf components can be found in Table 3-2. Requirements and reasoning for the design decisions can be found further on.

Table 3-2: Overview of the off-the-shelf components used to build the hydraulic part of the test setup

Category	Component	Specific name
Fluid	Silicon oil	Lobotherm BAP 500 [21]
Tubing	Flexible hose	HSKHF10 by Kramp [22]
Tubing	Rigid hose	85132 by Henco [23]
Pumps	Diaphragm pump	FL3308 by Rohs Motor [24]
Valves	Solenoid valve 50ms	0757-22139057 dc 12v by Candy-ho [25]
Valves	Solenoid valve 200ms	2W-025-08 by Senya Pneumatic [26]
Valves	Manual ball valve	Brass ball valve ACS PN40 by Sferaco [27]
Sensors	Temperature sensor	DS18B20 by SparkFun electronics [28]
Sensors	Pressure sensor	(Gravity water pressure sensor by DFROBOT [29]
Sensors	Flow sensor	Flow Meter, 0.6 L/min → 10 L/min by RS Pro [30]
Temperature regulation	Heating element	3kW, 240V by RS Pro [31]
Temperature regulation	Cooling unit	90s by Regloplas [32]

Fluid

The realised stage 1 is an example of an air-to-air heat exchanger. However, since the measurement focusses on mechanical strength, the accurate fluid and therewith heat transfer coefficient is irrelevant for this setup. Due to the constant volume under pressure, water was chosen over air as a fluid for the stage 1 setup. For stage 2, the fluid can be replaced with a temperature and pressure resistant silicon oil for around 80 €/L. Here a closed system should be considered, since that requires less fluid. Roughly estimated, a closed system includes about 2 L, whereas an open system with the current design needs about 21 L due to the size of the reservoirs.

Tubing

The components were chosen according to the requirements of stage 1 (80°C, 7 bar). Tubing was needed in two different places: (i) to steadily connect the reservoirs with the pumps and (ii) to bring the fluid to the unit cell. The second type of tubing needed to be flexible to allow for the dismantling of the testing unit. For easy handling, two different types of tubes were used: A rigid tube for the connection between reservoir and pumps and flexible hoses with a small bending radius around the unit cell. The tubes are connected by a press coupling as well as ½" threads [33].

Pumps

The fluids had to be pumped in the system to create a constant pressure and temperature. Within the test setups, air bubbles can occur or small particles can get loose when the sample fails. In contrast to other pumps, diaphragm pumps are not affected by those small abrasive elements. The specifications of the chosen pump can be found in Table 3-3. It is suited for the requirements of stage 1. The flow of 6 L/min (about half the flow in a normal household tap [34]) proved to be sufficient to keep the pressure and temperature in the unit cell constant.

Table 3-3: Specification of the diaphragm pump [24]

Pressure	9 bar
Flow	6 L/min
Temperature	0-100°C
Voltage	12 V DC
Power	72 W

Valves

The pressure in the unit cell is regulated with valves at the inlet and outlet of the unit cell. The positions of the valves around the unit cell are marked in Figure 3-7a. Initially, electromechanical solenoids were foreseen to regulate the pressure in a software-controlled way. For this purpose, a pressure sensor would read out the current pressure and the valve would open or close accordingly. Thereby, the faster the switching time of the valve and the higher the impulse frequency from the control unit (Arduino), the faster the valve reacts to keep the pressure stable. In Figure 3-7b, Solenoid valves with a switching frequency of 200 ms and one control unit were installed. However, it was found that the on/off control did not react fast enough to hold the pressure constant. The pressure was uncontrollable and big spikes occurred. Improvements were made by adding a second control unit and improved valves with a faster switching rate of 50 ms (Figure 3-7c), but these were dismissed as well. Reason for the difficulties of keeping the pressure constant was the shockwave caused by the rapid closing of the valve. This so called water hammer effect caused a viscoelastic deformation of the sample that caused the volume for the fluids to change. The bending of the sample to one side caused the valves of that side to react. As a consequence, the bending of the sample changed and the valves of the other side adjusted. No stable situation could be reached. Electromechanical valves were replaced by manual ball valves (Figure 3-7d). The safety valves, which are automatically activated in case of overpressure, remained.

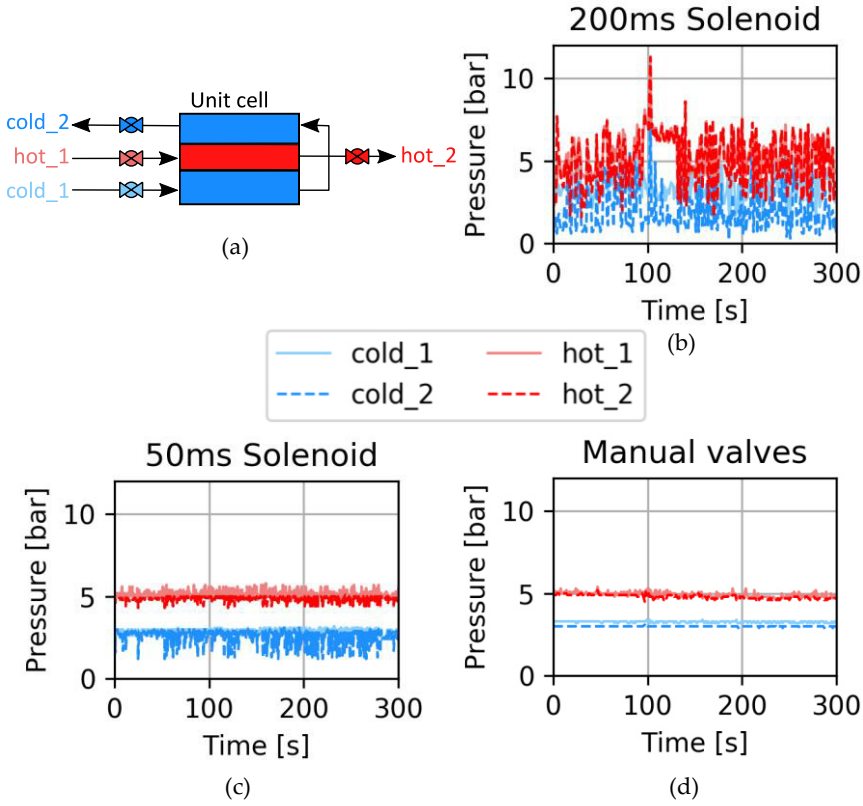

Figure 3-7: Pressure in the unit cell over time controlled by different valve types. Pressure aimed at Pcold=3 bar and Phot=5 bar. (a) overview scheme with position of the four valves, (b) one control unit and solenoid valves with a switching rate of 200 ms, (c) two control units and solenoid valves with a switching rate of 50 ms and (d) manual control with ball valves

Sensors

Sensors are required to read out temperature, pressure and flow rate. Overall, the setup was planned to run creep tests over several days, therefore the readout for the experimental data is sufficient in the range of seconds. However, for a feedback loop to control the setup, a faster reaction would be necessary. Yet, after the electromechanical valves were replaced by manual ball valves, the reaction time of the pressure sensors was no longer essential to control the pressure. Also, the feedback of the temperature sensor to the heating element was not crucial in speed, since the temperature change in water is slow anyway. The flow sensor in combination with the temperature sensor controlled the temperature in the unit cell. It was aimed for a steady flow, which does not require fast read-out of the sensors. All sensors have to be waterproof up to 80°C and 7 bar. In addition, the flow sensor has to be able to read a

flow value at least as high as the pumps can provide. Sensors were chosen accordingly with accuracy of ±0.5°C for the temperature sensor [28], ±0.01 MPa for the pressure sensor [29] and ±0.094 L/min for the flow sensor [30].

Temperature regulation

Heating was realised with a submerged heating element in a 12 L barrel. The heating speed was calculated according to Equation (3-1) to pick a suited power of the heating element.

$$Q = m\,c\,(T_h - T_c) \rightarrow\ t = \frac{Q}{P} \tag{3-1}$$

With Q as required energy to heat water, calculated from the mass of water m, the heat capacity of water c and the temperature difference between hot (T_h) and cold (T_c) water. Together with the power of the heating element P, the time t can be calculated. To ensure heating in a decent amount of time, a high power element with 3 kW was chosen, resulting into a heating speed of 1/17°C/s (~3.5°C/min). Within about 20 min, the setup is ready for testing at 80°C. Silicon oil can heat up faster and it would be possible to reach 185°C in 20 min with the chosen heating element.

The cold fluid has to stay constant at room temperature. To avoid heating due to the heat transfer via the sample, cooling is required. A cooling unit was available and used. The pumping pressure provided by the unit is limited to 3.8 bar and therefore supported by an external pump, as described earlier in *Pumps*.

3.4.3 System control

Data acquisition (*DAQ*) and the *Control* are performed by an Arduino microcontroller unit, which is connected to a computer running LabVIEW [35]. The read-out values of the temperature and flow sensors give the input and the loop regulates the heating element and the pumps as an output. In an event of a *Pressure drop*, the system will automatically shut down. The schematic is visualised in Figure 3-8.

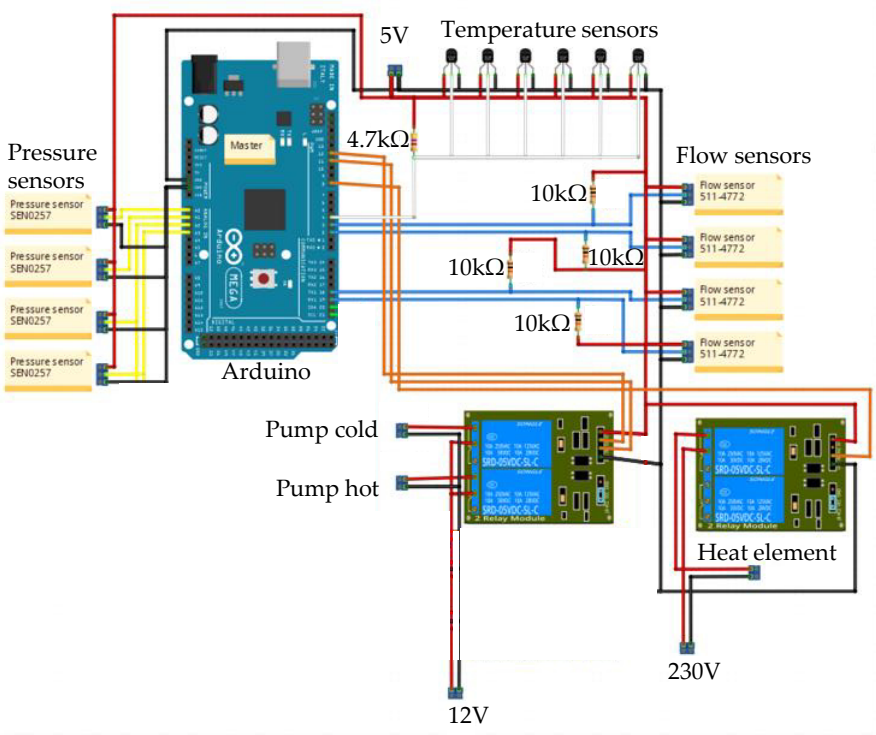

Figure 3-8: Wiring scheme of the control panel, including Arduino with its connections to the relays and sensors

DAQ

The data acquisition (DAQ) of the setup was planned to run tests over several days and has to handle several input and output signals at the same time. Due to these requirements of a steady performance with the ability to process signals in parallel, LabVIEW was chosen for the DAQ.

Control

As a control unit, National Instrument cards were considered, but due to their cost an Arduino based system was chosen instead. It has the advantage of available libraries due to a big open source community. The chosen Arduino needed four interrupt pins to read out the flow sensor. An Arduino Mega 2560 fulfils these requirements [36]. To communicate with LabVIEW, the open-source interface Linx was used [35].

Pressure drop

In the event of sample failure, the system will shut down by stopping the pumps and reduce the pressure by opening the automatic valves to release the fluid in the

reservoirs. Failure is detectable from a drop in pressure on the high pressure side. The system was calibrated by calculating the normal pressure drop due to material roughness and changes in diameter. Based on it, the threshold in pressure difference was determined to define sample failure. It was chosen over the measurement of an absolute value to be able to change the pressure during the experiment. The most critical location where a pressure drop occurs during normal operation is between the tubing and the outlet of the sample clamping area. Due to space restrictions, the diameter has to reduce from 6 mm to 3 mm (Figure 3-9), causing a pressure drop of 0.25 bar calculated with the Darcy-Weisbach Equation (3-2) [37]. The pressure drop ΔP was calculated from the friction coefficient fr, the density of the fluid ρ, the length L and diameter D of the tube as well as the mean flow velocity $\langle v \rangle$.

$$\Delta P = fr\ \rho\ \frac{L}{D}\ \frac{\langle v \rangle^2}{2} \tag{3-2}$$

Experimentally, the cold fluid experiences a pressure drop of 0.26 bar over the full unit cell at 20°C, whereas the hot fluid system has a drop of 0.28 bar at the same flow rate. The calculated value and the experimentally measured values are in good agreement. The system shut down will be triggered when the pressure drops more than 10% in a steady state [38].

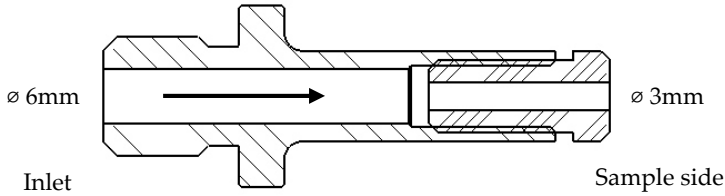

Figure 3-9: Schematic view of transition from ⌀6 mm to ⌀3 mm connector which causes the biggest pressure drop in the system

3.4.4 Mechanical parts

Figure 3-10 shows the full assembly of the mechanical parts. Number (1) is the base block, which connects the assembly to the table, and is in contact with (2) the glass plate. The first sealing ring (3) is placed inside the square spacer (4). It seals between the glass (2) and the spacer (4) as well as between the spacer (4) and the first sample wall (5). In between the two sample walls (5), a sealing ring (3) and the U-shaped spacers (7) are placed. The setup is closed symmetrically with another square spacer (4) and sealing ring (3). The setup is closed off with a back plate (9). Fluid connectors of 6 mm (6) and 3 mm (8) are forming the inlet and outlet for the fluids. The technical drawings can be found in the master thesis of Paridaen [20].

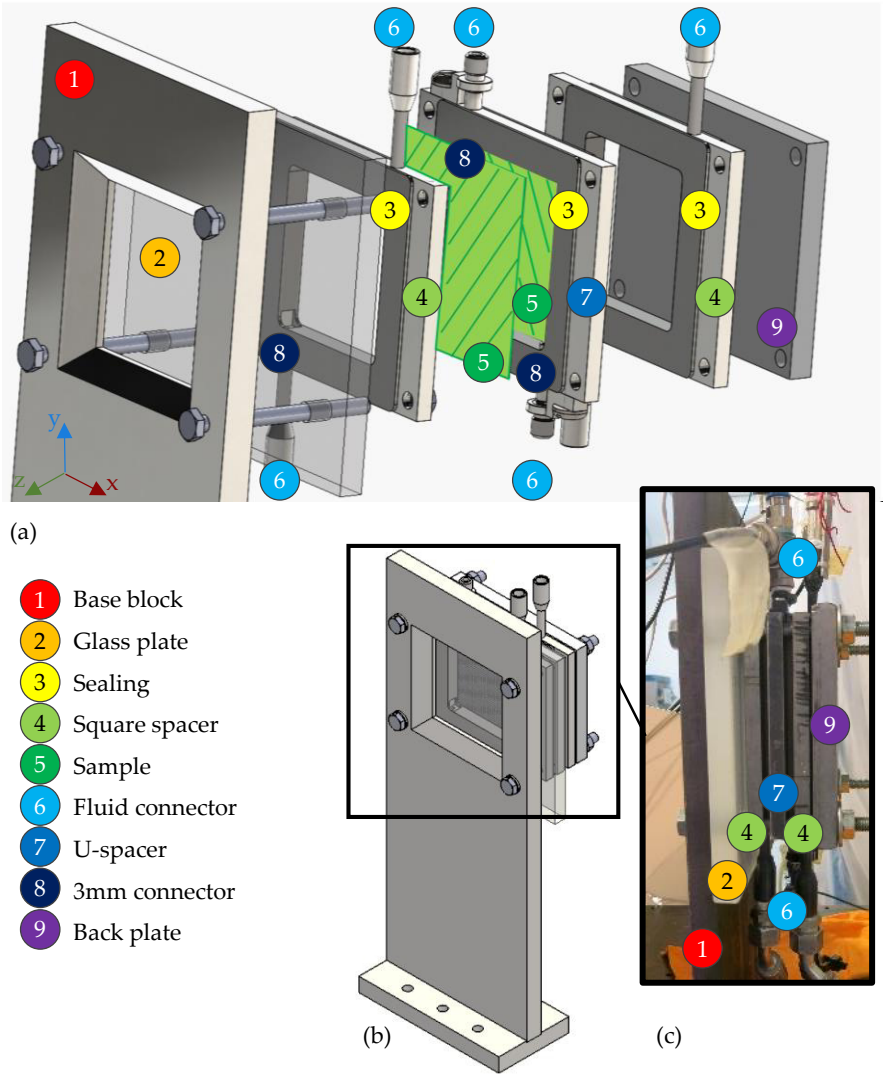

Figure 3-10: Assembly of the clamping unit around the sample, (a) exploded view of the 3D CAD model, (b) 3D CAD model, (c) photo

The components for the clamping were assembled by adding four M10 bolts through the glass, the frames, as well as metal plate holders. The connectors for the fluid were placed on opposite sides to have a crossflow in the sample.

The samples are not fixed in the setup in-plane except by the applied sealing pressure. This allows for thermal expansion as also typically provided in heat exchangers [15]. The out-of-plane movement is hindered by the glass and metal back plate, which both

represent the next composite walls. To vary the shape of the sample, the thickness of the spacers needs to be adjusted as necessary.

In Figure 3-11, two samples forming a unit cell are shown. The flat edge which is used for clamping, is shown in the CAD-image to show the structure of the sample. For the tests presented in this chapter, the samples do have a flat edge, but are not connected through welding. However, the setup was designed with the idea to be able to test welding connections as well. They are shown exemplarily in the image.

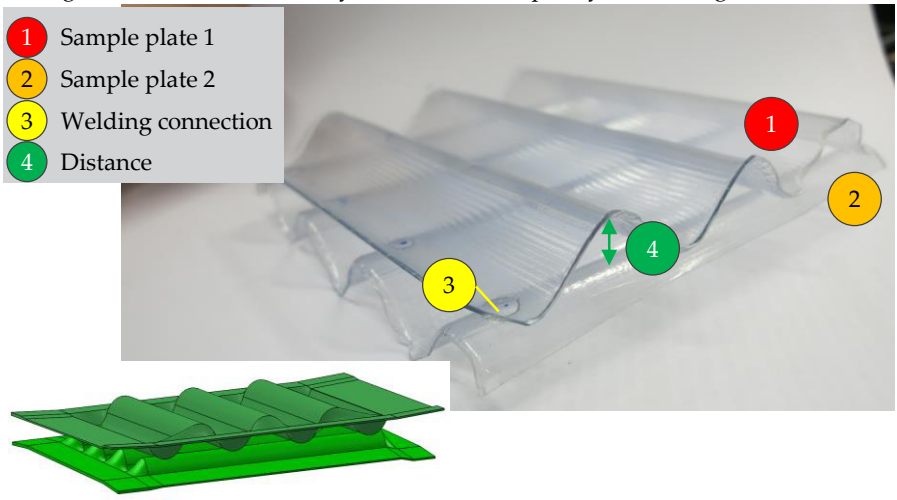

Figure 3-11: Unit cell made from two sinusoidally shaped plates

Spacer and connections – between two samples

In between the samples is the hot, pressurised fluid, on both outer sides is the cold unpressured fluid. The sample needs to be clamped tightly to create a closed chamber for the fluids. The distance between the walls and therewith the depth of the fluid chamber is dictated by the space between the walls. For a rigid clamping, this space needs to be maintained. Rigid metal plates in the correct thickness were chosen as spacers. To be able to place the metal plate in between possibly connected samples, a demountable solution as in Figure 3-12a is needed. The designed spacers are U-shaped, allowing for placement in between the walls of the unit cell. The two U-shaped pieces connect at the fluid inlet and outlet. Inlet and outlet are tightened with screw connections. 3 mm wide drilled holes in these screws serve as the channel for the fluid.

Sealing

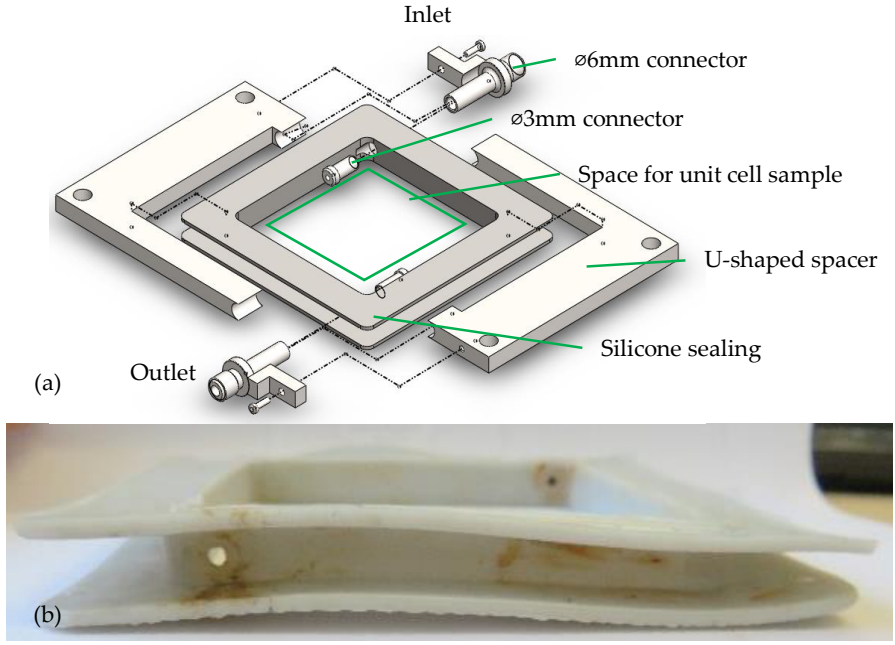

Figure 3-12: Silicone sealing (a) Explosion view of middle layer including silicon sealing, U-shaped spacers and fluid connectors, (b) photography of silicon mould with its cavities for the fluid inlet

Each individual sample wall needs to be sealed towards the spacer (Figure 3-12). Different materials were tried to seal fluid in the unit cell. Vacuum sealing tape, typically used in composite production for vacuum bags, could not withstand the pressure in the setup and was difficult to remove to change samples. Liquid sealing as used in engine blocks was pushed out at higher pressures. In the end, the chosen material was a silicone rubber with a high tear strength which vulcanizes at room temperature [39]. It was poured in a polyoxymethylene mould. Big advantages are that the silicone is flexible and allows to be positioned around the unit cell. This press-fit sealing allows for movement of the sample due to thermal expansion and can withstand temperatures up to 250°C. Small cavities are kept open for inlet and outlet of the fluids into the unit cell. To bring the sealing in position, especially in between the sample walls, the silicon sealing is stretched slightly.

Spacer and connections – on outer sides of samples

The cold fluid chambers on the outer sides of the sample pair were designed similar to that of the hot fluid, but as a rigid frame without u-connection. The sealing can be placed around the spacer. The channel for the cold fluid is also 3 mm wide to match the inlets of the hot fluid.

Glass

The setup relies on optical strain measurements, which takes place through glass and a fluid. Hence, it was relevant to choose perfectly flat glass without waves or distortions. Furthermore, the glass needs to be able to withstand the pressure and temperature of the hot fluid. Under normal operation, the glass will only be in contact with the low pressure, cold fluid, but in case of a sample failure, the hot fluid might reach the glass. A 15 mm thick borosilicate glass called Borofloat 33 by Mennes GmbH was ordered as it is suited for up to 35 bar. Holes were added to allow for clamping it with bolts.

Table

The overall setup is placed on a welding table. For safety reasons, the water reservoirs are placed underneath the table, whereas the electronic components are on top. In case of leakage, the amount of water on the table and therewith close to the electronics would be limited to the content of the piping and sample.

3.5 Measuring of unit cell deformation

Common instruments to measure strain are strain gauges, optical fibres, extensometer or digital image correlation. To study the geometrical influence of the material, a full-field measurement is needed. Therefore, strain gauges and extensometers were discarded. Optical fibres need to be embedded or attached to the sample material. The production in extrusion and the subsequent thermoforming of the shaped, smooth surface make this procedure very difficult. Therefore, digital image correlation (DIC) was chosen as a measurement technique.

3.5.1 Digital image correlation (DIC)

DIC is a full-field method to measure deformation and strain based on optical images [40]. To analyse out-of-plane movement as needed for the 3D-structure of the samples, two cameras are required. This is the same effect as for the human eyes. With one eye, only 2D vision is possible, with a second one in a slightly different position, a 3D image can be computed. The cameras are placed as shown in Figure 3-13 and synchronised images are taken.

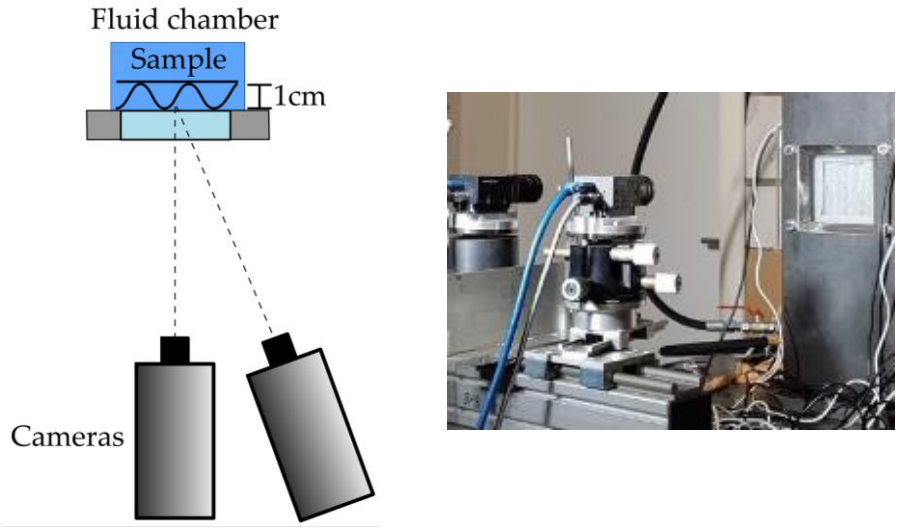

Figure 3-13: DIC cameras oriented on sample in theory and practically in the setup

This technique requires a calibration to assess the dimensions, position and angles of the two cameras. For the calibration, a regular grid of high contrasting dots as in Figure 3-14a is moved and rotated in the area of interest. During the actual test, a traceable pattern that deforms with the sample is needed on the specimens. For that purpose, a so called speckle pattern, a random distribution of high contrasting speckles is added to the samples (Figure 3-14b). For this purpose, a white base coat was applied using waterproof airbrush paint [41], while the black speckles were applied using matt black acrylic spray paint [42].

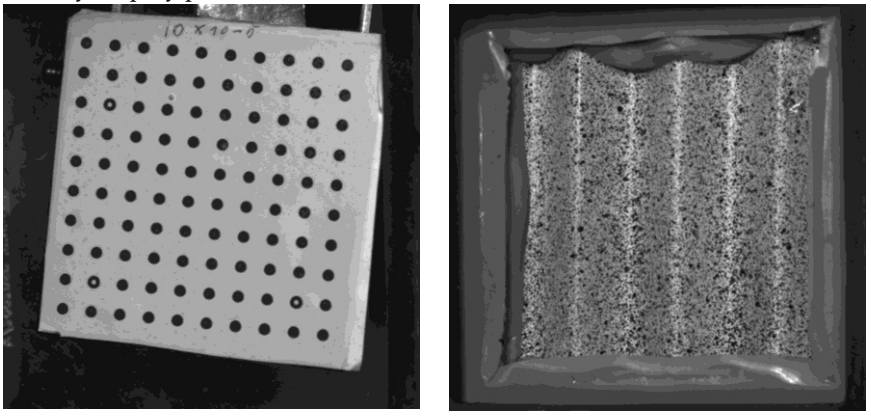

(a) (b)

Figure 3-14: DIC on the heat exchanger unit cell sample: (a) calibration grid and (b) speckle pattern on test sample to trace displacement and deformation

Both cameras take images at precisely the same time so that the position of the cameras can be calculated from the different viewpoints on the calibration grid. The triggering and data acquisition is done with the software VIC-Snap [43]. The synchronisation of the cameras is also used when recording experiments.

In a post-processing step, each speckle image of the sample is divided in subsets, the yellow squares in Figure 3-15 [44]. The individual subsets are overlapping a certain amount of pixels, called the step size. The movement and deformation of these subsets is calculated from the images in sequence. The better the calibration and the more traceable the pattern, the lower is the so called projection error and the higher the measurement accuracy. To do this analysis, the software VIC-3D [45] was used. It is specialised on the measurement and visualisation of DIC data and allows to evaluate deformation and strain at every position on the specimen.

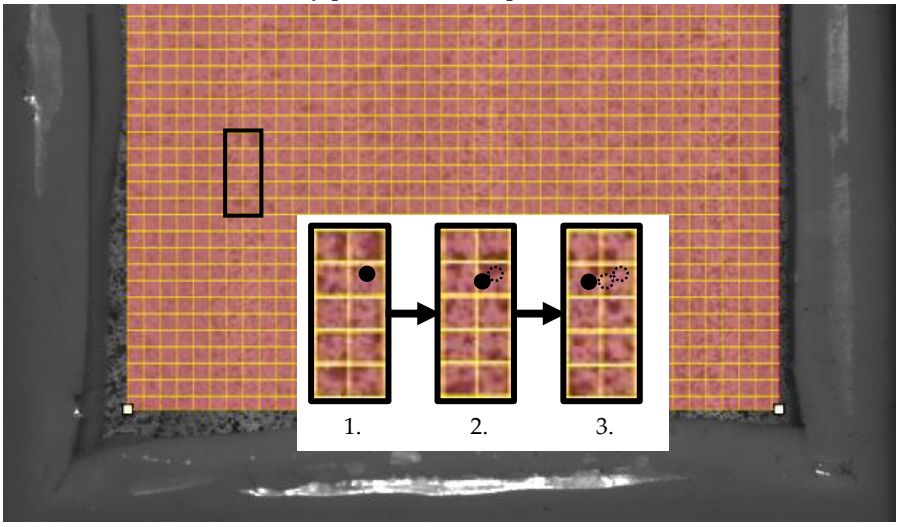

Figure 3-15: Post-processing principle of DIC, yellow squares are subsets, movement is traced by comparing current speckle position in subset to position before (black dot as example)

3.5.2 DIC through air, glass and water

In general for DIC a good vision is required. The setup to test heat exchanger material is in particular challenging, since the vision of the cameras on the sample is disturbed by glass and a transparent fluid. Therefore, a good *Light* that shows the contrasting pattern well, is of high importance. For the *Calibration* of the cameras, a special holder was needed due to the limited space in the calibration area and the movement of the fluid from the movement of the target. Lastly, the *Post-Processing* can be executed, considering the specific circumstances of the setup. For these experiments, cameras with a focal length of 35 mm, an aperture of F1.6 on CCD sensor cameras with 3.1 µpx and 4242 x 2830 image resolution.

Light

DIC in general, and especially in a fluid, requires a lot of light to limit the camera's shutter time and the size of the aperture, which gives a high in-depth sharpness. Different forms of lighting were tried for the setup, their results are displayed in Figure 3-16. LED strips around the glass or in front had to be dismissed due to insufficient illumination of the sample (Figure 3-16a) and reflections (Figure 3-16b). The red regions in Figure 3-16b and c are oversaturation detected by the software VicSnap [46]. Bright spot lights caused an irregular illumination on the structured sample (Figure 3-16c). The 3D histogram is irregular and the gradient plot shows a wide variety of brightness values in x- and y-direction. Only diffuse background light by a Profilux LED and a halogen light could provide enough diffuse lighting to illuminate regularly as shown in Figure 3-16d. Histogram and gradient plot show a very good distribution in y-direction. In x-direction, the brightness value changes slightly with the structure of the sample, making the flanks of the waves appear darker than tip and valley.

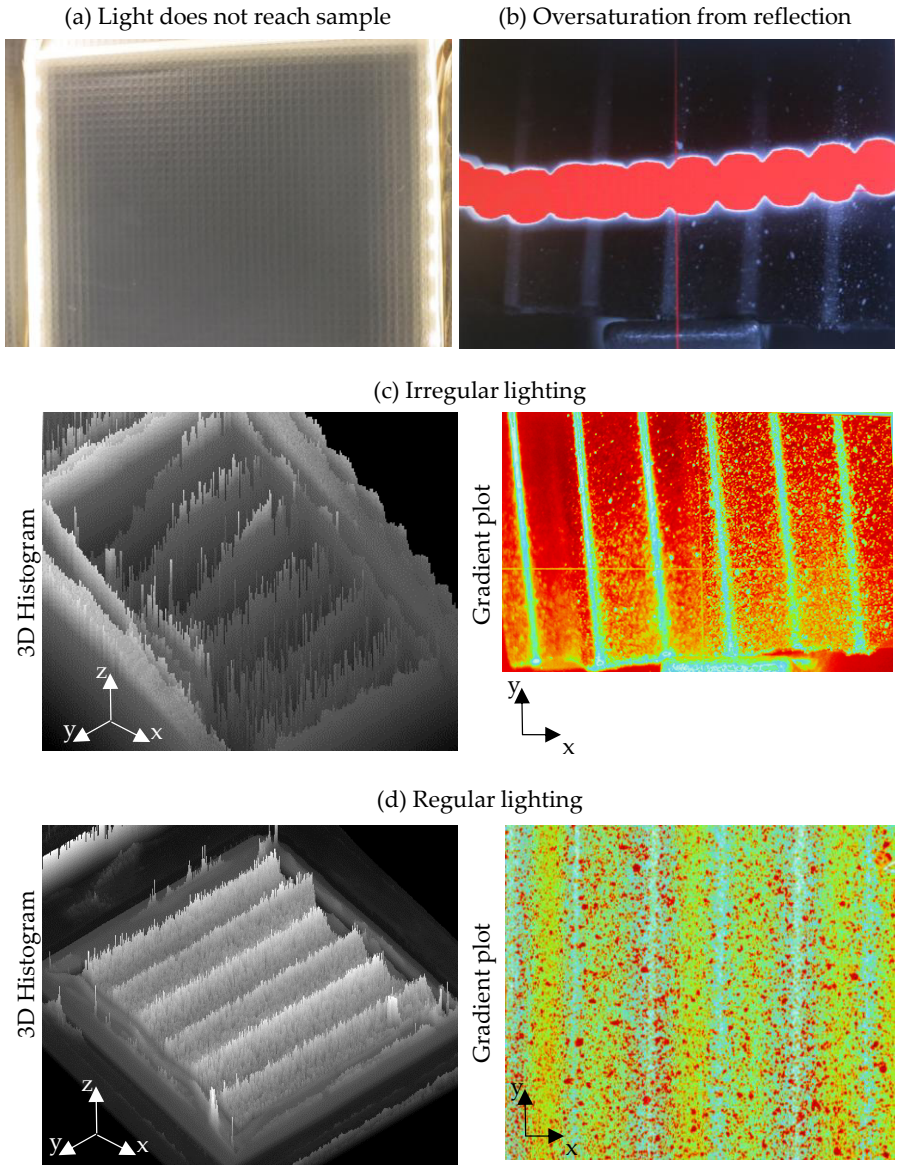

Figure 3-16: Dismissed methods to illuminate structured sample with LED strips, (a) LED on glass edge, (b) LED in front of glass, (c) spot light in front of glass. (d) Diffuse light from different light sources could illuminate well.

Calibration

The calibration of a 3D-DIC setup is typically done with a handheld calibration grid, moved in the volume of interest. In fluid, handheld calibration caused a high calibration error due to movement of the hand and target and therewith of the fluid.

Since the testing setup is closed from all sides, an alternative fluid chamber filled with the same test fluid had to be placed behind the glass to calibrate the setup. Since Stage 1 uses water as fluid, the amount of liquid spent on the calibration, is less relevant. This is not the case for stage 2 which uses expensive oil. In that case, the fluid chamber should be smaller than it is now to limit the amount of fluid needed. That limits the depth of the space available for calibration. The area of interest, that has to be calibrated, is directly behind the glass and takes almost the full width of the alternative fluid chamber (Figure 3-17). Due to the space restriction and the movement of the fluid caused by movement of the target, the calibration was not trivial.

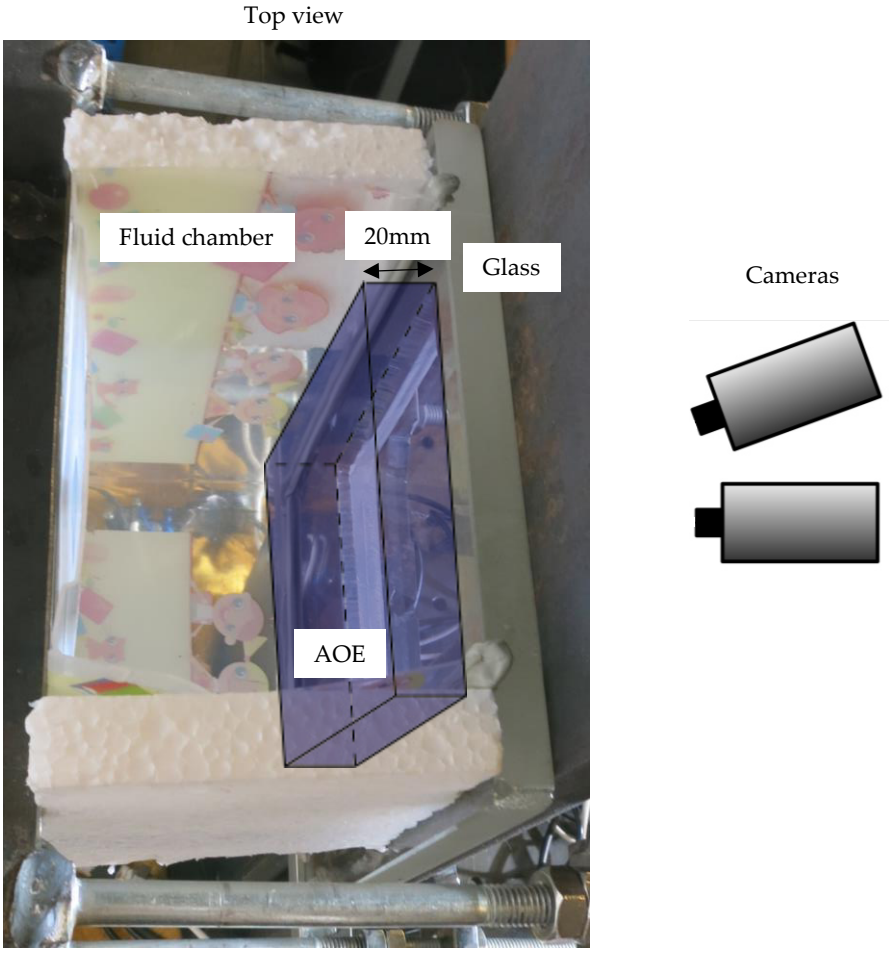

Figure 3-17: Alternative fluid chamber for calibration of the DIC setup. The area of interest is marked in blue. Space constraints are especially relevant, if the fluid chamber needs to be smaller to save fluid.

For a good calibration, the calibration grid has to be moved in all areas of the volume that should be calibrated. Therefore, it needs to be able to move with six degrees of

freedom (3 translational and 3 rotational). For the difficult calibration in the fluid behind glass, a steady fixture of the target was required and designed as a 3-axis system to calibrate the full field automatically with linear stepper motors (Figure 3-18). Rotation of the target was done manually.

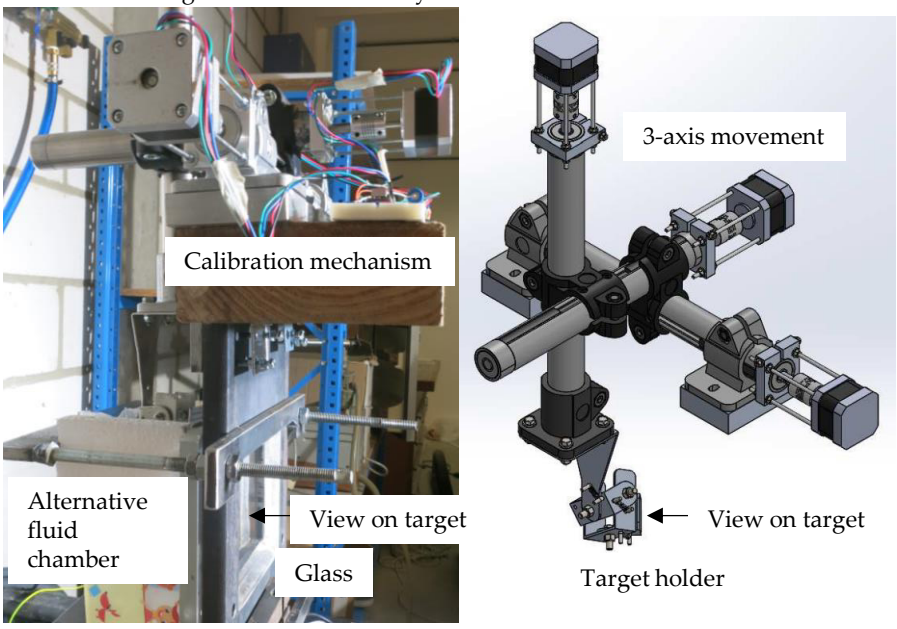

Figure 3-18: Automated 3-axis calibration with linear stepper motors. Alternative chamber for fluid added to provide space for calibration [47]

Post-Processing

Commonly, DIC is used without obstacles between the cameras and the sample. In this setup, glass and fluid are causing distortion effects in the images. To exclude distortion, the use of two angled glass plates and cameras oriented perpendicular to the glasses were considered [48] (Figure 3-19a). M.A. Haile et al. [49] tested the difference between submerged and non-submerged images on elastic rubber and found that an available correction algorithm [50] can compensate for the distortion of the glass. Therefore, a single glass window was used to build the setup and the correction algorithm used. One camera was placed perpendicular to the glass, while the other one was at an angle of 20° (Figure 3-19b).

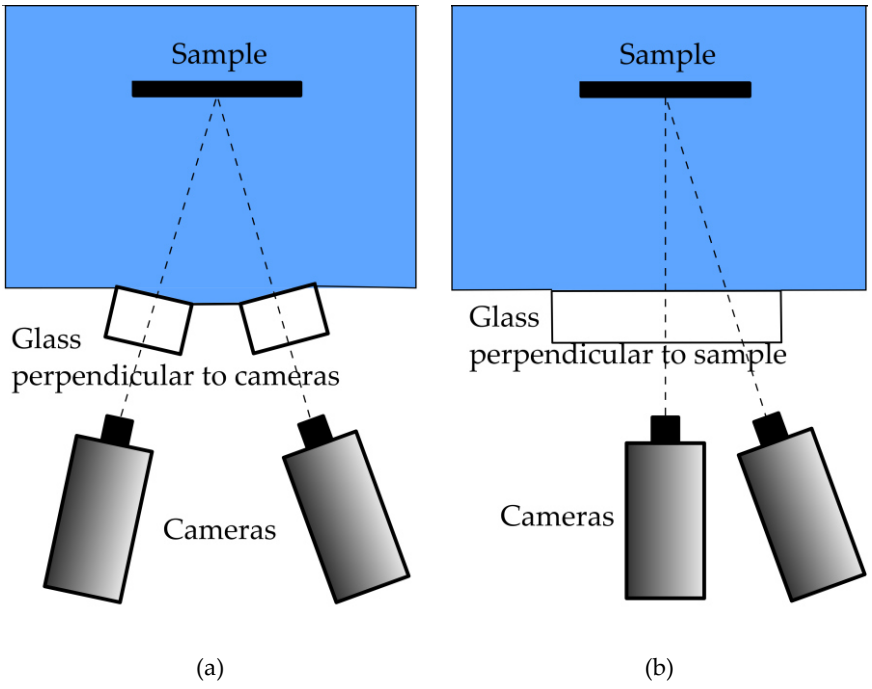

Figure 3-19: 3D-DIC system (a) with both cameras perpendicular to glass to avoid distortion [48] and (b) chosen system in this chapter with one perpendicular and one angled camera

The images can be interpreted by using the software Vic-3D [45]. As a first step, the calibration images are analysed by the software and a score is given. The lower the score, the more accurate the position of the grid compared to the calculated position by the calibration model [51]. If the value is too high, the calibration is insufficient for a precise analysis of the test images. Calibration scores were compared for calibration images through glass with and without fluid. Without fluid, the score was low when held by hand or with the automated target holder. Since the automated calibration takes a lot longer than a handheld calibration, the latter would be preferred without fluids. For the calibration in water, the manual calibration score was more than three times as high as for the target holder and too high to provide a sufficient calibration value. The target holder provided a good calibration score.

Also, the post-processing of the test images was done in the software Vic-3D. Standard settings for the subset size (29) and step size (7) gave a good result with a low projection error. The average speckle size was at 6 px^2, resulting in a high amount of information per subset and therefore a high accuracy of the result [52]. These settings were used to interpret the results of the following tests.

3.6 Experiments

Figure 3-20 shows the build of the setup to test unit cells for the use in heat exchangers. Two different circuits of fluid are controllable: A hot, high pressure one between two sample plates and a cold circuit on the outer sides of the samples with a constant low temperature and low pressure. Strain measurement is possible with 3D-DIC through a vision panel in the setup. A speckle pattern on the sample allows for the correlation of the movement, deformation and strain in a post-processing step.

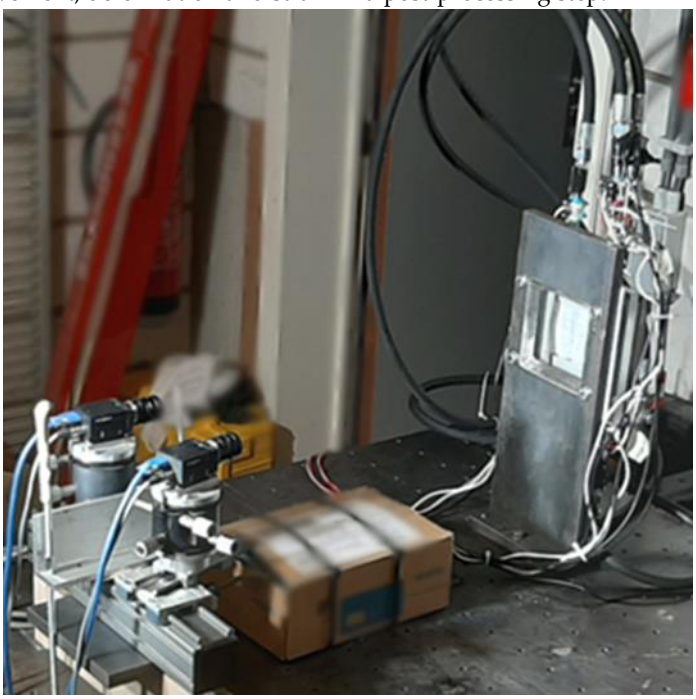

Figure 3-20: Photography of the finished setup

Two different sample shapes were used to prove the concept of the test setup. Thereby, temperature, flow and pressure were monitored and DIC images taken with 1 frame per second. The pressure was first aimed to 1.5 bar on the pressured side (behind the visible sample) and then increased to 4 bar. The temperature was not elevated, since the sample material showed weaknesses already at low pressures and room temperature. The flow was kept constant at 2.3 L/min.

3.7 Test results

3.7.1 Quality control

The strength of a glue connection was validated with injected dogbones, cut in half and reconnected with glue. Three dogbones were used per batch as shown in Figure 3-21 and results of all batches in Table 3-4. For comparison, the pure material

without cut was tested as well. All glued cases showed a lower tensile strength and were very brittle compared to the pure uncut reference samples. Welding of the material or a better surface treatment and adhesion might have improved the result. However, in a heat exchanger, the welding spots are typically not loaded in pure tension and experiencing only very small displacements due to the mechanical fixation in the heat exchanger. The "Solvent HCOOH" or "Loctite Superglue 3 Precision" are possible adhesives for polycarbonate.

Figure 3-21: Dogbone samples which have been cut and re-joined using a glue connection to test the tensile strength of the connection

Table 3-4: Overview of the results of tensile tests on glued connections of PC-5%CF at 1.5 mm/min, 23°C

Glue	F_{max} [N]	Displacement at F_{max} [mm]	STDEV (F_{max})
no glue, uncut	**345**	**3.8**	**3**
Solvent HCOOH	265	0.4	41
LoctiteSuperglue3Precision	236	0.3	26
Pattex Primer	181	0.3	35
Bison Kombi Snel Epoxy	169	0.2	41
LoctiteGoSnelUniversal	76	0.1	15
Pattex Contact	23	0.3	9
Bison Polymax crystal express	broken before test		

This PC+5% carbon fibre was also extruded to be tested in the developed setup and to have a good comparison to the simulated PC plates. Together with data from wind tunnel testing, the material and shape ideally would have been used to estimate the realistic performance of a heat exchanger. However, due to open issues in production like too high feeding rate, sizing, temperature or low feeding speed, gas got trapped or occurred in the extruded material and it showed too many voids to be leakage-free

and was not considered further (Figure 3-22). The following tests are performed on commercially available HDPE material as flat sheets and thermoformed to sinusoidal samples.

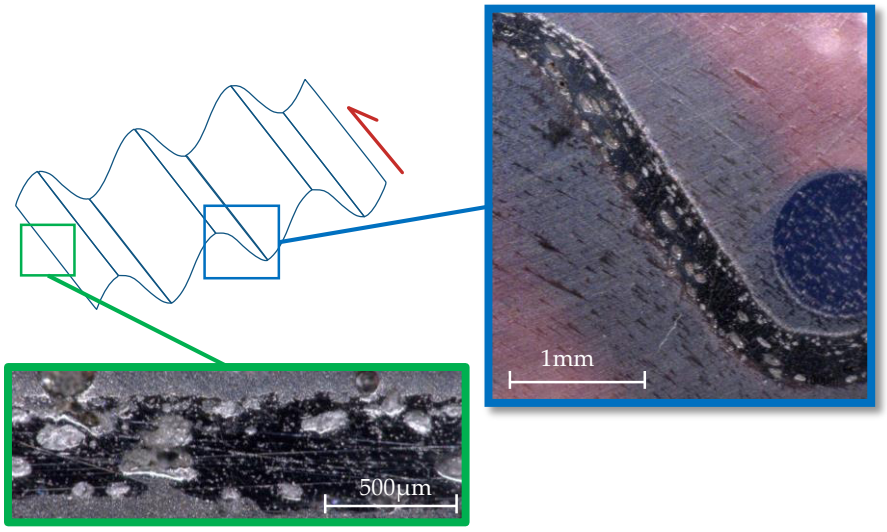

Figure 3-22: Schematic view of initial unit cell sample from extruded polycarbonate with 5wt% of carbon fibre, air bubbles due to production. Air bubbles can be seen in close-up images of the cross-section

3.7.2 Flat sample

A flat sample was observed with DIC during the increase of pressure. Figure 3-23 displays the deformation in the z-direction dependent on the pressure difference between both sides of the fluid. In this case, the fluid on the outer side is pressured lower than the backside of the visible sample. As expected, the analysed images show a strong bending from the side of the higher pressure. The sample starts to touch the glass at a pressure difference of about 2.5 bar, which reduces the speckle recognition significantly. Before that, the speckle recognition is also not perfect. The contrast of the speckles probably becomes too low when the sample deforms and blocks some light. More diffuse light sources could be tried to solve the issue. Overall, the resolution is good enough to see deformation and strain. The strain concentration is showing a cross-like shape of the diagonals of the samples. The sample is stretched between the sample frame and the buckled out centre, causing tension in this direction and compression in the diagonals. Despite this big deformation, the sample strains only about 2.4%. As in a real heat exchanger, the heat exchanger wall (here sample) is not rigidly clamped, but allows for a certain amount of movement if stress is caused by thermal expansion and pressure. This reduces the strain on the material, because there are no membrane stresses.

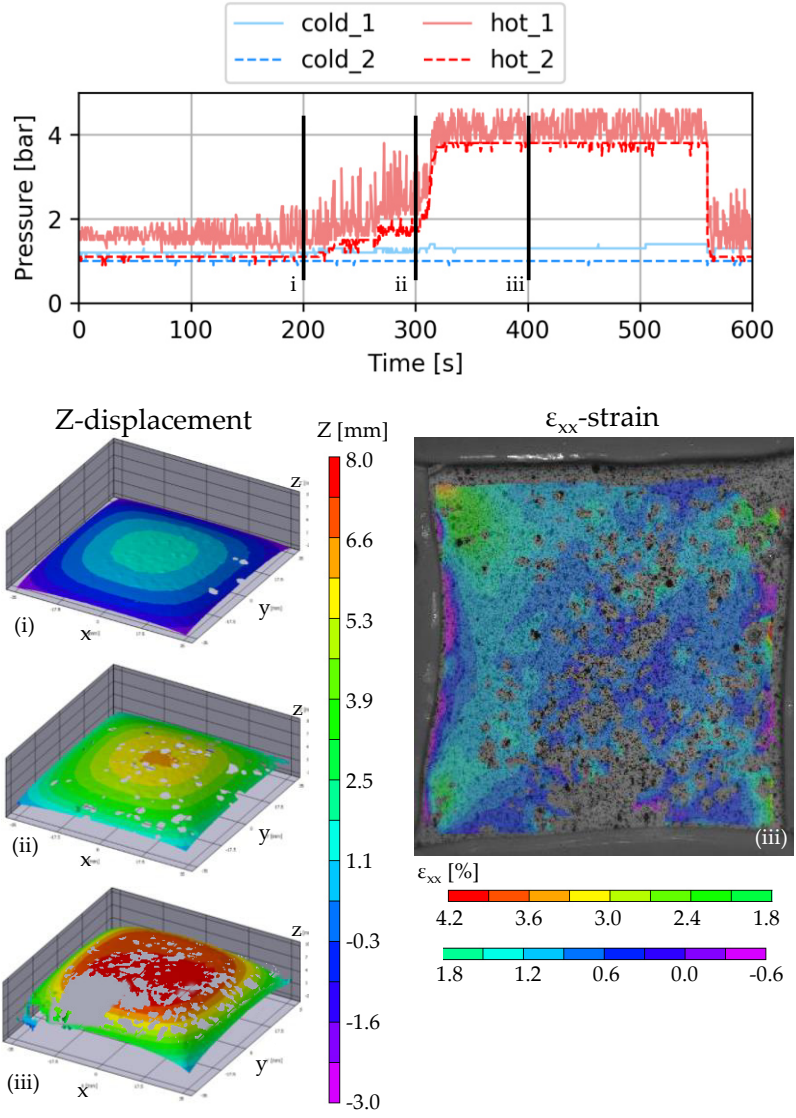

Figure 3-23: DIC images on flat sample, pressure over time. Deformation in z-direction dependent of pressure difference between hot and cold fluid: (i) Δp=0.35 bar, (ii) Δp=0.80 bar and (iii) Δp=2.70 bar and strain concentration ε_{xx} at highest Δp

3.7.3 Sinus wave sample

The test of a sample with a sinus wave shape was successfully measured until a pressure difference of 2 bar was reached, as can be seen in Figure 3-24. The strain is clearly concentrated at the tips and valleys of the shape. The speckle pattern is

recognized until the sample deforms strongly and is pushed against the glass. With this sinusoidal shape, a point contact with the glass is desired, since it simulates the contact points to the adjacent plate in a real heat exchanger. The contact over the full length as it is here the case with the glass, idealises the contact. Added spots could improve the realism of the contact with sacrifice of visual access.

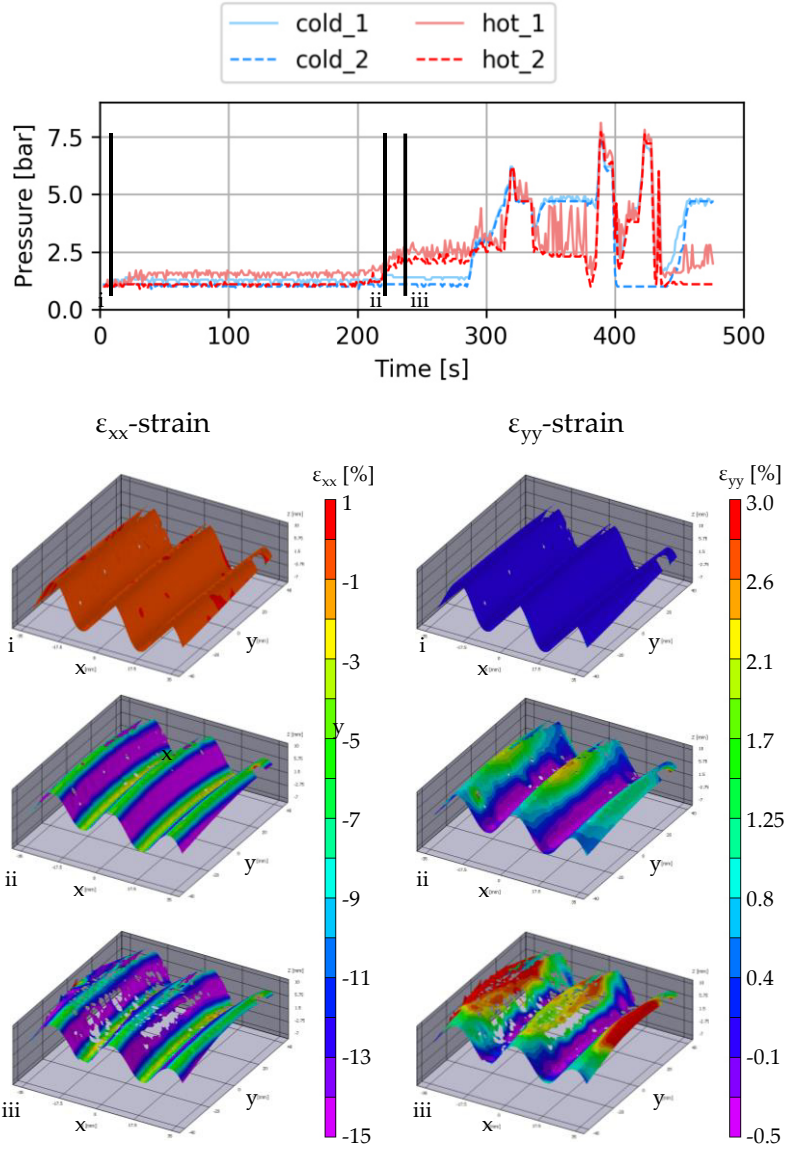

Figure 3-24: DIC images on sinus wave shaped sample, pressure over time. Strain concentration in x and y direction in sine wave shaped sample. Deformation due to pressure differences: (i) Δp=0 bar, (ii) Δp=0.55 bar, (iii) Δp=1.10 bar

Like an accordion, the sinus waved sample intends to deform mainly in x-direction. In case of the thin HDPE material, the frame hinders part of the deformation. This blocking of movement causes compressive strains up to -13%. In the y-direction, the structural stiffness is higher, limiting strains to 3%, similar to strain in the flat plate.

Due to the strong deformation in the y-direction, the test fails at higher pressure differences. The sample deforms and blocks inlets/outlets of the fluid. It was assessed that the pressure was no longer controllable at that point.

3.7.4 Comparison of experiment and simulation

From the numerical simulation it is known that the highest stress concentration in a unit cell is 44.2 MPa with maximum conditions of 70°C and 7 bar. The experimentally tested material was HDPE (as the main component). Its maximum tensile strength at room temperature is 21 MPa [53] and decreases with temperature. At 70°C, a strength of around 8 MPa can be expected. Due to the expected low performance of the material, the experiment was performed at room temperature and the pressure increased stepwise. The test was stopped at a pressure difference of 1.10 bar due to big deformations in the material. It was concluded that HDPE in flat or sinus wave shape is not suited for the application, since it withstood neither the temperature nor the pressure. The simulation gave a relevant input on the expected load on the sample.

3.8 Conclusions of subcomponent testing

To evaluate the strength of a material and structure for a heat exchanger, prototype testing is required to test connection points and pressure as well as temperature gradients accurately. No setup was found in literature that tests heat exchangers while analysing the mechanical performance of structure and connections. Therefore, a unique unit cell test-setup was designed, providing the relevant characteristics of a full-scale heat exchanger with a smaller amount of material. The build-up of a pressure difference as well as a temperature gradient has been demonstrated. Furthermore, displacement and strains were successfully measured using DIC through glass and water after it was proven that the applied speckle pattern on the sample is traceable. Slight improvement can be achieved by increasing the light intensity to ensure a stronger contrast of the speckles.

With the performed tests, the setup shows good potential for comparative studies between different curvatures and angles of the shape. It also fulfils the requirements to be able to study welding connections. The setup was designed for a demand in the Compohex project. The chosen material failed too early to demonstrate the full capability of the setup.

The setup bears further potential. With the current design, the thickness of the spacer is fixed, allowing to test only unit cells that have the same distance between the plates as the previously tested one. A more modular solution would allow for different types of plates. By reducing the thickness of the sample shape, care needs to be taken of the fluid inlet and outlet to realise a complete flow in the chamber. In a modular design also other shapes like tubes could be considered, since this is a second very common shape for heat exchangers [18].

To move to stage 2 of the design requirements (220°C and 8 bar), several costly adjustments need to be made. The water needs to be replaced by another fluid. Silicon oil is recommended due to the low expansion coefficient and the similar viscosity to water. Other fluids, like refrigerants or slight acids, need to be considered carefully and might require a change in components like the metal heating reservoir. Likewise, the currently used cooling unit is not suited for another fluid than water. Most components are not suited for the high temperature like the tubing, the pumps, valves and sensors. However, the design of the rigid components including the glass is made for the higher requirements. By replacing off-the-shelf components, a functioning setup for different fluids at higher temperature and pressure can be assembled.

In addition, standardised mechanical tests can be performed at elevated temperature to provide a faster experiment to screen a wide range of materials. In that case, the geometrical structure is not taken into account, but the results can be used as input for material model. In practice, both methods are required to assess the heat exchanger design performance.

References

[1] M. Arie, D. Hymas, F. Singer, A. Shooshtari, and M. Ohadi, "An additively manufactured novel polymer composite heat exchanger for dry cooling applications," *International Journal of Heat and Mass Transfer*, vol. 147, 2020, p. 118889.

[2] J. Sun, J. Zhuang, H. Jiang, Y. Huang, X. Zheng, Y. Liu, and D. Wu, "Thermal dissipation performance of metal-polymer composite heat exchanger with V-shape microgrooves: A numerical and experimental study," *Applied Thermal Engineering*, vol. 121, 2017, pp. 492–500.

[3] Q. Wang, X. Han, A. Sommers, Y. Park, C. T'Joen, and A. Jacobi, "A review on application of carbonaceous materials and carbon matrix composites for heat exchangers and heat sinks," *International Journal of refrigeration*, vol. 35, 2012, pp. 7–26.

[4] K. Song, S. Hong, S. Lee, and H. Park, "Effect of mechanical properties in the weld zone on the structural analysis results of a plate-type heat exchanger prototype and pressurized water reactor spacer grid," *Journal of nuclear science and technology*, vol. 49, 2012, pp. 947–960.

[5] V. Zipf, A. Neuhäuser, D. Willert, P. Nitz, S. Gschwander, and W. Platzer, "High temperature latent heat storage with a screw heat exchanger: Design of prototype," *Applied Energy*, vol. 109, 2013, pp. 462–469.

[6] M. Mortean, L. Cisterna, K. Paiva, and M. Mantelli, "Development of diffusion welded compact heat exchanger technology," *Applied Thermal Engineering*, vol. 93, 2016, pp. 995–1005.

[7] M.A. Arie, A.H. Shooshtari, and M.M. Ohadi, "Experimental characterization of an additively manufactured heat exchanger for dry cooling of power plants," *Applied Thermal Engineering*, vol. 129, 2018, pp. 187–198.

[8] J. Wajs, D. Mikielewicz, and E. Fornalik-Wajs, "Thermal performance of a prototype plate heat exchanger with minichannels under boiling conditions," *Journal of Physics: Conference Series*, IOP Publishing, 2016, p. 032063.

[9] R. Trojanowski, T. Butcher, M. Worek, and G. Wei, "Polymer heat exchanger design for condensing boiler applications," *Applied Thermal Engineering*, vol. 103, 2016, pp. 150–158.

[10] "Moldex3D 14.0 [computer software], https://www.moldex3d.com/," 2018.

[11] "Digimat 2016-MAP [computer software], https://www.e-xstream.com/products/digimat/overview," *e-xstream*, 2016.

[12] "Ansys Fluent, MPCCI 2017 [computer software], https://www.ansys.com/products/fluids/ansys-fluent," *Ansys*, 2017.

[13] "Abaqus 6.14 [computer software], http://130.149.89.49:2080/v6.14/," *Dassault Systèmes Simulia Corp*, 2014.

[14] M. De Paepe, L. Cardon, W. Van Paepegem, and et al., "SBO Project Endreport, SBO project no.150013 - Composite Heat Exchangers (COMPOHEX)," 2020.

[15] "CB group, https://www.cbgroep.be/," 2018.

[16] "Atlas Copco, https://www.atlascopco.com/en-au/compressors/wiki/compressed-air-articles/aftercooler," 2020.

[17] R. Sakko, "Waste heat recovery from flue gsaes using polymer heat exchangers," *https://heatmatrixgroup.com/*, Heat Matrix, 2019.

[18] S. Kakaç, H. Liu, and A. Pramuanjaroenkij, *Heat exchangers: selection, rating, and thermal design*, CRC press, 2012.

[19] "BOYD cooperation: https://www.boydcorp.com/thermal/liquid-cooling/liquid-heat-exchangers/plate-fin-heat-exchangers.html," 2021.

[20] R. Paridaen, "Assessment of a test setup with pressurised flow at elevated temperature for small heat exchangers elements," Ghent University, Belgium, 2019.

[21] "Lobotherm silicon oil BAP 500, https://www.boewing.de/en/products/item/105-chemical/580-lobotherm_%C3%96l_bap_500_80_en.html," 2019.

[22] "Hydraulic tube DN10 2SC DIN857, https://www.kramp.com/shop-es/en/p/hydraulic-hose-en857-2sc-dn10–HSKHF10," 2019.

[23] "Tubing D16x*2 25m, https://www.toolstation.nl/shop/p85132?channable=e10897.ODUxMzI&gclid=EAIaIQobChMImenC2YSO3wIV0ed3Ch3PZAMjEAQYASABEgI8RvD_BwE," 2019.

[24] "Diaphragm pump type FL3308 , https://www.banggood.com/12V-72W-Water-Diaphragm-Pump-6L-20mm-Water-Pump-Diaphragm-Self-Priming-Sprayer-Pump-p-1493500.html?cur_warehouse=CN&ID=6216039," 2019.

[25] "Solenoid 0757-22139057 dc 12v, https://articulo.mercadolibre.com.ar/MLA-723606089-valvula-de-solenoide-12v-12-entrada-agua-normal-cerrada-_JM," 2019.

[26] "Solenoid valve, https://www.banggood.com/nl/14-inch-Electric-Solenoid-Valve-For-Water-Air-Gas-Diesel-12V-DC-p-978719.html?rmmds=category&cur_warehouse=CN," 2019.

[27] "Manual ball valve, https://nl.rs-online.com/web/p/manual-ball-valves/4578822/," 2019.

[28] "Temperature sensor DS 18 B20, https://www.antratek.be/temperature-sensor-waterproof-ds18b20?gclid=EAIaIQobChMIkoLooMTg3gIVA853Ch03LADaEAQYAiABEgKjevD_BwE," 2019.

[29] "Pressure sensor 5VDC, https://www.dfrobot.com/product-1675.html," 2019.

[30] "Flow sensor (0,6 - 10l/min), https://nl.rs-online.com/web/p/flow-sensors-indicators/5114772/," 2019.

[31] "heating element 3kW 11" long, https://benl.rs-online.com/web/p/water-heater-elements/4676819/," Jan. 2019.

[32] "Regloplas 90s, https://www.regloplas.com/en/products/detail/water-up-to-90c-16/90s/," 2019.

[33] "1/2" connection to 16mm tube, https://www.toolstation.nl/henco-pers-puntstuk/p19274," 2019.

[34] "https://victoriaplum.com/blog/posts/understanding-water-pressure," 2021.

[35] "Labview [computer software], http://belgium.ni.com/labview," *National Instruments Corporation,*, 2015.

[36] "Arduino Mega 2560, https://befr.rs-online.com/web/p/processor-microcontroller-development-kits/7154084/," 2019.

[37] V. Savi, D. Kneževi, D. Lovrec, M. Jocanovi, and V. Karanovi, "Determination of pressure losses in hydraulic pipeline systems by considering temperature and pressure," *Strojniški vestnik-Journal of Mechanical Engineering*, vol. 55, 2009, pp. 237–243.

[38] A. Bahadori, *Natural gas processing: technology and engineering design, Chapter 7: Safety relive valves design*, Gulf Professional Publishing, 2014.

[39] "CS25 condensation cure silicone, https://www.easycomposites.co.uk/#!/resin-gel-silicone-adhesive/rtv-silicone-rubber/condensation-cure-mould-making-silicone-rubber-rtv.html," 2019.

[40] B. Pan, D. Wu, and Y. Xia, "An active imaging digital image correlation method for deformation measurement insensitive to ambient light," *Optics & Laser Technology*, vol. 44, 2012, pp. 204–209.

[41] "Wicked white colour, http://www.artobi-airbrush.be/verf-airbrush-custom/acryl/createx-wicked-colors/wicked-white-60ml/a-6681-20000567," 2019.

[42] "Ambersil Black matt spray paint RAL 9011 https://benl.rs-online.com/web/p/spray-paint/6783082/?cm_mmc=BE-PLA-DS3A-_-google-_-CSS_BE_NL_Facilities_Cleaning_%26_Maintenance_Whoop-_-

(BE:Whoop!)+Spray+Paint-_-6783082&matchtype=&pla-577877946174&gclid=Cj0KCQjw–GFBhDeARIsACH_kdaWgGlH-JPegorCJ1FDd4CHPk4YnXWUBZIgdKAjP7LflQlfUAqfD4waAsdfEALw_wcB&gclsrc=aw.ds," 2019.

[43] "VIC SNAP 8 [computer software], Correlated Solutions."

[44] M.A. Sutton, J.J. Orteu, and H. Schreier, *Image correlation for shape, motion and deformation measurements: basic concepts, theory and applications*, Springer Science & Business Media, 2009.

[45] "VIC-3D 8 [computer software], Correlated Solutions."

[46] "VIC SNAP 8 [computer software], Correlated Solutions."

[47] D. Ghesquiere, "Automation of a test setup for composite heat exchange elements: Flow control and DIC on fully submerged samples," Ghent University, Belgium, 2019.

[48] S. Gupta, V. Parameswaran, M.A. Sutton, and A. Shukla, "Study of dynamic underwater implosion mechanics using digital image correlation," *Proceedings of the Royal Society A: Mathematical, Physical and Engineering Sciences*, vol. 470, 2014, p. 20140576.

[49] M. Haile and P. Ifju, "Application of elastic image registration and refraction correction for non-contact underwater strain measurement," *Strain*, vol. 48, 2012, pp. 136–142.

[50] H. Schreier, "Variable Ray Origin Camera Models for Accurate DIC Measurements Through Glass and Glass/Water Interfaces," International Digital Image Correlation Society, 2017.

[51] *VIC-3D software manual*, Correlated solutions, .

[52] D. Lecompte, A. Smits, S. Bossuyt, H. Sol, J. Vantomme, D. Van Hemelrijck, A.M. Habraken, "Quality assessment of speckle patterns for digital image correlation," *Optics and lasers in Engineering*, vol. 44, 2006, pp.1132-1145.

[53] N. Merah, F. Saghir, Z. Khan, and A. Bazoune, "Variation of Mechanical Properties of HDPE Pipe Material with Temperature," *J. Plast. Rubber Compos. Macromol. Eng*, vol. 35, 2006, pp. 226–230.

Chapter 4

Coupon testing at elevated temperature with digital image correlation

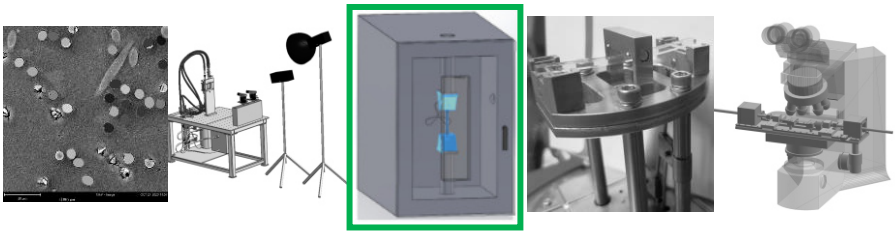

Coupon scale

Abstract: To compare many materials in short time, standardised tests offer great potential; however, composites with thermoplastic matrix are not sufficiently classified by a single test result. Temperature determines the material behaviour significantly. Therefore, it is relevant to measure at different temperatures. Thereby, the strain measurement should not lack in quality compared to tests at room temperature. A test setup was assembled that combines DIC and a heat chamber of an electromechanical test bench. In tensile and creep studies, short and long-term behaviour was analysed. The results of these tests led to the journal paper "Thermo-mechanical coupling of a viscoelastic-viscoplastic model for thermoplastic polymers: Thermodynamical derivation and experimental assessment" by A. Krairi et al. [1].

4.1 Introduction to coupon testing

In chapter 3, testing under exact environmental and structural conditions for the specific case of a plate water to water heat exchanger was shown. To verify those tests numerically, and as a pre-selection for materials, standardised material testing is needed. The generation of the input data for constitutive material models is the aim of this chapter.

Many mechanical tests are standardised, because they are an essential part of any designing, manufacturing and optimisation process. Material needs to be characterised to ensure quality in production, as guidance in research and as safety warrant in service. In every design and development stage, standardised tests are consulted to ensure quantitative safety and qualitative benefits over another material. Especially for material choices depending on the application, engineers need quantitative comparable test results to make informed decisions along their process. For these reasons, standards like the ones for tensile testing [2] exist. They provide guidelines on how to test and how to interpret the results. However, especially for plastics and composites, one single value of strength does not describe the full behaviour of the material under the influence of temperature, humidity, strain rate or long-term loading. In contrast to metals, plastics do not have a distinct yield point and their behaviour changes with the environmental conditions. For the simulation or application of polymers in a heat exchanger standardised testing needs to be combined with the specific environmental conditions.

In literature, tests on polymers and composites have been performed under different variations of these conditions, though the challenge lays in the precise measurement of the true strain on the sample. Strain is together with stress the main value required for material models to accurately predict material behaviour.

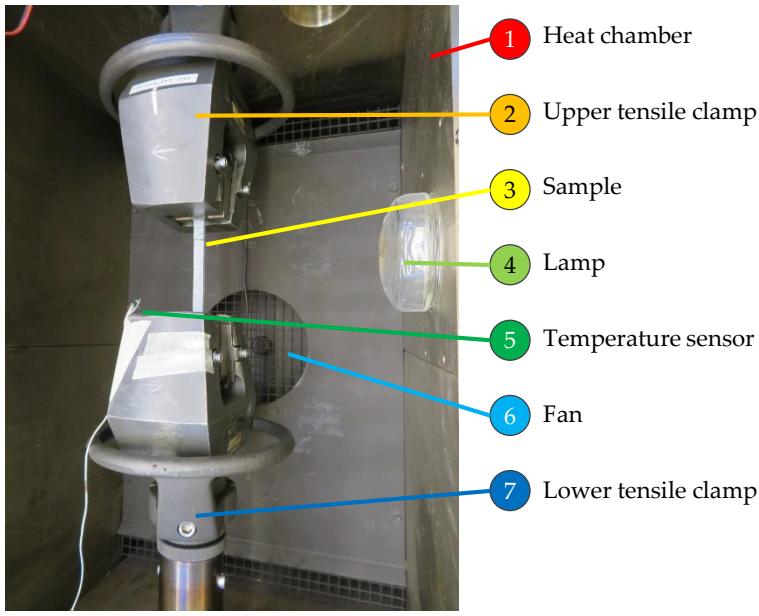

Figure 4-1: Electromechanical testing machine Instron 5800R: Tensile clamps installed in the heat chamber. Dog bone sample clamped

In this chapter, precise measurements of stress and strain on a dogbone sample under tensile load and temperature (Figure 4-1) are applied. First, the accuracy for standardised tests is proven, since they are the basis for advanced testing. Afterwards, the effect of environmental influences is studied, assessing the testing procedure and limits of commercially available equipment and providing solutions for upcoming issues. Thereby, the accurate measurement of strain was of particular importance, since it is often not considered decently in literature, but essential for the later use in predictions and simulations. 3D-digital image correlation (DIC) was used directly on the sample surface and through the glass of the heat chamber. It has the advantages over other methods of measuring full-field and independent of the temperature in the heat chamber. In addition, no pressure is applied on the sample, which can be convenient for softened material of flexible sheets. Individual influences were analysed to confirm the accuracy of the measurement and the importance of critical testing.

4.2 Material and methods

All materials were provided as dogbones, since their shape limits the possible region of material rupture. The dimensions were based on DIN EN ISO 527-4 [3] Type 1B with a length of the parallel edges of at least 60 mm, a width of 10 mm and a thickness of 4 mm (Figure 4-2).

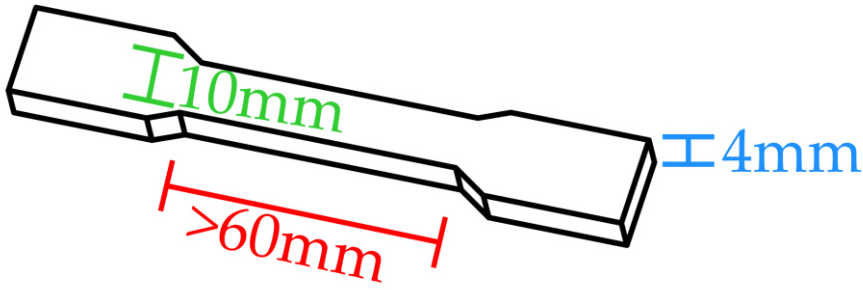

Figure 4-2: Dogbone in the dimensions according to DIN EN ISO 527-4 [3], Type 1B

For section 4.3, dogbones were injected from polyamide 6 (PA6) and partially filled with a carbon fibre content of 20 wt%/13 vol%. The used fibres are short (around 100 µm) carbon fibre from two different manufacturers (Astar [4] and Safran [5]). For testing, the samples were used dry as mould or were conditioned according to ISO 1110 [6] to reach an accelerated equilibrium 23°C/RH50%. Tensile tests were performed following ISO 527 [7].

In section 4.4 materials were used to demonstrate the test method. Used materials were polypropylene with graphite fillers from company Technoform (PP-GF), polyphenylene sulphide with graphite fillers (PPS-GF), PA6 and PA6 reinforced with Safran carbon fibres from company Leartiker. Procedures were based on the standards; diversions are reported in the according paragraphs. For all tests of this chapter, the electromechanical test bench Instron 5800R with 1 kN or 10 kN load cell and a heat chamber was used for the study at elevated temperature [8]. Strain was measured with 3D digital image correlation or an extensometer for comparison.

4.2.1 Strain measurement technique

To measure displacement and calculate strain with DIC, one or two (or more [9]) cameras are used. With one camera, a 2D image with in-plane movement can be traced and no complex calibration is needed. In contrast, 3D-DIC based on two cameras is able to capture out-of-plane displacement. It requires a calibration to localise the position and angles of the two cameras towards each other. In this chapter, two CCD cameras (charge-coupled device cameras) [10] were used to build a 3D system, although only planar movement needs to be measured. Small out-of-plane movements like a misalignment of the clamps or sample thinning due to Poisson's ratio can falsify the in-plane result if taken with 2D-DIC only. 3D-DIC can compensate, since it measures the out-of-plane movement as well [11]. The used system was calibrated with a grid of eleven by six 1 mm big dots with a distance of 5 mm between them shown in Figure 4-3. The size and distance of the dots is determined by the distance of

the sample to the cameras. The amount of dots was chosen according to the area of interest, which equals the size of the dogbone and the possible position where the sample can be clamped.

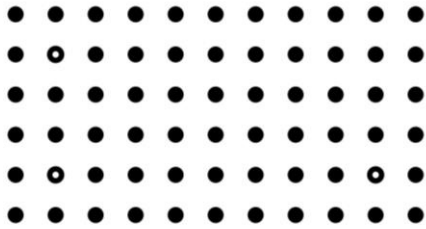

Figure 4-3: Calibration grid for 3D-DIC, 11x6 dots, distance 5 mm, dot diameter 1 mm

On the test samples, a random speckle pattern had to be applied to allow the software to calculate the deformations in pattern and therewith of the sample. It is commonly applied using black and white paint, if the specimen does not offer a suited design by nature. For the experiments in this chapter, a white base coat was applied using matt airbrush paint [12]. The fine droplets of airbrushing allows for high deformation of the sample without breaking the paint layer. The black speckles were applied using matt black acrylic spray paint [13].

Both cameras take images at precisely the same time using the software Vic-Snap [14] so that the position of the cameras can be calculated from the different viewpoints on the calibration grid commonly using a pinhole-model. A pinhole model as in Figure 4-4 assumes that all light rays are reflected from the original real image in an undisturbed way. The rays are bundled at a fixed point, the pinhole, and form the image on the sensor. The algorithm in the used software Vic-3D [15] calculates the position of the real image from the sensor image. The test images are recorded and interpreted in the same way, allowing the algorithm to calculate position and deformation of the sample throughout the test. Thereby, it also calculates the quality of the calculated position in comparison to the real position, expressed in the value of the projection error.

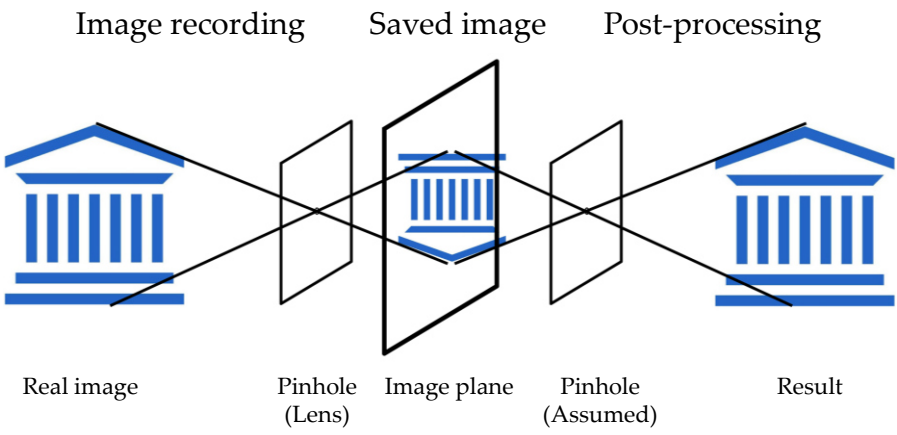

Figure 4-4: Analysis of an image: Image is recorded with a camera, resulting in a stored image. The post-processing software interprets the stored image to reconstruct the position of the real image. In the standard pinhole-model an undisturbed lens is assumed for the reconstruction.

4.2.2 Engineering and true stress-strain-curve

With DIC, different stress-strain curves can be calculated. Two relevant ones will be discussed more in detail: engineering and true curves. With an engineering approach, the cross section of the sample is assumed constant, whereas for a true approach, the cross section is assumed to change over time. Both have their specific purpose:

- The **engineering stress-strain curve** is used for the knowledge of the performance with given dimensions and forces. From engineering values, toughness and ultimate tensile strength can be calculated directly.
- In a material model, **true stress-strain curves** are needed. Engineering stress-strain curves have a misassumption of the material getting weaker over time. In reality, it is the opposite: Strain hardening takes place and due to the change in cross section, which is taken into account in the true approach, the material gets stronger. With true values, the stress state is known at any point in the material [16].

Figure 4-5 illustrates the difference. The curves are almost identical. After the ultimate tensile strength at around 3% strain, the engineering stress is going down whereas the true stress stays almost constant.

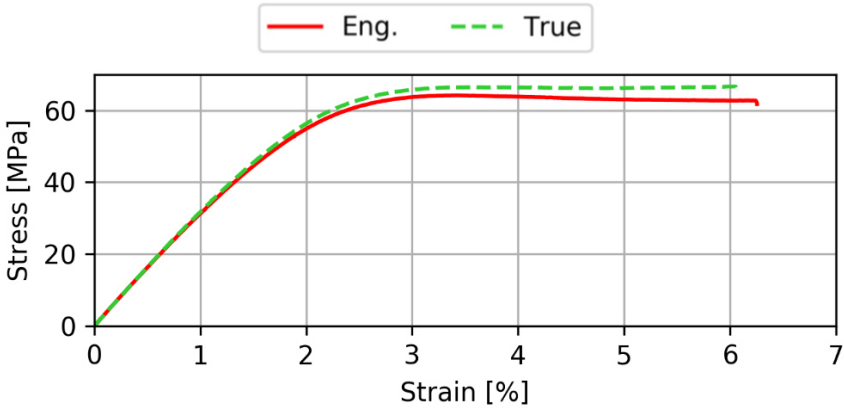

Figure 4-5: Difference between engineering and true stress-strain-curve. Example on PA6 matrix dried to 0% relative humidity

Stress and strain are in both cases based on the force and displacement. The force is measured with the load cell of the machine. The strain can be measured in different ways. Easiest, but least precise one is to read out the displacement of the crosshead of the machine and calculate the strain from that displacement [17]. Hereby, for example slippage between samples and clamps or inside the machine is not accounted for. Precise measurements along the loading direction can be done by using extensometers, strain gauges or DIC. For the engineering values, any of these methods is possible. To calculate true values or to measure and consider the Poisson's ratio, biaxial measurements are required, since the cross section of the sample is changing. Biaxial extensometers, optical fibres, strain gauges rosettes or DIC are available, whereby DIC is the preferred method, since it is independent of the temperature in the heat chamber and offers a full-field measurement. DIC allows in addition to measure the engineering strain or different true strains, whereby here the Hencky strain was chosen, since it agrees with the output of the finite element software ABAQUS. To calculate stress and strain from force F, gauge length L and initial cross section A_0, the following formulas are needed for engineering stress (Equation (4-1)) and strain (Equation(4-2)), true stress (Equation(4-3)) and strain (Equation(4-4)) respectively [18].

$$\sigma_{eng} = \frac{F}{A_0} \tag{4-1}$$

$$\varepsilon_{eng} = \frac{\Delta L}{L} \tag{4-2}$$

$$\sigma_{true} = \frac{F}{A_0}\,(1 + \varepsilon_{eng}) \tag{4-3}$$

$$\varepsilon_{true} = \ln\left(1 + \varepsilon_{eng}\right) \tag{4-4}$$

The speed of the test can be given as displacement rate in mm/min ($\dot{u}_{eng}$) used to execute the experiment or as numerical strain rate in 1/s ($\dot{\varepsilon}_{num}$), common for post-processing and numerical models. The displacement rate is thereby based on the crosshead speed (Equation (4-5)) with Δu as the relative displacement and time t. The strain rate is the derivative of the experimental time versus the measured strain (Equation (4-6)), i and n are the limits of the linear region. This version of the strain rate provides the relative displacement and is therefore independent from the original dimensions.

$$\dot{u}_{eng} = \frac{\Delta u}{t} \tag{4-5}$$

$$\dot{\varepsilon}_{num} = \frac{\sum_i^n \frac{\varepsilon_{eng_{i+1}} - \varepsilon_{eng_i}}{t_{i+1} - t_i}}{n} \tag{4-6}$$

4.2.3 Long-term prediction methods

The life-time for a heat exchanger is roughly 20 years. For this time, it needs to be ensured, that the material withstands the creep load and environmental conditions. A testing time with that duration is not feasible. Since this is an issue for basically all long-time applications, methods were found that can replace the long testing time and still give a good assumption of the life-time behaviour. ISO 899-1 [19] and ASTM D 2990 [20] are tackling the issue, focussing on a testing time of at least 1000 h (42 days) to create a trend curve at the expected load and temperature. The curve can be extrapolated to estimate the creep after several years. An even faster testing method is based on the so called Time-Temperature-Superposition principle (TTSP), which claims that the effect of time and temperature on the material are interchangeable [21,22]. Instead of a long testing time at the service temperature, higher testing temperatures can be applied for shorter times. Due to the elevated temperature, the material weakens. Polymers react to small increases of temperature by becoming more ductile and have lower strength, because of their viscoelastic behaviour [23]. This is equivalent to the effect of time. If a material weakens a lot with small increase in temperature, it is also over time not resistant to the applied load at the service temperature. To quantify this effect, individual tests at elevated temperature can be combined to a so called master curve. In practice that means, a material is loaded for a certain small duration at several temperatures including the temperature in service. Each test from each temperature delivers thereby an individual

testing curve. All these curves can be plotted together, forming the master curve [24]. A schematic can be seen in Figure 4-6. This method is traditionally used for amorphous materials in the visco-elastic range without fillers. When the method is transferred to semi-crystalline composites, the validity of TTSP has to be checked [25,27].

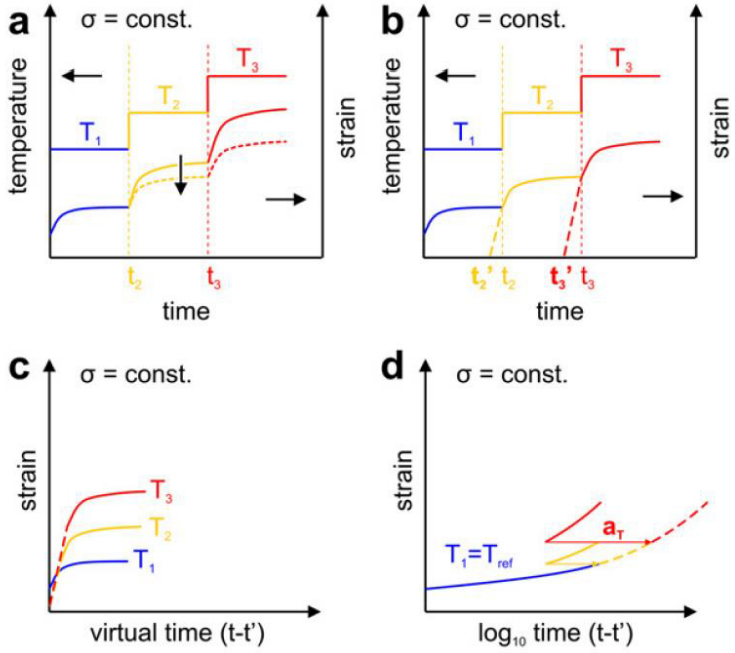

Figure 4-6: Illustration of stepped isothermal method (SIM), the same test is repeated on the same sample at different temperatures: To create a master curve for long-term prediction, several steps are necessary: (a) compensation of thermal expansion, (b) splitting experiment into individual events, (c) individual events plotted, (d) curve shifting with shift factor a_T [25]

To produce curves at different temperatures, two methods are common: one sample is tested throughout all temperatures (SIM – stepped isothermal method, Figure 4-6a-d) or per temperature a new sample is taken (TTSP, Figure 4-6c-d).

Using a classic test bench, TTSP and SIM deliver comparable master curves [26,27], but the amount of samples needed is higher for TTSP than for SIM, because the experimental variation between samples needs to be taken into account for the overlay of curves with TTS. For SIM, the different temperatures are applied to the same sample, eliminating the error due to differences in clamping and material [28]. According to ASTM D6992 one sample is sufficient for SIM, if the quantitative values are confirmed with two short term creep tests [29]. In the application of TTS, three samples would be required per temperature step [26], typically resulting in more than 20 samples, depending on the amount of temperature steps. In the SIM method, a bigger error is introduced due to the little amount of material used. In addition, the

sample is constantly loaded, also during the heating phase between two temperature steps. This time is removed during the post-processing, falsifying the time-temperature history of the sample. Lastly, in case of humidity sensitivity, a constant climate needs to be ensured, since the material is exposed to higher temperatures far longer than with TTS. Overall, both methods show that accelerated tests are a valid method to estimate life-time behaviour reasonably well and therefore cost-effective [30]. As a basis for a good long-term prediction, the test setup and method is validated in short-term tests.

4.3 Standard testing methods on coupons

4.3.1 Tensile testing

To demonstrate a standardised tensile test according to ISO 527-2 [31], samples of pure PA6 matrix material were compared to short fibre reinforced ones (20 wt%/13 vol%.). Fibres with similar properties of two different brands (Astar and Safran) were compared. Five samples were used per material, providing sufficient information about statistical scatter around the average. The tests were performed at room temperature with a speed of 1 mm/min (≈ 1.45E-04 s^{-1}), a gauge length of 75 mm and a distance between the clamps of 115 mm. Due to a very good material quality, the scatter on the ultimate tensile strength (UTS) and matching strain is very low, as shown in Table 4-1. Thereby, the stiffness (Equation (4-7)) is calculated in the linear region between 0.05% and 0.25% strain [32].

$$Stiffness[GPa] = \frac{Stress(0.25\%) - Stress(0.05\%)}{0.25\%Strain - 0.05\%Strain} : 1000 \qquad (4\text{-}7)$$

Table 4-1: Test results of tensile tests at 23°C and 0%, respectively 50% relative humidity

	0% humidity			50% humidity		
	Stiffness [GPa]	**UTS [MPa]**	**Strain at UTS [%]**	**Stiffness [GPa]**	**UTS [MPa]**	**Strain at UTS [%]**
PA6 Matrix	3.2 ± 0.1	62.7 ± 2.5	9.92 ± 8.06	1.3 ± 0.1	41.2 ± 1.7	28.13 ± 2.02
Astar	16.0 ± 0.8	181.8 ± 2.3	2.24 ± 0.01	10.6 ± 0.5	130.7 ± 1.6	4.12 ± 0.05
Safran	17.1 ± 0.5	211.7 ± 0.7	3.72 ± 0.14	11.0 ± 1.0	161.3 ± 2.2	6.41 ± 0.25

The average curves are displayed in Figure 4-7. For comparison with other test data, the engineering values are plotted here. The pure matrix material is weaker than the reinforced material, resulting in about a quarter of the ultimate tensile stress, but reaching a strain about three times as high for most samples. The results were compared to literature results on PA6 with 20 wt% short carbon fibres [33]. There the carbon fibre improved the strength of the pure matrix from 73 MPa to 110 MPa, which is significantly less improvement than from the fibres used here. In literature, the elongation at break is with 6% also higher, indicating a more effective fibre-matrix interaction in the material tested here. The fibre length in the literature material is unknown, which might explain the different values. However, the trends in the material behaviour are the same, short carbon fibre increases the ultimate tensile strength and decreases the strain at break.

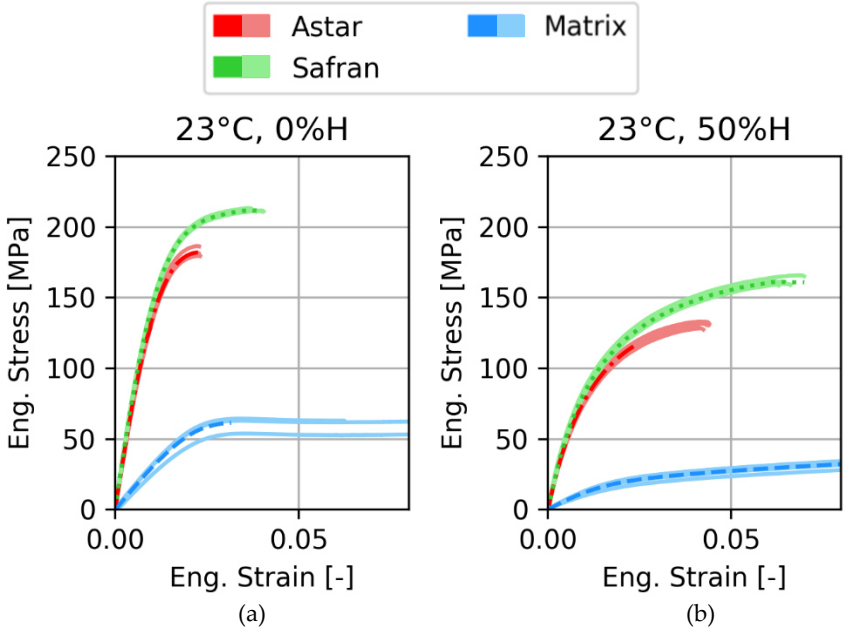

Figure 4-7: Tensile tests at (a) 0% and (b) 50% humidity on two different carbon fibre reinforced PA6 samples (Astar and Safran) and pure PA6 matrix. 5 repetitions per test, one darker averaging curve per material

From the samples tested here, two at 0% moisture content failed in a brittle manner, due to imperfections in the material. The failure of the other matrix samples is ductile, showing slight necking before failure. From the reinforced samples, Safran fibres show the strongest reinforcement with the largest elongation of the reinforced samples. Astar fibres are causing a slightly more brittle behaviour. Tensile tests on the pure fibres would be necessary to evaluate, if the fibres have different strength due to the production process.

Samples that were conditioned in 50% humidity show a lower stress resistance and a higher elongation overall, due to the moisture sensitive PA6 matrix. The relation between the different types of samples remains the same: Safran fibre reinforces the strongest, followed by Astar. In a design process, this standardised test could help to make a choice for a fibre type. Despite the similar dimensions, concentrations and properties, one fibre type performed better than the other.

4.3.2 Measurement of Poisson's ratio

In the context of standardised tests, the Poisson's ratio was also measured. The Poisson's ratio ν is the ratio between the longitudinal elongation ε_{xx} and the contraction perpendicular to the force ε_{yy} (Equation (4-8)) [32].

$$\nu_{xy} = -\frac{\Delta\varepsilon_{yy}}{\Delta\varepsilon_{xx}} \tag{4-8}$$

It can be determined by measuring the two principal strains during a tensile test [34]. To demonstrate this method and for later use in chapter 5, the Poisson's ratio of PP-GF was measured. PP-GF is a highly filled polypropylene with 75 wt% (50 vol%) graphite flakes and was injected to dogbone samples. In a standardised tensile test [32] at 1 mm/min ($4.4*10^{-5}s^{-1}$) and 20°C, DIC was used to measure the mean values of the principal strains (Figure 4-8).

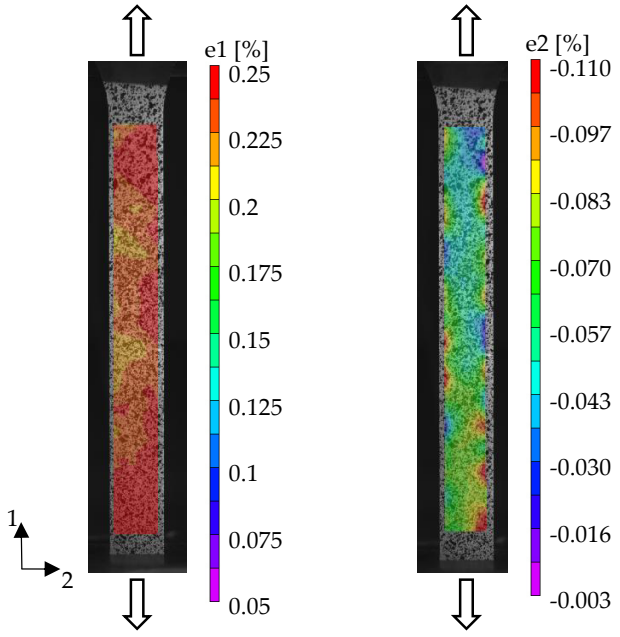

Figure 4-8: Principal strains at 0.25% longitudinal strain. Averaged full-field values used to calculate Poisson's ratio

Four different samples were tested under the same conditions, resulting in the stress-strain curves in Figure 4-9a. Normally, the Poisson's ratio should be determined from the linear region between 0.3% and 1.5% strain [32]. Since the material behaves very nonlinear, the linear region is limited to the very beginning of the curve, the standard recommends to determine the Poisson's ratio between 0.05% and 0.25% longitudinal tensile strain [2]. The curve is not linear in that region. Nevertheless, the Poisson's ratio plotted over the longitudinal strain, shows a constant value in the suggested region and was therefore evaluated as valid. An averaged Poisson's ratio of 0.24 was identified at 20°C (Figure 4-9b). The same ratio could be confirmed for 80°C, excluding that the Poisson's ratio is temperature dependent between 20°C and 80°C. In literature, a Poisson's ratio can be found between 0.17 and 0.23 for pure graphite [35] and of 0.43 for pure polypropylene [36]. Due to the high graphite content, the measured Poisson's ratio is plausible, a further validation could be done by applying numerical homogenization with the Mean Field Homogenization method (in casu Mori-Tanaka Mean Field Homogenization).

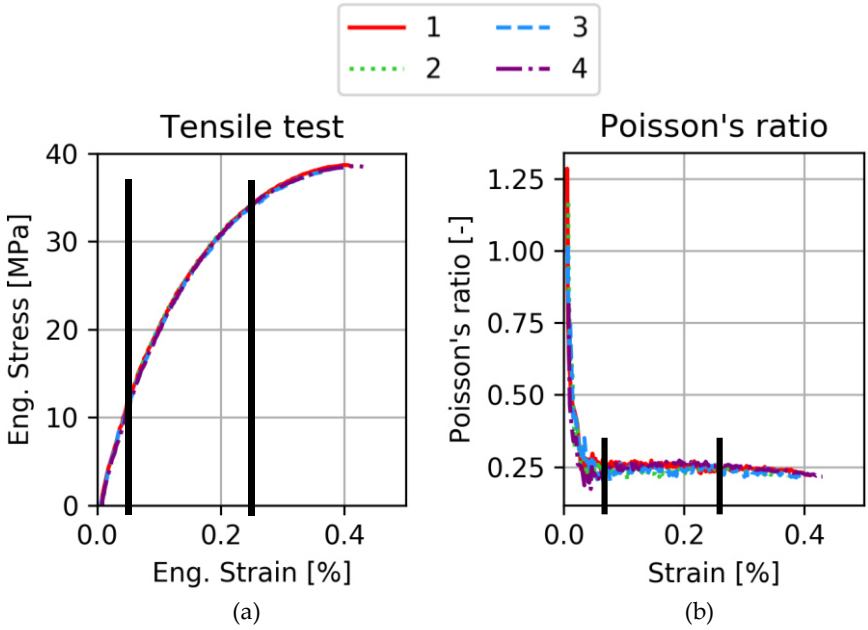

Figure 4-9: Poisson's ratio determined from tensile test on PP-GF (a), four repetitions. Black lines frame the area the Poisson's ratio is averaged from. (b) The Poisson's ratio is steady between the black lines

4.4 Tensile testing beyond the standard methods

Machine suppliers offer tools to adapt the environment of testing to the requirements on the material in later service. Force-displacement curves at elevated temperature are well known in literature, but the strain is calculated based on the machine displacement only [37]. This result is not accurate since it gives the displacement of the cross-head and not of the sample only. To measure precise strain, especially true strain, at elevated temperature, DIC is the most convenient method. To ensure the correctness of the measurement, different aspects of the testing need to be carefully considered and machine specific adjustments are necessary. In the following section, the challenges that occurred using an electromechanical test bench (Instron 5800R) are discussed. While the solutions are specific to this machine, the considerations are relevant for other machines as well. With well executed experiments, engineering and true strain can be successfully measured on the sample surface, providing essential data for engineering design and material modelling.

4.4.1 Testing at elevated temperature

For the testing at elevated temperature, the heat chamber of Instron with a range of -100°C until +350°C was used, as displayed in Figure 4-10 [8]. A fan distributes the hot air in the chamber. The door has a vision panel for optical observation; inside the chamber is a single light bulb for easier visual access.

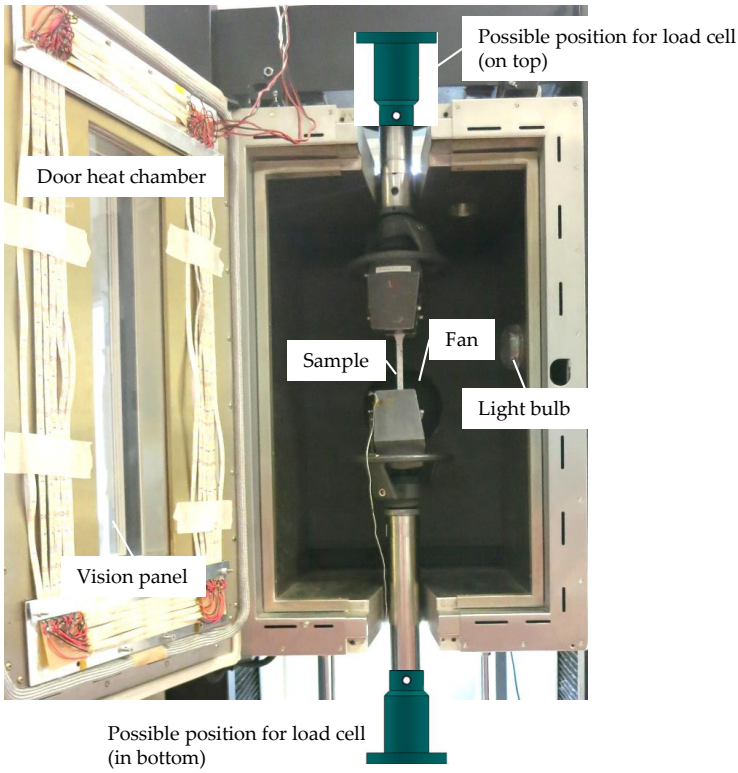

Figure 4-10: Components of the heat chamber

Heating of the chamber takes up to 20 min according to the machine manual [8], the heating of a PA6 sample in 4 mm thickness in theory 9s/10°C. However, the heating of the clamps and therewith the stabilising of the temperature in the heat chamber takes in practice about 1 h as tested with an additional thermocouple. Furthermore, the sample should be conditioned before testing [38]. This can be done in an external heat chamber or in the bottom of the test chamber, if damage due to testing of other samples can be excluded. If an external chamber is used, the sample should be equilibrated in the testing machine before clamping. A.D. Drozdov et al. recommend to wait 10 min after clamping, but before loading [38]. This allows the temperature in the heat chamber to become stable again after opening the chamber to clamp the sample.

Tensile and creep tests in tension were planned at higher temperature, since heat exchangers are prone to fail in creep during their 20 year life time. Especially the accuracy of load and displacement measurement need to be considered carefully to achieve valid stress-strain curves.

4.4.1.1 Load cell

During creep tests with a dead-weight load, issues with the load cell were discovered. Initially, the load cell was mounted on top of the heat chamber, as Figure 4-10 shows. When a fixed weight of 440 N was applied at room temperature, the load measurement remained steady. At a temperature of only 40°C in the heat chamber, the measurement of the load cell changed (Figure 4-11). The stream of hot air and physical connection between the clamp in the heat chamber and the load cell via the metal rod led to an increase of temperature in the load cell, which effects the strain gauges inside the load cell, which is falsifying the measurement. Eventually, the load measurement at this relatively low temperature is stabilising, but the absolute measurement needs to be corrected and adjusted to every temperature change.

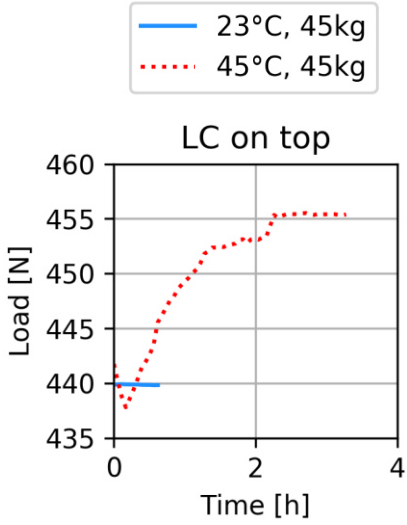

Figure 4-11: Shift in load measurement caused by temperature when the load cell (LC) is mounted on top of the setup

To avoid the heating through upstreaming air, the load cell was placed in the bottom. Although it improved slightly, the load measurement was not stable enough, since heat was still transferred through the metal rod connecting the load cell with the clamp. As a solution, a cooling system for the load cell was devised. Cooling ribs connected to pressurised air were placed around the rod connecting the load cell and the bottom clamp. The effectiveness of this solution was demonstrated using a thermocouple Type k. As shown in Figure 4-12 with a weight of 44.6 kg, the cooling is sufficient to keep the temperature at the load cell below 27°C, even if the heat chamber is heated to 240°C with a heating rate of 13°C/min on average.

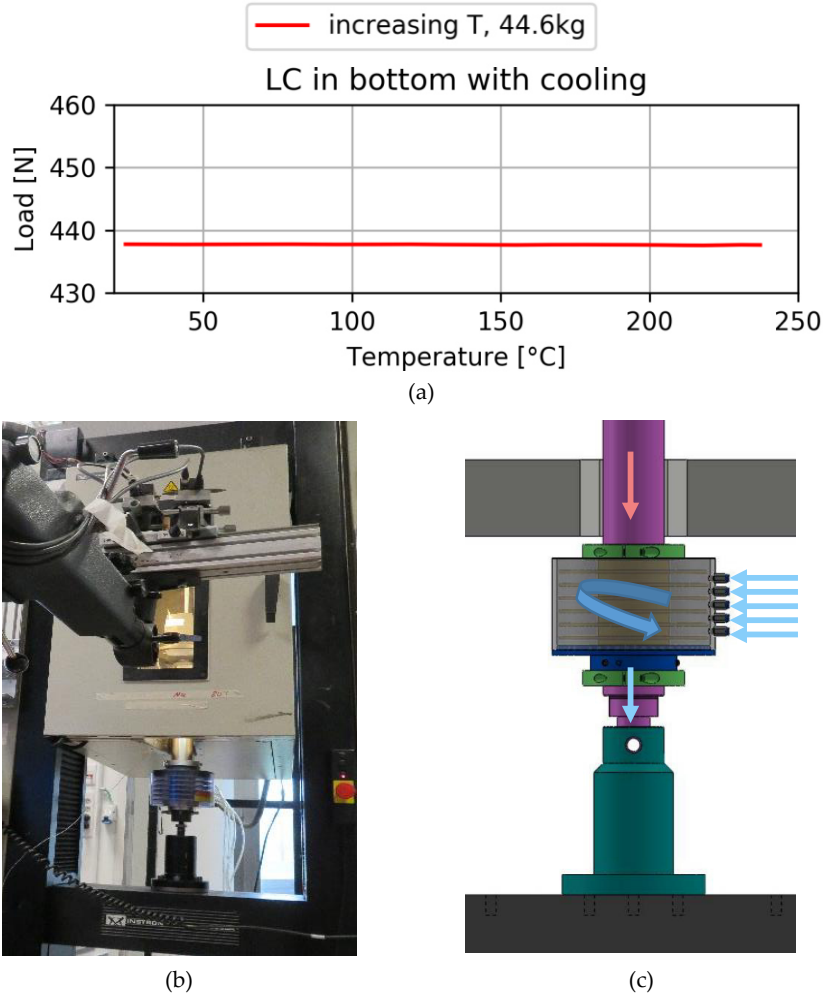

Figure 4-12: (a) Stable load measurement until 240°C when the load cell (LC) is mounted on the bottom of the setup and an additional cooling is installed (b) photo and (c) schematic of the cooling unit

The load measurement can also be influenced by the fan in the heat chamber (Figure 4-13a). The active fan makes the heat chamber vibrate. However, if there is adequate clearance between the fixed rods connecting machine frame and clamps and the chamber, these vibrations are not transferred and the measurement is accurate. Alternatively, if the bottom rod is not fixed to the frame, but a dead-weight is used as part of a creep test, the air flow caused by the chamber can lead to a swinging motion of the bottom weight and therewith unexpected load on the sample. The addition of guiding rods on the bottom weight (Figure 4-13b) proved to be sufficient against the movement and a dry run showed there is no significant friction that could influence the result. Metal hooks connecting the upper and the lower clamp ensured the safety of the setup in case of sample failure.

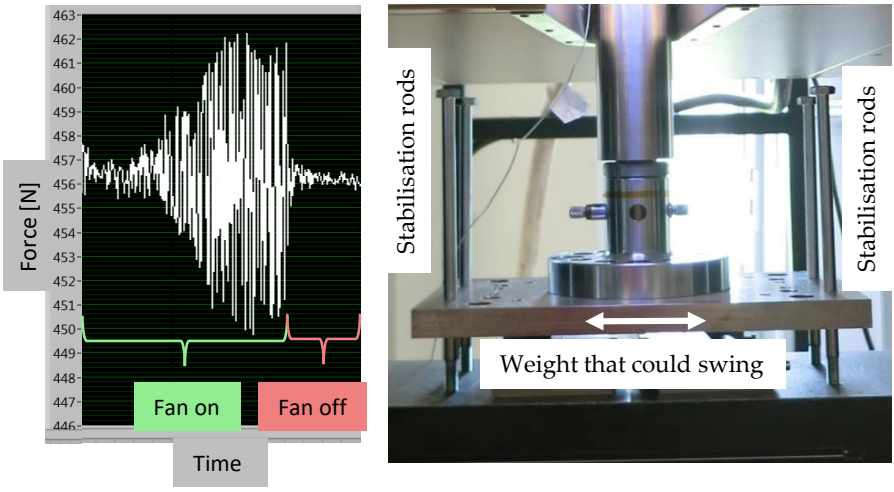

Figure 4-13: Issues with fan and thereby airstream in heat chamber: (a) Screenshot of load measurement showing vibrations in case of contact between heat chamber and rods and (b) swinging of creep weight solved by stabilisation rods

4.4.1.2 Temperature control

The heat chamber controls the temperature with a precision of ±2°C [8]. Temperature was additionally measured with a thermocouple type K, which has an accuracy of ±2.2°C. This was sufficient to confirm the accuracy of the temperature at temperatures above 100°C. However, at lower temperatures the light bulb integrated in the chamber can influence the temperature, if no liquid nitrogen is attached for cooling. An infrared thermometer measured 98°C on the cover of the light bulb after 1 h in service. Due to it, an increase of 1°C/20 min (Figure 4-14) was noticed in the full chamber if the chamber was at room temperature. To avoid heating, a different source of light needs to be used, if visual access is required at all times. The solution will be presented in the following section.

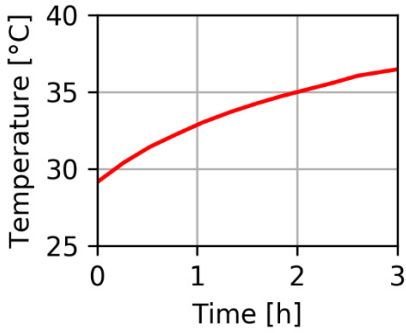

Figure 4-14: Temperature increase due to the light bulb in heat chamber only

4.4.1.3 DIC through glass of heat chamber

When installing DIC cameras, typically the angle between the cameras is recommended to be bigger than 30° to ensure a good 3D image. When testing in a heat chamber, the angle of the cameras towards each other is limited due to the relatively small width of the window. In addition, the cameras need to be placed relatively far away (50 cm) from the vision panel of the heat chamber to ensure the chamber can be opened for example to switch samples, as shown in Figure 4-15a. This led to a maximum angle of 20°, which has the advantage of less likely distortion due to the glass [39].

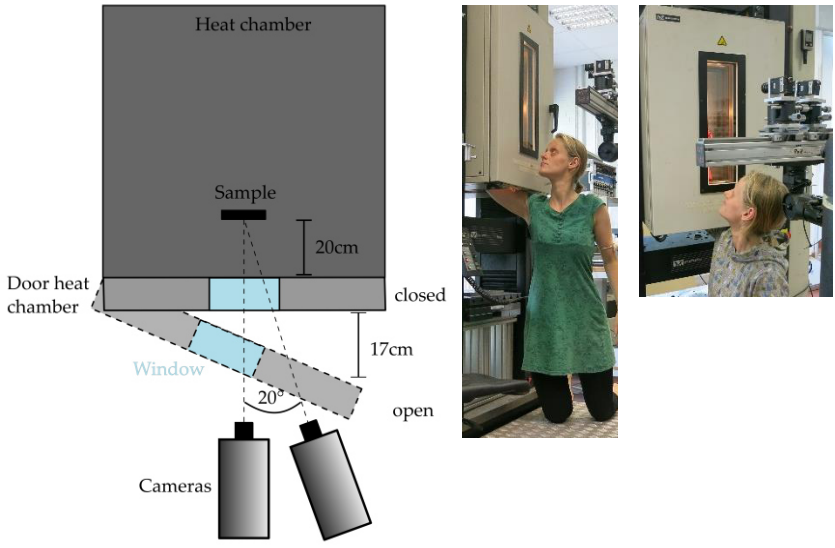

Figure 4-15: (a) Space restrictions to access sample in heat chamber and (b) manual calibration of DIC cameras inside the heat chamber from bottom opening

To perform a DIC measurement, the position of the cameras needs to be calibrated. A classic, dotted calibration target in the size of the area of interest was also used for the tests in the heat chamber. The calibration was done at the same temperature as the testing temperature to ensure, glass, air and light have the same properties as during the test. This means, the calibration had to be performed inside the heat chamber with a closed door. To access the testing space with the calibration target, an opening in the bottom of the heat chamber was found to be sufficient (Figure 4-15b). With a heat resistant glove, the sample could be held and moved in the space accordingly.

Sufficient light is needed to have good quality images for the analysis [40]. If the sample is placed inside the heat chamber about 20 cm behind the glass, light sources from outside the chamber through the glass can enhance the brightness, but an internal light source is needed due to reflection and light diffusion through the glass. LED strips with a protective rubber cover were used to create a sufficient, diffuse light on the sample (Figure 4-16). Temperature-resistant LEDs (above 100°C) could not be found. LED lights lose their luminosity faster when they are in warm environment, but the decrease was found to be gradual enough to not influence the result on DIC.

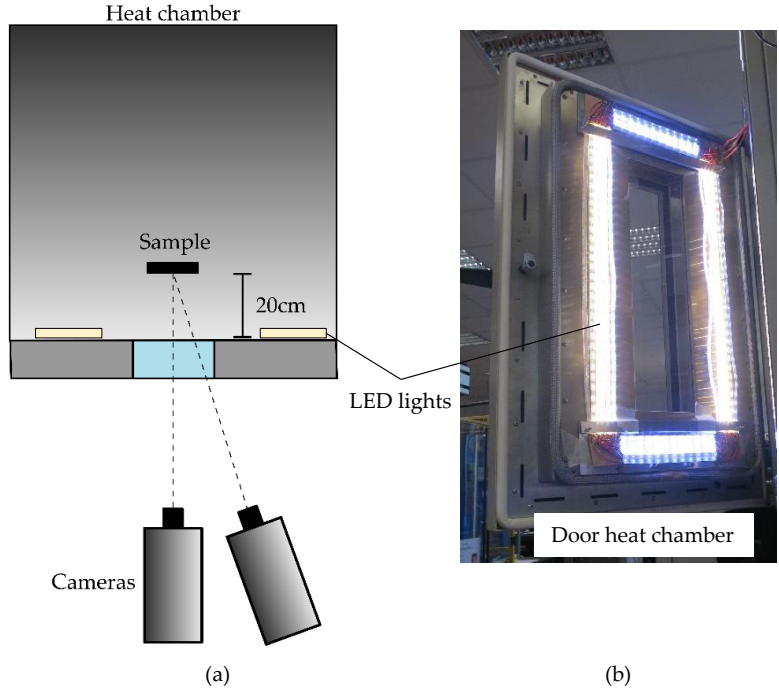

Figure 4-16: Light sources for DIC in heat chamber, (a) schematic of LED lights on the inside of the heat chamber door and (b) photo

The difference between only outer light and additional LED strips is obvious when the images are compared as in Figure 4-17. The software supplier of the DIC software Correlated solutions recommends high contrasts for a good speckle detection [41]. High contrasts in photography are defined as a wide spectrum on the intensity in a histogram [42]. By adding the LED strips, the width in the histogram increases (Figure 4-17b). Due to the extra light closer to the sample, also the overall brightness increases.

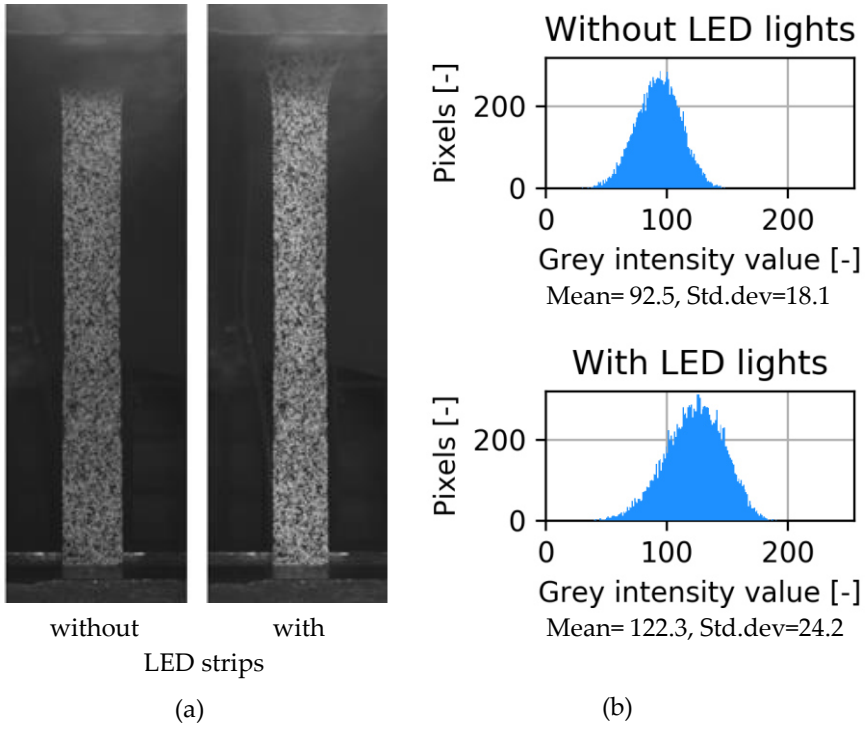

Figure 4-17: Difference in illumination without and with added LED strips (a) photo and (b) histograms

For direct DIC on the sample, the post-processing of the images can be done by a standard pinhole-model that assumes that all rays origin from a single point and the rays are undisturbed. By adding a refractive layer like glass in the heat chamber door or a different medium than air, the projection error increases (Figure 4-18a). Different authors dealt with the issue of projection error due to distortion [43]. The need for a compensation of refraction is increasing with the distance between the object and the refractive surfaces [44]. In addition, curvature of the glass [45] or big angles to the glass are increasing the error [46]. Several authors tackled the issue mathematically [47,48]. H.W. Schreier developed a flexible algorithm that assumes not a fixed pinhole position, but a flexible position for every pixel [49] called variable ray origin (VRO)

(Figure 4-18b). This model is implemented in the software VIC3D [50] and was used to analyse the experiments performed through the glass of the heat chamber and chapter 3. For planar surfaces, the projection error is low despite the deflection of the glass, but the more complex the sample shape is or the paths of the reflected rays are, the bigger the error grows [49].

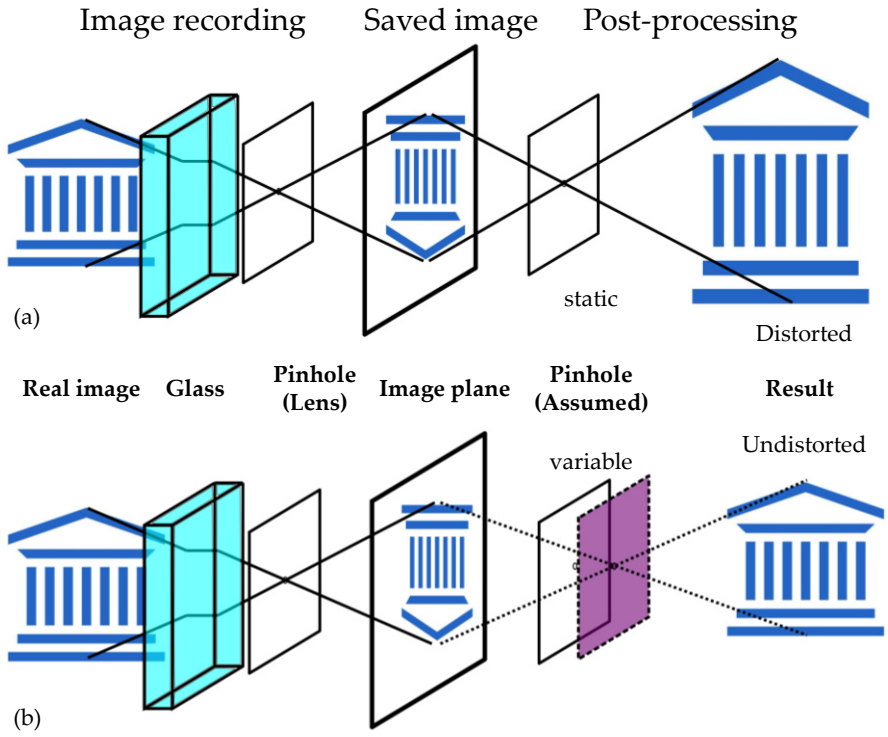

Figure 4-18: Pinhole model with glass, (a) traditional pinhole model causing distorted image plane and (b) variable pinhole model (VRO) giving undistorted image

The accuracy of the VRO model was verified in two steps. Correct planar movement tracking was tested in a small setup, strain was verified by a tensile test in the heat chamber. Both methods are described in detail in the following: For the planar movement, a glass plate was placed upright to create a distorted testing zone through the glass and an undistorted one above the glass as in Figure 4-19a and b. To test the abilities of the VRO model, a zone of silicone oil was added in addition to the glass. This resulted into three zones, namely: (i) air, (ii), air-glass-air and (iii) air-glass-oil, abbreviated to (i) air, (ii) glass and (iii) glass+oil. Each zone was calibrated individually with a grid. Afterwards, a speckled sample was placed in two zones at the same time and moved 1 mm in x-direction with a micrometre stage. The results are shown in Figure 4-19c and d.

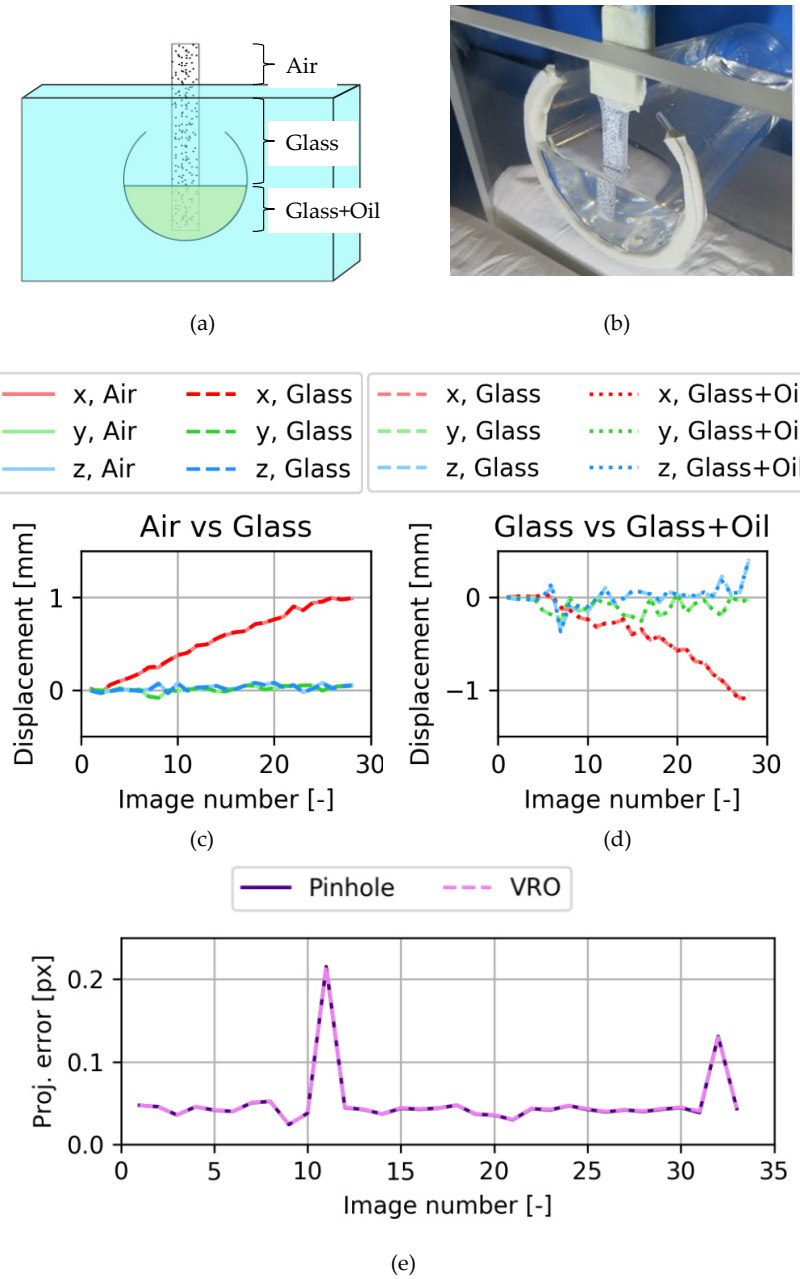

Figure 4-19: Accuracy of movement tracing with 3D-DIC: (a) Schematic of different zones (b) sample through glass and oil, track of displacement in x-direction by comparison: (c) comparison between air and glass and (d) comparison between glass and glass+oil. (e) Influence of post-processing model on projection error in case of glass+oil

No differences are visible between the different zones that were compared at the same time. The noise in the comparison between glass and glass+oil can be attributed to the elongated arm holding the sample, causing more vibration while manually turning the micrometre screw. Nevertheless, the analysis with Vic3D shows a perfect match between the zones. The results were also analysed with a pinhole-model. It shows that the calibration scores of submerged images could be significantly (more than 50%) improved by using the VRO model over the pinhole model. However, with both methods, the calibration score was acceptable. Furthermore, the tracking of movement was accurate with both models. A comparison of the projection errors shows, both models analyse the speckle images in the same quality (Figure 4-19e). Thereby, the pinhole model computes one picture on average in 0.8 s, whereas the VRO takes with 1.3 s almost double as long. Due to the very close placement of the sample behind the glass and the fairly small angles of the cameras, no specific algorithm is needed to track planar rigid body movement in this setup accurately.

The accuracy of the overall strain measurement of DIC through the glass of the heat chamber was validated with an extensometer at room temperature (Figure 4-20). Therefore the dynamic extensometer 2620-601 from Instron with a gauge length of 12.5 mm and 5 mm travel was used. The DIC analysis was in this case only performed in between the rubber bands of the extensometer to analyse the same area only. Engineering strain was used and a simple longitudinal expansion assumed to match the level of information retrievable by the extensometer. In comparison, the extensometer showed more noise than DIC, as visible in the zoomed area of Figure 4-20b. The noise is occurring due to imperfect contact caused by a slightly curved sample surface. The engineering strain between extensometer and DIC differs by 3.8±1.4% on the average force value. For a certain force value, the strain values of extensometer and DIC were compared and the deviation given in percentage. The difference is caused by a combination of the imperfect contact and the different size of the analysed gauge length, since the DIC vision is hindered by the rubber bands of the extensometer. Overall, the curves describe the same shape and the difference is small.

To also validate the different models of a DIC strain measurement, pinhole- and VRO-models were compared on the same analysis. No difference was detected in strain distribution between the two models. It seems, in relatively simply distorted setups with small camera angles, the assumption of a pinhole-model is valid and both models can be used to analyse these DIC images. Thereby, the pinhole-model achieves faster results and was chosen. In more complex distorted images, the VRO model might be needed.

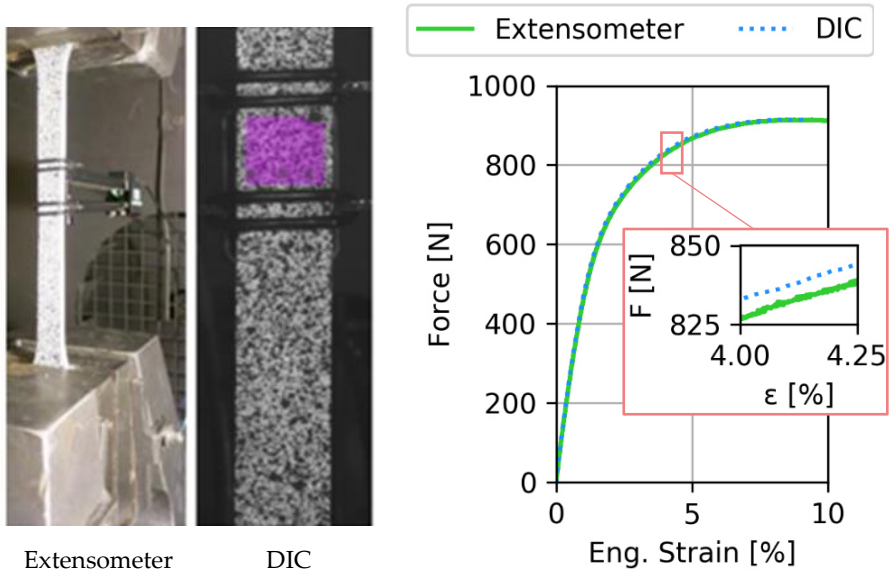

Figure 4-20: Comparison between extensometer and DIC through glass of heat chamber, (a) Measurement areas of extensometer and DIC on sample, (b) difference in strain measurement between the two methods on the example of PP

These comparisons confirm the correctness of the displacement and strain measurement with DIC through the glass of the heat chamber. The calibration was performed under the same visual circumstances and the same temperature as the test, ensuring a valid calibration and therewith correlation of the measurement results.

4.4.1.4 Results

Tensile tests were performed at 20°C and 80°C on material used for heat exchangers, here polypropylene (PP-GF) and polyphenylene sulphide (PPS-GF) filled with graphite from the company Technoform. According to the data sheet, PP-GF has an operation temperature of up to 80°C, PPS-GF of up to 200°C [51]. Figure 4-21 shows the stress strain curves of tensile tests with a strain rate of 1mm/min (≈ 6E-05 s^{-1}). The repeatability on the samples is good, showing a standard deviation of the stress of less than 3.5% for four PP samples and 7.3% for three PPS samples per temperature. The strain field is homogeneous, as presented earlier for the Poisson's ratio (Figure 4-8). In Figure 4-21a, PP is presented. The difference in temperature of 60°C is influencing the result significantly. At 80°C, the material has a double as high strain at break, but at half the strength than at 20°C. A similar behaviour could be found on polypropylene reinforced with 30 wt% glass fibre with an ultimate tensile strength at room temperature of 47 MPa and an elongation of 4.1% [37]. With an increase in temperature

of 60°C, the elongation at break increases by 1/3 whereas the ultimate tensile stress drops 50%. The here tested PPS in Figure 4-21b decreases its strength by less than 10% and its ductility is not influenced in that temperature region. Also literature confirms, a PPS laminate with woven carbon plies is hardly affected by an increase in temperature from room temperature to 120°C [52]. Reason for the different reduction in strength of PP and PPS composite due to an increase in temperature of 60°C is the complexity of the polymer. PP has a simple chain structure whereas PPS has phenolic rings, which cause stronger intermolecular forces and subsequently a higher melting point [53]. In addition, the glass transition temperature, hence the temperature when the material changes from a brittle to an rubbery state, is lower for PP than for PPS. The results illustrate how important it is to test polymers and composites at different temperatures to evaluate their applicability for a certain operation temperature. Knowing the phase transitions and the according mechanical behaviour is essential for choosing a design material.

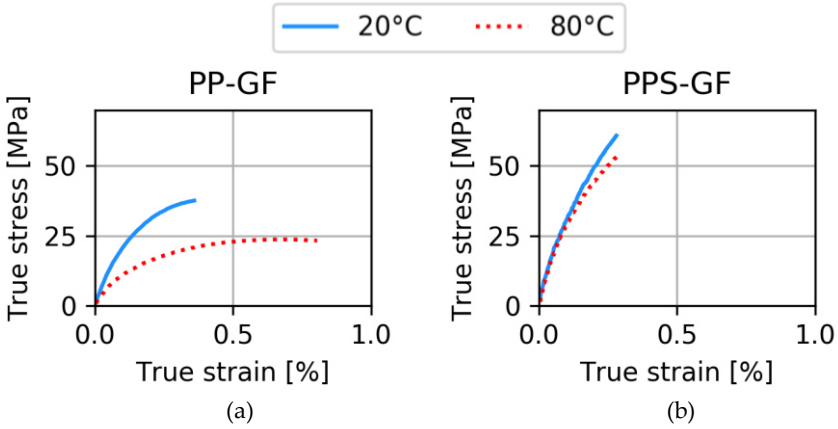

Figure 4-21: Effect of temperature on (a) PP-GF and (b) PPS-GF in tensile test

This can also be confirmed by our study on carbon fibre filled polyamide 6 in the master thesis of H. Van Leynseele [54]. Figure 4-22 shows the change in ultimate tensile strength (UTS) and strain at break for different temperatures and different filler contents. With an increasing filler content, the UTS increases and the strain at break reduces, due to an increased brittleness. For 0% carbon fibres, the strain at ultimate tensile strength is given. Nevertheless, this behaviour is not linear, neither the increase in brittleness due to filler content nor the influence of temperature on differently filled polymers.

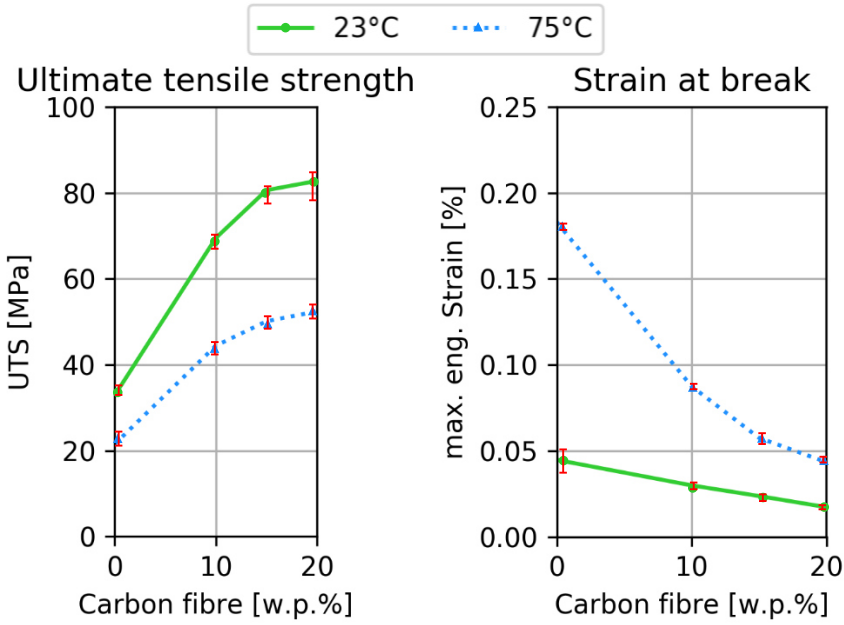

(a) (b)

Figure 4-22: Influence of temperature and filler content on (a) ultimate tensile stress and (b) strain at break, three samples per data point, PA6 with 10% graphite flakes and variations of short carbon fibre content (0, 10, 20 wt%)

Standardised mechanical tests are helping to create a database of comparable test results. However, to evaluate the specific behaviour of a part in service, it is important to test at the used temperature and with the correct filler content, since behaviour is not linear and therefore difficult to estimate. In addition, other external influences like the humidity are changing the material behaviour as well. The challenge of testing at a specific humidity is explained in the next section.

4.4.2 Testing in concern of humidity

Depending on the used materials, composites can also be influenced by humidity.
As in previous tests, a standard tensile setup was used. The two most extreme humidity levels were compared, using an oven at 80°C to dry half the PA6-samples prior to testing and a decalcified water bath at 50°C to saturate the other samples. After 15 days, the samples in the water bath reached equilibrium at a moisture content of 6.8 wt% (calculated with respect to the dry weight). In literature, around 9 wt% are reported for PA6 [55,56]. A different grade of PA6, and different settings during the production will have caused the difference. The tensile tests in Figure 4-23 were performed at 23°C and strain rates of 5 mm/min ($10^{-3}s^{-1}$) and 0.5 mm/min ($10^{-4}s^{-1}$). The

comparison between dry and saturated samples shows that the tensile strength and elongation is influenced significantly by humidity for PA6. Water works as a plasticizer to the polymer, the water absorption weakens the hydrogen bonds in the matrix and causes more flexible molecular chain movements [57]. The strain rate dependency at the different moisture levels is also very clearly demonstrated. Whereas the ultimate tensile strength of dry PA6 is increasing with increasing strain rate, the ultimate strength of saturated specimens stays the same despite changing strain rate. This is confirmed by a study from literature on PA6 at different strain rates and relative humidity. The higher the humidity, the smaller the strain rate dependency [57,58]. The higher failure strain at higher strain rate for wet samples is probably defect controlled, typically the failure strain decreases with increasing strain rate.

In all tests with an elevated moisture content, the stability of the humidity level needs to be questioned critically. For the performed tests here, the weight loss was less than 0.05% as measured by weighing the wet samples before and after the test. The low temperature and the relatively short testing time of 40 min (at 0.5 mm/min until 25% strain) are limiting the moisture loss without using an environmental chamber.

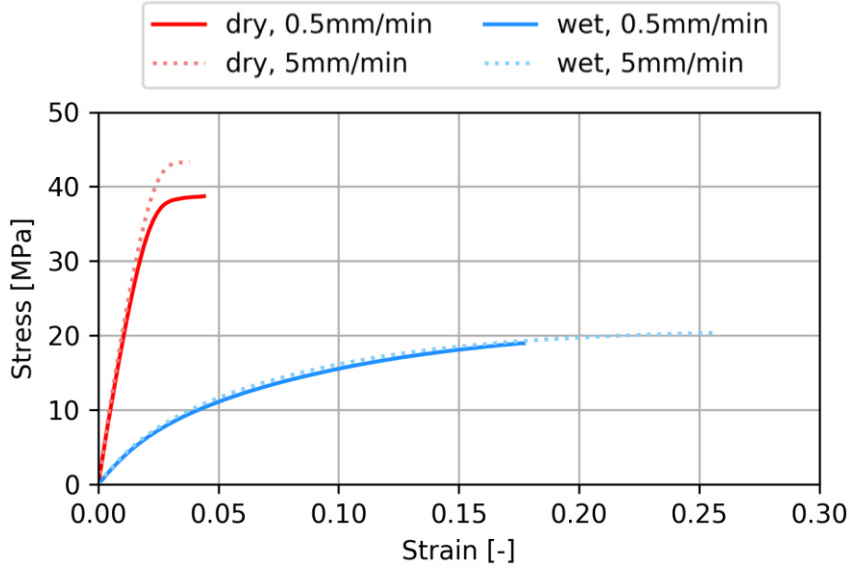

Figure 4-23: Influence of moisture on tensile tests on pure PA6, data measured at two different strain rates and humidity levels

At higher temperatures or for longer lasting experiments, the samples dry out more, changing the characteristics of the polymer, resulting in invalid tests. Figure 4-24 illustrates creep tests at different temperatures. The creep compliance shows the rate that strain increases with if a constant stress is applied. Especially at 75°C it can be seen

that the creep compliance drops over time due to a stiffening of the sample during the test. This stiffening is caused by a loss of moisture. Ideally, this would be avoided by using an environmental chamber [59,60], which allows the moisture level in the air to be controlled. However, due to a lack in availability, alternative approaches were investigated. Specifically, samples were covered with different coatings in an attempt to seal the moisture in the sample without affecting the tensile strength. In addition, the coating had to be suited for DIC. In the time that was spent, no suitable coating was found. The main issue was the drying time of the liquid coatings, allowing the sample to dry out while the coating was drying. Sealing tapes were also considered, but these seem to be made for liquid water instead of water evaporation. In literature, no adequate method description of sample sealing could be found. Descriptions of "specimens were sealed" [61] or "specimens were sealed tightly" [62] were not enough to understand the coating to protect the sample from moisture loss.

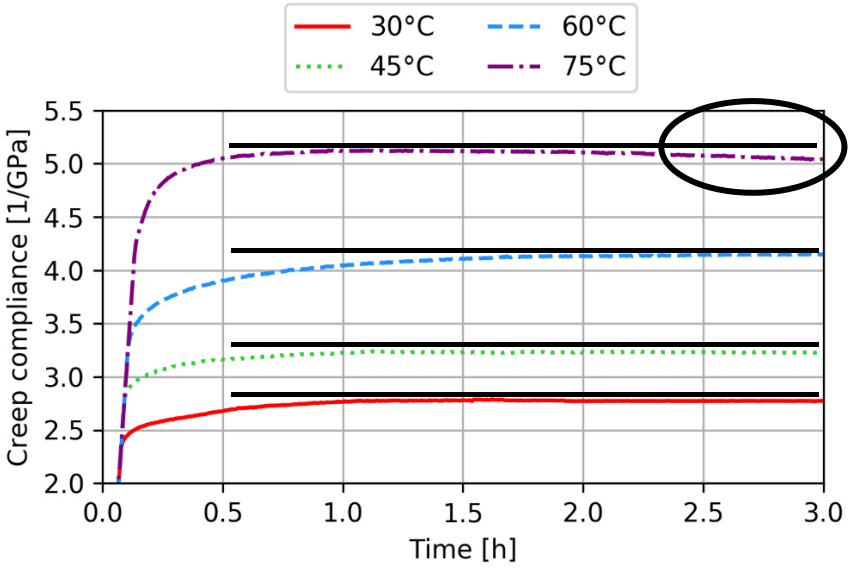

Figure 4-24: Creep test of wet PA6, moisture loss at higher temperatures causes drop in creep compliance

The influence of humidity on the test result has been shown. The lower the humidity, the higher the strain rate dependency. As such, a constant moisture content during testing is essential to generate trustworthy test results, especially when considering tests that take a relatively long time such as creep experiments. Without an environmental chamber with humidity control, the accuracy of the result cannot be ensured. For that reason, samples were used in dry condition only, since an increase in temperature limits the chance of moisture uptake during the test.

4.4.3 Long-term predictions from coupon testing

For long-term measurements, the stability of the testing system is even more crucial than for short-term tests. The moisture content was decided to be low with an initial moisture content of 0%, since samples absorb moisture slower than they lose moisture, especially at elevated temperature. The testing system including humidity, lighting, and temperature turned out to be stable for several days throughout the tests. Literature shows that the stability of a DIC strain measurement is only at risk, if the cameras move independently from each other [11]. By securing the cameras and cables tightly, the DIC calibration could be kept valid. To validate the studies, calibrations were performed before and after long-term tests and the speckle images were analysed based on the different calibrations. The results of strain were identical.

Using the DIC setup, creep tests were performed on unreinforced PA6 loaded with a dead-weight of 30 kg. Each sample was loaded for 3 h at one specific temperature. The resulting curves from different experiments were used in Figure 4-25 to estimate the long-term behaviour by curve shifting according to the Time-Temperature-Superposition principle (TTSP).

The slopes of shifted curves are matched with the slope of the curve at lower temperature to create an overlap. The resulting curve, the master curve, shows the predicted long-term behaviour. Despite the relatively low stress of 7.35 MPa, the material shows a high increase in strain with each increase in temperature. This leads to a long-term prediction of several decades. The resulting master curve can be used to estimate the strain at that constant creep load at the reference temperature (here 23°C) after a certain amount of time. The strain is thereby the combination of instantaneous strain plus the time-dependent change due to creep.

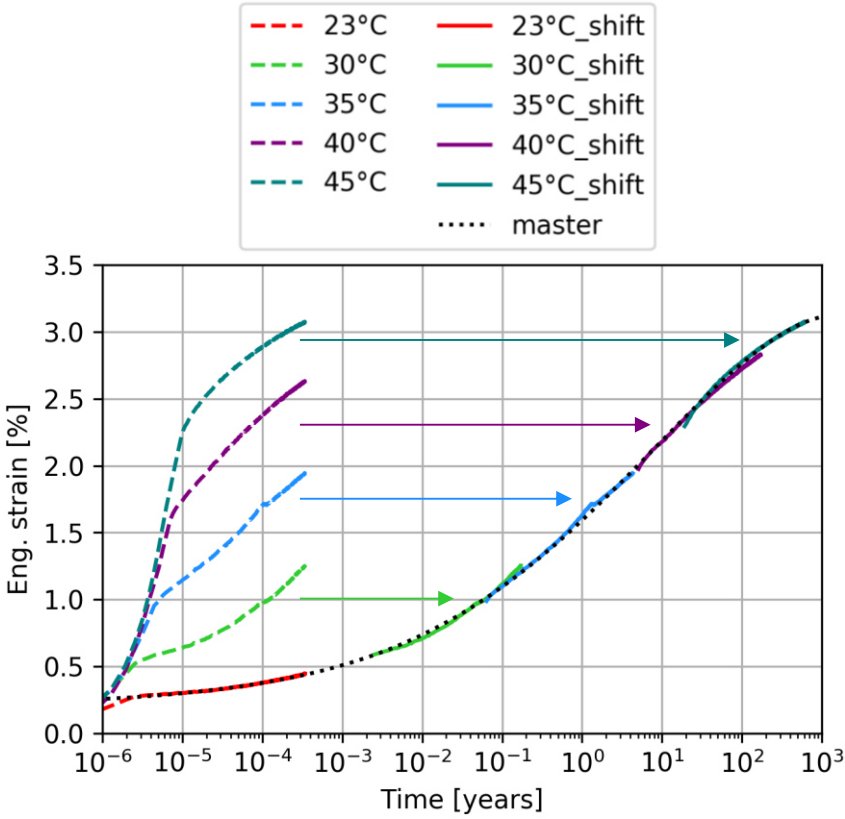

Figure 4-25: Long-term prediction with curve shifting (TTSP) of unreinforced PA6 under a load of 294 N

For long tests at relatively low loads, a dead weight can be recommended rather than the load control of the machine, because with the load control, the value oscillates around the set value which can cause an overshoot on the electromechanical Instron 5800R. For higher loads as applied on reinforced composites, the safety of a dead weight could not be ensured. In this case, the load control of the machine had to be used. Figure 4-26 shows the uncertainty of three different measurements. After an initial overshoot 310±16 N, the tensile curves are on average steady at 1997 N ±13 N. In a tensile curve on the same material, ±13 N results to an uncertainty of the strain value of 1.1%.

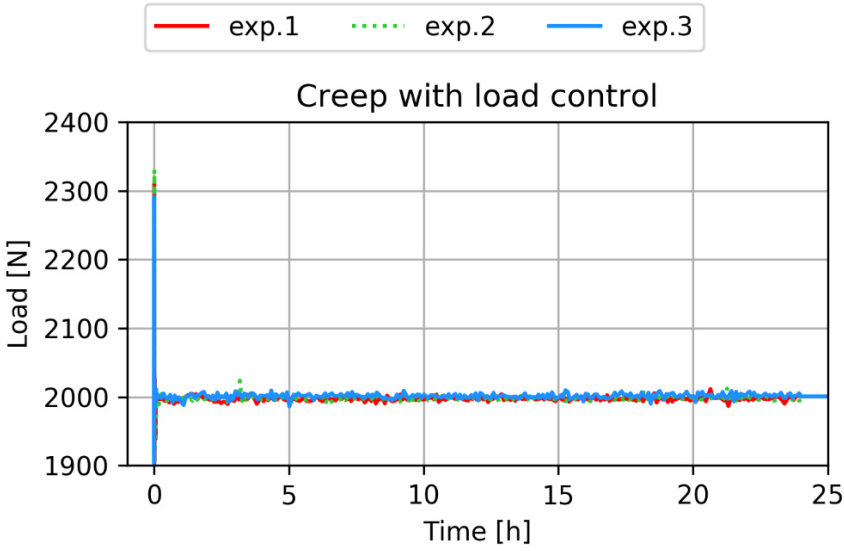

Figure 4-26: Load evolvement over testing time due to creep test with load control at 2 kN of electromechanical test bench instead of a constant dead weight

With this low uncertainty in strain measurement, the long-term behaviour of PA6 reinforced with Safran carbon fibres was estimated. The stepped isothermal method (SIM) [29] was used. This method is based on the principle of TTSP, but with a single sample only. Instead of loading per temperature a new sample, one sample is loaded and the temperature stepwise increased. The method has the advantage of saving time and samples, but has a higher risk of systematic errors, since a defect in the tested sample falsifies the result for the full estimation. The sample is loaded at a starting temperature, here 35°C. Every 3 h the temperature is increased to trigger an event that equals an increase in time. The raw data was recorded and is displayed in Figure 4-27. By applying a shift factor on the raw data (Figure 4-27a), the strain at a constant load of ca. 2000 N load can be displayed over 20 years. The same experiment was repeated twice, showing a slight divergence of 1.9% in Figure 4-27b. After the initial, uncontrolled overshoot, the scatter due to the load control and the divergence between

the two tested samples is very low for experimental testing. The reproducibility of the long-term prediction is high for the two tested samples.

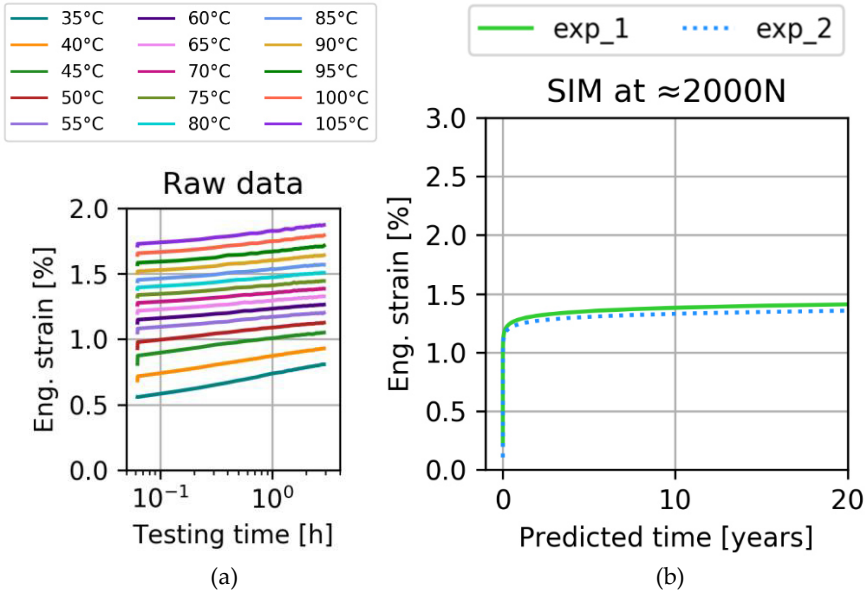

Figure 4-27: (a) Raw data of one stepped isothermal creep test on electromechanical test bench and (b) long-term prediction master curves of two PA6-CF samples over 20 years, loaded with 2 kN

The application of TTSP and SIM on creep tests in the electromechanical test bench resulted in a master curves that predict the strain corresponding to a constant load. Both methods were applied successfully on dry samples in a constant creep loading. DIC could track the strain and displacement, lights inside the heat chamber improved the image quality. For small loads, a dead weight can be recommended, since it ensures a constant load on the sample. Higher loads can be realised by the cross-head of the electromechanical test bench, whereby an initial overshooting of the load is likely. Depending on the strength of the sample material, the overshoot might be negligible as here with a short overloading with 3.6% of the ultimate tensile strength.

4.5 Thermo-mechanical material model

Isothermal tensile tests on polypropylene, executed according to the findings of this chapter, were successfully used to calibrate and validate a thermo-mechanical material model developed for the Compohex project by A. Krairi [1]. Yield stress, isotropic hardening and the viscoplastic function are based on experiments at 23°C and different strain rates (Figure 4-28a). Based on these experiments, the model can predict behaviour at different temperatures and strain rates. Additionally, tests were

performed at 60°C with various strain rates and successfully compared to the prediction of the model (Figure 4-28b). Furthermore, creep tests or humidity dependent material could be a valid input for future modelling.

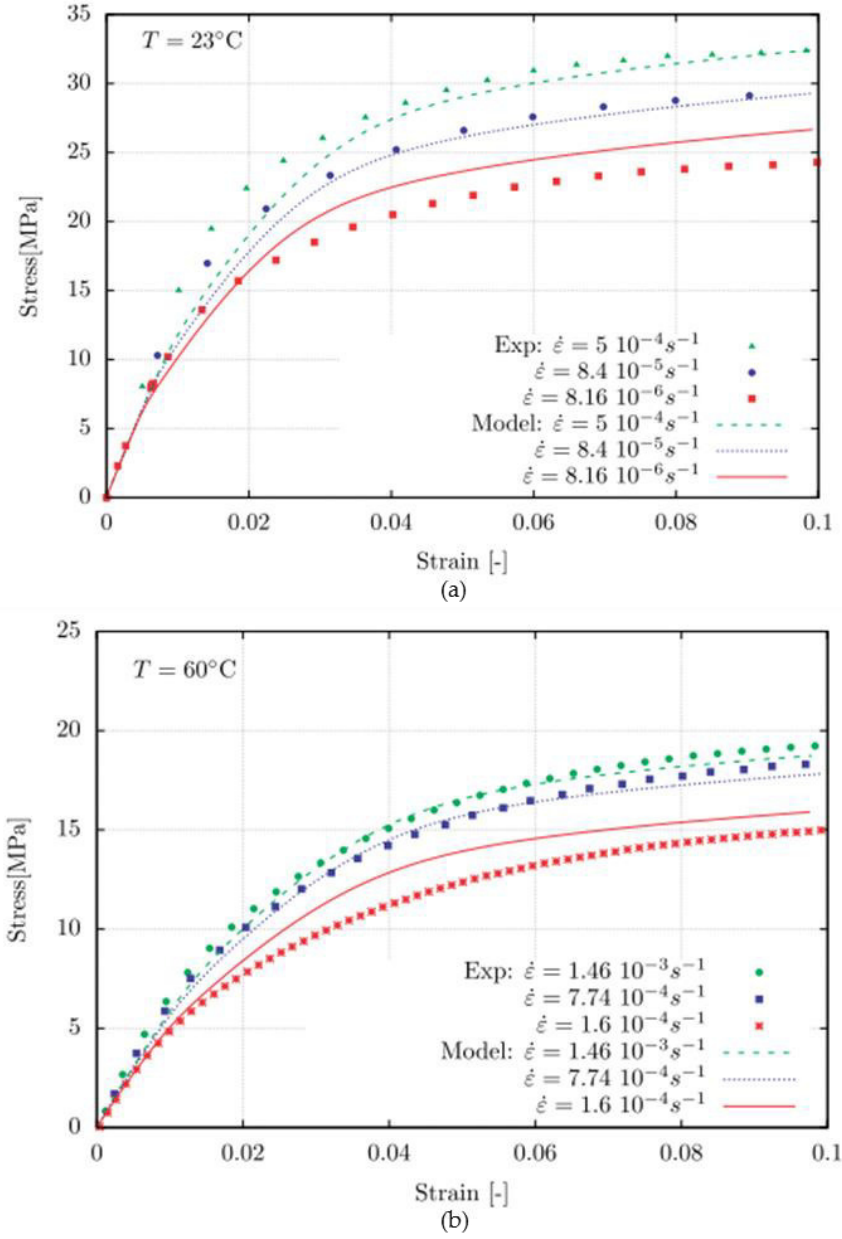

Figure 4-28: Experimental data of PP used to (a) calibrate a thermo-mechanical model at 23°C and (b) validate it at 60°C [1]

4.6 Conclusions of advanced tensile and creep testing

3D-Digital image correlation was successfully used to measure strain on samples in a heat chamber. Comparisons with clip-on extensometer showed very good agreement. It was found that calibration behind glass and sufficient light in the heat chamber are essential for successful measurements. With this technology, it is possible to correctly measure strain in standardised tests and tests at elevated temperature. For very slow strain rates and long creep tests, care needs to be taken that the setup remains stable. Conditioned samples have the tendency to dry out at higher temperature and longer testing times. An environmental chamber with humidity control is recommended for those tests. No other solution was found here, so unfortunately, no long-term test results with humidity could be obtained.

For dry samples, accurate long-term predictions with TTSP and SIM are possible on an electromechanical test bench. To achieve an accurate loading, a dead weight was used. With the current setup, loads were limited to 45 kg to ensure safety. The load control setting of the machine adds a small uncertainty to the measurement, but allows for a construction of a master curve at higher loads (equivalent to a dead weight of 203 kg). The data obtained from standard tensile tests was used for long-term predictions, which in turn was used to calibrate material models to predict the behaviour at different strain rates, stresses and temperatures with very good correspondence.

References

[1] A. Krairi, I. Doghri, J. Schalnat, G. Robert, and W. Van Paepegem, "Thermo-mechanical coupling of a viscoelastic-viscoplastic model for thermoplastic polymers: Thermodynamical derivation and experimental assessment," *International Journal of Plasticity*, vol. 115, 2019, pp. 154–177.

[2] *ASTM D638 Standard Test Method for Tensile Properties of Plastics*, ASTM International, 2014.

[3] *DIN EN ISO 527-4: Bestimmung der Zugeigenschaften Teil 4; Prüfbedingungen für isotrop und anisotrop faserverstärkte Kunststoffverbundwerkstoffe*, DIN Deutsches Institut für Normung e.V., 1997.

[4] "Zoltek px35 50K carbon fibre, [online: https://zoltek.com/products/px35/]," 2020.

[5] "Hexcel 12K carbon fibre, [online: https://www.hexcel.com/Products/Fabrics-Reinforcements/Carbon-Fiber-Reinforcements]," 2020.

[6] *ISO 1110 Plastics — Polyamides — Accelerated conditioning of test specimens*, International Organization for Standardization, 2019.

[7] *DIN EN ISO 527-3: Bestimmung der Zugeigenschaften Teil 3: Prüfbedingungen für Folien und Tafeln*, DIN Deutsches Institut für Normung e.V., 2003.

[8] *3119-400 Series Temperature, Controlled Chambers, Reference Manual - Equipment*, Instron Limited, Coronation Road, High Wycombe, Bucks HP12, 3SY, United Kingom: Instron SFL, 2006.

[9] I. Miskdjian, M. Hajikazemi, and W. Van Paepegem, "Automatic edge detection of ply cracks in glass fiber composite laminates under quasi-static and fatigue loading using multi-scale Digital Image Correlation," *Composites Science and Technology*, vol. 200, 2020, p. 108401.

[10] "Grasshopper 3 specifications, https://www.flir.com/products/grasshopper3-usb3/, [online access 07/2019]."

[11] "A good practices guide for digital image correlation," *International Digital Image Correlation Society*, 2018.

[12] "Golden High Flow Titanium White 8549-1 https://www.artobi-airbrush.be/verf-airbrush-custom/acryl/golden-highflow-opaque-30-ml/golden-high-flow-titanium-white-8549-1/a-6275-20000561," 2019.

[13] "Ambersil Black matt spray paint RAL 9011 https://benl.rs-online.com/web/p/spray-paint/6783082/?cm_mmc=BE-PLA-DS3A-_-google-_-CSS_BE_NL_Facilities_Cleaning_%26_Maintenance_Whoop-_-(BE:Whoop!)+Spray+Paint-_-6783082&matchtype=&pla-577877946174&gclid=Cj0KCQjw–GFBhDeARIsACH_kdaWgGlH-JPegorCJ1FDd4CHPk4YnXWUBZIgdKAjP7LflQlfUAqfD4waAsdfEALw_wcB&gclsrc=aw.ds," 2019.

[14] "VIC SNAP 8 [computer software], Correlated Solutions."

[15] "VIC-3D 8 [computer software], Correlated Solutions."

[16] W.D.J. Callister, *Materials science and engineering : an introduction*, New York (N.Y.) : Wiley, 2007.

[17] H.B. Motra, J. Hildebrand, and A. Dimmig-Osburg, "Assessment of strain measurement techniques to characterise mechanical properties of structural steel," *Engineering Science and Technology, an International Journal*, vol. 17, 2014, pp. 260–269.

[18] "https://www.continuummechanics.org/energeticconjugates.html, [online: 07/2021]," 2021.

[19] *DIN EN ISO 899-1 Kunststoffe - Bestimmung des Kriechverhaltens - Tiel 1: Zeitstand-Zugversuch, 2015*, Deutsches Institut für Normung e.V., .

[20] *ASTM D2990 Standard test method for tensile, compressive, and flexural creep and creep-rupture of plastics, 2009*, ASTM International, .

[21] L. Boltzmann, "Zur Theorie der elastischen Nachwirkung," *Annalen der Physik*, vol. 241, 1878, pp. 430–432.

[22] J. Dealy and D. Plazek, "Time-temperature superposition—a users guide," *Rheology Bulletin*, vol. 78, 2009, pp. 16–31.

[23] J. Jansen, "Understanding Creep Failure of Plastics," *Plastics Engineering*, Jul. 2015.

[24] J.D. Ferry, *Viscoelastic properties of polymers*, John Wiley & Sons, 1980.

[25] F. Achereiner, K. Engelsing, M. Bastian, and P. Heidemeyer, "Accelerated creep testing of polymers using the stepped isothermal method," *Polymer Testing*, vol. 32, 2013, pp. 447–454.

[26] W. Grellmann and B. Langer, *Deformation and fracture behaviour of polymer materials*, Springer, 2017.

[27] J.G. Zornberg, B.R. Byler, and J.W. Knudsen, "Creep of geotextiles using time–temperature superposition methods," *Journal of geotechnical and geoenvironmental engineering*, vol. 130, 2004, pp. 1158–1168.

[28] T. Jones, W. Doggett, C. Stanfield, and O. Valverde, "Accelerated creep testing of high strength aramid webbing," *53rd AIAA/ASME/ASCE/AHS/ASC Structures, Structural Dynamics and Materials Conference 20th AIAA/ASME/AHS Adaptive Structures Conference 14th AIAA*, 2012, p. 1771.

[29] *ASTMD6992-03: Accelerated Tensile Creep and Creep-Rupture of Geosynthetic Materials Based on Time-Temperature Superposition Using the Stepped Isothermal Method*, ASTM International, 2015.

[30] R.W. Thomas and J.A. Nelson, "The Stepped Isothermal Method for Estimating the Long-Term Creep Strain and Creep Rupture Strength of Polypropylene."

[31] *DIN EN ISO 527-2 Plastics — Determination of tensile properties — Part 2: Test conditions for moulding and extrusion plastics*, Deutsches Institut für Normung e.V., 2012.

[32] *DIN EN ISO 527-1 Plastics — Determination of tensile properties — Part 1: General principles*, Deutsches Institut für Normung e.V., 2012.

[33] J. Liang, Y. Xu, Z. Wei, P. Song, G. Chen, and W. Zhang, "Mechanical properties, crystallization and melting behaviors of carbon fiber-reinforced PA6 composites," *Journal of Thermal Analysis and Calorimetry*, vol. 115, 2014, pp. 209–218.

[34] Instron, "Determination of Poisson's ratio," *https://www.instron.us/en-us/our-company/library/glossary/p/poissons-ratio, 15/05/2021*.

[35] J. Boylan, "https://www.azom.com/properties.aspx?ArticleID=516 [online]," 2001.

[36] "Polymer Database, https://polymerdatabase.com/polymer%20physics/Poisson%20Table.html [online 07/2021]," 2021.

[37] M. Eftekhari and A. Fatemi, "Tensile behavior of thermoplastic composites including temperature, moisture, and hygrothermal effects," *Polymer Testing*, vol. 51, 2016, pp. 151–164.

[38] A. Drozdov, "Effect of temperature on the viscoelastic and viscoplastic behavior of polypropylene," *Mechanics of Time-Dependent Materials*, vol. 14, 2010, pp. 411–434.

[39] N. Lovaas, "Viewing Through a Window," *https://correlated.kayako.com/article/77-viewing-through-a-window*, 2021.

[40] B. Pan, D. Wu, and Y. Xia, "An active imaging digital image correlation method for deformation measurement insensitive to ambient light," *Optics & Laser Technology*, vol. 44, 2012, pp. 204–209.

[41] "Correlated solutions, Vic-3D v7 Testing Guide," 2010.

[42] M. Bhojasia, "https://www.sanfoundry.com/digital-image-processing-questions-answers-histogram-equalization/ [online 07/2021]."

[43] B. Pan, H. Xie, Z. Wang, K. Qian, and Z. Wang, "Study on subset size selection in digital image correlation for speckle patterns," *Optics express*, vol. 16, 2008, pp. 7037–7048.

[44] Y.-H. Kwon and J.B. Casebolt, "Effects of light refraction on the accuracy of camera calibration and reconstruction in underwater motion analysis," *Sports biomechanics*, vol. 5, 2006, pp. 315–340.

[45] A. Barta and G. Horváth, "Underwater binocular imaging of aerial objects versus the position of eyes relative to the flat water surface," *JOSA A*, vol. 20, 2003, pp. 2370–2377.

[46] M.A. Sutton and C. McFadden, "Development of a methodology for non-contacting strain measurements in fluid environments using computer vision," *Optics and Lasers in Engineering*, vol. 32, 1999, pp. 367–377.

[47] X. Ke, M. Sutton, S.M. Lessner, and M. Yost, "Robust stereo vision and calibration methodology for accurate three-dimensional digital image correlation measurements on submerged objects," *The Journal of Strain Analysis for Engineering Design*, vol. 43, 2008, pp. 689–704.

[48] Y. Kwon, "A camera calibration algorithm for the underwater motion analysis," *ISBS-Conference Proceedings Archive*, 1999.

[49] H. Schreier, "Variable Ray Origin Camera Models for Accurate DIC Measurements Through Glass and Glass/Water Interfaces," International Digital Image Correlation Society, 2017.

[50] M. Simonsen, "Application Note AN-1802: Variable Ray Origin Calibration," *https://correlated.kayako.com/article/8-vro-calibration-in-vic-3d*, 2020.

[51] J. Caprano, *Technoform Heat transfer solutions*, Technoform Kunststoffprofile GmbH, 2019.

[52] B. Vieille, J. Aucher, and L. Taleb, "Influence of temperature on the behavior of carbon fiber fabrics reinforced PPS laminates," *Materials Science and Engineering: A*, vol. 517, 2009, pp. 51–60.

[53] "The Essential Chemical Industry - online https://www.essentialchemicalindustry.org/polymers/polymers-an-overview.html," 2013.

[54] H. Van Leynseele, "Creep and Tensile Testing On Polyamide 6 Under Specific Environmental Conditions: Experimental Approach," Promoter Wim Van Paepegem, UGent, Master of Science in Sustainable Materials Engineering, 2018.

[55] S. Gerbig, "Polyamide Moisture Absorption | Relative Dimensional Change of Various Nylon Products, https://knowledge.ulprospector.com/1390/polyamide-moisture-absorption/," 2014.

[56] "AMILAN™ Nylon Resin, https://www.toray.jp/plastics/en/amilan/technical/tec_003.html [online 07/2021]."

[57] E. Parodi, G.W. Peters, and L.E. Govaert, "Prediction of plasticity-controlled failure in polyamide 6: Influence of temperature and relative humidity," *Journal of Applied Polymer Science*, vol. 135, 2018, p. 45942.

[58] J.-L. Tsai and J.-C. Huang, "Strain rate effect on mechanical behaviors of nylon 6–clay nanocomposites," *Journal of composite materials*, vol. 40, 2006, pp. 925–938.

[59] V. Fabre, G. Quandalle, N. Billon, and S. Cantournet, "Time-Temperature-Water Content equivalence on dynamic mechanical response of Polyamide 6, 6," *Polymer*, vol. 137, 2018, pp. 22–29.

[60] R. Scaffaro, N.T. Dintcheva, and F. La Mantia, "A new equipment to measure the combined effects of humidity, temperature, mechanical stress and UV exposure on the creep behaviour of polymers," *Polymer testing*, vol. 27, 2008, pp. 49–54.

[61] A. Benaarbia, A. Chrysochoos, and G. Robert, "Influence of relative humidity and loading frequency on the PA6. 6 cyclic thermomechanical behavior: Part I. mechanical and thermal aspects," *Polymer Testing*, vol. 40, 2014, pp. 290–298.

[62] N. Jia and V.A. Kagan, "Effects of time and temperature on the tension-tension fatigue behavior of short fiber reinforced polyamides," *Polymer composites*, vol. 19, 1998, pp. 408–414.

Chapter 5

Small coupon test with dynamic mechanical analysis

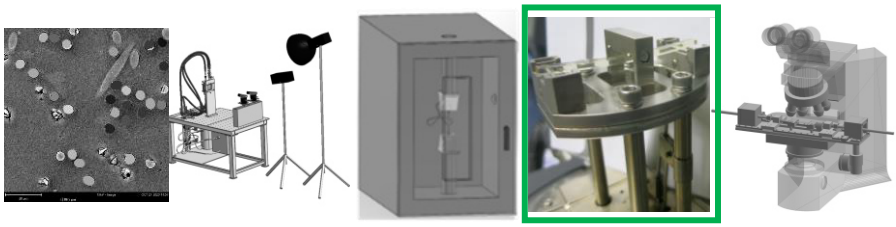

Small coupon scale

Abstract: Dynamic mechanical analysis (DMA) is a method of mechanical material characterisation with the advantage of precise measurement under small loads, small samples and therewith a fast response to thermal changes. Before the method could deliver reliable results, analysis on the method itself was needed. It was found, that the measurement accuracy and repeatability is strongly influenced by (i) the testing fixture and corresponding loading mode and (ii) the sample preparation. In combination with finite element simulations and in-situ strain measurements by digital image correlation (DIC), the main influences on measurement accuracy of 3-point bending DMA were identified and subsequently used to determine measurement guidelines. Using these guidelines, DMA measurements allow quantitative assessment of the viscoelastic response for rigid polymer and composite materials. This chapter is based on the publication "Influencing parameters on measurement accuracy in dynamic mechanical analysis of thermoplastic polymers and their composites" [1].

5.1 Introduction to small coupon testing

In the previous chapters, the focus laid on the creep testing of polymers and composites at elevated temperatures with subcomponents and dogbone coupons. Especially for the accelerated creep testing, the testing time is typically longer than one day, since the heating of the big chamber and the clamps takes a significant amount of time. Due to the big volume, the temperature accuracy during testing is limited, which can falsify the result of temperature sensitive materials. In addition, the setup requires DIC for a precise measurement of the displacement, which is time intense to set up and bears a certain risk of external, falsifying influences. For faster tests with more accuracy, dynamic mechanical analysis (DMA) tests will be considered in this chapter. The used instrument, a Q800 manufactured by TA instruments [2] can be seen in Figure 5-1.

DMA is a classical technique to determine the thermal transition temperatures in materials by looking at changes in the mechanical response due to temperature [3]. Although a certain mechanical response is measured, there is no need for it to be correct in terms of absolute values as the thermal transition is measured by a relative change in the mechanical response. However, if the correctness of the mechanical property measure can be guaranteed, this technique offers the possibility to characterise the viscoelastic behaviour. The used DMA has a very high temperature accuracy, the sample size is limited to a few millimetre thickness, which ensures fast heating and the load can be applied quasi-static or sinusoidal. A typical displacement is around 100 μm (Figure 5-1b).

The DMA measures the phase lag between the applied load and the sample's response. In an ideal elastic case, the sample would react to an applied force immediately without any phase lag. In a complete viscous case, all energy of the applied force would dissipate; the response curve would lag a full wave behind. In a visco-elastic case, as it is typical for polymers and composites, the response is somewhere in between the pure elastic and the viscous one. From the ratio, the elastic portion called storage modulus, and the viscous one, the loss modulus, can be calculated. The ratio itself is called tanδ and is a measurement of the inherent damping of the material.

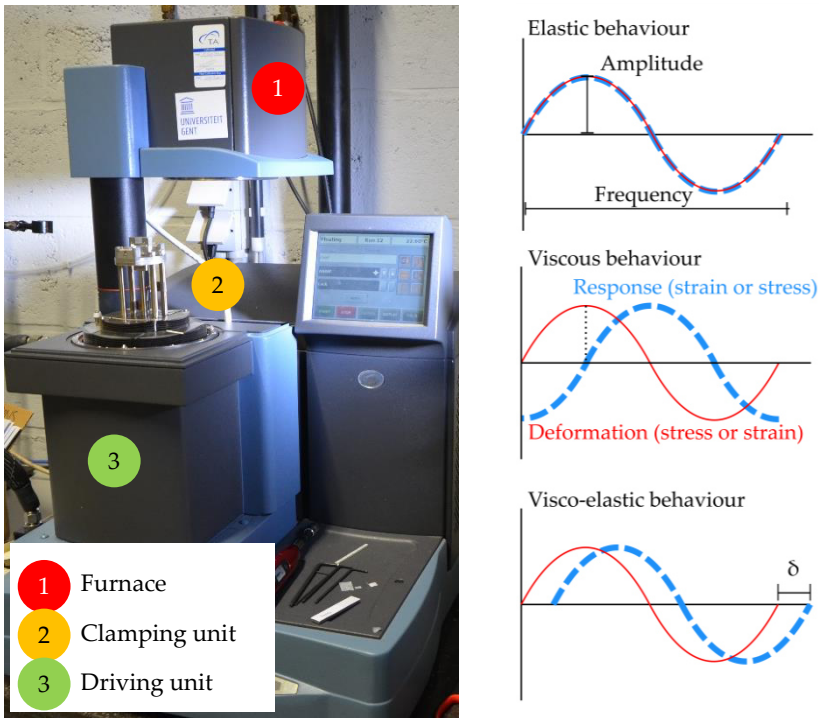

(a) (b)

Figure 5-1: Dynamic mechanical analysis (DMA) setup (a) photo and (b) clarification of the movement

As such, the technique is directly capable of determining the linear viscoelastic material response in function of temperature for virgin and reinforced polymers. With this method, curing cycles and crystallinity can be measured [4]. Furthermore, the data can be used for long-term predictions of material behaviour using for example the Time-Temperature-Superposition principle (TTSP) [5] or as input in numerical simulations, predicting the creep performance of structural components. For this, the repeatability of the results is of high importance to avoid extrapolation of possible inaccuracies. While older journal articles stress the purely qualitative value of DMA results [6], more recent ones allow for quantitative usage [7]. However, it was found by the author, that, if no precautions are taken (arbitrary settings), the scatter on the acquired data can be very large, in some cases up to 50%. Hence, any long-term predictions based on data with this amount of scatter are not reliable. Finding and eliminating the sources of scatter is essential for good measurements.

Especially for long-term predictions, the data is usually plotted on a logarithmic scale displaying several orders of magnitude of for example modulus values. However, this logarithmic representation of the data conceals the measurement accuracy at a fixed

point in time or temperature [7,8]. However, if the data is plotted on a linear scale and magnified to a limited range on the y-axis as in Figure 5-2 the zoom of the linear scale often reveals a big scatter between repeated tests. This logarithmic scaling is typically the default option, since many materials show a big drop in modulus over a broad temperature range due to thermal transitions such as the glass transition temperature. Reproducibility can falsely be assumed since for the higher values, the logarithmic scale squishes the curves closer together. Moreover, the amount of measurement repetitions is not always mentioned in literature or can be very low [9,10], which hides an uncertainty of the data.

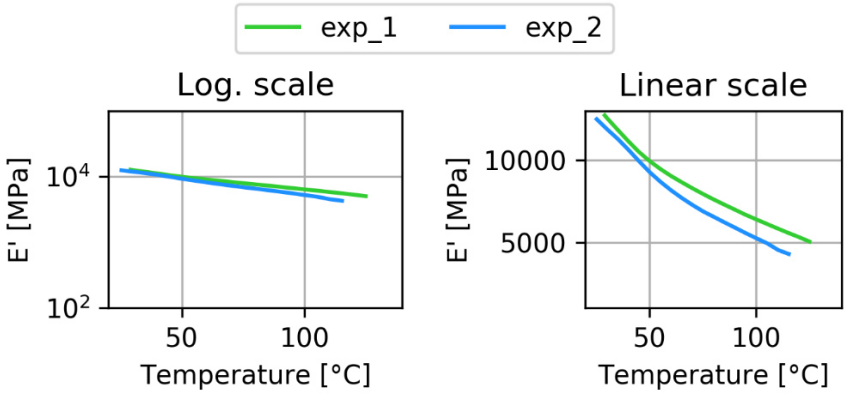

Figure 5-2: Same DMA-result of PESU in (left) logarithmic scale with seemingly good reproducibility of repeated tests and (right) linear scale showing deviating results

In this chapter, the accuracy of DMA results to obtain quantitative data is analysed and evaluated. Measurement parameters are defined based on a study of published literature and their effect on the results is determined. In addition, the experiments are accompanied by finite element analysis and optical strain measurements through digital image correlation to allow a better understanding of the displacements induced by DMA test equipment. This is first done for a PESU polymer material that has high temperature resistance (no thermal transitions within the temperature range observed) and could be obtained in a high quality grade ensuring material homogeneity (absence of micro-voids and defects) and repeatability. Thereafter, the principles are applied to determine the response of a polymer composite based on polypropylene used in heat exchangers. In addition to the findings that were published in a journal paper [1], the effect of the sample geometry is discussed in this chapter.

5.2 Overview of possible parameters influencing DMA measurement accuracy

In the following paragraphs, the testing parameters for DMA in 3-point-bending loading mode are discussed, focussing on the following four aspects:

- specimen (size, dimensional accuracy),
- fixture (pre-stress),
- machine settings (heating rate, amplitude, frequency),
- measurement repetition (number of tests, samples and cycles).

Next to the 3-point bending clamp in Figure 5-3a, other loading fixtures, such as cantilever bending (Figure 5-3b), tensile clamp (Figure 5-3c) or compression clamp exist. However, these other clamp types are typically not suited to determine the viscoelastic response of rigid polymer bulk materials due to the material stiffness and the very limited load range of most DMA equipment. In addition, the measured result involves clamping effects due to the rigid clamping of parts of the sample.

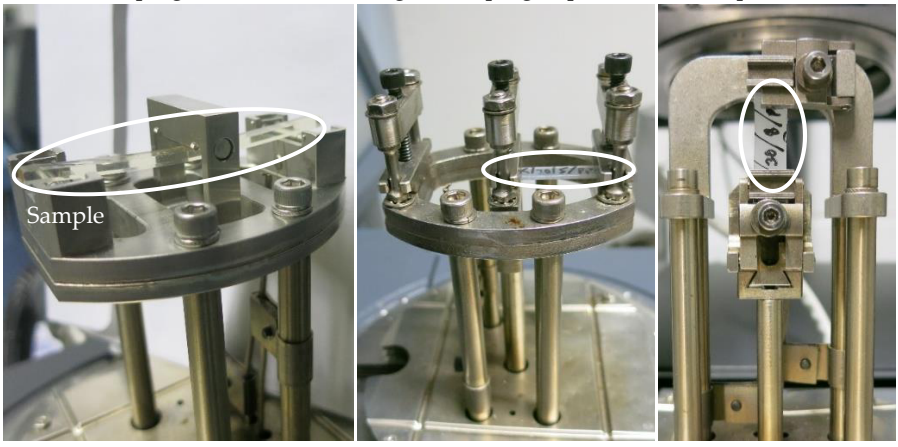

(a) (b) (c)

Figure 5-3: Different DMA clamps (a) 3-point bending clamp, (b) single cantilever and (c) tensile clamp

5.2.1 Sample dimensions and dimensional accuracy

The required sample dimensions differ by instrument, fixture type and material stiffness, but recommendations can be found in the device's manual [3] and testing standards such as ASTM D790 [11] and others [12]. Different manufacturers offer 3-point-bending fixtures for which the samples require similar dimensions. The specimen length is defined by the gauge length of the fixture with addition of a certain overhang of the sample against slippage [12]. The specimen thickness should be

chosen such that the resulting bending stiffness is less than a third of that of the fixture [3]. The span length to thickness ratio (ST-ratio) should be at least 10 for pure polymers [13]. Some authors advise large aspect ratios especially for anisotropic [9] or glassy material [14]. Others stress that strict limitations of sample dimensions are required for repeatable measurements [14,15]. The specimen's width is typically only limited by material or the width of the fixture [16,17] or considered as of negligible importance [18]. Some standards mention typical specimen dimensions with a width of 12 mm [13] or 13 mm [12] without stating the reason for this value. The accuracy of the dimensions is described as uniform [19], rectangular [12], accurate [3] and parallel [16,20], but the exact details remain vague at times. Only very few standards specify that the thickness or width variation should be less than ±2% [13] respectively ±3% [21] over the full length measured at five points along its length. Overall, the advised sample size and accuracy varies per manufacturer and fixture, but limiting rules and explanations for the boundaries are rarely provided.

5.2.2 DMA fixture

For samples with a high bending stiffness, cantilever or 3-point-bending fixtures are typically used since the flexural loading allows for higher deformation (e.g. strain level up to 1%) at a load within the usually low limits of the instrument's load cell [16]. Since the deformation in bending fixtures is not influenced by clamping effects, this option is to be preferred [6]. Nevertheless, the clamping or bolting of the fixture to the DMA machine itself, could introduce variability in the measurement. In bending fixtures, a pre-stress is required to prevent the sample from shifting in the fixture. The amount of pre-stress must be well chosen [6,9,22,23]. If the pre-stress is too low, the sample is insufficiently clamped, whereas if it is too high, the dynamic result will be influenced [9]. Temperature effects can cause a change in properties, which can span several orders of magnitude. If the temperature influence is of interest, the selection of a good pre-stress value becomes even more cumbersome. A pre-stress amplitude valid for a glassy material state might become invalid by an increase of temperature causing creep in the rubbery state of the material. Some instruments deal with this problem using an automatic adjusting static strain [6,23]. However, this has the drawback that the loading conditions change during the measurement.

5.2.3 DMA settings

For the mechanical response, it is important to have a homogeneous temperature over the complete sample. Consequently, for non-isothermal experiments, the heating rate can severely affect the results, as a temperature-lag can exist between the core of the specimen and the nearby thermocouple. To ensure a constant temperature, it is either recommended to keep the heating rate lower than 5°C/min [3] or to insert an isothermal waiting time (dwell time) of several minutes [3,22] before the actual test. Self-heating of thicker samples can be avoided by not fully exhausting the available frequency range [7]. All commonly available DMA instruments have a large amplitude

range of at least 1000 μm, but recommended amplitudes are for all kind of fixtures below 50 μm [17,24]. Furthermore, for 3-point-bending fixture of TA Instruments the advised amplitudes are narrowed down to 25-40 μm [16]. The smaller the amplitude, the more crucial the specimen's geometrical accuracy becomes, since perfect contact between sample and clamp needs to be ensured with a low load transfer from the fixture to the specimen [14]. This is confirmed in the studies of Lee-Sullivan and Shao [6,25] which conclude that higher amplitude resulted in lower standard deviations of the results. Limitations on the amplitude are dynamic effects, the instrument's upper force limit [16] and higher strains which can fall outside the linear viscoelastic region of the specimen. Also, the occurring strain rate by amplitude and frequency can influence the mechanical response as A. Margossian [22] showed by comparing the differences in results between 10-500 μm/min, showing a stiffer response at higher strain rates.

5.2.4 Repetitions

Most studies do not mention the amount of repetitions per experiment [7,15,26]. Some standards propose two specimens per experiment [13,19]. While some authors re-use one sample for several tests [10,15], others advise to always take a new sample, even if the test has been performed purely in the viscoelastic region of the material [12]. Also a combination is possible where a sample is taken for each new experiment, but the test is repeated several times in one run, since the first cycle might diverge from the average [6].

5.3 Materials and methods

5.3.1 Materials

To limit the influences on the experiments in the parametric study, a highly creep resistant polymer with low sensitivity to moisture was chosen, i.e. polyether sulfone (PESU, Veradel A-301, Solvay). PESU is an amorphous thermoplastic with a glass transition temperature higher than 200°C and a Poisson's ratio of 0.41 [27,28]. In a next step, the results of this study were verified by using a polypropylene based tubular injected composite with a filler content of 75 wt%/50 vol% graphite flakes, i.e. PP-GF from the company Technoform [29]. The material has its melting point at 165°C and a Poisson's ratio of 0.24. For testing purposes, the 24.5 mm diameter tube was cut in sections. The outer part of the tube section was always loaded in compression in 3-point-bending. The change in moment of inertia for the specimens cut from tubular material compared to perfect rectangular beams was negligible (<0.32%). Due to its application in heat exchangers, the thermo-mechanical properties and the viscoelastic properties of this material in particular are very relevant.

5.3.2 Specimen preparation for DMA tests

All samples were 60 mm long. The thickness was given by the production process, for PESU 2.09±0.01 mm and for PP-GF 1.57±0.01 mm. This results into a span to thickness ratio of 24 (50 mm 3-point-bending fixture) and 32 respectively. The width resulted from the manual cutting preparation process with a maximum variation over the length of one sample of 1.5%, which is a divergence of less than ±0.05 mm. The cut edges were polished with grinding paper down to 5-µm grain size to ensure the accurate geometry; the angles were measured and any variability was limited to 90.0±0.5°, verified through optical microscopic measurements. Due to the curvature of the tube sector, the angle of the PP-GF samples was not as precise (90±3°) as for the flat PESU samples and the width varied more amongst different samples (Figure 5-4). However, the precision of the width within one individual sample was the same as for the flat samples.

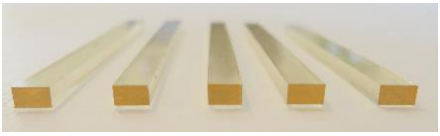

(a)

(b)

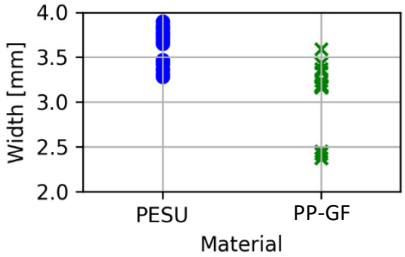

(c)

Figure 5-4: Accurately cut DMA samples: (a) PESU, (b) PP-GF graphite-filled polypropylene samples and (c) the variation of the width amongst different samples (each sample on its own has a variation of less than 1.5%)

5.3.3 DMA testing procedure

Dynamic Mechanical Analysis was performed on a TA Instruments DMA Q800 [2] set-up using a 50 mm 3-point-bending fixture with support rolls with a diameter of 3.15 mm and 15 mm span clamp with 0.4 mm rolls. Tests were conducted at 35°C to ensure the machine reached a stable temperature without the necessity for active liquid nitrogen cooling. In DMA, several tests with parameter sweeps can be performed: amplitude, frequency, and temperature sweep. Literature's recommendation for settings provides machine-specific settings for every sweep. To create material-specific testing parameters, results from one parameter sweep provide guiding values for others. A testing procedure was established to define the relevant parameters and limitations according to the requirements of the tested material (Figure 5-5). First, an amplitude sweep is performed to determine the stable linear-viscoelastic (LVE) region of the material and to choose a suitable amplitude to perform the successive frequency sweep. The purpose of the frequency sweep is either to

determine the viscoelastic properties at a fixed temperature or to be the basis for the TTSP [5]. For the latter, a subsequent temperature sweep is performed to detect thermal transitions of the material. The parameters are influencing each other partially; therefore, sweeps can be looped to iterate the optimal testing conditions.

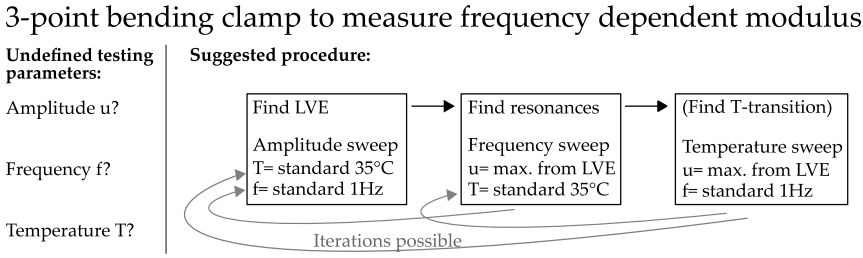

Figure 5-5: Developed testing procedure based on PESU samples

5.3.4 DMA testing results

Output parameters of DMA are typically storage modulus (E′), which is a measure for the elastic behaviour, the loss modulus (E′′), which indicates the viscous part and the phase shift tangent delta (tan δ), which is the ratio between E′ and E′′ and indicates the damping ability of a material. Typically DMA-curves are represented in Figure 5-6. They are all based on the dimensions of the sample as well as the measurement of force and displacement during the test. Thereby the three output parameters are dependent from each other. From two of them, the third can be calculated.

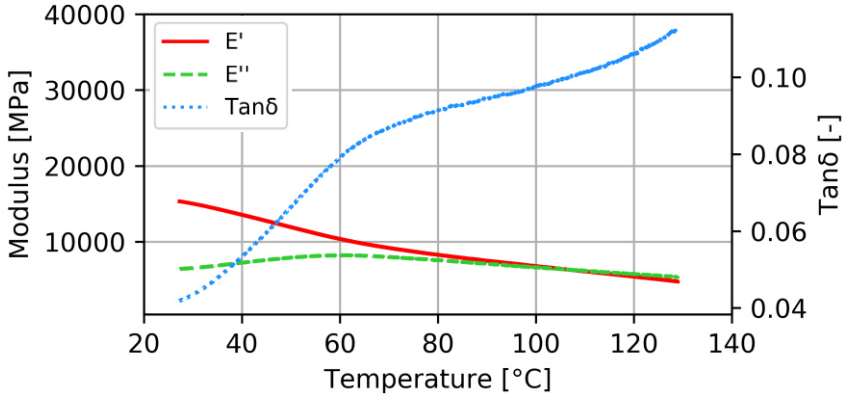

Figure 5-6: Typical output parameters from DMA test on example PP-GF: Storage modulus (red), loss modulus (multiplied by 10, green) and tangent delta (blue)

The storage and loss modulus were chosen as representative results from the DMA test. As in every DMA device, the storage modulus E' is calculated as in Equation (5-1) [30] from stress σ and strain ε. The equation shows, the modulus is based on the force F loading the sample, the displacement u, the Poisson's ratio ν, the energy dissipation δ as well as the dimensions of the sample: gauge length L, width w and thickness d.

$$E' = \frac{\sigma}{\varepsilon}\cos(\delta) = \frac{FL^3\left[1 + \frac{12}{5}(1+\nu)\left(\frac{t}{L}\right)^2\right]}{4uwd^3}\cos(\delta) \tag{5-1}$$

To express the systematic error of the measurement, the relative error is used. This error is the same for all tests conducted in the same system. Different results of the same material were compared in terms of their deviation by using the standard deviation. To be able to compare the results of different materials with different moduli, a statistical method called z-test was used. All tests were performed on the same DMA machine under the same conditions, therefore all test data from all material was considered as one population, but inside this population in different material groups. For comparison, the tests needed to be normalised. Therefore, each test result was subtracted from the average of the full population and divided by the population's standard deviation. The scatter of the result can then be expressed as the standard deviation of the normalised values per material as shown in Equation (5-2) and is unit-free. It is calculated according to the following example for a population containing material A and material B. The data is standardised (squared brackets) and its standard deviation calculated with x as measuring value, $\bar{X}$ as average, *stdev* as standard deviation and n as amount of results.

$$\sigma_{A_{Norm}} = \sqrt{\frac{\sum_{i=1}\left(\left[\frac{\left(x_{A_i} - \bar{X}_{AB}\right)}{stedv_{AB}}\right] - \bar{X}_{A_{Norm}}\right)^2}{n_{A_{Norm}} - 1}} \tag{5-2}$$

Summarised, the standard deviation for different materials was divided by the average to provide the percentaged deviation from the average. This deviation is in the following also called scatter.

5.3.5 Comparing strain measurements with DIC

The strain was also measured externally to analyse its distribution over the sample. Digital image correlation, a visual, contactless, and full-field 3D deformation measurement technique, was utilised to visualise strain distribution over the sample and to verify the movement of the drive shaft (Figure 5-7). This is achieved by means of two cameras, which trace the sample, by following an applied optical pattern. In the post-processing, the obtained images are compared over time and the differences are correlated to strain. For this purpose, a fine speckle pattern was applied to the sample

and to the loading nose, which allowed tracking of the deformation and movements. The results were analysed using the commercial software package Vic-3D [31].

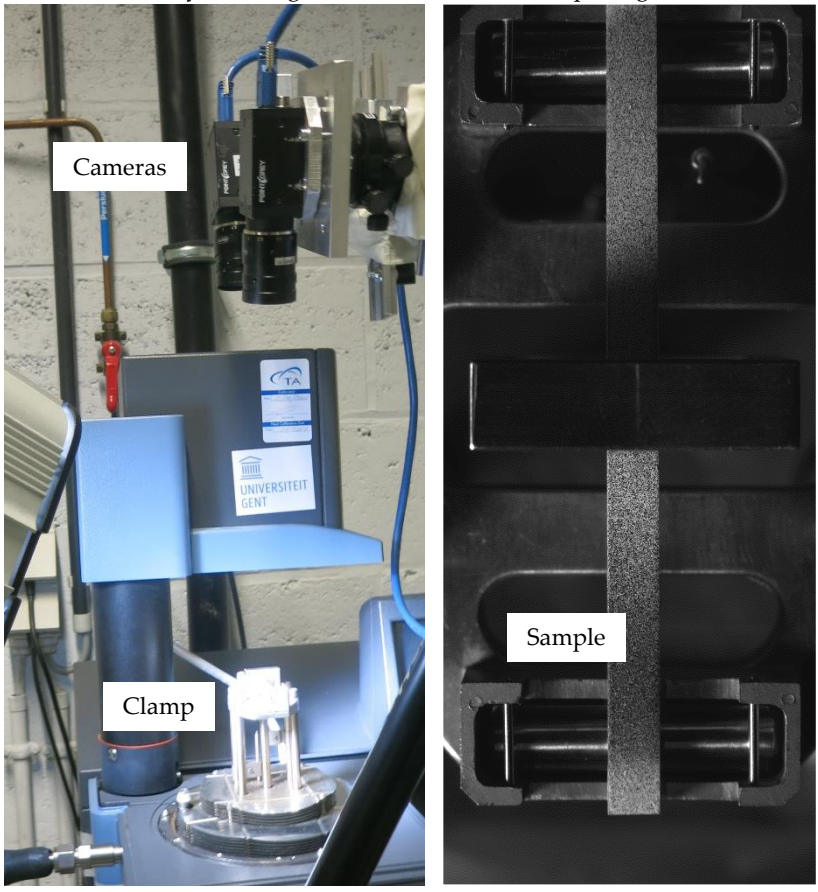

Figure 5-7: DIC on DMA, (left) setup, (right) camera vision: (a) top view and (b) side view with speckle pattern on sample and loading nose

5.3.6 Numerical framework of DMA tests

Next to experimental analysis, a numerical approach was taken. It has the advantage of eliminating the uncontrollable influences in the experiments. The workflow is visualised in Figure 5-8. A 3D finite element model (FEM) was constructed, using the commercial software ABAQUS [32]. The model replicates the dynamic 3-point-bending-test using realistic material models, dimensions and boundary conditions. The viscoelastic behaviour in each material point is defined by the instantaneous elastic properties and the Prony series in the time domain. The material input parameters have been determined from the experimental campaign at the reference temperature.

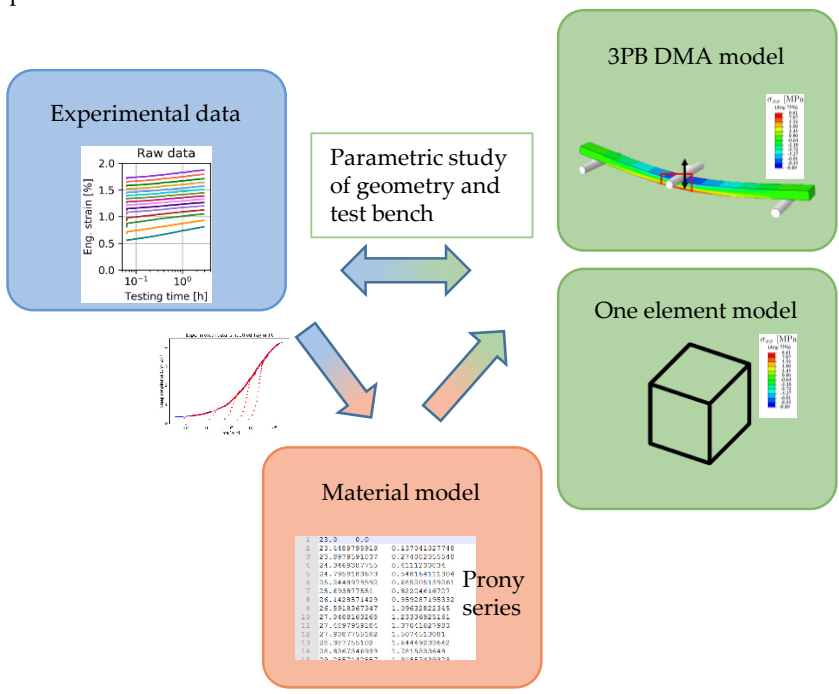

Figure 5-8: Overview of interaction points between experimental and numerical work

The geometry of the specimen and the position of the holders correspond to the experimental setup. The dynamic response of the virtual test is processed similar to the real experimental test: the displacement and reaction force outputs in the time domain are converted into the frequency domain with the Fast Fourier Transformation (FFT) to determine the phase lag. The numerical dynamic response is obtained using a dynamic implicit solver. The size of the finite elements along the specimen and around the contact areas was determined by a mesh convergence study. In the area of the contact zone in longitudinal direction, the mesh was refined. In the constant width and thickness direction, no refinement was needed. The resulting finite element mesh can be seen in Figure 5-9.

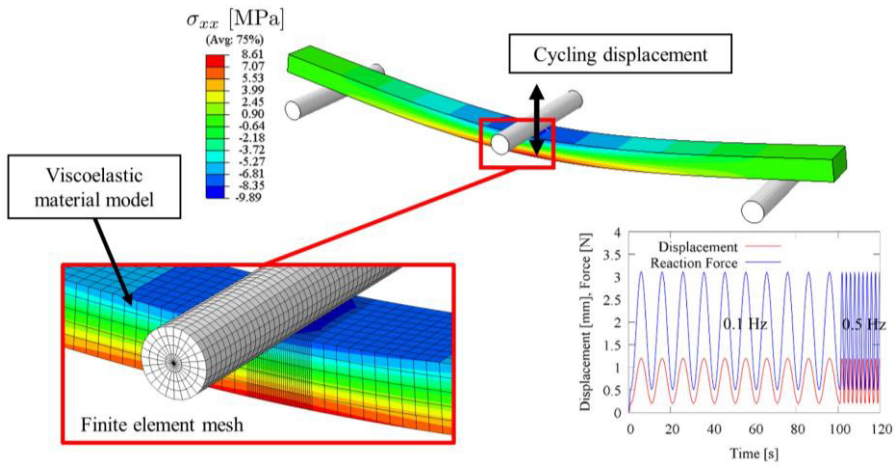

Figure 5-9: 3D finite element model of the 3-point-bending-test under cycling displacement. The mesh is refined in the contact areas with supports and shaft. Dynamic response of the reaction force at different frequencies

5.4 Results and Discussion on DMA tests

5.4.1 Development of generic guidelines based on PESU

In order to develop a system for more accurate DMA measurements, different parameters were varied on the pure polymer PESU. In the following paragraphs, the scatter of a result is used only for comparison within one graph. For each graph, the tests were performed with the same settings except for the one parameter that was under investigation. Comparison between different graphs is not valid, since several parameters can be different. At first, the DMA system on its own is analysed, followed by the shape of the sample. Based on the conclusions there, ideal parameters are chosen to perform measurements for a high reproducibility.

5.4.1.1 DMA fixture choice and clamping conditions

To ensure good clamping, the influencing parameters need to be identified. In the following, the clamp is described and contact areas analysed. The used clamped was the so called Rock-n-roll clamp of TA Instruments [33]. It is a 3-point bending clamp (3PB) with special sample support. The overall clamp and the support area are illustrated in Figure 5-10. Instead of rigid clamp supports, this clamp has rolling pins, which should support uneven samples and enable a perfect contact between clamp and sample. On the downside, the pins are rather flexible in their holders, allowing the span length of the sample to vary up to 50±1 mm on the span, which would result in an error of 6% on the storage modulus. However, for testing, the rolls were manually readjusted to have a very limited shift. By doing this, the error could be kept below 0.6%.

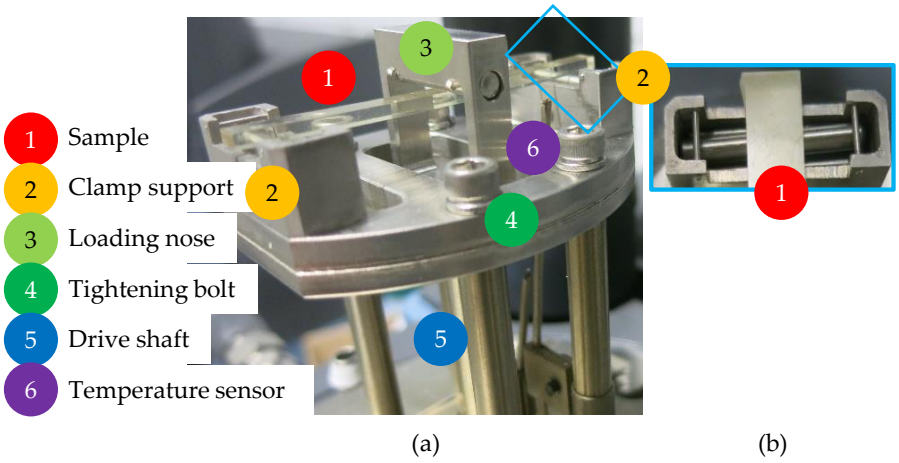

Figure 5-10: (a) 3-point bending clamp in DMA with span length of 50 mm and (b) flexible roll pins as clamp support

The clamp is attached to the DMA machine using four bolts. Split washers underneath the bolt help to maintain the applied torque. The effect of fixing these bolts to the machine was compared for (i) hand tightened bolts without measuring control and likely, below 0.1 Nm; (ii) bolts randomly tightened with a torque wrench, giving each bolt a random different torque in the range 0.1-1.7 Nm; and, (iii) all bolts tightened with a torque of 1.01 Nm. For each setting, the machine compliance was calibrated and resulted in similar values within the machine specific recommended region. Thereby the machine compliance was with ~0.3µm/N far lower than the sample compliance of >320µm/N for PESU samples. The same set of five samples was taken for each of the three settings, allowing recovery time and random order to exclude influences. After the test, the torque wrench fixed bolts were tested and showed the same level of torque before and after the test. The results are given in Figure 5-11; the vertical axis is comprised to a small range of values to show the difference of the curves. The tests with a torque of 1.01 Nm show an almost constant modulus from the beginning of the initiation phase until the end of the testing phase (here 5 minutes). Randomly tightened bolts in the range 0.1-1.7 Nm showed a higher modulus in the start-up period, but in the testing phase, the modulus was similar to the tests at 1.01 Nm except for one outlier. Hand-tightened bolts however resulted in an overall lower modulus, even though the modulus was constant from the beginning of the test on. The scatter on the average storage modulus was with 2.4% scatter for bolts tightened with 1.01 Nm slightly lower than for the other methods (3.2% for random 0.1-1.7 Nm and 3.4% for hand-tight). For the initialising phase, equally tightened bolts result in a steadier modulus from the beginning of the test on compared to the randomly tightened bolts. For the testing phase, a torque between 0.1-1.7 Nm should be chosen for a repeatable value of the modulus.

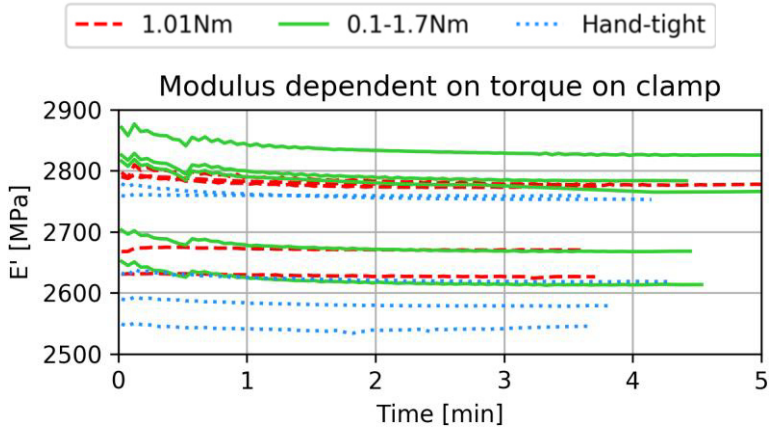

Figure 5-11: Influence of the torque values of the fixture on the storage modulus. Effect on PESU samples with bolts tightened by hand without force control, tightened individually randomly in the range of 0.1-1.7 Nm and uniform torque of 1.01 Nm on all bolts. Five samples per group.

After the clamp is installed, the sample can be placed. Locking the drive shaft and therewith closing the clamp can be done prior to a test via pushing a button in the software or is done automatically by the software in the initiating phase of a test. When the drive shaft is locked prior to testing, the shaft freezes at the position it was when the button was pushed. If it is done automatically, the drive shaft falls on the sample until contact is detected by force measurement. To ensure contact between the clamp and the sample before testing and therefore avoid a peak in bending force, it has shown to be effective to place a small weight (here 22 g) on top of the clamp and to lock the drive shaft prior to testing, Figure 5-12. After the start of the test, the shaft is unlocked, but does not drop down onto the sample.

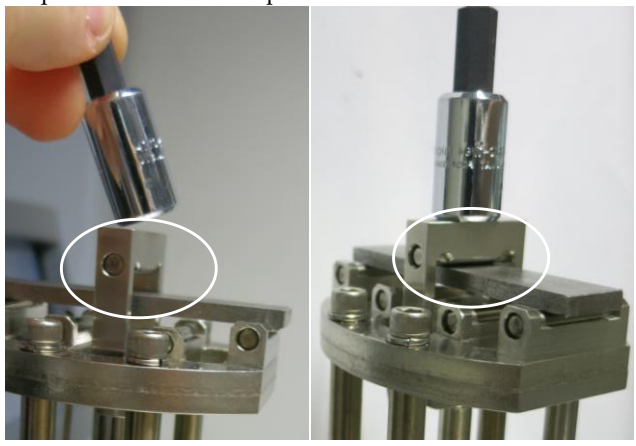

Figure 5-12: Weight placed on top of drive shaft to ensure contact between sample and clamp at start of test

During the test, the software offers two possible settings to hold the sample in place. The first option is a static pre-force value that should be chosen similar to the expected force level during the test to ensure clamping, but prevents breakage. Pre-force is always applied in the initiation phase of the experiment. In the test phase, this static force can be replaced by a second option, the force track. This setting adjusts the static force dynamically as a percentage to the dynamic force that is applied to test the sample. Especially, when the modulus of the sample changes due to circumstances like temperature, the flexible method helps to stay in the linear viscoelastic region of the sample. The static force should be bigger than the dynamic force to ensure clamping during all times. The standard value for the static force is 125% of the dynamic force. It is compared in Table 5-1 with 101% and 200% to see if the standard value is suited for a stiff sample in 3-point-bending. The different settings were applied to the same set of five samples in random order and with sufficient recovery time. The modulus and scatter values between these tests are overall found to be very similar. There is however, a small decreasing trend visible in the storage modulus and an increasing trend in the loss modulus for increased values of the static force. The scatter values for 101% are a little higher than for the other values. A higher value should be chosen. Yet, high static forces need to be avoided to not risk to test outside of the linear viscoelastic region (as the total force applied is the sum of the static and dynamic force). Since the overall impact seems to be small, the standard setting of 125% compared to the dynamic force is retained for all following tests.

Table 5-1: Average, standard deviation and scatter of storage and loss modulus dependent on the amount of static force during the dynamic test on narrow PESU-samples

Static force (with respect to dynamic force)	101%	125%	200%
Average E′	2931	2920	2911
STDEV E′	61	60	57
Scatter E′	2.1%	2.0%	2.0%
Average E′′	26.8	27.3	28.6
STDEV E′′	0.7	0.7	1.0
Scatter E′′	2.7%	2.5%	3.4%

5.4.1.2 Comparison DMA experiment and simulation

To verify the correspondence of experiments and numerical analysis, a comparison was made on dynamic tests. Figure 5-13 shows experimental data, simulated data from one element and from a full simulated beam. The data from one element is generated by simulating only one cubical element with the same boundary conditions of the full test. Geometry does not have an influence on this test. The data of the experiment and of the single element conform well. If the simulation considers the full

beam, the numerical prediction is up to 0.8% lower than the one from the experiment, which is negligible and explainable.

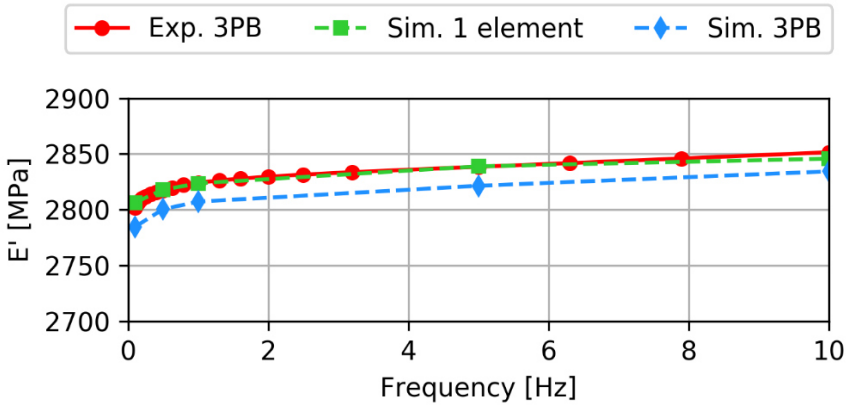

Figure 5-13: Dynamic frequency sweep, experiment and simulation in comparison

The reason can be found in the calculation of the modulus. For the simulation, Euler-Bernoulli beam theory was assumed. The calculation from the DMA testing is based on the Timoshenko beam theory. The difference is the assumption in the Euler-Bernoulli beam theory that every cross-section-plane stays perpendicular to the neutral axis, whereas Timoshenko takes out-of-plane bending into account (Figure 5-14). For beams with low shear and torsion stresses, both theories should give the same result. For the DMA experiment, in case of big amplitudes (here 500 µm), the results differ slightly. Timoshenko beam theory should be used for more accurate simulations. The error of less than 1% was considered negligible.

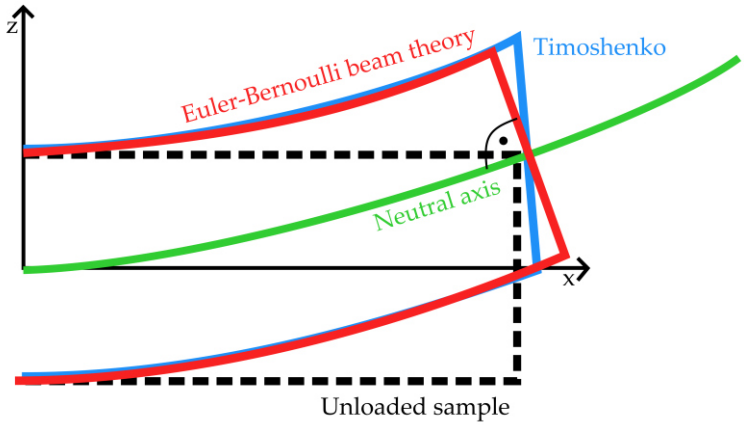

Figure 5-14: Difference between Euler-Bernoulli beam theory and Timoshenko beam theory in cross section plane

The equations to calculate strain either by the Euler-Bernoulli beam theory (Equation (5-3)) or Timoshenko (Equation (5-4)) are based on geometrical values (length L between supports, width w of the sample and thickness d of the sample) as well as the displacement u, which is equivalent to the amplitude. The difference is a factor in the denominator based on the Poisson's ratio ν added by Timoshenko.

Euler-Bernoulli beam theory:

$$\varepsilon_{Euler} = \frac{6du}{L^2} \tag{5-3}$$

Timoshenko formula used by Q800[34,35]

$$\varepsilon_{Timoshenko} = \frac{6du}{L^2\left[1 + \frac{12}{5}(1+\nu)\left(\frac{d}{L}\right)^2\right]} \tag{5-4}$$

For the considered span of the beam, the span-to-thickness ratio is more than 20. For this span-to-thickness ratio, the transverse shear deformation is assumed to be negligible and simple Euler-Bernoulli theory applies. However, since the accuracy of the storage modulus is very critical to measure very small changes over time (e.g. in long-term creep under low stress amplitude), all corrections are taken into account. Therefore, the Timoshenko beam theory is applied. Furthermore, the finite element model uses a fine mesh of solid elements through the thickness of the beam, and is hence equivalent with Timoshenko beam theory.

5.4.1.3 Relevant dimensional accuracy of the specimens

The simulations are an effective method to investigate the influencing parameters on the final result. In contrast to an experiment that is subjected to many uncontrolled influences, in a simulation a single aspect can be changed at a time. To evaluate the effect of the sample geometry, aspects were changed numerically to create imperfect, yet realistic scenarios. Different widths and lengths were simulated as well as deviations in sample width, parallelism, symmetry and clamping angle. In Figure 5-15a, the perfectly shaped reference geometry is shown from two perspectives. Figure 5-15b contains images of the variations in geometry followed by their effect on the modulus calculation (Figure 5-15c). All applied changes are realistically possible errors, except for the very big rotation of 8.5°. The variation on the sample geometry is bigger than the error in clamping. As a result, in the graph the modulus is more affected by the sample dimensions than by the clamping symmetry. In the following, the individual aspects will be analysed and additional studies performed where needed.

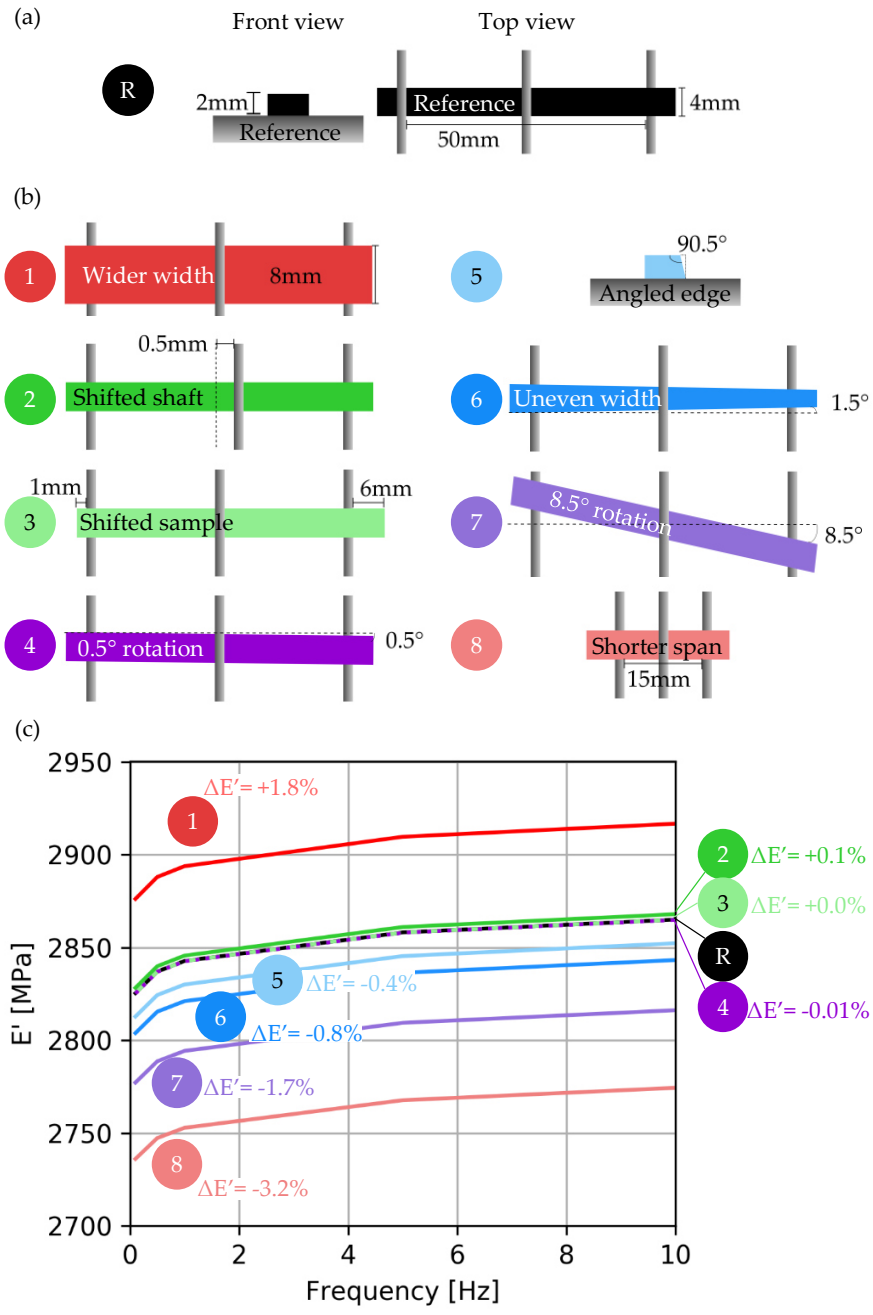

Figure 5-15: Changes in sample geometry and position and its effect on the storage modulus compared to the reference. (a) reference geometry, (b) changed geometries and positions, (c) effect on storage modulus

The effect of dimensions

The change in width or span length (case 1 and 8 in Figure 5-15), changed the result the most, since the sample dimensions thickness, width and span length are directly applied in the calculation of the modulus. As there is rarely any guideline provided in test standards for the specimen's width, narrow and wide specimens were compared (Figure 5-16). The narrow PESU samples were 3.6 mm wide, the wide ones 7.6 mm. Narrow samples were found to have a slightly lower average (2902±63 MPa) than wide samples (2932±54 MPa). The FE simulation (red symbols) confirms the trend that narrow samples have a slightly lower storage modulus (2843 MPa) than wide samples (2894 MPa). The experimental tests have a scatter of 2.2% (narrow samples) and 1.8% (wide samples) when the same displacement is applied. The result of the simulation are within the range of experimental scattering data, the results are therefore matching.

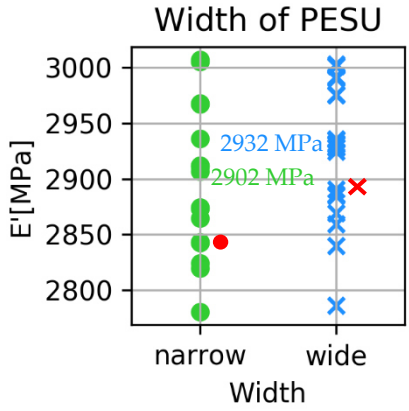

Figure 5-16: Effect of the sample width on the storage modulus. Each symbol corresponds to a measurement on a single specimen (20 per width), average written next to group. Simulation values for PESU next to measurement data in red

Reason for the difference in average values of about 1 % is the Poisson's effect. It causes a slight variation in stress distribution over the sample width, displayed in Figure 5-17 as dark blue centre on the sample. Due to the compression of the bending nose, the sample widens on the upper surface in the transverse direction (width direction) and is thinning on the tensile bottom side. This is causing a saddle effect in the sample. This effect is stronger pronounced in wider samples and falsifies the result slightly. To measure an apparent bending modulus as close as possible to the theoretical value, the sample must be constrained in deformation as little as possible by the setup. Therefore, long, narrow samples are preferred [36]. However, the stress field is not affected significantly, as the experimental and numerical studies on different widths show. For consistent results in a testing campaign, it is especially important to use samples with an equal width.

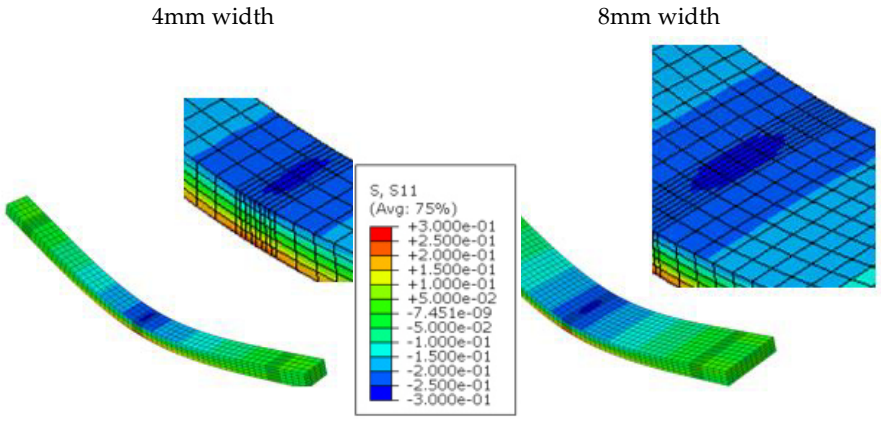

Figure 5-17: Contour plot of the stresses in the longitudinal direction of the sample obtained using finite element analysis. Samples width of 4 mm (left) and 8 mm (right) compared at the same displacement

The effect of shaft shifting

The shifting of the shaft (case 2 of Figure 5-15) is the result of the amount of play the drive shaft of the DMA has in the machine as well as the play of the clamp. The clamp shaft is added on the drive shaft with a dovetail connection, which introduces a slight uncertainty in position, Figure 5-18. The assumption of a shift in drive shaft of about 0.5 mm to one direction is a realistic error and causes, according to the simulation only a very small deviation from the reference value.

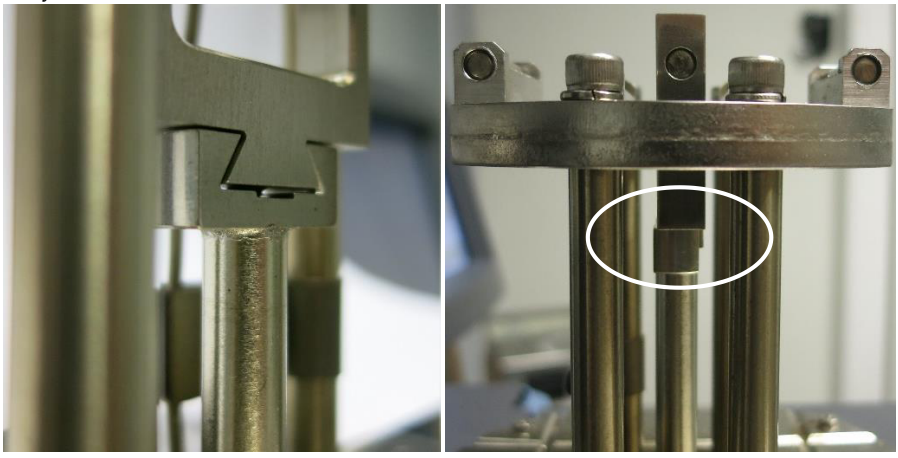

(a) (b)

Figure 5-18: (a) Dovetail connection between drive shaft of DMA machine and clamp, (b) able to cause a small uncertainty of the accurate position of the middle loading nose of the 3PB clamp

The effect of sample shifting

The shifting of the sample (case 3 in Figure 5-15) and resulting difference in overhang, did not reflect the requirement of a certain overhang, as stated in the standard [12]. As long as the sample does not slip from the clamp, the calculated stress fields and corresponding modulus stay the same. Nevertheless, the sample should be positioned as central as possible for the sake of symmetry.

The effect of sample rotation

The rotation as in case 4 or 7 of Figure 5-15 does not influence the result of a static test. This is shown in Figure 5-19a, where an exaggerated mismatch of 10° between specimen and fixture line does neither numerically nor experimentally show a difference. In this static test, experimental DIC images were compared to finite element (FE) simulation on the basis of the strain fields of Figure 5-19b and c.

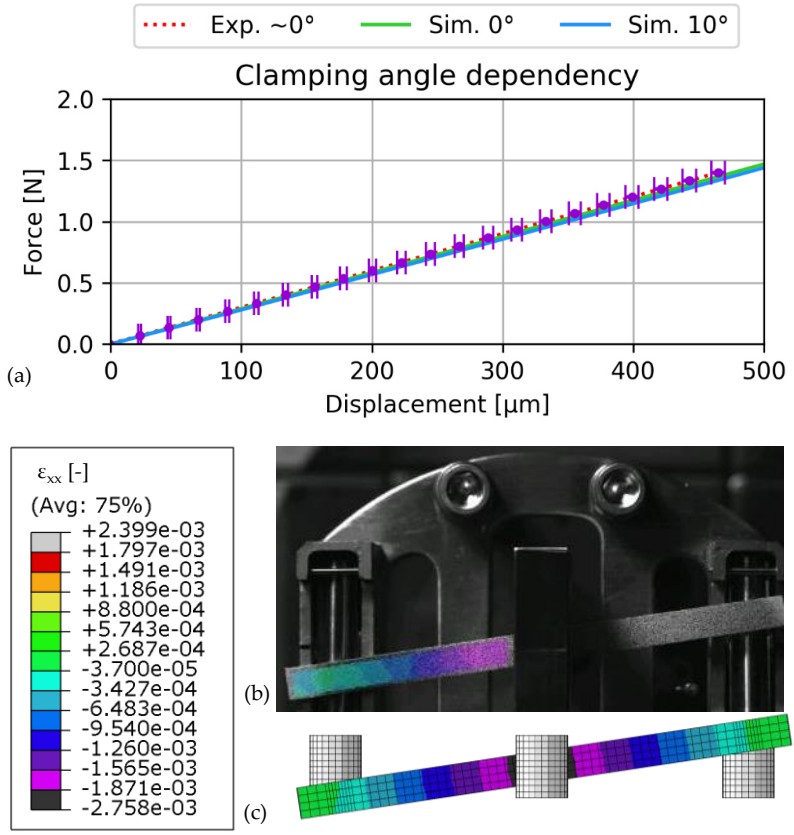

Figure 5-19: Influence of the sample misalignment in static testing (0.2 N/min). (a) Force-displacement-curve of simulations and experiments dependent on rotation angle and strain fields of (b) experiment and (c) FE-simulation in same colour scale

The orientation of the strain field is less pronounced in the DIC image, probably due to the flexible support roller that causes an unclear effect and overall the resolution of the DIC. The found order of magnitude is the same for experiment and simulation. This confirms that the experimentally measured data and that of the simulation is comparable and the parametric study is valid. As before, the change in one parameter, here of the sample rotation, was tested in a dynamic simulation. A rotation of 0.5° was found to reduce the storage modulus by 0.1% and a rotation of 8.5° caused 1.7% of inaccuracy.

The effect of angled edges

Lastly, the effect of imprecise sample preparation with angled edges (case 5 and 6 from Figure 5-15) cause a drop in modulus as well. Especially the angled edge in thickness direction of only 0.5°, which causes on its own a drop of 0.4% is critical. In manual sample production, bigger inaccuracies are likely. A very high precision, as shown in Figure 5-20 is needed for reproducible, correct measurements.

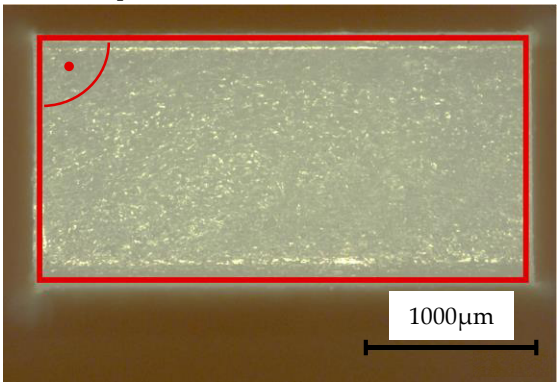

Figure 5-20: High precision of angle accuracy and parallel edges on DMA sample

Conclusion

In conclusion, the sample dimensions and the accuracy of a rectangular cross-section of the sample have the biggest impact on the modulus. The position of the clamping, namely the sample rotation or a shift in symmetry from the shaft or the sample position, is secondary.

5.4.1.4 Study on repetitions within one measurement

In DMA, it is possible to program the same loading cycle several times in one experiment. It was observed that the first measured cycle was higher in modulus than the following cycles. In a frequency sweep from 1-25 Hz the same loading cycle was applied 100 times (Figure 5-21). Of the 100 cycles, the first one deviates significantly more (15.7 MPa) from the next cycle, while the subsequent sequences gradually converge. An unsteady first cycle also occurred in amplitude sweeps. However,

between the second and third cycle, the difference becomes small (difference of 2.4 MPa over the whole frequency range), and further cycling is not required to determine an accurate value. In addition, the gradual drop in modulus is typical for material relaxation. However, it was verified that the samples fully recover after a relaxation and a second test on the same samples shows the same values and behaviour. Also self-heating is unlikely to cause the drop in modulus, since the amplitude and509 frequency are low and it is known from a temperature sweep that a drop of 20 MPa is caused by a temperature difference of 5°C.

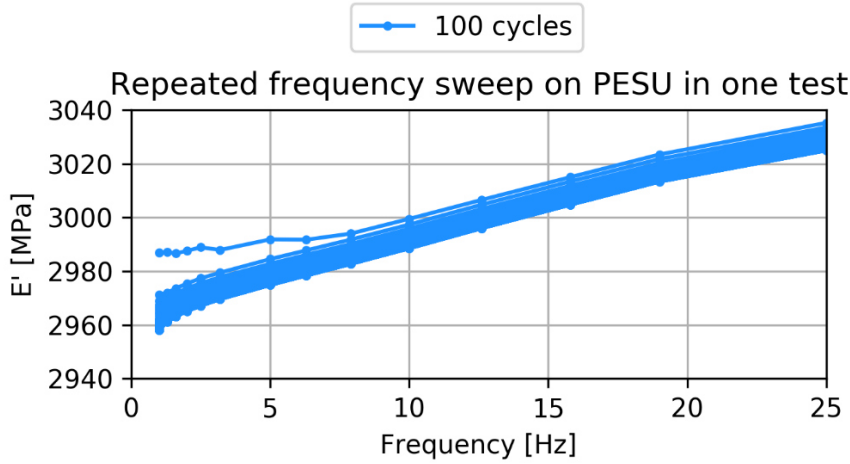

Figure 5-21: Frequency sweep on PESU, no initiation time like isothermal step, sweep from 1-25 Hz, 100 cycles within the same test

The reason for the divergent first cycle can be found when observing the displacement with DIC at 25 fps (Figure 5-22a). A test at 1 Hz is repeated six times within one run. Each cycle consists of four stabilisation loops and three averaging loops from which the moduli are calculated (standard setting for Q800 DMA). The measurements show that between each cycle, the machine reduces the amplitude and restarts for the next cycle. The required amplitude of 500 µm is reached at the first cycle, but the amplitude is taking place at a different displacement. To keep the sample in place, a static force is applied. This static force is set at 125% of the force used for testing. As Figure 5-22b shows, the static force is 0.9% off and gets more precise with each cycle. This shows that the machine is not fully set yet at the first cycle, which causes the deviating storage modulus between the first and the subsequent cycles in cyclic measurement sweeps as in previous Figure 5-21. Note that the displacement during the four averaging loops vary about 2 µm, which is due to the limits of the DIC measurement.

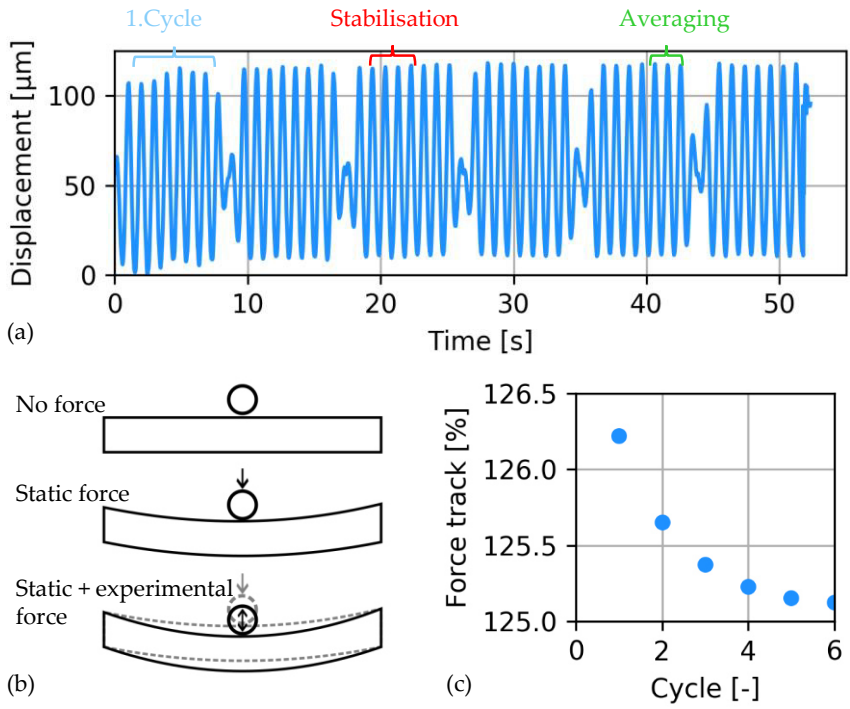

Figure 5-22: DIC footage of a frequency sweep at 1 Hz. (a) Seven sweeps within one test on a PESU sample, amplitude 500 µm. Each cycle contains four stabilisation and three averaging loops. (b) Static force holds sample under pre-tension, experimental force moves it. (c) static force is percentage of experimental force

5.4.1.5 Study on repetitions on different samples

As in every other mechanical test, a representative result for a batch of materials should be the average of the results from the same repeated test. In DMA, it depends on the type of sweep how many repetitions are needed for a quantitative result. One test is for example sufficient, if amplitude or frequency sweeps are used only to identify valid test regions as these ranges are much larger than the variation expected within one material. For a quantitative use of amplitude and frequency sweeps, however, the amount of tests is relevant. Therefore, it was tested how many results from different tests need to be combined to receive the same average value. The considered data set contained 20 test results, generated by testing different samples with comparable settings. To know how many repetitions are necessary, combinations of different tests were formed and the standard deviation compared. From the 20 available test results, 2 results were randomly taken (allowing repetitions) and the standard deviation calculated. This was done 50 times (grey curve at "number of considered tests"=2 in Figure 5-23). From those 50 standard deviations, the overall

standard deviation was calculated again, forming the first dot of the red curve. The same procedure was repeated with higher numbers of taken values (3 to 20), forming in total 50 grey random curves and one red standard deviation curve. Both plots show a greater variation in standard deviation if x is small. The different curves converge with an increasing number of x. Thereby the standard deviation improves steeply for a smaller x and flattens out at higher numbers. For amplitude sweeps, it seems to take around thirteen tests to have a very stable standard deviation, but already at around five repetitions, the curve is flattening and the improvement with adding further tests is decreasing with the amount of tests added. For the frequency sweep, the curve starts to flatten at six repetitions and stabilises at eight. For cost-efficient testing five amplitude sweeps and six frequency sweeps can be advised. That way the standard deviation stays the same, no matter which different test combination was chosen.

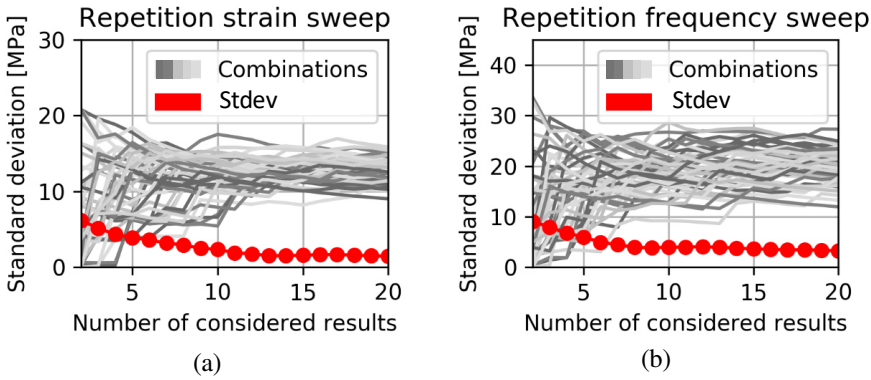

Figure 5-23: Randomly combined test data from the same 20 tests: a) amplitude sweep results at 50 µm, b) from frequency sweep at 1 Hz to determine how many tests are statistically required for a repeatable test result. The red line shows the variation between different combinations, the lower, the higher the repeatability

5.4.2 Choice of material-specific testing parameters

After finding influencing parameters concerning clamping and geometry, the input parameters for the software were optimised. Therefore, a self-developed testing procedure is applied on the polymer PESU and the composite PP-GF. To show the effect of material-specific optimisation, these tests on PESU are compared to tests according to machine-specific literature recommendations and tests that are in the range of the capability of the DMA, but not optimised (arbitrary).

5.4.2.1 DMA settings for PESU

To find material-specific settings different tests are needed: The amplitude sweep was performed to find the area of viscoelastic response. The viscoelastic region is recognizable from a constant storage modulus over increasing amplitude and a linear increase of stress [16]. Figure 5-24 displays five repeated strain sweeps with different amplitude ranges. All tests show a linear viscoelastic response of the sample between 0.01-0.3% strain, respectively an amplitude of 20-650 µm, resulting in a measured modulus of 2943±32 MPa. At lower amplitudes, the response is in the noise level range of the measurement, and thus the measurement is not accurate. At larger amplitudes, the viscoelastic region is exceeded, which can be noticed by the drop in storage modulus and the stress-strain curve deviating from the linear curve.

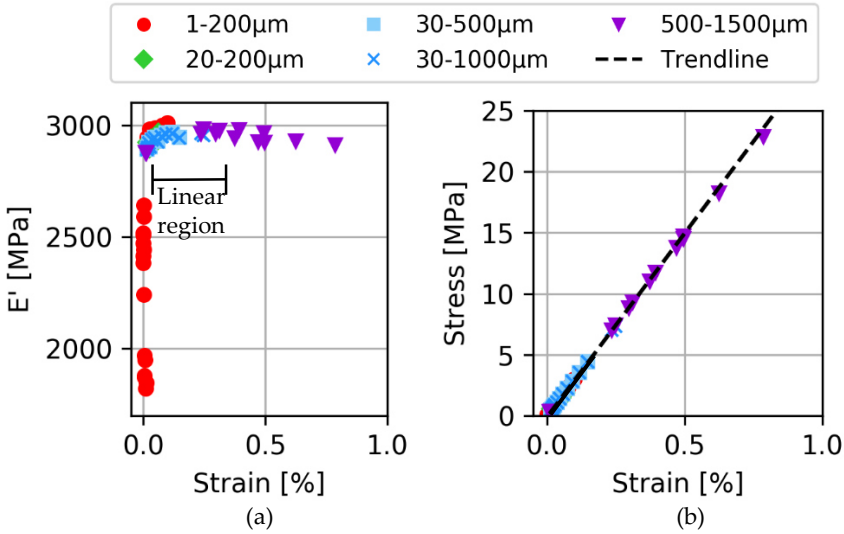

Figure 5-24: Amplitude sweep of PESU with aspect ratio 25, five repetitions, but with different amplitudes. (a) Storage modulus, (b) stress over strain with black linear trend line

Further analysis showed that amplitudes at the higher end of the linear viscoelastic range are preferred, since the noise on the result is lower, 4.2% for 0.01% strain amplitude in comparison to 1.5% for 0.25%strain amplitude, see Figure 5-25. For the PESU specimens, 0.25% bending strain correspond to an amplitude of 500 µm.

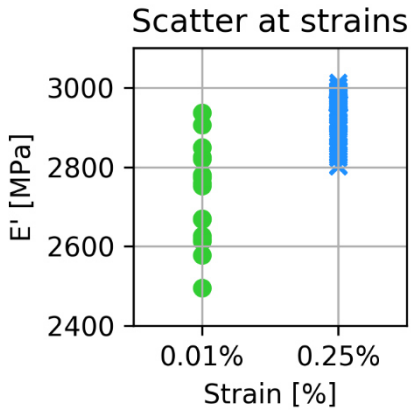

Figure 5-25: Comparison between small (0.01%, 20 µm) and big (0.25%, 500 µm) amplitude within valid test range for PESU at 1 Hz

Due to the sample loading at higher frequencies, a resonance is created in the sample, the sample fixture and the actuator. At a certain frequency, when one of the so called eigenfrequencies of the system is matched, unwanted resonances can occur which make the measurement invalid. The theoretical natural frequency of the sample based on a simple supported beam in 3-point-bending under its own weight is at 509 Hz and therewith not on its own responsible for the detected resonance. Therewith the combination of sample, fixture, and actuator leads to unstable areas of resonance. To detect those frequency values, a frequency sweep can be performed. Figure 5-26 shows a frequency sweep up to 50 Hz on PESU material. Indications for resonance are sudden changes in or negative values of the moduli. Two 3-point-bending fixtures, which differ mainly in span length, were compared to illustrate the sensitivity of the system. The 15 mm fixture shows smooth, valid curves until 40 Hz, the 50 mm fixture until 20 Hz. For higher frequency values until 50 Hz, the resonance falsifies the result of the modulus. Despite the bigger frequency range, the 15 mm fixture is not recommended, since the low span to thickness ratio approaches the sensitivity limits of the machine and leads to a lower storage modulus, which was also confirmed by the FE-model.

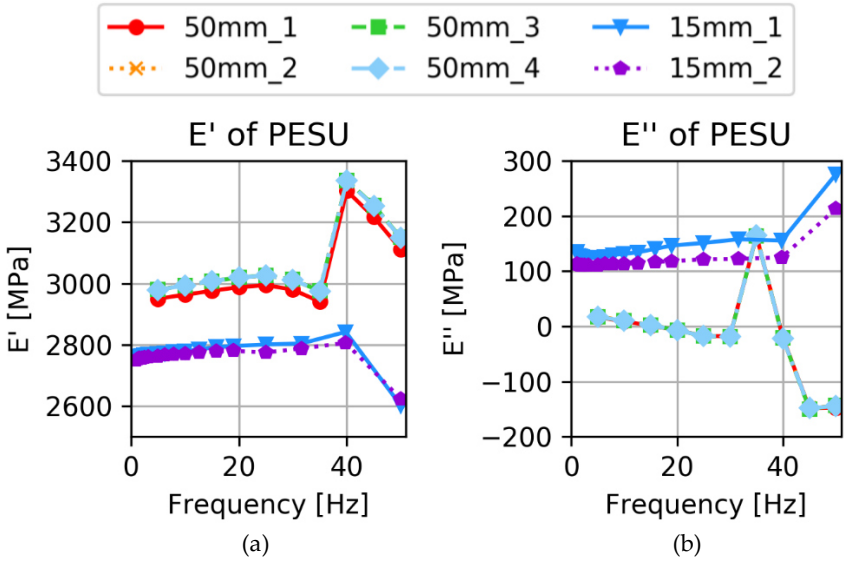

Figure 5-26: Inconsistency of storage (a) and loss (b) modulus at higher frequencies due to resonance because of high sample stiffness for 15 and 50mm span fixtures at 0.25% strain, experiment repeated on six different samples

The combination of a certain amplitude and a frequency, leads to a maximum velocity v per applied cycle on the sample that can be calculated with Equation (5-5), where f is the frequency and u the amplitude:

$$v(t) = 2\pi f u \cos(2\pi f t) \tag{5-5}$$

Figure 5-27 plots multiple data points from several tests as function of the storage modulus (at highest point of sine curve) over the velocity (at highest speed). For low amplitudes (below 20 µm) in combinations with low to medium frequencies (below 20 Hz), the modulus scatters significantly more than for higher values. This combination equals a velocity of 1250 µm/s. This confirms the findings of the scatter at low amplitudes. Above 1500 µm/s, the modulus does not seem to change with the velocity of the test. The test illustrated that the strain rate does not have a significant influence on the modulus when tested in the correct amplitude and frequency range.

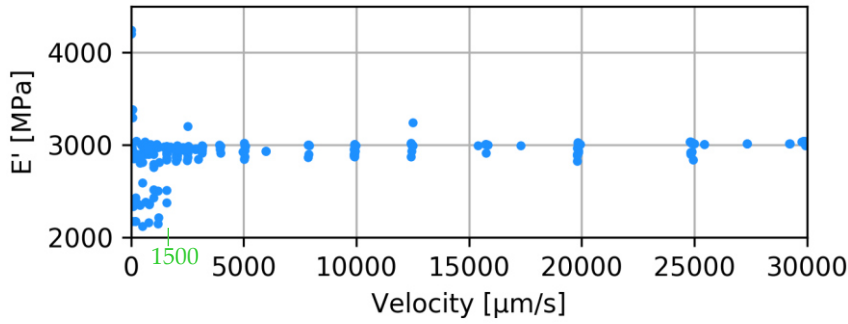

Figure 5-27: Data points from multiple tests showing the independence of the modulus from the velocity when a stable amplitude is reached

5.4.2.2 DMA settings for PP-GF

The above developed testing procedure was also applied on a much stiffer composite material, being a highly graphite-filled polypropylene (PP-GF), with a slightly curved surface due to the specimens being cut from a tubular section, as to see in Figure 5-28.

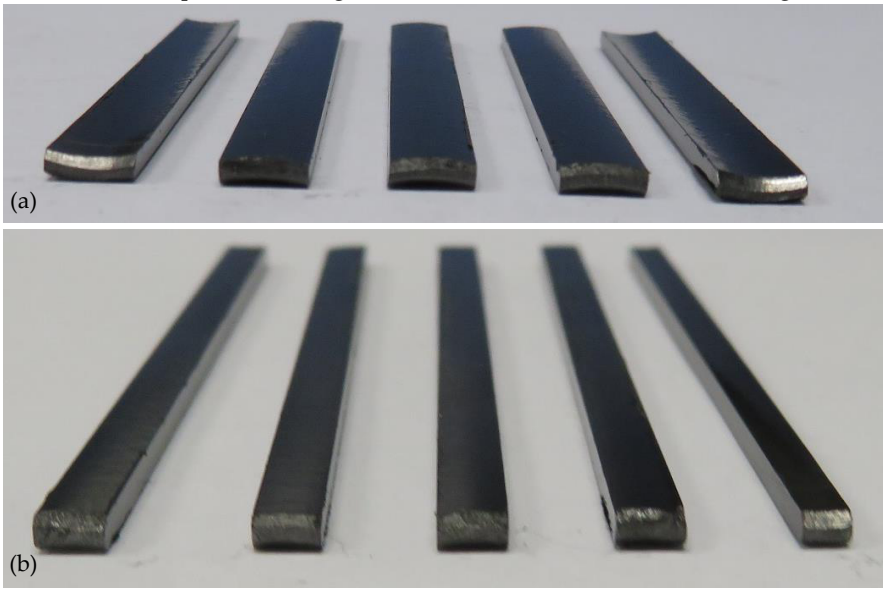

Figure 5-28: PP-GF samples cut from tube and therefore with slight curvature: (a) wide samples, (b) narrow samples

The influence of the width was tested on these samples deviating in shape from a rectangular beam (Figure 5-29). Samples of 2.9 mm width were compared with 5.7 mm wide samples. The average storage modulus of wide samples is here significantly higher, not only because of the Poisson's ratio, but mainly because of the bigger arc.

The narrow PP-GF samples have a scatter of 8.3%, while the wide samples have a scatter of 10.0%. This is the opposite behaviour than for the PESU samples. Likely, the scatter increases with a wider sample of Tech-PP due to the curvature of the material. If the sample is cut in a slight angle to the curvature, the test becomes less reliable. With a flat sample or a narrow sample and therewith small arc, the effect is less pronounced. Due to the present curvature, narrow samples were used for the following sweeps on Tech-PP to limit the scatter effect.

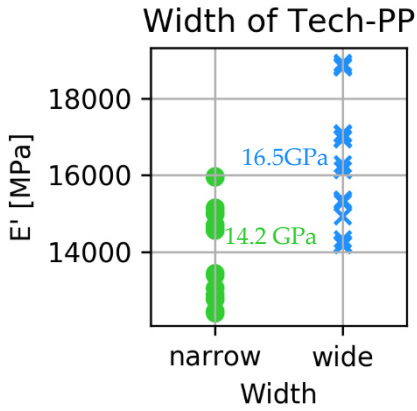

Figure 5-29: Effect of the sample width on the storage modulus. Each symbol corresponds to a measurement on a single specimen (20 per width), average written next to group

The amplitude sweep should only serve qualitative purpose to find the valid amplitude region at 1 Hz. The test in Figure 5-30 is showing a linear, stable behaviour only in the small strain region, namely between 0.004% and 0.011%, respectively 10 µm and 25 µm. The limits are lower and the range smaller than for PESU, since PP-GF is above its glass transition at room temperature and hence has a more nonlinear behaviour.

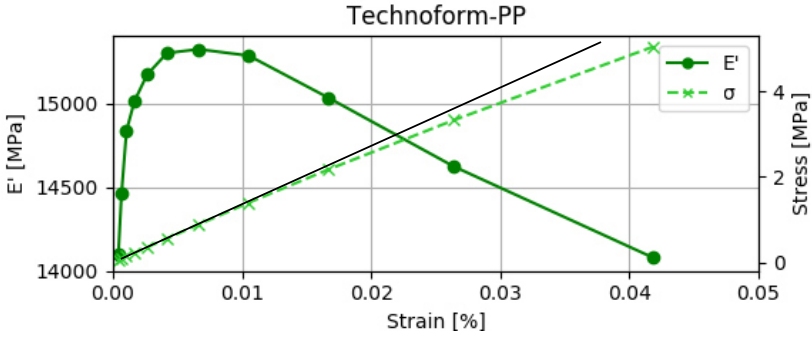

Figure 5-30: Amplitude sweep of PP-GF, 1 Hz; Plotting storage modulus and stress over strain to interpret valid test region

A frequency sweep at 0.01% strain was performed to evaluate the scatter of results (Figure 5-31). The storage modulus shows a smooth curve for all tests and the loss modulus stays positive. Due to the different specimen stiffness and geometry, the complete 1-30 Hz range was stable. The scatter on the storage modulus per frequency is with 1.7% smaller than the averaged scatter of 2.6% on the loss modulus. At 1 Hz, the storage modulus is 15.27 ± 0.26 GPa and the loss modulus is 0.58±0.02 GPa.

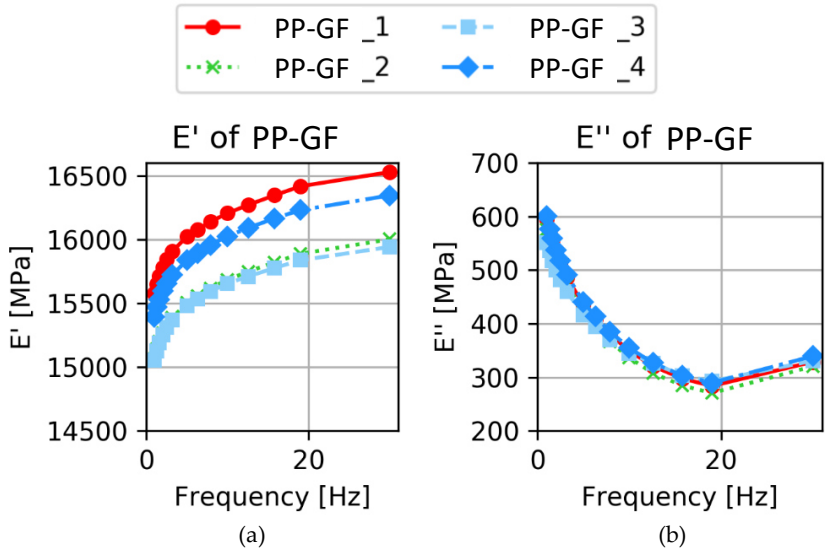

Figure 5-31: Storage (a) and loss (b) modulus in frequency sweep of PP-GF 35°C, experiment repeated on four different samples

A temperature scan on PP-GF (Figure 5-32) shows the temperature dependence of the polypropylene based composite. Within 5°C difference, the storage modulus drops 5% (0.70 GPa). Therefore, a stable temperature is very important during the testing of temperature sensitive material. The peak visible on the curve of the loss modulus shows a material transition [26].

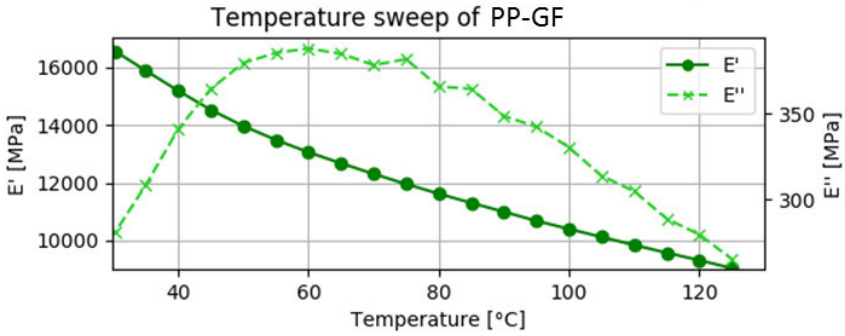

Figure 5-32: Temperature sweep of PP-GF, 1 Hz, 20 µm, modulus over temperature to show temperature dependency of material between 30-130°C

With this information on the linear viscoelastic region, the frequency range, and the temperature range, it would for example be possible to perform sweeps for Time-Temperature-Superposition, as performed in the following chapter.

5.4.2.3 Influence of recommended DMA settings

In literature, settings for the experiment, for example the limits for amplitude or frequency, are given in a generic way. This study suggests a procedure to adapt settings depending on the tested material. In Table 5-2, different possible amplitude and frequency ranges are listed. Arbitrary represents the maximum possible range of the machine; machine-specific follows literature recommendations and material-specific tests are results of this study. The difference in amplitudes between the material specific settings for PESU and PP-GF shows, no generic rule can do justice to both. The frequency sweep of material-specific settings is much more limited than in machine-specific settings.

Table 5-2: Different settings of amplitude and frequency for DMA tests

Categories	Arbitrary	machine-specific	material-specific	
			PESU	PP-GF
Amplitude	0-1000µm	25-40µm	20-650 µm (best 500 µm)	10-25 µm
Frequency	1.6e-3 to 200 Hz	1.6e-3 to 200 Hz	0.1-40Hz	1-30 Hz

To show the importance of the settings, tests on PESU were performed in three different settings. The results are displayed in Figure 5-33.

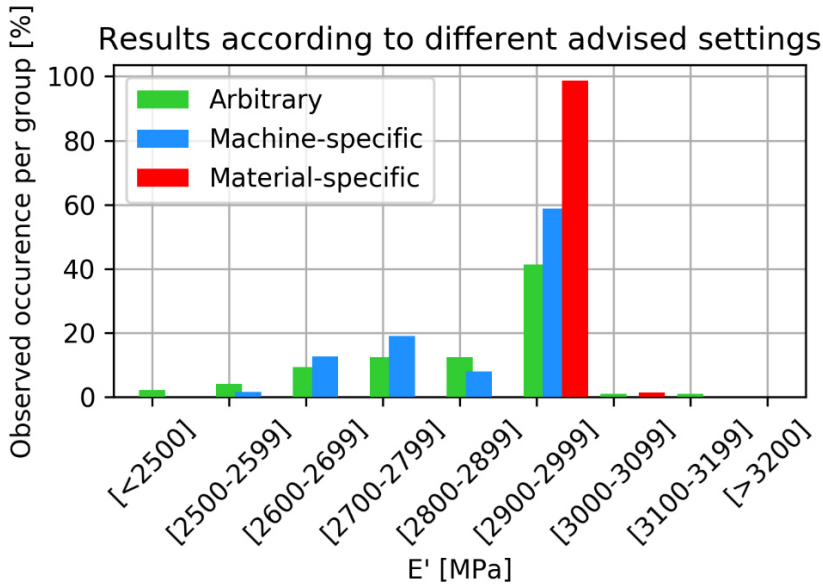

Figure 5-33: Distribution of results depending on the settings. Experiments using PESU, 1 Hz in different bending fixtures. Tests according to recommendations of this study (material specific) were compared to tests according to machine-specific settings described in literature and to tests aribrary chosen from the possible settings. Each colour-group contains more than 60 samples

The results of this study, adapted to machine and material, show a scatter of only 0.6% and have no significant outliers. Tests following settings recommended in literature have a broader distribution of measured values, resulting in a scatter of 3.7% on the average storage modulus, but deliver results in the correct order of magnitude, slightly underestimating the stiffness. The results of arbitrary tests however have a scatter of 17.6% and cause outliers in both directions with a difference of up to 60% compared to the average modulus. Hence, they do not deliver trustworthy results without an extensive study to eliminate the outliers. This shows that in order to use DMA test data to quantify the viscoelastic nature or long-term material response of materials, very specific guidelines should be followed. Moreover, this study was performed on a high-grade temperature and moisture stable material, and other polymers might be even more sensitive. However, this result also shows, suboptimal executed DMA tests are almost exclusively underestimating the storage modulus. Therefore, even safety applications that are based on arbitrary results are not compromised.

5.5 Conclusions of DMA testing

Dynamic mechanical analysis (DMA) in a 3-point-bending setup allows studying the linear-viscoelastic region of materials. In this research, PESU has been tested to determine, which factors and parameters easily increase the scatter of repeated measurements and therewith make the results less useable in quantitative sense. The developed measurement system has successfully been applied to the graphite filled composite PP-GF as well. With the optimised settings, the PESU sample showed a scatter on the storage modulus of only 0.6%. The graphite filled composite PP-GF had with 1.7% a slightly higher scatter. Despite the low experimental scatter on PESU, the dimensional accuracy of the sample is the determining factor for the precision. In theoretical calculations, the storage modulus should scatter up to 1.6% due to the remaining dimensional inaccuracy. The good experimental results should be taken with a slightly higher scatter to ensure a safe application. Overall, the experimental scatter can be kept low, if following guidelines are respected:

- The accuracy in dimensions should at least be as precise as ±2%.
- The span-to-thickness ratio should be higher than 10.
- The width is not limited as long the contact pressure can be ensured over the full width and precision can be assured. However, due to Poisson's ratio and in case of not perfectly flat samples, smaller widths are advised.
- The alignment mismatch between the specimen's centreline and the fixture can be neglected for mismatch angles coming from specimen aligning by the naked eye.
- The limitations in frequency and amplitude cannot be given generically, but require material and setup specific adjustments. For new materials or material in new dimensions, a testing procedure is recommended.
- The first cycle of a sweep does not appear as stable as results from the second cycle on. It is recommended to have at least one iteration within one test and take the results of the last iteration only.
- An amplitude sweep determines the linear viscoelastic region. From the range of possible amplitudes, the highest should be chosen for stable results. For determination of the viscoelastic region in a homogeneous material, a single sweep is sufficient, to use the modulus quantitatively, at least five but ideally twelve repetitions are recommended.
- A single frequency sweep can be used to detect resonances, however, to use the modulus quantitatively, at least six and ideally thirteen repetitions are recommended.

The results of this study allow for sufficient boundary conditions for the test settings to enable repeatable, accurate measurement of the storage and loss modulus. In the next chapter, these improved settings form the basis for long-term predictions.

References

[1] J. Schalnat, D.G. Gómez, L. Daelemans, I. De Baere, K. De Clerck, and W. Van Paepegem, "Influencing parameters on measurement accuracy in dynamic mechanical analysis of thermoplastic polymers and their composites," *Polymer Testing*, vol. 91, 2020, p. 106799.

[2] TAInstruments, *Thermal analysis - Q800 Specifications*, 2010.

[3] A. Mettler-Toledo GmbH, *Thermal Analysis in Practice: Tips and Hints*, 2016.

[4] Y. Gonzalez-Garcia, J. Mol, T. Muselle, I. De Graeve, G. Van Assche, G. Scheltjens, B. Van Mele, and H. Terryn, "A combined mechanical, microscopic and local electrochemical evaluation of self-healing properties of shape-memory polyurethane coatings," *Electrochimica acta*, vol. 56, 2011, pp. 9619–9626.

[5] J. Dealy and D. Plazek, "Time-temperature superposition—a users guide," *Rheology Bulletin*, vol. 78, 2009, pp. 16–31.

[6] P.L.-S.D. Dykeman, "Guidelines for performing storage modulus measurements using the TA Instruments DMA 2980 three-point bend mode - I. Amplitude effects," *Polymer testing*, vol. 19, 2000, pp. 199–164.

[7] C. Grein, K. Bernreitner, and M. Gahleitner, "Potential and Limits of Dynamic Mechanical Analysis as a Tool for Fracture Resistance Evaluation of Isotactic Polypropylenes and Their Polyolefin Blends," *Wiley InterScience*, 2004.

[8] M. Tajvidi, R.H. Falk, and J.C. Hermanson, "Time–temperature superposition principle applied to a kenaf-fiber/high-density polyethylene composite," *Journal of Applied Polymer Science*, vol. 97, 2005, pp. 1995–2004.

[9] T.H. Lee, F.Y.C. Boey, and N.L. Loh, "Characterization of a fibre-reinforced PPS composite by dynamic mechanical analysis: Effect of aspect ratio and static stress," *Composites Science and Technology*, vol. 49, 1993, pp. 217–223.

[10] B. Brylka, M. Schemmann, J. Wood, and T. Böhlke, "DMA based characterization of stiffness reduction in long fiber reinforced polypropylene," *Polymer Testing*, vol. 66, 2018, pp. 296–302.

[11] *ASTM D790-10 Standard Test Methods for Flexural Properties of Unreinforced and Reinforced Plastics and Electrical Insulating Materials*, ASTM international, 2010.

[12] *ASTM D5023-15 Standard Test Method for Plastics: Dynamic Mechanical Properties: In Flexure (Three-Point Bending).*, ASTM International., 2015.

[13] *ASTM D7028-15: Glass Transition Temperature (DMA Tg) of Polymer Matrix Composites by Dynamic Mechanical Analysis (DMA)*, ASTM International, 2015.

[14] I.M. McAninch, G.R. Palmese, J.L. Lenhart, and J.J. La Scala, "DMA testing of epoxy resins: The importance of dimensions," *Polymer Engineering and science*, vol. 55, 2015, pp. 2761–2774.

[15] G. Swaminathan, K.N. Shivakumar, and L.C. Russell Jr, "Anomalies, influencing factors, and guidelines for DMA testing of fiber reinforced composites," *Polymer Composites*, vol. 30, 2009, pp. 962–969.

[16] TAInstruments, *Dynamic mechanical analyse*, TA Instruments, 2016.

[17] Mettler Toledo AG, "Dynamic Mechanical Analysis - Sets New Standards," 2014.

[18] PerkinElmer, *A Beginner's Guide: Dynamic Mechanical Analysis*, 2008.

[19] *ASTM D4065: Plastics: Dynamic Mechanical Properties: Determination and Report of Procedures*, ASTM International, 2012.
[20] TAInstruments, *DMA Online Help*, Waters LLC, 109 Lukens Drive, New Castle, DE 19720: .
[21] *DIN EN ISO 6721-1: Plastics - Determination of dynamic mechanical properties. Part 1: General principles*, ISO, 2011.
[22] A. Margossian; S. Bel; R. Hinterhoelzl, "Bending characterisation of a molten unidirectional carbon fibre reinforced thermoplastic composite using a Dynamic Mechanical Analysis system," *Composites: Part A*, vol. 77, 2015, pp. 154–163.
[23] *ASTM D5026: Standard Test Method for Plastics: Dynamic Mechanical Properties: In Tension*, ASTM International, 2015.
[24] *PerkinElmer DMA 8000*, PerkinElmer, 2013.
[25] Q. Shao and P. Lee-Sullivan, "Guidelines for performing storage modulus measurements using the TA Instruments DMA 2980 three-point bend mode - II. Contact stresses and machine compliance," *Polymer Testing*, vol. 19, 2000, pp. 239–250.
[26] P. Zhang and T. Kraus, "Anisotropic nanoparticles as templates for the crystalline structure of an injection-molded isotactic polypropylene/TiO2 nanocomposite," *Polymer*, vol. 130, 2017, pp. 161–169.
[27] *Technical data sheet: Veradel A-301 polyethersulfone*, Solvay Specialty Polymers, 2014.
[28] Solvay, "Radel® PPSU, Veradel® PESU & Acudel® modified PPSU: Design Guide, Version 6," 2014.
[29] J. Caprano, *Technoform Heat transfer solutions*, Technoform Kunststoffprofile GmbH, 2019.
[30] *TA Instruments, "2980 DMA Stress-Strain Equations*, 2002.
[31] *Vic-3D manual*, Columbia, SC: CorrelatedSolutions, 2010.
[32] *Abaqus User Documentation*, RI, USA: Dassault Systems Simulia Corp, 2017.
[33] E. Verdonck, *Dynamic mechanical analysis*, TA instruments, 2018.
[34] T. Instruments, *2980 DMA Stress-Strain Equations*, 2000.
[35] T. Instruments, *DMA Modulus Equations*.
[36] D. Wowk and C. Marsden, "The effects of test set-up on the apparent flexural modulus of thin angle-ply laminates using standard four-point bend testing," *Materials Characterisation*, 2018, p. 101.

Chapter 6

Long-term predictions from small coupon tests

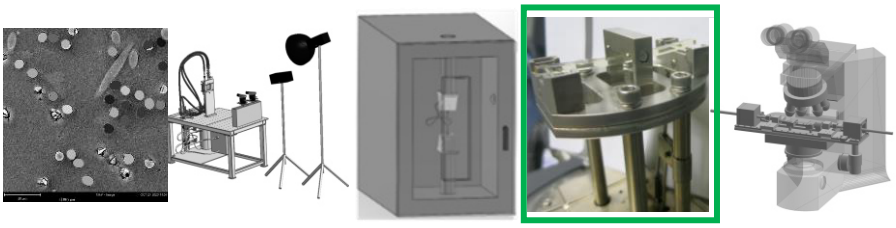

Small coupon scale

Abstract: Based on reliable test results, achieved with dynamic mechanical analysis (DMA), long-term predictions can be made. To make predictions, a method called stepped isothermal method (SIM) can be used. Therefore, the same test is repeated at different temperatures and the results post-processed. Two different tests methods are available to obtain SIM data: (i) static creep tests and (ii) dynamic frequency sweeps. In this chapter, both methods are compared. It was found, that for predictions up to a decade the methods are interchangeable and the predictions reproducible. Thereby, care needs to be taken in the reproducibility of the experimental raw data and the TTSP optimization using shift factors. This study is published as "Long-term stiffness prediction of particle filled polymers by dynamic mechanical analysis: frequency sweep versus creep method" [1].

6.1 Introduction to stepped isothermal method (SIM) testing

In this chapter, the procedure for accurate, repeatable DMA testing is used to make long-term predictions for graphite filled polypropylene used for heat exchanger applications. As the expected lifetime of a heat exchanger is 20 years, during which they are prone to failure by creep, test time needs to be accelerated. The extrapolating Time-Temperature-Superposition principle can be used [2]. Based on the theory of Boltzmann, time and temperature have comparable effects on the material behaviour in the visco-elastic region. Instead of long testing times, a range of temperatures can be used to simulate the accelerated test. A master curve can be fitted and will predict, depending on the chosen method for the raw data, either stress or strain in an extended range of time. This method is especially useful for polymers and polymer-based composites where temperature has a strong effect on the deformation-rate.

TTSP data can be obtained using a Dynamic (Thermo-) Mechanical Analysis (DMA) instrument, which is equipped with an accurate thermal chamber. The thermal stability of the setup is of high importance for the accuracy of the TTSP [3]. Limitations of the method depend on the type of material and the chosen temperature range. Visco-elastic, non-crystalline materials are typically rheologically simple, they show a strong temperature dependence, and are therefore well suited for the superposition principle [4]. Predictions of other materials are considered valid as well if the variation of shift factors versus temperature is linear [5]. This has been confirmed amongst others for pure PP [5] and reinforced samples [6,7] by comparing master curves from stepped isothermal method (SIM) (one sample tested at all temperatures) to real time creep data [5,8].

Because the master curve is generated by overlaying and shifting curves obtained at different temperatures, great care needs to be taken in the testing procedure as each error will be amplified throughout the TTSP [9]. The accuracy of the shifted data depends on two factors: (i) repeatability of the raw data and (ii) the reproducibility and accuracy of the shifting factors. The repeatability and accuracy of acquiring quantitative mechanical data using a DMA instrument has been described in the previous chapter. It was proven that several aspects including the choice of loading mode, appropriate fixture and especially the sample preparation can significantly improve the quality of the data. Uniform dimensions and flat, parallel edges have been manifested essential for repeatable results. The reproducibility and accuracy of the shifting factors in TTSP relies on manual or automatic shifting and overlaying of data from different temperatures to generate a master curve [9]. The introduced scatter due to the shifting process remains unclear. Although many studies exist [10], the factors

that contribute to scatter on TTSP results are not well documented. This is mainly due to the fact that the number of samples used to generate a master curve is often very small. According to ASTM D6992 one SIM-creep sample is sufficient, if the quantitative values are confirmed with two short term creep tests [11]. Nevertheless, this does not ensure the repeatability and accuracy of long-term predictions. In addition to uncertainty in the final result, there are two different methods to generate raw data for the master curve and their comparability remains unclear: (i) dynamic frequency sweep [12,13] and (ii) static creep test [5,14]. In a frequency sweep, a range of frequencies is chosen and applied as a cycle on the sample. The procedure is repeated at different temperatures. In the post-processing of the TTSP, the time-dependent material behaviour can be estimated from the frequency, which is the reciprocal of time. In a static creep test, the sample is loaded with one specific load and held constantly for a certain amount of time. Repetitions at different temperatures also allow the use of TTSP here.

To limit the uncertainty, the two different methods to generate a master curve were compared and their scatter was calculated. As basis for the two different methods, raw data was generated by creep tests or by frequency sweeps. Effects on the SIM data related to specimen preparation, measurement reproducibility, number of specimens and shifting method are investigated as well to ultimately conceive a better workflow for generating master curves through TTSP. Small samples are used as they require little material and allow for a faster heating time and temperature homogenisation compared to large-scale specimens, reducing the required testing time [14]. Furthermore, in contrast to other TTSP-studies on reinforced polypropylene [15], the filler content is significantly higher and the fillers smaller.

6.2 Material choice

Pure polypropylene (PP) has been successfully studied in TTSP by other authors [8,11,16]. The tested material here was a polypropylene with graphite filler, called PP-GF from company Technoform [17]. The composite tested had a graphite flake content of 75 wt% (50 vol%), enhancing the flexural modulus from about 1500 MPa for pure PP [18] to 6550 MPa with an elongation at break of 0.6% [17]. This material is used for heat exchanger applications in very aggressive environments, where (stainless) steel and other expensive alloys are not sufficiently resisting the corrosive agents in the fluids. Due to its relatively high thermal conductivity (14 W/mK) and its high strength it is a suited material for a heat exchanger (Table 2-3).

6.3 Specimen preparation for DMA testing

The used material is made for tubular heat exchangers and was therefore only available in tube form. For testing purposes, thin strips with dimensions (length x width x thickness) of (63.47 ± 1.2) mm x (7.53 ± 0.7) mm x (1.51 ± 0.1) mm were cut along the length of the tube, shown in Figure 6-1a. In chapter 5, the samples were used with the curvature to test the procedure on a complex shape. Here, the material was flattened before testing by applying a pressure of 5 bar at 160°C. A flat sample allows a homogeneous load distribution during testing. It was verified that the material had not changed physically in filler-matrix distribution with scanning electron microscopy (Phenom table-top XL SEM) (Figure 6-1b), nor that the crystallinity was affected (differential scanning calorimetry (DSC)), Figure 6-1c. The difference in melting enthalpy, 20.3 J/g for the curved sample and 21.8 J/g for the flat sample, was considered negligible. The microstructure of materials can change closer to the melting point, however, the mechanical analysis, even close to the melting point, did not show anomalies.

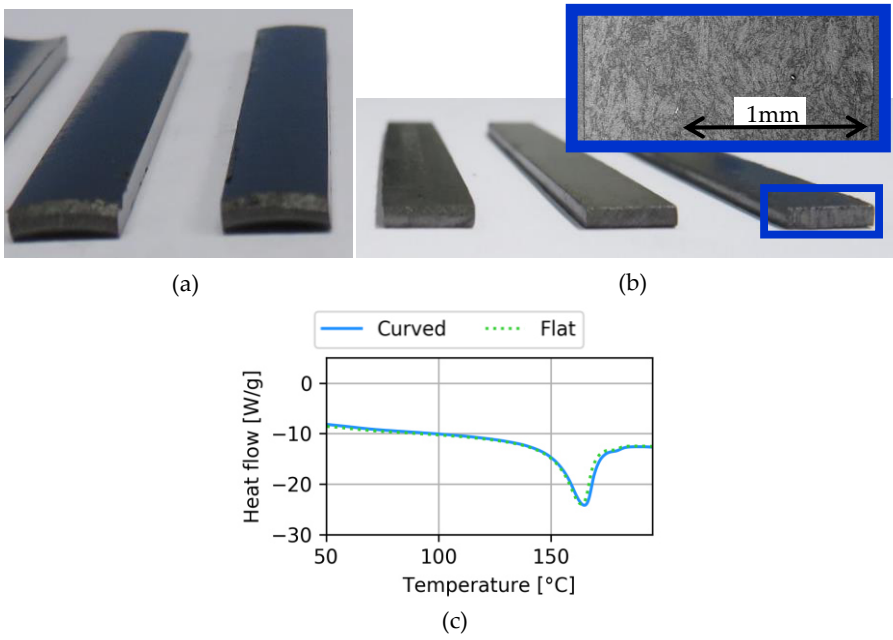

Figure 6-1: DMA samples of PP-GF (a) originally curved shape and (b) flattened samples with very straight, polished edges and close-up electron microscopic image SEM. (c) DSC curves of curved and flat samples show that the crystallinity (melting enthalpy) did not change due to flattening

6.4 DMA experiments and post-processing

The reference temperature for the master curve shifting is set at 45°C, since this is a common temperature for air to air heat exchangers [19] and falls in the range of thermal water treatments, a common application for the PP-GF. The range for the SIM procedure is between 35°C and 145°C. The lower bound is chosen to be well above the glass transition temperature (around -10°C), but below the reference temperature. The upper bound is limited by the melting point of the highly filled PP (+160°C). Preliminary shifting of individual curves showed a sufficient overlap at a step size of 10°C.

The used DMA was a Q800 from TA Instruments (18 N max. load, 20 mm max. displacement, 0.1°C temperature accuracy) with a 50 mm span 3-point bending clamp. For the comparative study, pre-tests were performed to derive the required parameters to perform SIM experiments based on creep (Cr-SIM) or frequency sweeps (FS-SIM).

6.4.1 Procedure for SIM creep test (Cr-SIM)

In the Cr-SIM measurements, the stress value is the only variable to choose. In general, the load level varies depending on the application. In TTSP, different authors apply between 6 and 40% of the ultimate stress (Table 6-1). The applied stress found in literature is typically chosen around 10% of the ultimate flexural stress.

Table 6-1: Applied stress levels for TTSP on different materials in literature

Material	Applied stress [MPa]	Ultimate stress [MPa]	Percentage [Applied/Ultimate]	Clamp	Setup
Epoxy-GL	40 [20]	350 [20]	11%	Bending	DMA
HDPE	2 [21]	25 [10]	8%	Bending	DMA
PA6	5 [22]	50 [23]	10%	Tension	Classic
PEEK	10 [24]	165 [25]	6%	Bending	DMA
PP	14 [10]	36 [10]	38%	Cantilever	DMA
PP-GL	-	-	10-60% [15]	Tension	Classic
PP-textile	-	-	20-30% [26]	Tension	Classic

In conventional 3-point bending tests at 23°C, the failure strength of PP-GF is at 41.1 MPa, measured with a strain rate of 1.6 $10^{-4}s^{-1}$ [17,27]. This matches with the order of magnitude (34.7 MPa) of the tests from the DMA machine, measured at the same

strain rate (1600 µm/min), but at 35°C. From the 3-point bending test, the load level for the creep tests of SIM (Cr-SIM) was chosen. The linear visco-elastic region (LVE) is between 0.015% and 0.03% strain, respectively 40 µm and 90 µm of displacement, which corresponds to 2.25 MPa and 4.50 MPa. These stress levels correspond to 6-15% of the ultimate stress and hence are in good agreement with the stress levels chosen by other authors (Table 6-1).

6.4.2 Procedure for SIM frequency sweep (FS-SIM)

The procedure used for frequency sweep testing (Figure 6-2) is based on chapter 5 [28]. An amplitude sweep is performed to locate the linear visco-elastic region. In a following frequency sweep based on the LVE boundaries, potential measurement resonances can be detected and these frequencies are excluded for further testing. The lower limit ensures that the experiments can be done in a reasonable timeframe, while the upper limit is determined by the eigenfrequency causing resonance of the specimen within the testing apparatus. Lastly, in a temperature sweep, any transition phases can be seen as in a classic thermal DMA study. After these pre-tests, all parameters are known for a successful frequency sweep SIM (FS-SIM).

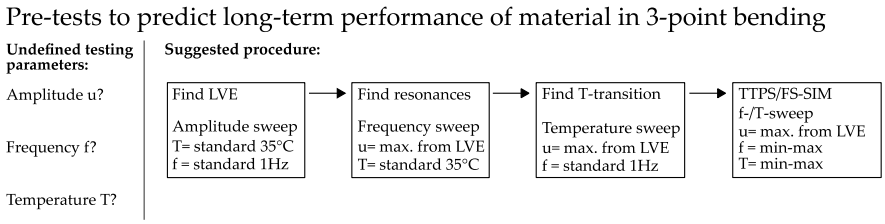

Figure 6-2: Schematic overview of the testing procedure for frequency based stepped isothermal method (FS-SIM) [28]

Following the example of Brown et al. [29], stress can be plotted over strain rate to prove the linear dependency. Therefore, 3-point bending tests at different strain rates were performed and plotted in Figure 6-3 (presenting the linear dependency in logarithmic scale). The same tests were repeated at higher temperature, verifying that FS-SIM will be also valid at elevated temperature. The strain rate dependency of this reinforced polypropylene is in good agreement with the strain rate dependency of neat PP. Filled and unfilled materials have a drop of about 10 MPa in ultimate strength per strain rate change of 10^{-2} s^{-1} [30,31].

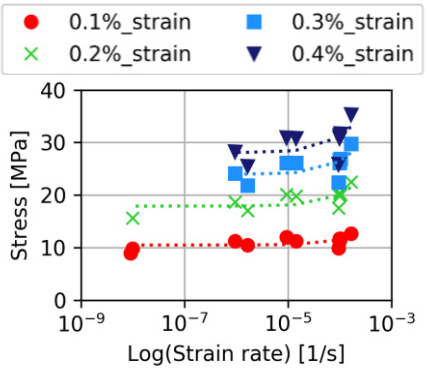

Figure 6-3: Linear (presented in logarithmic scale) strain rate dependency of PP-GF at different strains, tested in DMA 3-point bending, 35°C, dotted linear trendlines are added

6.4.3 Shifting of SIM curves

The resulting SIM-data are shifted horizontally to generate a master curve at the reference temperature (45°C). The shift factor a_T is used to shift and match curves of different temperatures [32]. In literature, many optimisation methods for the shift factors have been described. Examples are matching first derivatives, area minimisation between the curves, minimizing the arc-length of the master curve or minimizing the total sum of squares (TSS) [33]. The latter is an optimisation method that calculates the distance between the curves in the overlapping area and improves the shifting of the neighbouring curves by minimising the sum of squares of that distance. Very few studies have been performed on the actual influence on the resulting curves caused by different shift factors, but agreed on the consistency of this type of optimisation [34]. Manual shifting will be compared to the TSS to evaluate the influence of a shift factor optimisation.

6.5 Results and discussion on SIM tests in DMA

6.5.1 Results of Cr-SIM

The Cr-SIM was performed at a stress level of 2.25 MPa. In between the temperature steps, a heating phase and an isothermal step take place, ensuring a stable temperature distribution inside the sample. This phase takes in total up to 7 min. During this phase, the sample is only loaded with a small force ensuring contact, not with the creep load, allowing a re-loading to compensate for thermal expansion. In addition, thermal expansion is limited to the thickness direction in 3-point bending and the material has a low expansion coefficient ($2.2*10^{-5}$ 1/K).

The creep compliance J [mm^2/N] can be transferred into strain ε [-] according to Equation (6-1) by multiplying it with the stress σ [MPa] or by using the displacement a [mm], the thickness d [mm] and the span length L [mm].

$$\varepsilon(t) = J(t)\,\sigma = \frac{6\,a(t)\,d}{L^2} \tag{6-1}$$

This allows for a long-term prediction of strain over time, given in Figure 6-4. The typical primary and secondary creep phases can be seen in the predicted curve. The creep (strain) rate is high in the beginning of the prediction and becomes constant during the second creep phase. The third creep failure phase cannot be observed here.

The reproducibility was tested by repeating the same test on three different samples, resulting within 20 years to a scatter around the average of ±5.7%. At higher stress levels, the strain is proportionally higher. The creep strain predicted at 1 year increases by 5.5 percentage points for 2.25 MPa versus 4.25 MPa for the graphite-filled PP. This is significantly lower than unreinforced matrix material with an increase of 17.5%, when the stress is increased by 2 MPa [35]. As expected, pure polypropylene is more affected by an increase in stress than this highly graphite filled PP.

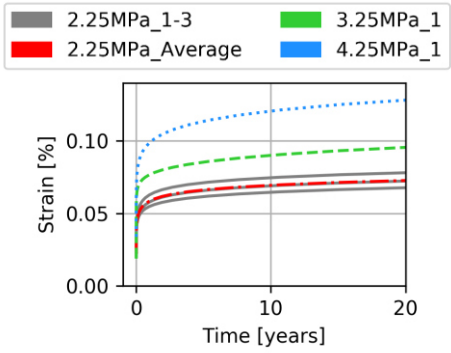

Figure 6-4: Repeatability of three Cr-SIM curves on different samples and two curves at higher stress levels with reference temperature 45°C

The duration of the isothermal step at each temperature differs in literature. For this chapter, experiments of 3 h as recommended for classic tensile benches by ASTM D6992-03 [11] were performed. In post-processing the time was shortened, to see the effect on the master curve (Figure 6-5). It was found that a reduction down to 15 min [14] dwell time delivered comparable master curves with a very good overlap for the first five years and a divergence after 20 years of 4%. The saved time could be used for repetitions of tests to measure the inherent material uncertainty. However, shorter dwell times of for example 2 min are not reliable anymore.

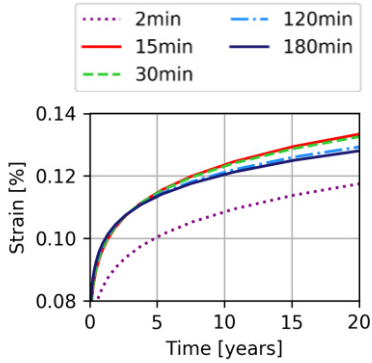

Figure 6-5: Long-term predictions based on individual isothermal creep tests at 45°C, 4.25 MPa. For testing times above 15min, the overlap is good within a time span of 20 years

To verify the results, a creep test of 2.5 days (real-time) is performed and the data is extrapolated to longer test times using a curve fit with exponential and logarithmic part (Equation (6-2)). Real–time and extrapolation agree very well with data obtained from TTSP (Figure 6-6). There is a small difference between both predictions at long-term, but this is negligible considering the scatter on the results measured on different samples. The strain ε [-] is time t dependent; A, B, C and D are unit free variables [-].

$$\varepsilon(t) = A\, e^{(Bt)} + C\, log(t) + D \tag{6-2}$$

In 10 years, the stiffness decreases by a factor 4. In comparison pure PP reduces its stiffness by factor 7.5 [5] whereas glass fibre reinforced PP shows a decrease by factor 3.5 over 10 years [14]. The reinforcement with graphite flakes thus increases the creep resistance compared to pure PP material and results in a similar creep resistance as glass fibre reinforced PP.

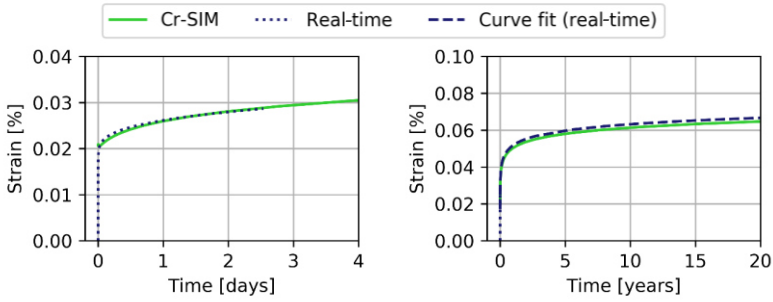

Figure 6-6: Static creep test at 35°C over 2.5 days as reference (dotted) against predicted test for 20 years (solid) and curve fit (dashed) based on real test data

6.5.2 Results of FS-SIM

The isothermal amplitude sweeps show the LVE to be between 0.002% (5 μm) and 0.02% (60 μm). The highest amplitude was chosen for further tests, since the previous chapter showed an improved reproducibility with higher amplitudes [28]. The frequency was varied between 0.01 Hz and 30 Hz and isothermal frequency sweep curves were performed. By shifting in the frequency domain, following Equation (6-3), a master curve can be generated. The shifted frequency $f_{shifted}$ [Hz] is calculated from the raw data f_{raw} [Hz] and the shifting factor a_T [-].

$$f_{shifted} = f_{raw} + a_T \tag{6-3}$$

Figure 6-7a shows the original raw data of the stress versus the linear frequency. Stress was chosen as y-component for the comparison of the different SIM methods. However, the method is equally applicable to commonly used storage or loss modulus. The optimised shift factors (Figure 6-7b) closely followed the ideal case, namely linearly increasing with temperature. In this case, using the actual shift factors or those obtained by a linear fit did not result in a different master curve (Figure 6-7c), further proving that the TTSP is applicable here. By applying a fitting Taylor function, the individual curves at different temperatures can be combined to a smooth master curve.

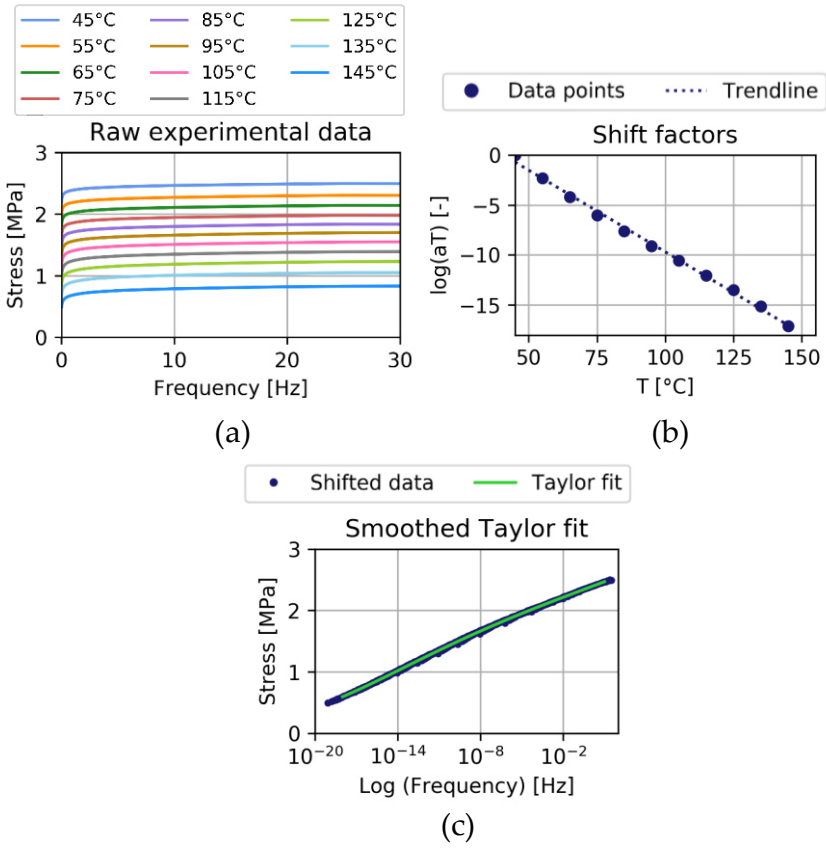

Figure 6-7: FS-SIM from raw data to master curve; (a) raw data at different temperatures, (b) optimised shift factors with TSS, (c) Taylor fit of shifted temperature curves

The master curve can be plotted as stress over time when constant strain is applied [12,13]. The stress σ [MPa] is calculated from the storage modulus E' [MPa], the strain ε [%], the phase shift δ [-], the force F [N], as well as the sample dimensions [mm] (span length L, width w, thickness d) as illustrated in Equation(6-4):

$$\sigma(t) = \frac{E'(t)\varepsilon}{\cos(\delta(t))} = \frac{3F(t)L}{2wd^2} \tag{6-4}$$

The frequency $f_{shifted}$ [Hz] can be transferred into time domain t [s] with Equation(6-5):

$$t = \frac{1}{f_{shifted}} \tag{6-5}$$

FS-SIM was performed four times on different samples to assess the repeatability. As can be seen in Figure 6-8, the curves overlap very well, which states an excellent

reproducibility for these results. For a prediction of 20 years, the expected stress for an applied strain of 0.014% lays between 1.57 MPa and 1.74 MPa for the four repetitions. This results in a standard deviation of 0.06 MPa, which corresponds to a divergence on the average stress of maximal ±3.4%. Furthermore, Figure 6-8 also shows two samples tested at strains slightly above the linear visco-elastic region. The shift factors remain linear and the resulting curves have the same shape as the ones obtained within the LVE region, thus potentially the shifting is also valid outside of LVE. Due to the higher strain a higher stress was obviously observed.

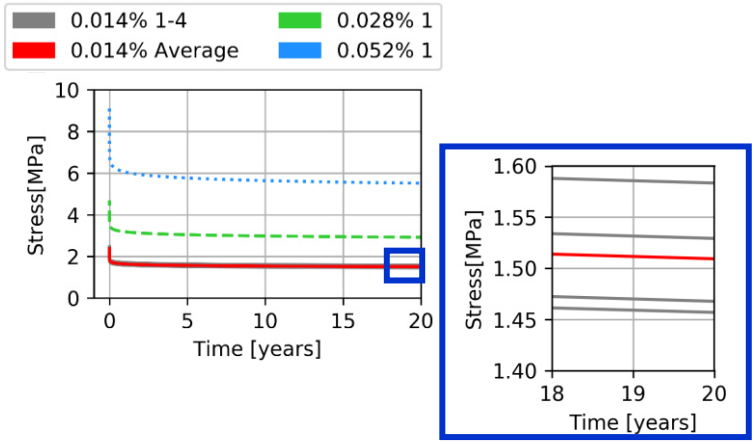

Figure 6-8: Repeatability of FS-SIM, tests with the same parameters on four different samples and two tests at higher strain levels, Tref=45°C

6.5.3 Effect of shift factor optimisation

One aim of this study is to assess how sensitive the long-term predictions are to variations in the shift factor and to scatter of the experimental data. For this purpose, optimal shift factors were determined by using the total sum of squares method. In addition, a worst case scenario of shifting inaccuracy was established for one data set of Cr-SIM.

For the worst-case scenario, the shift factors were determined by artificially increasing them as to simulate a non-optimised, subjective shifting error. The magnitude of subjective shifting is difficult to quantify, because it depends on the operator and the software used. When manually determining shift factors, it is possible to obtain results that are on par with optimisation methods. However, this requires a large number of iterations where for each pair of curves, the data is plotted and the shift factor adjusted. Consequently, it is likely that the shift factors are only coarsely estimated, which could introduce a significant error. This would for example be the case when the curves are

shifted on a scale where all curves are visible. To determine the effect of non-optimised shifting, random values of +10% and +20% were chosen to add to the calculated optimised shifting factors. The boundaries should serve for a rough determination of the worst possible, but realistic scenario.

Figure 6-9a-c display the overview of shifted curves over the time frame of 20 years for the case of optimised shift factors, +10% and +20% respectively. On this scale, the difference between optimised curves and +10% artificially introduced shifting error seems acceptable, while the case with +20% error clearly results in a bad overlap. When only one temperature transition between the reference curve T1 and the first shifted curve T2 is in focus (Figure 6-9d), the optimised shift factors lead to a nice overlap between T1 and T2. With an increase in shift factor of +10%, the shifted curve T2 moves further away from the reference curve T1 and the resulting match appears to be poor. The +20% increased shift factor, leads to a shift that is not matching. In Figure 6-9e, the impact of these shift factors is shown on the master curve predicting 20 years. The increase of shift factor of +10% leads to a variation of 7.4% strain and for the +20% shift factor to 13.3%. This shows that the master curve is not that sensitive to variations in the shift factor. However, every improvement of the shifting factor will lead to a smaller scatter on the master curve. From the study in chapter 5, it is known that experimental results can scatter up to 18%, if the tests are not executed carefully [28]. Subjective shifting errors or the ones from different optimisation methods are likely to be lower than +10% [34]. Therewith, the scatter of the experimental data is the main source of uncertainty.

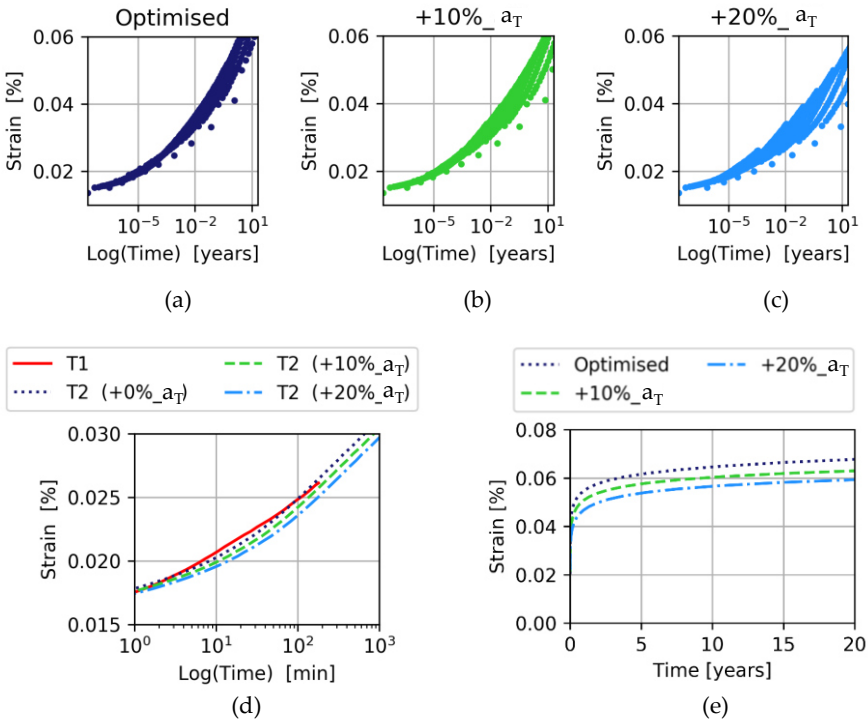

Figure 6-9: Curve shifting optimised with the total sum of squares and variations on the shift factors a_T of +10% and +20%: (a-c) shifted raw data at a scale of 20 years with different shift factors, (d) focus on only two curves at a time, here the first TTSP-shift between T1=45°C and T2=55°C (e) the resulting master curves for 20 years prediction based on different shift factors

The same Cr-SIM experiment was carefully repeated three times on different samples, resulting in a low experimental scatter. With optimised shifting on these data sets, the shift factors differ 3.3% from each other and the impact on the strain prediction at 20 years is ±5.7%.The biggest difference between two curves was 11.7%. These highest and lowest curves were taken and the shift factors were manually changed by 10%, creating the biggest possible divergence between those two datasets (Figure 6-10). The combination of high variation in shift factors caused by the scatter in experimental data and the deliberately inserted shifting error results in a deviation on the strain after 20 years of ±16.2%. The combination of experimental and shifting scatter results in a very significant deviation of the master curve. Both scatters need to be kept low for reproducible results.

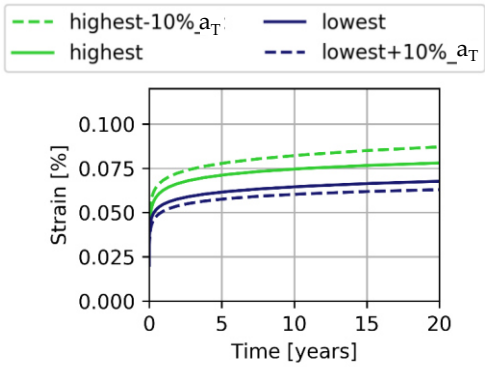

Figure 6-10: Same experiment on different samples. Optimised shift factor a_T varied by 10% to create worst-case scenario of manual shifting

6.5.4 Comparison Cr-SIM and FS-SIM

To compare the results of creep and frequency sweep SIM curves, both results need to be brought into the same domain, namely stress over strain at a given point in time. To be able to compare the values, the changing variables in both methods were zeroed (delta). Therefore, from the Cr-SIM values, the initial strain was subtracted and from the FS-SIM the initial stress. The result will be called delta strain or delta stress. The same technique was successfully used by J. Ahlström to compare stress versus strain controlled loading [36]. It is valid under the assumption that the secondary creep stage is linear. The delta of stress, respectively strain, describes the change in value between initial value and time dependent one. The principle is clarified in Figure 6-11.

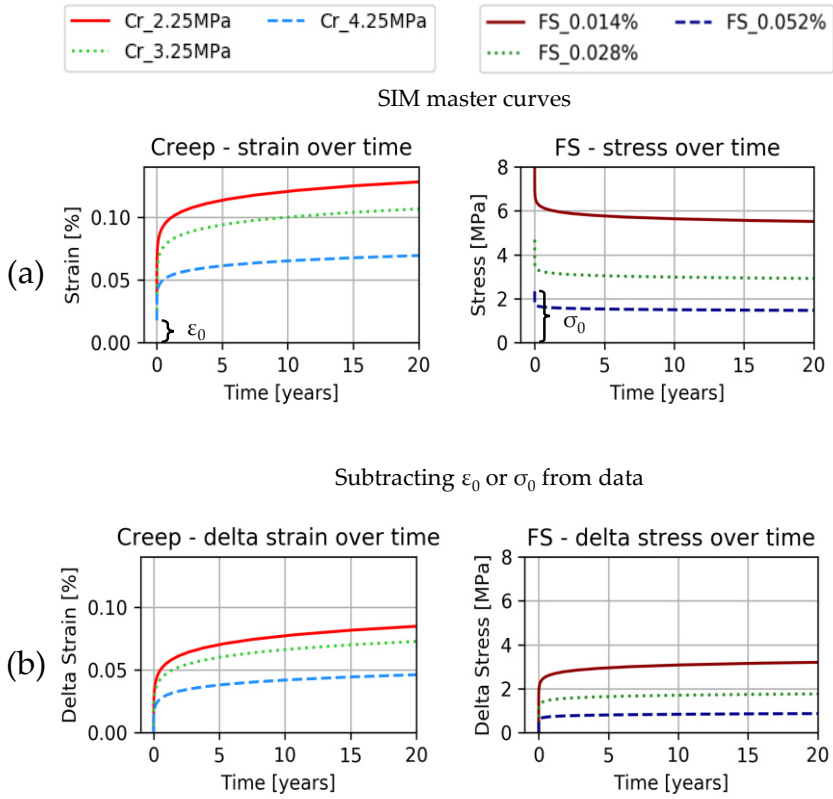

Figure 6-11: Principle to compare predicted data from creep and frequency sweep: (a) shifted data plotted over time, (b) absolute delta strain respectively stress data over time

Figure 6-12 compares data at the start of the test (0 years) and after 10 and 20 years. Also 40 years was included to extend the prediction beyond what is needed for the case study of a heat exchanger. The initial values (Figure 6-12a) are overlapping well, showing that without the factor of time, there is no difference between load or displacement control. If a certain strain is imposed, this will result in a corresponding stress and if this stress is imposed, the corresponding strain will be the same as in the displacement controlled test. Also for shorter predictions, for example 10 years as in Figure 6-12b, the methods are very comparable and deliver a similar slope with a difference of less than 10%. For longer periods (20 years or 40 years), the predictions differ more. Frequency sweep data appears to be conservative in stress prediction, whereas creep data is more conservative in strain. This can be explained by the generation process of the raw data. In the course of time, the creep-based curves are shifting almost double as much with time as frequency based curves, because load controlled tests can lead to failure, whereas displacement controlled tests are

stabilising. This study showed, for the period of one decade, Cr-SIM and FS-SIM are interchangeable. For longer predictions, the results differ more and the testing method that correlates to the application should be chosen. To some extent, the long-term tests can be compared to the quasi-static tests, showing an expectable lower slope. The derived linear curves allow to predict strain for a chosen stress level and vice versa.

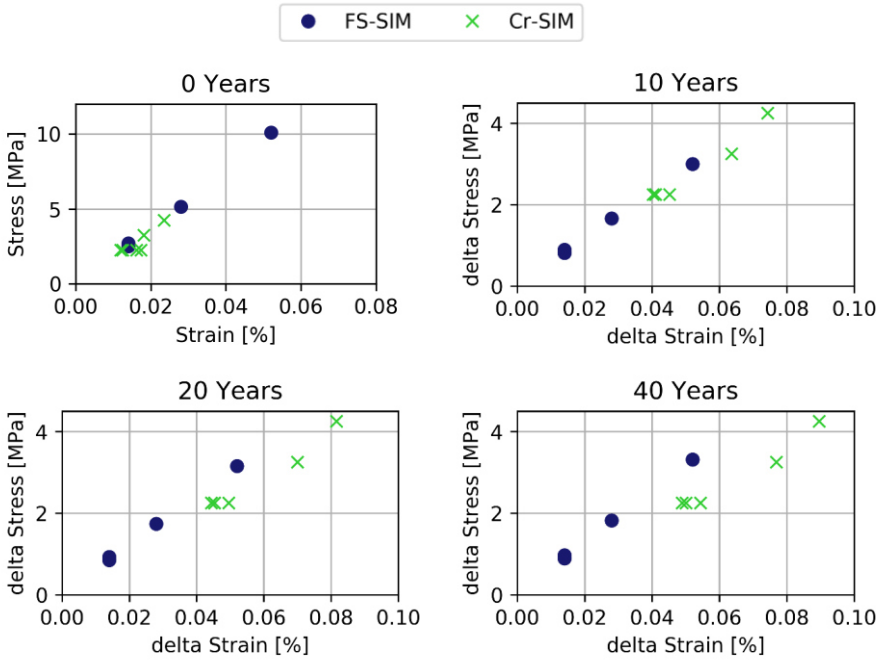

Figure 6-12: Stress over strain at different predicted points in time (0, 10, 20 and 40 years). Values from Cr-SIM and FS-SIM in comparison

The difference in testing time required to make these predictions, is significant. To reach an estimation of 20 years for the material in service, the temperature range needs to be bigger for Cr-SIM (35-105°C) than for FS-SIM (35-75°C). However, to be able to shift curves to a master curve, the curves at different temperatures need to overlap. A temperature step of 10°C was chosen. In a frequency sweep, the curves overlap well if each test covers the range of 0.01-30 Hz, requiring a testing time of 108 min per temperature, which results to 9.6 h for the full FS-SIM dataset. For Cr-SIM, it was found that a reduction to 15 min dwell time per temperature step was giving reliable results, adding up to a total time of 2.9 h, a third of the frequency sweep tests.

6.6 Conclusions of long-term DMA tests

In this study, the long-term performance of graphite-reinforced polypropylene was estimated, using stepped isothermal method (SIM). The DMA 3-point bending clamp

was used to perform quasi-static bending tests on the same machine, providing a suited alternative to traditional test benches to identify the linear visco-elastic region of the tested material. SIM curves were generated in creep (Cr-SIM) and frequency sweeps (FS-SIM) and shifted according to Time-Temperature-Superposition principle (TTSP). Both methods result in comparable mid long-term estimates for stress, respectively strain, which means, the methods are exchangeable for the prediction of up to 10 years. For longer predictions, the application of the material becomes relevant, because long-term effects are dependent on the type of loading.

The total testing time for a prediction via FS-SIM is about 10 h, whereas the prediction for 20 years via Cr-SIM only takes about 3 h. As such, creep is the faster method to generate a data set.

The accuracy of the shifting for long-term prediction has been studied as well. It shows that with an optimisation of the shift factor, scatter on the strain prediction after 20 years can be kept well below ±10%. If an optimisation method or careful manually shifting is used, the scatter on the long-term prediction depends partially on the accuracy of the shifting, but mainly on the repeatability of the raw data. Therefore, close attention needs to be paid while producing the raw data for long-term prediction. Here, the maximum scatter on the unshifted raw data is half as much for the frequency sweep, compared to the creep tests (on average ±2.5% in contrast to ±4.8%). The master curves from FS-SIM have a scatter of ±3.4%, while the ones from Cr-SIM vary by ±5.7%.

In conclusion, creep and frequency based tests in DMA deliver comparable mid-term prediction, whereby creep delivers the result in shorter time, but frequency sweep results in higher accuracy. For longer predictions, the load or displacement control needs to be chosen dependent on the actual application of the testing material. An optimisation method for the shifting should be used to minimize the uncertainty of the predicted curves to the experimental scatter mainly.

References

[1] J. Schalnat, L. Daelemans, I. De Baere, K. De Clerck, and W. Van Paepegem, "Long-term stiffness prediction of particle filled polymers by dynamic mechanical analysis: Frequency sweep versus creep method," *Polymer Testing*, 2021, p. 107368.

[2] L. Boltzmann, "Zur Theorie der elastischen Nachwirkung," *Annalen der Physik*, vol. 241, 1878, pp. 430–432.

[3] W. Knauss, "The sensitivity of the time-temperature shift process to thermal variations—A note," *Mechanics of Time-Dependent Materials*, vol. 12, 2008, pp. 179–188.

[4] M. Herdy, "Introductory Theory Manual ViscoData and ViscoShift," 2003.

[5] F. Achereiner, K. Engelsing, M. Bastian, and P. Heidemeyer, "Accelerated creep testing of polymers using the stepped isothermal method," *Polymer Testing*, vol. 32, 2013, pp. 447–454.

[6] T. Jones, W. Doggett, C. Stanfield, and O. Valverde, "Accelerated creep testing of high strength aramid webbing," *53rd AIAA/ASME/ASCE/AHS/ASC Structures, Structural Dynamics and Materials Conference 20th AIAA/ASME/AHS Adaptive Structures Conference 14th AIAA*, 2012, p. 1771.

[7] K. Alwis and C. Burgoyne, "Stepped Isothermal Method for CreepRupture Studies of Aramid Fibres," *Special Publication*, vol. 230, 2005, pp. 181–194.

[8] W. Grellmann and B. Langer, *Deformation and fracture behaviour of polymer materials*, Springer, 2017.

[9] K.G.N.C. Alwis and C.J. Burgoyne, "Time-Temperature Superposition to Determine the Stress-Rupture of Aramid Fibres," *Applied Composite Materials*, vol. 13, Jun. 2006, pp. 249–264.

[10] V.S. Chevali, "Flexural creep of long fiber thermoplastic composites: effect of constituents and variables on viscoelasticity," The university of Alabama at Birmingham, 2009.

[11] *ASTMD6992-03: Accelerated Tensile Creep and Creep-Rupture of Geosynthetic Materials Based on Time-Temperature Superposition Using the Stepped Isothermal Method*, ASTM International, 2015.

[12] S.E. Zeltmann, K.A. Prakash, M. Doddamani, and N. Gupta, "Prediction of modulus at various strain rates from dynamic mechanical analysis data for polymer matrix composites," *Composites Part B: Engineering*, vol. 120, 2017, pp. 27–34.

[13] Z. Jia, A.V. Amirkhizi, W. Nantasetphong, and S. Nemat-Nasser, "Experimentally-based relaxation modulus of polyurea and its composites," *Mechanics of time-dependent materials*, vol. 20, 2016, pp. 155–174.

[14] J. Jansen, "Failure analysis of plastic parts using DMA analysis," Webinar by Netzsch, 2020.

[15] P. Bakonyi and L.M. Vas, "Analysis of the creep behavior of polypropylene and glass fiber reinforced polypropylene composites," *Materials Science Forum*, Trans Tech Publ, 2013, pp. 302–307.

[16] A. Drozdov, "Creep rupture and viscoelastoplasticity of polypropylene," *Engineering Fracture Mechanics*, vol. 77, 2010, pp. 2277–2293.

[17] J. Caprano, *Technoform Heat transfer solutions*, Technoform Kunststoffprofile GmbH, 2019.

[18] "Material property data, http://www.matweb.com/reference/flexuralstrength.aspx," 2020.

[19] Toshiba, "Air to air heat exchangers," 2017.

[20] S.K. Ghosh, P. Rajesh, B. Srikavya, D.K. Rathore, R.K. Prusty, and B.C. Ray, "Creep behaviour prediction of multi-layer graphene embedded glass fiber/epoxy composites using time-temperature superposition principle," *Composites Part A: Applied Science and Manufacturing*, vol. 107, 2018, pp. 507–518.

[21] M. Tajvidi, R.H. Falk, and J.C. Hermanson, "Time–temperature superposition principle applied to a kenaf-fiber/high-density polyethylene composite," *Journal of Applied Polymer Science*, vol. 97, 2005, pp. 1995–2004.

[22] M. Hadid, B. Guerira, M. Bahri, and A. Zouani, "Assessment of the stepped isostress method in the prediction of long term creep of thermoplastics," *Polymer testing*, vol. 34, 2014, pp. 113–119.

[23] "Data sheet PA6, http://matweb.com/search/DataSheet.aspx?MatGUID=8d78f3cfcb6f49d595896ce6ce6a2ef1&ckck=1," 2021.

[24] A. Fairhurst, M. Thommen, and C. Rytka, "Comparison of short and long term creep testing in high performance polymers," *Polymer Testing*, vol. 78, 2019, p. 105979.

[25] "Data sheet PEEK, http://polymerdatabase.com/Commercial%20Polymers/PEEK.html," 2021.

[26] J.G. Zornberg, B.R. Byler, and J.W. Knudsen, "Creep of geotextiles using time–temperature superposition methods," *Journal of geotechnical and geoenvironmental engineering*, vol. 130, 2004, pp. 1158–1168.

[27] *ISO 178 Plastics — Determination of flexural properties*, International Organization for Standardization, 2019.

[28] J. Schalnat, D.G. Gómez, L. Daelemans, I. De Baere, K. De Clerck, and W. Van Paepegem, "Influencing parameters on measurement accuracy in dynamic mechanical analysis of thermoplastic polymers and their composites," *Polymer Testing*, vol. 91, 2020, p. 106799.

[29] E. Brown, R. Willms, G. Gray, P. Rae, C. Cady, K. Vecchio, J. Flowers, and M. Martinez, "Influence of molecular conformation on the constitutive response of polyethylene: a comparison of HDPE, UHMWPE, and PEX," *Experimental mechanics*, vol. 47, 2007, pp. 381–393.

[30] M.M. Shokrieh, V.A. Joneidi, and R. Mosalmani, "Characterization and simulation of tensile behavior of graphene/polypropylene nanocomposites using a novel strain-rate-dependent micromechanics model," *Journal of Thermoplastic Composite Materials*, vol. 28, 2015, pp. 818–834.

[31] P. Reis, L. Gorbatikh, J. Ivens, and S. Lomov, "Strain-rate sensitivity and stress relaxation of hybrid self-reinforced polypropylene composites under bending loads," *Composite Structures*, vol. 209, 2019, pp. 802–810.

[32] S. Naya, A. Meneses, J. Tarrıo-Saavedra, R. Artiaga, J. López-Beceiro, and C. Gracia-Fernández, "New method for estimating shift factors in time–temperature superposition models," *Journal of thermal analysis and calorimetry*, vol. 113, 2013, pp. 453–460.

[33] A. Maiti, "A geometry-based approach to determining time-temperature superposition shifts in aging experiments," *Rheologica Acta*, vol. 55, 2016, pp. 83–90.

[34] N.I.M. Yusoff, E. Chailleux, and G.D. Airey, "A comparative study of the influence of shift factor equations on master curve construction," *International Journal of Pavement Research and Technology*, vol. 4, 2011, p. 324.

[35] R.W. Thomas and J.A. Nelson, "The Stepped Isothermal Method for Estimating the Long-Term Creep Strain and Creep Rupture Strength of Polypropylene," *Proceedings of the 2013 Society of Plastics Engineers (SPE)International Polyolefins Conference, Houston, TX, USA*, 2013.

[36] J. Ahlström and B. Karlsson, "Fatigue behaviour of rail steel—a comparison between strain and stress controlled loading," *Wear*, vol. 258, 2005, pp. 1187–1193.

Chapter 7

Interface study on debonding of a single fibre from the polymer matrix

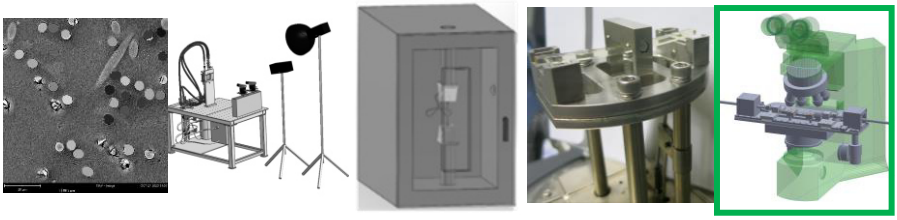

Interface scale

Abstract: Mechanical failure of composite materials does not only occur on a macroscopic level, but also on a microscopic level. The main failure mechanism there is the debonding between matrix and fibres. However, the debonding mechanism is not well explored yet in literature. Especially the combination of short fibres in thermoplastic matrix is hardly assessed. Based on existing experimental approaches described in literature, a test method was developed and the equipment, a small-scale tensile stage that can be used under a microscope, was designed. Preliminary experimental results on fully embedded short fibres were obtained and can form the basis for future experiments.

7.1 Introduction to the study of debonding

As discussed in the previous chapters on macro-scale, properties such as the shape of the material, the filler content and the fibre orientation play major roles for the strength of the compound. Predictions of the long-term performance in creep load considering the structure and macro-scale of the compound were made. However, weakening of the composite over time does not only occur on macro-scale, but initiates often from micro-scale in form of debonding between fibres and matrix.

In general, the load transfer between reinforcing fibres and the polymer matrix has an important effect on the strength of the polymer. For example, very good adhesion allows large tensile forces to be transferred, resulting in a stronger material. Load is transferred from the matrix to the fibre [1]. Therefore, (i) adhesion between fibre and matrix, (ii) the friction due to surface roughness of the fibre and (iii) the pressure due to shrinkage strain during manufacturing are key parameters [2] and influence the overall strength of the composite [3]. To understand the load transfer mechanism, an isolated fibre has been studied in different ways in literature with sample shapes similar to the schematic in Figure 7-1. From these studies, some aspects of the debonding mechanism under tension are known:

- Debonding starts at the fibre ends and grows inwards [2,4,5]
    - For perpendicular loaded fibre ends located at the edge of samples, it was assessed that the shear stress is the highest at the fibre tip [6], due to the difference in stiffness between fibre and matrix [7]
- The interface between matrix and fibre is defined by more than just adhesion
    - If the interface is broken and tensile load applied longitudinal to the fibre, there is a relative displacement between matrix and fibre. Friction due to surface roughness can still transfer load from the matrix to the fibre [5]
- Increasing longitudinal load on fibres in matrix leads to fibre fragmentation
    - The fibre breaks initially in random sizes [6]. A saturation level of a steady filament length can be reached and is called critical length [2]
    - Each fibre break leads to immediate, not progressing local debonding [6]

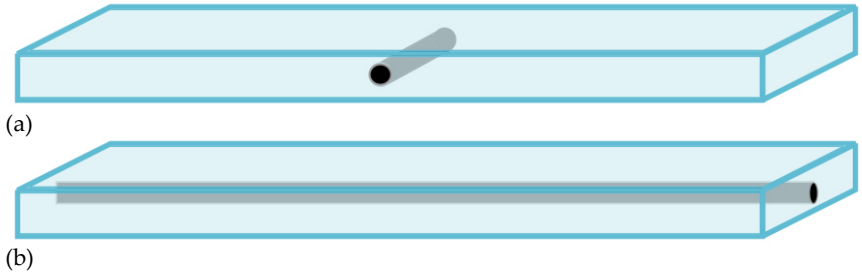

Figure 7-1: Typical single fibre samples with exposed fibre ends: (a) perpendicular to loading direction and (b) longitudinal fibre

To study these influences, samples with a single fibre were produced. Most of these studies were performed on glass-fibre/epoxy [8] or carbon-fibre/epoxy [9]. Epoxy has the advantages of being transparent (for optical observation), limited shrinkage (limited stresses around the fibre), stiff behaviour and good adhesion with many fillers [6]. Few studies [10,11] have been performed on thermoplastic resin, which makes the existing material model validation poor. The fibre geometry is typically one long fibre of several centimetres reaching over the full specimen length [6,7,12,13]. Consequently, the fibre ends are exposed. Already in the 1990s, it was noted that shorter, fully embedded fibres would be favoured over an end-to-end fibre [13] to study the debonding inside the matrix. In addition, it was criticized that one single fibre without the influence of neighbouring fibres is not representative [4]. Since then, the debonding mechanisms on individual fibres remained relatively unstudied, especially on short fibres fully embedded in thermoplastic matrix under load. This limits the accuracy of the material models used in the previous chapters. For quantitative measurements on debonding, numerical analysis of the stress is required, since experimental instrumentation reaches its limits. Therefore, the experiment needs to have simple boundary conditions. Furthermore, experiments entail to be broadly accessible to generate a big data set. Hence, measurements performed in a synchrotron deliver good results, but the amount of available data is limited by the availability and cost of such an experiment. In other words, there is a demand for experimental analysis of the debonding of short fibres in thermoplastics at accessible lab-scale. Those experiments could lead to a better understanding of the micro-scale failure mechanism between fibre and polymer matrix, which would improve the accuracy of micromechanical modelling and thereby the prediction of long-term behaviour of composites.

This chapter discusses a preliminary study intended to set directions for future debonding experiments. The goal is to visualise the debonding around a fully embedded fibre under tensile load. Therefore, a suited observation method is chosen, the device to apply tensile force designed and the adequate sample manufactured. New aspects of the research are:

- Development of a test set-up
- Fibre in thermoplastic matrix instead of epoxy
- Carbon fibre with small diameter (compared to for example glass fibres)
- Fully embedded fibre instead of exposed fibre ends
- Fibre orientation longitudinal and perpendicular to load direction
- In situ observation during the mechanical loading instead of ex situ
- Comparison of single fibre and multiple embedded fibres

7.2 Test methods to study debonding

Debonding is typically quantified with the tests listed in Figure 7-2. In the following, the methods will be shortly summarised and their advantages and disadvantages discussed.

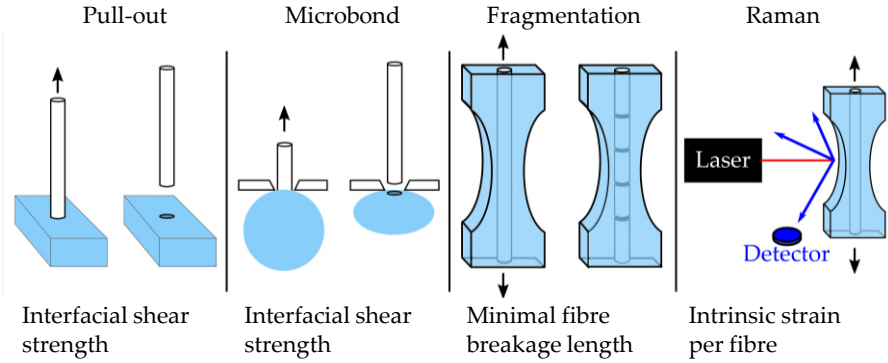

Figure 7-2: Classic single fibre debonding tests in tension

7.2.1 Pull-out test

In a standardised pull-out test, a fibre is embedded in a block of polymer matrix. The fibre is pulled out of the matrix material, while the tensile force is recorded, allowing the interfacial shear stress to be calculated directly. This method is especially suited for newly developed fibre topologies like barbs. For the sample preparation, a dedicated machine is available that prepares specimens automatically [14]. Limitations are the difficult handling of the often fragile fibres, especially of brittle fibres with a low critical length [15].

7.2.2 Microbond test

The microbond test uses a fibre with a droplet of polymer matrix around it. By pulling the fibre through a hole in a vice plane, the matrix droplet is sheared off. The method is applicable for many different fibre-matrix combinations and the sample preparation does not require special equipment. However, similarly to the pull-out test, the droplet size is limited due to the critical fibre length. In addition, it is challenging to obtain a pure shear movement rather than droplet slippage or fibre breakage [15].

7.2.3 Fragmentation test

For the fragmentation test, a long fibre is embedded over the full length in a polymer matrix. In a tensile test, the sample is pulled beyond the strength of the fibre. The fibre breaks into smaller fragments until the fragments have reached a minimum length. At this point, the fibre does not break further. This fibre length is called the critical fibre length. It is determined in general by the type and diameter of the fibre, but also by the specific adhesion strength to the surrounding matrix [15] and can be measured optically under the microscope.

7.2.4 Raman spectroscopy

Raman spectroscopy is the only listed technique, for which several fibres can be embedded in one single sample. During a tensile test, electromagnetic radiation with a certain wavelength is sent with a laser locally into the sample while the reflected energy is captured by a spectrometer. This allows to determine molecules, concentrations and constituents in form of peaks in the spectrogram. Stress concentrations along the fibres can be noticed as a change in reflected frequencies. Differences cannot only be shown for a single fibre, but also comparison studies with samples with multiple fibres are possible. Thereby the effects of neighbouring fibres are observable [16]. Very good adhesion between fibre and matrix is needed to observe fibre breakage [17].

7.2.5 Motivation for the chosen method

In all cases, the load direction is parallel with the fibre direction, resulting in shear stress at the interface. In addition, all methods are able to measure either the force or the fragmentation length quantitatively, from which in both cases the interfacial shear strength (IFSS) can be calculated. However, a comparison of results shows that the values vary significantly amongst the methods [1,18,19], see Figure 7-3. X. Ji et al. [20] performed a study on treated and untreated carbon-epoxy, supplying different laboratories with the same materials and curing cycles. The results show a huge discrepancy between different labs and different methods, revealing the difficulty to measure accurately. Several reasons come into play including the non-standardised method of testing, the difficult sample production due to the small scale and the post-

processing of the results. The IFSS is highly dependent on the stress distribution along the fibre, which is caused by the debonding force, the fibre cross-section, and the embedded length [1]. Depending on the production method, a shrinkage pressure occurs as in the pull-out test or can be minimal as in the micro-droplet approach. Furthermore, imperfections like incomplete wetting of the fibre or impurities on the fibre itself falsely decrease the result, especially on short embedded lengths. As a result, the values scatter significantly, both between tests using the same method and between the average results of different test methods. Similar scatter was also revealed in a different comparison study between testing methods [1], showing the generality of the issue.

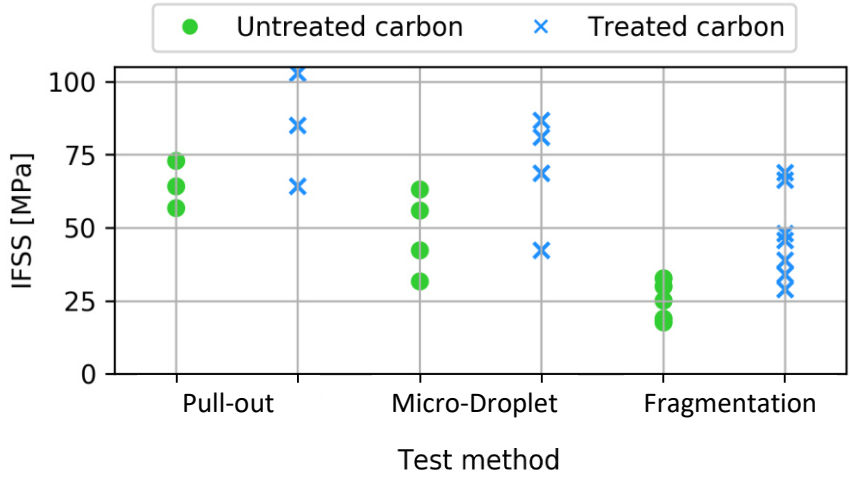

Figure 7-3: Data from literature: Disagreement of single fibre testing methods on the interfacial shear strength (IFSS) on carbon epoxy samples [20]

The discrepancy between the test methods shows that debonding is not understood well enough to use a generally valid method. For comparative studies in the same lab, all listed methods are valid and provide a good instrument, but for the development of a generally applicable method, more research is needed.

The goal of this chapter is therefore not to come up with an approach to calculate the interfacial shear strength, but to understand the mechanism of debonding deeper to build the basis for a valid experimental method and numerical validation. The visualisation of the interface seems the best approach. Therefore, the visual access of the fibre needs to be given. Since the fibre has a diameter of a few micrometres, microscopic techniques are required. To observe the magnified fibre in-situ, it has to stay in a fixed position during loading. In addition, load and displacement should be recorded during the experiment to allow simulation to extract quantitative data in a post-processing step. For the simulation, the boundary conditions of the test setup need to be simple. In the following, a tensile test is developed based on these requirements.

7.3 Methods to analyse debonding

To visualise the interface, different types of microscopy and computed tomography are possible. These techniques are explained briefly and the choice for light microscopy with polarising filter is motivated.

7.3.1 Scanning electron microscopy

Scanning electron microscopy (SEM) uses an electron beam instead of light to form an image. The electron beam is hitting the surface of the sample and electrons from the sample are emitted. A detector forms the image of the surface. The electron beam penetrates the surface up to a depth of a few micrometre [21]. The visualisation of an object in a deeper layer is not possible. Observation of an embedded fibre is only possible on exposed ends. For short, fully embedded fibres, the observation is impossible, even if the fibre has a high conductivity.

7.3.2 Micro–computed tomography

Micro–computed tomography, abbreviated as μ-CT, is an imaging technique to visualise the sample composition in depth. A large number of 2D x-ray images are taken while the sample is being rotated. The images can be computed to a 3D volume image, which reveals the internal structure of the sample non-destructively [22]. However, the full analysis of a sample takes time, which does not give the ability for in-situ measurements. In a synchrotron, the image acquisition is faster and the resolution higher, which allows with a specific setup for an analysis during loading. This technique is not available on lab-scale, since it is expensive with restricted accessibility.

7.3.3 Light microscope with polarised light

For a light microscope, different magnifications of up to x1000 are available, which is sufficient for the expected fibre diameter. The image is visualised instantly, which allows in-situ observations. In a transparent sample, light can be transmitted from the opposite side, showing various details of the sample. In addition, different filters increase the visibility. Colour filters for example, can remove background noise or increase the contrast. Polarising filters are used to visualise debonding. Their potential to show photoelasticity is also used in fibre fragmentation tests. Light microscopes have a suited order of magnification and are available in standard laboratories and will therefore be used for this study on debonding. Due to the choice of a light microscope, the test setup needs to fit in the given dimensions. Especially weight restrictions from the microscopic table and spatial restrictions in height were to consider.

7.4 Development of the setup to study debonding

For the observation of a sample under tension, a stage was needed that fulfilled certain requirements. Next to the standard requirement to apply tensile load, the stage had to allow the optical observation of the sample using transmitted light, i.e. light has to be able to pass from the bottom side of the stage to the top side. The requirements in detail are:

Movement:

- x-y-z-movement of the sample underneath objective to select and focus on a point of interest
- During a tensile test, the centre of the sample should stay in position under the microscope lens
- Low friction in mechanical pieces to ensure smooth movement

Clamping:

- Clamping of thin thermoplastic samples

Visual access

- The backlight through the sample must not be blocked by the clamp or bottom plate of the stage

Geometry:

- Restricted height to 40 mm of the full stage due to the limited z-range of microscope table and fixed focal length of lens
- Restricted weight of 1 kg on microscope table to avoid sagging or damaging the internal mechanics of the focussing system
- Possible revolver rotation of lenses to change magnification during experiment

Measurement:

- Record tensile load
- Measure displacement
- Record and save polarised images for post-processing

Off-the-shelf stages were not fulfilling these requirements, especially in terms of visual access and geometry. Therefore, a new, special purpose stage had to be developed. Due to the limited space under the microscope, it was necessary to consider the requirements and dimensions of the used microscope BX51 Olympus [23] from the beginning on.

Figure 7-4: Overview of developed tensile stage on microscope [23]

For the x-y-z-movement it was decided to position the stage on the table of the microscope. This allows for an easy adjustment in the three translational axes to bring the centre of the sample in focus of the length. Based on the given dimensions by the microscope, the tensile stage from Figure 7-5 was designed.

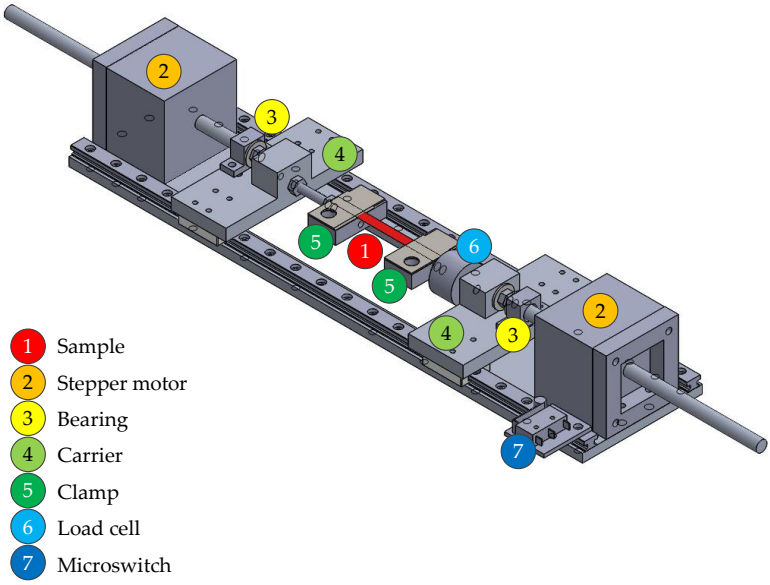

Figure 7-5: Components used to build the tensile stage

The tensile stage is designed symmetrically. The sample (1) is clamped in the middle of the tensile stage. Two linear stepper motors (2), one on each outer side of the stage, introduce the tensile force. The motors are synchronised to keep the middle of the sample at a constant position. The axes of the motors are connected via low friction sleeve bearings (3), shown in Figure 7-6. Initially, ball bearings were planned, but the height and weight restrictions did not allow for it. The bearings are attached to carriers, which are plates that move via ball bearing gliders on rails. Their function is to stabilise the setup and translate, together with the sleeve bearings, the rotational movement of the stepper motor to the axial displacement of the clamp.

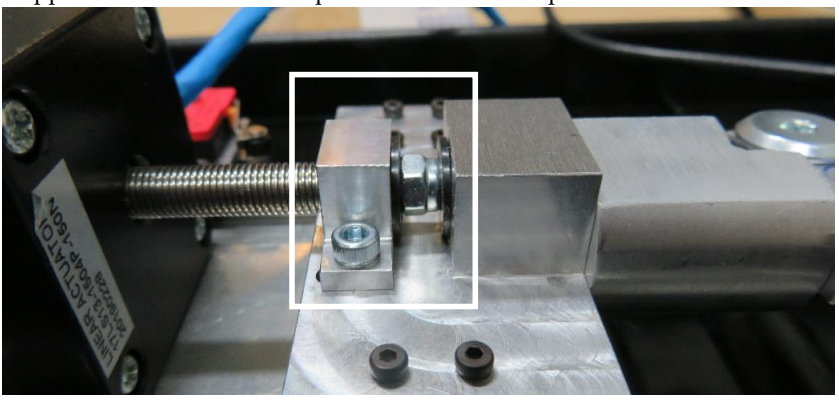

Figure 7-6: Low friction sleeve bearing to translate rotational movement of stepper motor to linear movement of the glider

Floating clamps (5) are holding the sample. A 100 N-load cell (6) between a clamp and a carrier measures the load directly without needing to compensate for the friction of the carrier. To keep the symmetry of the tensile stage, a solid rod in the length of the load cell was placed between the other clamp and carrier. The displacement of the stage is limited by the position of the stepper motors framing the full setup. To protect the stage from excessive displacements, microswitches (7) were installed.

The clamping of the sample is one sided with a flat headed screw with a diameter of the head of 10 mm. The big head helps to distribute the clamping force over the full clamping area. A two-sided clamping was not possible due to the revolver rotation of the lenses. A counter nut on the bottom of the screw was used rather than an internal thread in the clamp. Thereby, the torsion on the clamp could be kept low while tightening to protect the load cell and the overall structure. To avoid a rotation of the square-shaped washer and torsion on the sample, the washer is form-fitted in the top of the clamp, see Figure 7-7.

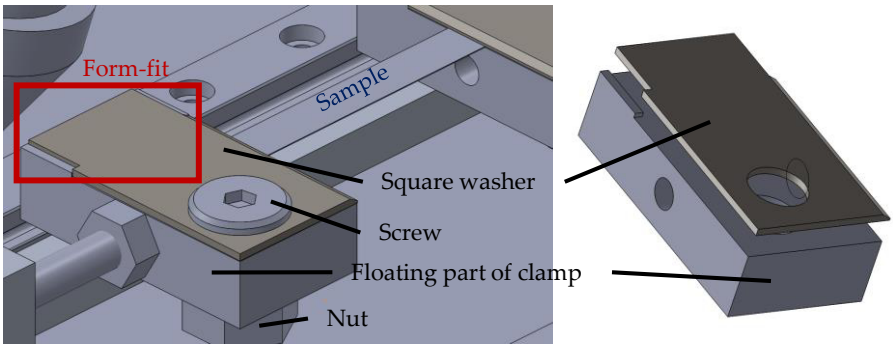

Figure 7-7: Clamp with flat headed screw and squared washer fitted in floating part of clamp

A bottom plate of 5 mm thickness ensures the stiffness of the full tensile stage. As the rest of the components, it is milled from aluminium to limit the mass as much as possible. The heaviest components are the stepper motors at 285 g each, which attributes to almost half of the allowed weight. With all components, the designed tensile stage weighs 1045 g and is thereby at the limit of the microscope table. Long-term tests showed that the stage is not sagging due to the weight. Otherwise, cut-outs in the base plate could have been added to reduce the weight.

The control of the stepper motors and the readout of the load cell of Figure 7-8 was realised with an Arduino Mega 2560 (8). The microstep driver (9) powered by a power unit (10) adjusted the precision for the desired strain rate. The signal of the load cell was amplified with an amplifier (11) to generate an output of ±10 V and read by a NI-card (12).

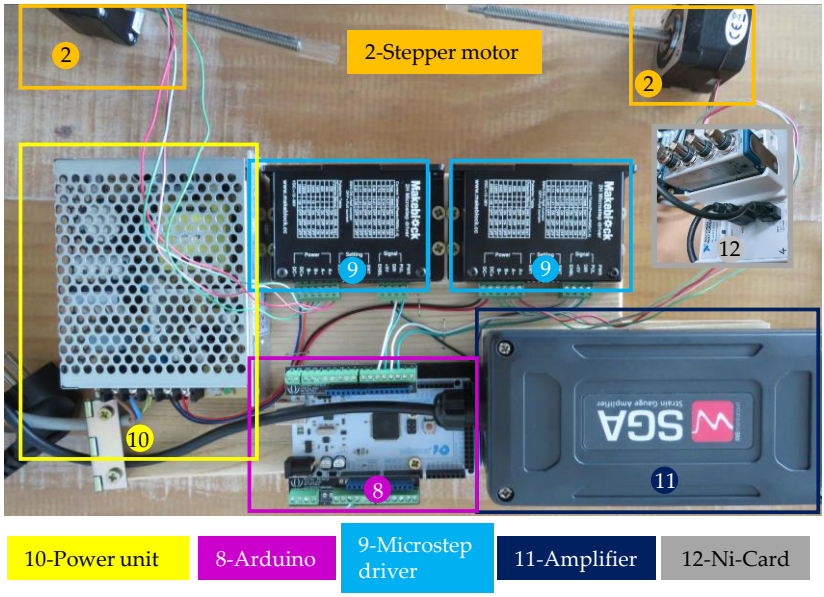

Figure 7-8: Components used to build control unit of the tensile stage

The control was written in LabVIEW [24]. In the graphical interface, Figure 7-9, the user can choose between a load- or displacement-controlled test, save details about the sample as well as describe motion and limits of the test. In case of a replacement of stepper motors or load cell, the relevant specifications can be changed accordingly. The displacement of the sample is assumed equal to the displacement of the stepper motors. For the polarised images, a video is recorded with Toupview [25] and manually synchronised with the data from the tensile stage in post-processing.

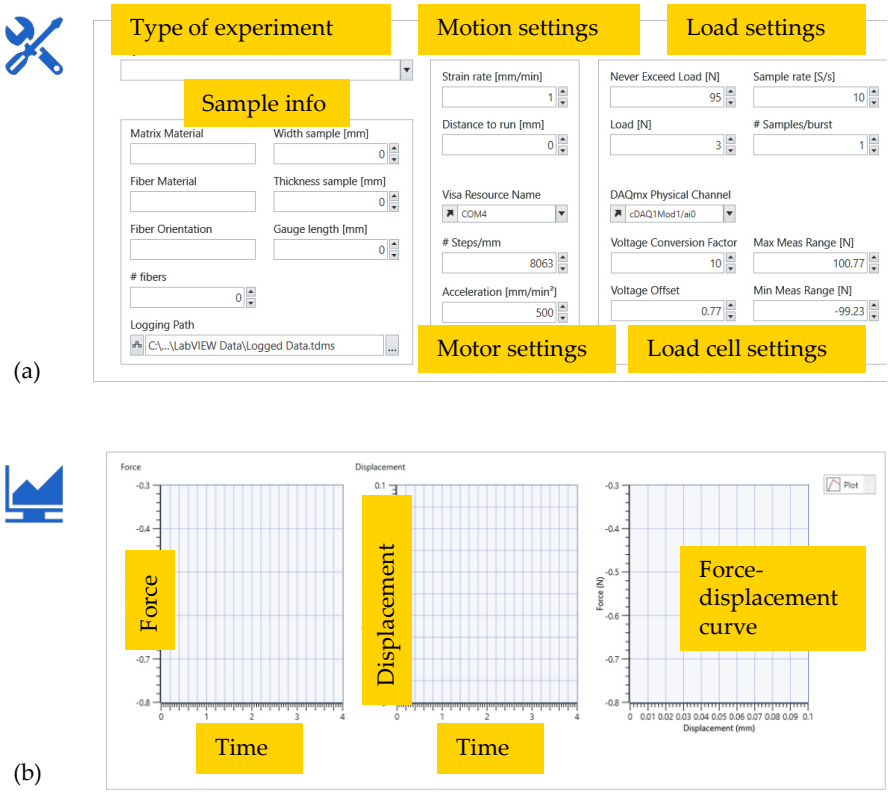

Figure 7-9: Interface of tensile stage control, written in LabVIEW, (a) settings for the experiment, (b) live plot of force and displacement during experiment

The functionality of the setup was verified to address concerns of vibrations by recording images while the motors were moving. The resolution of the images was good in the tested area, verified for a speed of up to 2 mm/min. The load cell was calibrated with a dead weight and during a displacement without applied load. It was found that the difference in theoretical load and practical load due to friction was with 0.1 N small and could be subtracted from the measured test result. Furthermore, the accuracy of the motor displacement was confirmed with a calliper with a resolution of 0.01 mm.

The specifications of the purchased components are to find in Table 7-1.

Table 7-1: Off-the-shelf components used for the tensile stage

Component	Specific name
Stepper motor	Reprap World Nema 17, 0.9° step, 2.1 kg*cm [26]
Microswitch	Mini microswitch with roller lever [27]
Load cell	DCE-100N load cell, tension, LCM Systems [28]
Arduino	Arduino Mega 2560 [29]
Amplifier	SGA Analogue Strain Gauge Amplifier LCM Systems [30]
Microstep driver	Makeblock 2h Microstep driver 2 A [31]
NI-card	NI 9215 BNC, +/- 10 V, 16-bit [32]

7.5 Analysing method to study debonding

The designed tensile stage is able to perform a tensile test and records load and displacement. For the optical analysis of the debonding inside the composite sample, the light microscope is used. In a transparent matrix, the relative displacement between fibre and polymer matrix is visible by using backlight. By adding a polarising filter, stress concentrations in the birefringent matrix can be visualised as well due to photoelasticity. Figure 7-10 illustrates the principle. Emitted light from a light source is polarised by a linear polariser, only allowing one orientation of waves to pass through and reach the sample. If there is no internal material orientation, the refractive index in all axes is the same. By applying load on a sample, the material is stretched in one direction, which changes the refractive index of that direction. That index influences the travelling speed of light. The light is split in the two principal strain directions, which reach the second linear polariser. The result is a colour map of stress concentrations in the matrix [33].

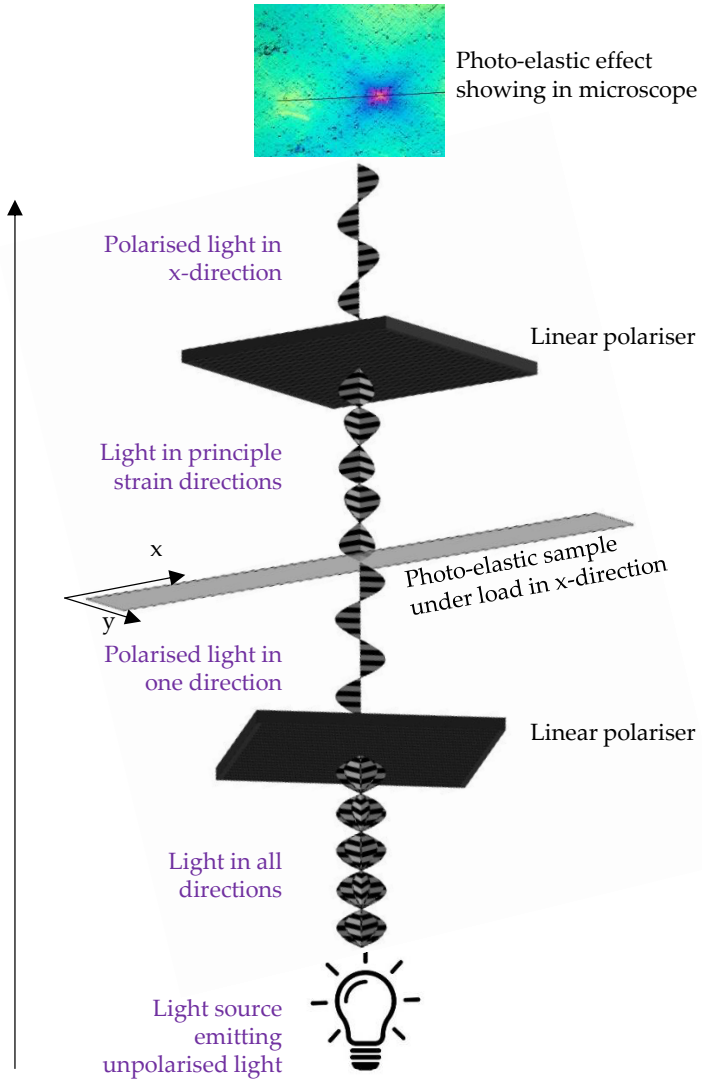

Figure 7-10: Schematic overview of light passing through linear polariser and sample, allowing the photoelastic effect to be visualised

The colour of the light changes with the direction it is polarised in the birefringent sample and in the linear polarisers. When the sample is stretched further, the colour changes. Thereby the same colour may repeat when the sample is loaded as in the tensile test in Figure 7-11.

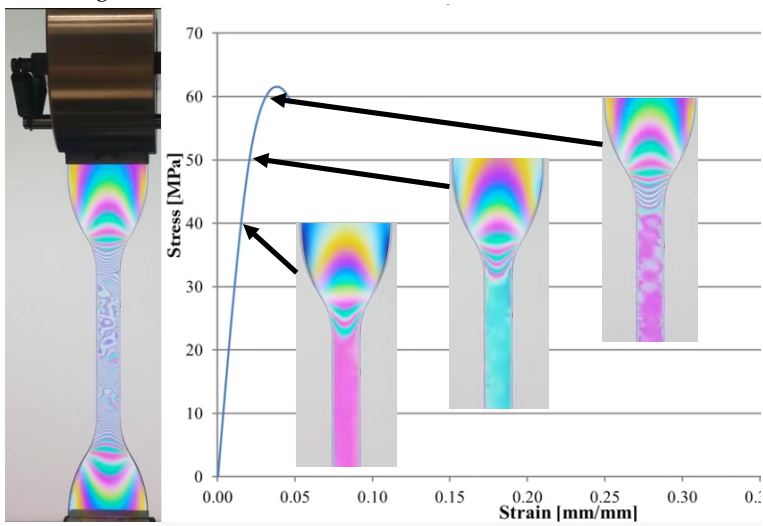

Figure 7-11: Tensile test on polycarbonate dogbone observed through a linear polariser[34]. The same colour pattern repeats during tensile loading. Colour differences show high stress concentration, especially in the clamping region

This shows, the overall colour is not a general indicator for stress, but the size of the gradient of colour between different positions is. The change in colour is visible in the HSV-spectrum, as seen in Figure 7-12. The spectrum is influenced by the polarisation angle expressed in the change in colour (**H**ue), the degree of polarisation, which defines the **S**aturation, and the brightness (**V**alue).

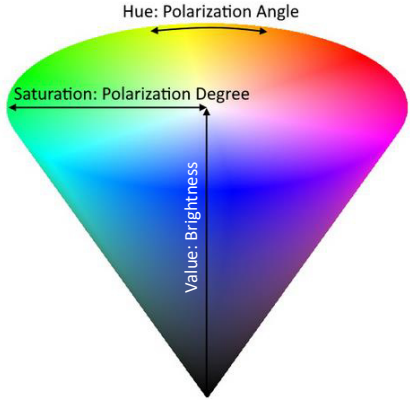

Figure 7-12: HSV spectrum polarised images are displayed in. The more intense the HSV value, the bigger the stress concentration [35]

7.6 Specimen preparation for debonding tests

To be able to visualise the debonding mechanism between fibre and polymer matrix longitudinal and perpendicular to the loading direction, samples were produced with a fibre oriented in loading directions (0°) and perpendicular (90°). In contrast to listed methods, both fibre ends were covered by the matrix to avoid open fibre ends that might falsify the observation [7]. In addition, with fibre embedded in the middle of the matrix, stress concentrations are also visible beyond the length of the fibre, providing a full image of the influenced area. By placing more than one fibre, the interaction of neighbouring fibres can be studied as well.

To develop a method that is able to predict the behaviour in a short fibre composite, a sample was designed that is close to the conditions of a normal composite, but with only very few, oriented fibres. Figure 7-13 shows the intended sample shape. This layout combines the embedding over the full fibre length as in the fragmentation test and the embedding of the fibre ends as in the pull-out test.

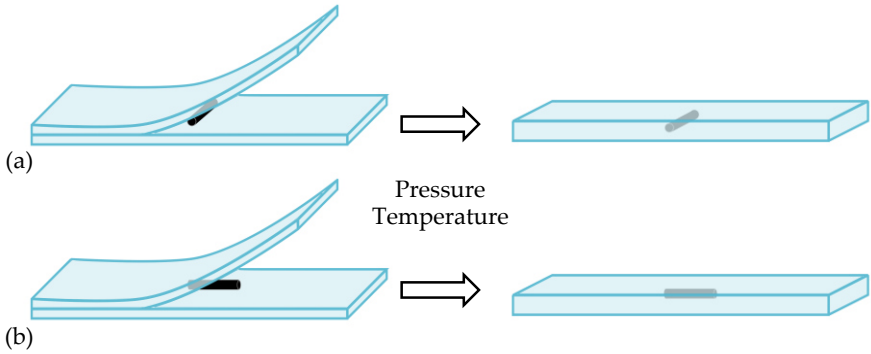

Figure 7-13: Ideal shape of the sample, short fibre fully embedded in matrix produced from two individual foils and a fibre. Fibre orientation in (a) 0° and (b) 90°

To produce the samples practically, a matrix was needed that turns birefringent under tension. Amorphous regions of polymers are randomly oriented. By pulling, the polymer chains align and form a birefringent pattern. A crystalline structure is already aligned and will not enhance that feature during stretching. Therefore, an amorphous or semi-crystalline matrix was looked for. The idea occurred to use thin films of matrix to ensure an even thickness of the matrix. The thickness was intended to be as low as possible to keep a high transparency and flexibility of the matrix to study the debonding between fibre and matrix at low displacements. PA6, which would have matched with some of the materials from the other studies, is commercially only available with a thickness of 500 µm and was therefore dismissed. The thinnest, commonly available film is plastic wrap made from low-density polyethylene (LDPE) with a thickness of 12.7 µm. It turned out to be very difficult to handle and align this

film. Therefore, a slightly thicker polyethylene (PE) film with a thickness of 70 µm was chosen. It was cut with parallel rolling blades to strips of 5 mm width and trimmed to a length of 60 mm. A short carbon fibre [36] was picked and placed on a polyethylene foil. The position was improved by pushing the fibre in the orientation of a grid of 0.5 mm that had been placed underneath the foil (Figure 7-14). A second film was carefully placed on top of the film with the fibre. Between glass slides, the foils were molten at 120°C and pressed with approximately 0.8 bar. By opening the glass plates and removing the sample immediately, rapid cooling was ensured which kept the crystallinity in the sample low and thereby the matrix transparent. The method would equally work for different polymers and fibres. A fully amorphous matrix is preferred, since it will show the strongest photoelastic effect.

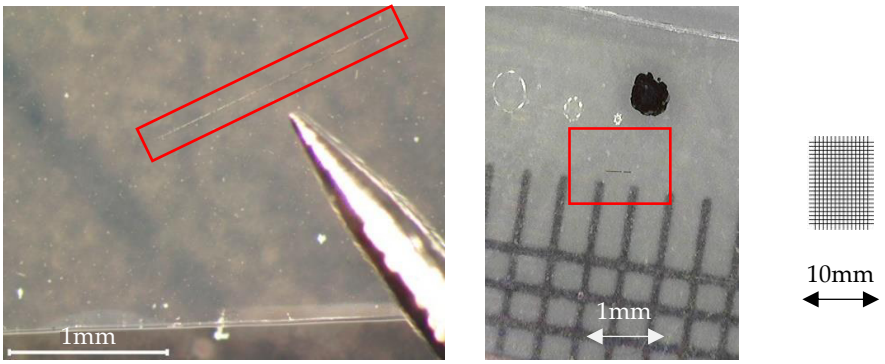

Figure 7-14: (a) Placement of carbon fibres with needle and (b) grid of 0.5 mm that helps visually to orient the fibre, (c) grid true to scale

Fibres were positioned in the matrix at different orientations. Single carbon fibres were embedded in matrix at 0° and 90° to the loading direction. Three fibres in parallel were embedded at 90°. The fibre diameter was 7 µm and the length was varied between 0.3 mm and 3 mm. The sample with three parallel fibres was of special interest, since it provides the basis to analyse if the outer fibres shield the load from the middle fibre. Therefore, the outer fibres were chosen to be 3 mm and the middle fibre half the length. An overview of the produced samples can be seen in Table 7-2.

Table 7-2: Overview produced samples with number of fibres, orientation, and fibre length

Amount fibres	Orientation	Length
Single fibre	0°	3 mm
Single fibre	0°	0.3 mm
Single fibre	90°	1.6 mm
Three fibres	90°	3.0 mm/1.3 mm/2.8 mm

7.7 Results and discussion on debonding

For the testing, the displacement speed was set to 0.5 mm/min. A study on polypropylene in fragmentation test [37] had found that a speed between 0.1 mm/min and 2 mm/min did not influence the result, but the clamping length did. Therefore, it was ensured that the initial clamping length was always the same, here 35 mm. In all experiments, the behaviour was symmetrical on both fibre ends. Due to the high magnification, only one fibre end is displayed.

7.7.1 0°-fibre orientation

Before any load was applied on the sample, stress concentrations were already visible at the fibre ends, as shown in Figure 7-15, Figure 7-17 and Figure 7-20 at 0% strain. This is due to residual stresses from the sample production, because carbon fibre shrinks less during cooling than the PE foil [6].

Figure 7-15 shows the increase of pulled out length depending on the tensile displacement in x-direction of a sample with a 0.3 mm and 3.0 mm long fibre. The debonding length increases with increasing displacement.

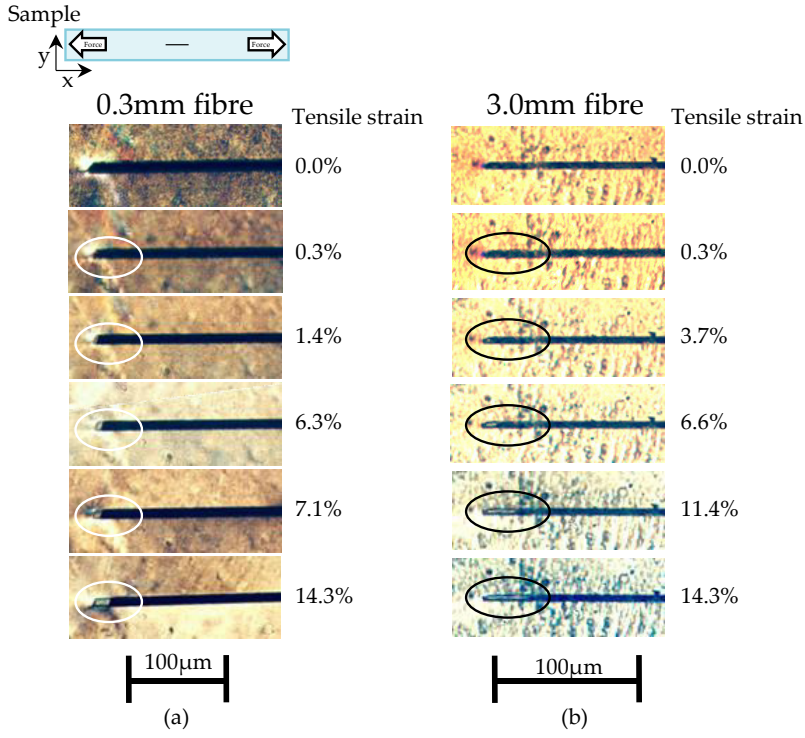

Figure 7-15: Strain dependent fibre pull-out on sample with (a) 0.3 mm and (b) 3.0 mm long fibre oriented in 0°-angle

Thereby, for both samples, the debonding increases exponentially as shown in Figure 7-16a. Both samples show a minimal debonding at the beginning of the tensile test. In the course of 5 mm displacement (14.3% strain), the pull-out length on the 3 mm long fibre increases about three times more than for the 0.3 mm fibre. A partial increase in pull-out length can be explained with the stiffening of a zone due to the fibre reinforcement. With a shorter fibre, the unreinforced area is smaller and carries more load compared to a sample with the same dimensions, but a smaller reinforced area. The debonding length on the fibre ends is longer because of the higher stress in the low stiffness area (Figure 7-16b). For quantitative comparisons, more tests need to be performed, since the scatter is likely to be high due to several influences, especially impurities in the samples.

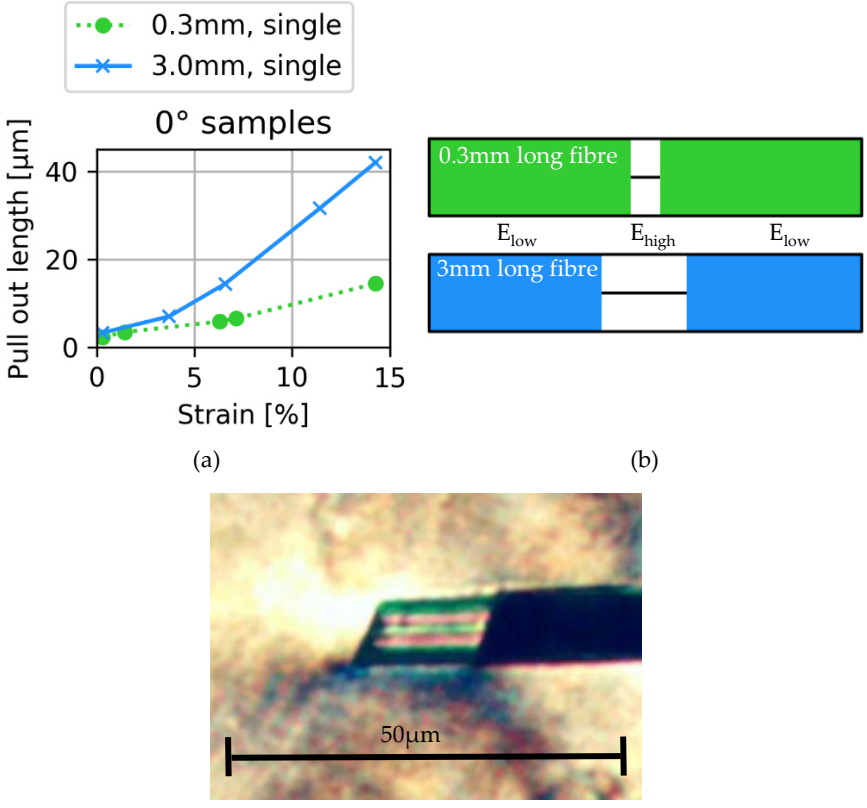

(a) (b)

(c)

Figure 7-16: (a) Pull-out length depending on the tensile strain and the fibre length, (b) simplified overview of low and high stiffness region, (c) residual stresses in matrix of a 0°-oriented 0.3 mm long fibre at 14.3% strain

As visible under polarised light in higher magnification (in Figure 7-16c), the debonded surface shows a photoelastic effect. To the current state, it remains unclear if this is caused by the curved surface of the created void, which interferes with the

light transmission or if residual stresses are visible. Prior studies have found residual stresses with Raman spectroscopy and explain it with frictional effects [6,38]. Overall, in 0°-oriented fibre, the failure mechanism is a pure fibre-pull-out. Fibre fracture does not occur, since the force is introduced only to the matrix. The load is mainly introduced to the fibre-matrix interface, not in the fibre itself.

In literature, 0°-tests were only found as fragmentation tests, which means that the fibre was also stretched and fibre fracture occurred. From the fragmentation test, a critical fibre length, the smallest occurring fraction of broken fibre, can be measured. Whether the critical fibre length can also be measured on fully embedded samples, remains unclear, also because the used matrix is very flexible. For fragmentation tests, the matrix has a significantly higher strain to failure than the fibre to ensure fibre fracture [39]. A very good adhesion between fibre and matrix and a certain critical fibre length would be needed to transfer sufficient tensile force to the fibre. From a normal fragmentation test, the critical fibre length for carbon fibre was found to be 300 µm [40,41]. In the experiments on fully embedded fibres, the longest fibre was 3 mm. In a normal fragmentation test, a fibre of at least 40 mm is used [41]. With a longer fibre, more surface adds to the bond between fibre and matrix and therefore more force can be transferred via the interface. It stands to reason that a critical fibre length can hence be determined in fully embedded fibres without applying direct tensile force on the fibre. A stiffer matrix than used here would be certainly required.

7.7.2 90°-fibre orientation

A single fibre was embedded perpendicular to the loading direction (Figure 7-17). As in the 0°-samples, residual thermal stresses were already visible before any load was applied. During the tensile test, the polarised light made it possible to see the growth of the debonding along the fibre, starting from the fibre ends.

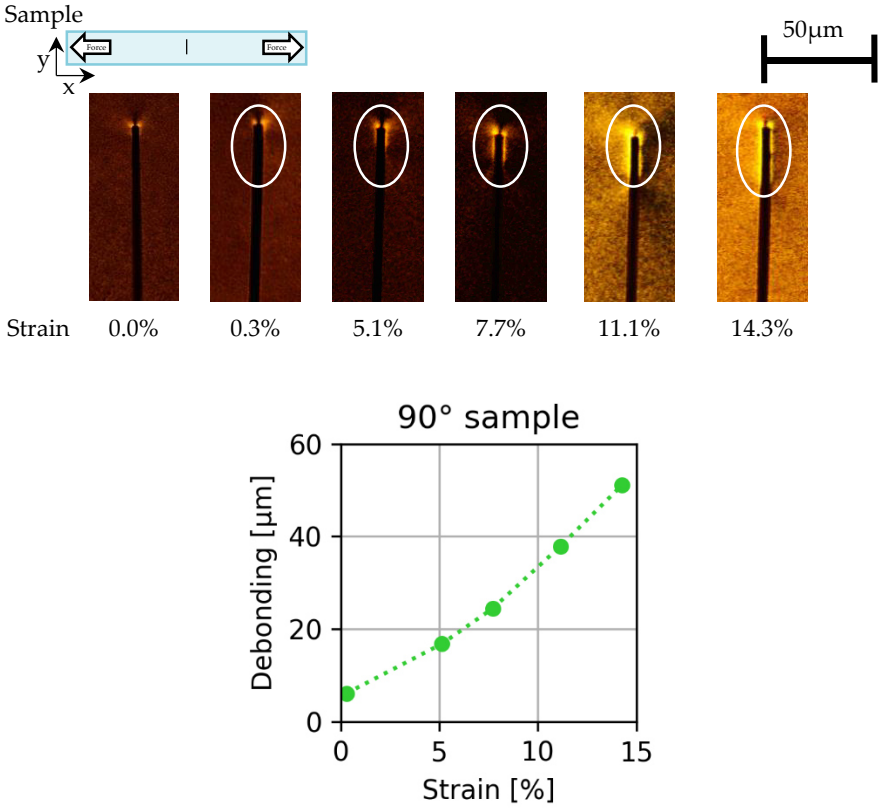

Figure 7-17: Fibre debonding of a single fibre, 90°-oriented, fibre length 1.55mm

In literature, fibre tests with glass-epoxy are dominant [4,7,12,13,42–45]. The sample thickness is typically 2 mm, which is significantly thicker than the foil samples of 0.14 mm used here. Initiating stresses for debonding can therefore hardly be compared. The fibre diameter of glass fibres used in literature varies between 17 µm [13] and 50 µm [42] and is therewith bigger than the 7 µm fibre used in this chapter. Without exception, all single fibres of single fibre tests in literature are spanning from one sample side to the other, which results in exposed fibre ends on both sides. The width of the sample determines the fibre length. Not all authors considered this dimension relevant to mention, but from visual estimation [4,12] and written information [42], it seems to be typically around 2 mm. Samples were loaded in transverse tension and debonding was observed starting from the fibre end and

moved sample-inwards as to see in the synchrotron image in Figure 7-18a. The higher the stress, the longer the debonding length (Figure 7-18b), which was measured visually [13,45]. It remained unclear if the sample fails at the fibre end because of the lack of protective matrix or because of the general stress state at the free edges.

In the study performed here on fully embedded and 90°-oriented carbon fibres, debonding was observed at the fibre end as well. The debonding length of the short, thin carbon fibre reached the same order of magnitude as the thicker, longer glass fibres. Thereby, it appears that the length of the fibre determined the debonding length. Since it has not been the objective of any found research, it is not known if the debonding length in samples with exposed fibre end also depend on the length of the fibre. However, it can be said that for both, embedded and exposed fibre ends, the debonding under transversal load starts at the fibre ends. The stiff fibre acts as an inclusion and concentrates the main stress to the discontinuous, sharp edge of the fibre. In addition to the geometry, the thermal shrinkage from production caused stress concentrations on the differently expanding materials of fibre and matrix.

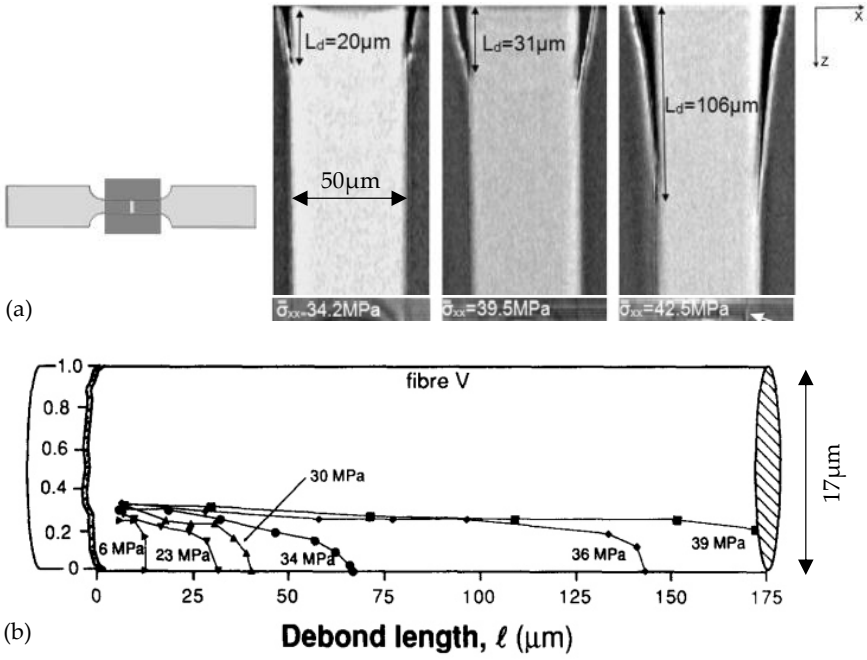

Figure 7-18: Debonding of glass fibre in epoxy, transversal load (a) debonding length with matrix opening observed in-situ in a synchrotron µCT-scan [42], (b) debonding range along the fibre [13]

7.7.3 Three parallel fibres, 90°-fibre orientation

The embedding of three fibres in parallel to each other requires attention to several dimensions. Next to fibre length and the orientation, the distances in x and y direction and the parallelism needs to be taken into account. Figure 7-19 shows these values for the produced and tested sample. Two full-length fibres surround one half-length fibre. The sample is produced symmetrical with almost parallel fibres and similar distances amongst them.

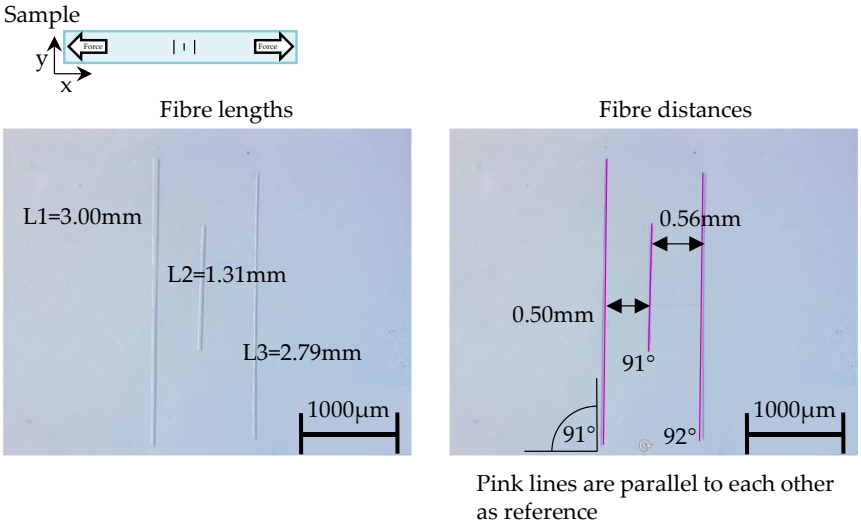

Figure 7-19: Three fibres in parallel with fibre length and distances to each other

Due to the distances between the fibres, a low magnification is needed to have all fibres in focus. The tensile test was performed at fiftyfold magnification (50x) with a field of view of 4.4 mm. At zero displacement and after 5 mm displacement (14.3% strain), the test was paused to record images of the fibre ends at higher magnifications (field of view of 1.1 mm (200x) and 0.44 mm (500x)), Figure 7-20. For this kind of study, the revolution of the objective revolver and the ability to move the microscopic table with the stage controlled in x- and y-direction is vital.

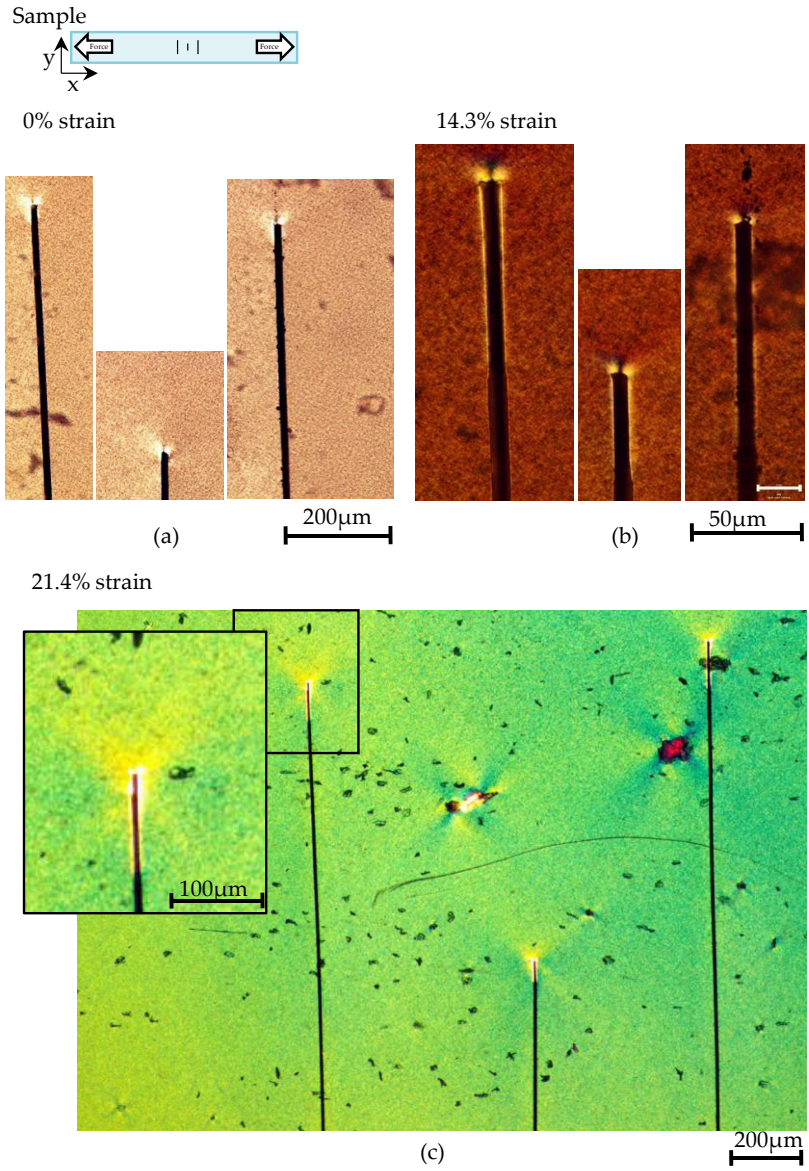

Figure 7-20: Sample with three fibres, 90°angle, 0%, 14.3% and 21.4% strain: (a) Stress concentrations at fibre tips before displacement due to shrinkage (magnification 200x), (b) Debonding length from fibre end until end of debonding zone measured per fibre (magnification 500x), (c) cross-shaped stress concentrations at fibre ends and inclusions (magnification 50x)

Before any displacement, stress concentrations due to shrinkage are visible as in Figure 7-20a. Already at that stage, the area of viscoelastic stress at the middle fibre appears over a smaller length of the fibre than at the longer outer fibres. At 14.3% strain

(Figure 7-20b), the debonding has moved along each of the fibres. It is assessed that the measurable debonding length is shorter for the short fibre than for the outer fibres. For all fibres, the stress concentration stays close to the fibre and does not reach far into the matrix. At 21.4% strain (Figure 7-20c) the stress concentration grew even further along the fibres and spread into the matrix.

During the production, also unwanted inclusions were embedded. In Figure 7-20c two relatively big inclusions can be seen with a clearly visible cross-shaped stress pattern. This pattern is also visible on the fibre ends, although less pronounced, probably due to the difference in size and corresponding effect on the stress state.

The debonding lengths were further analysed. The two long fibres (3 mm and 2.8 mm) in the three-fibre sample were showing the same debonding length along the fibre. The debonding length of the shorter middle fibre (1.3 mm) was shorter. However, a single fibre sample with a 1.6 mm short fibre, debonded the same distance as the middle fibre. Therefore, it can be concluded that the two neighbouring fibres in the three-fibre sample have no noticeable effect on the debonding length in a test executed at 1 mm/min strain rate until 14.3% strain (5 mm displacement) (Figure 7-21).

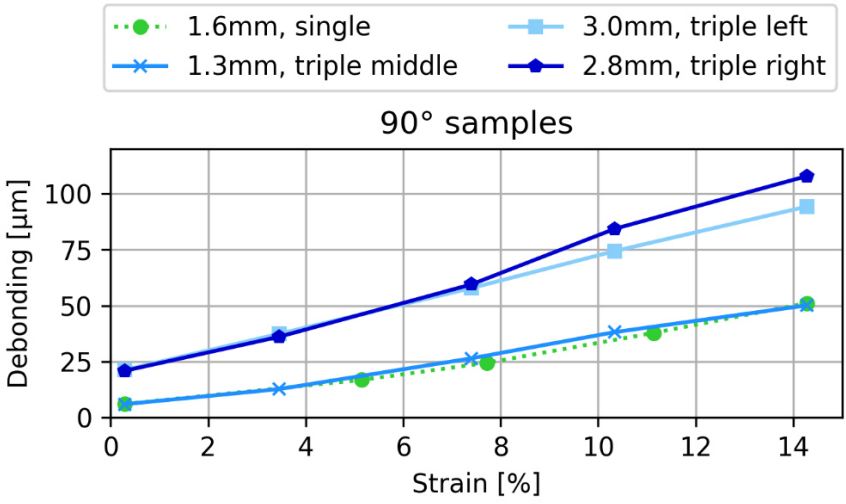

Figure 7-21: Debonding length in 90°-samples comparing single embedded fibre to three fibres in parallel. No significant difference can be noticed in the debonding length of the half-length fibres

The fibre diameter is 7 µm, the distance between the fibres 500 µm, so almost 72 times the fibre thickness. It is likely that the big distances in the three-fibre sample are causing each fibre to carry the full load of the tension. However, in a composite material, the fibre distances are much smaller, as the cross section of an injected short fibre composite in Figure 7-22 shows. Despite the relatively low fibre content of 13 vol% (20 wt%), the fibres are closer together than in the produced three-fibre

sample. Smaller, more realistic distances between the three fibres should be chosen to study the influencing effect. From this study, it is found that with a spacing of 0.5 mm, neighbouring fibres do not affect the debonding on the fibre ends.

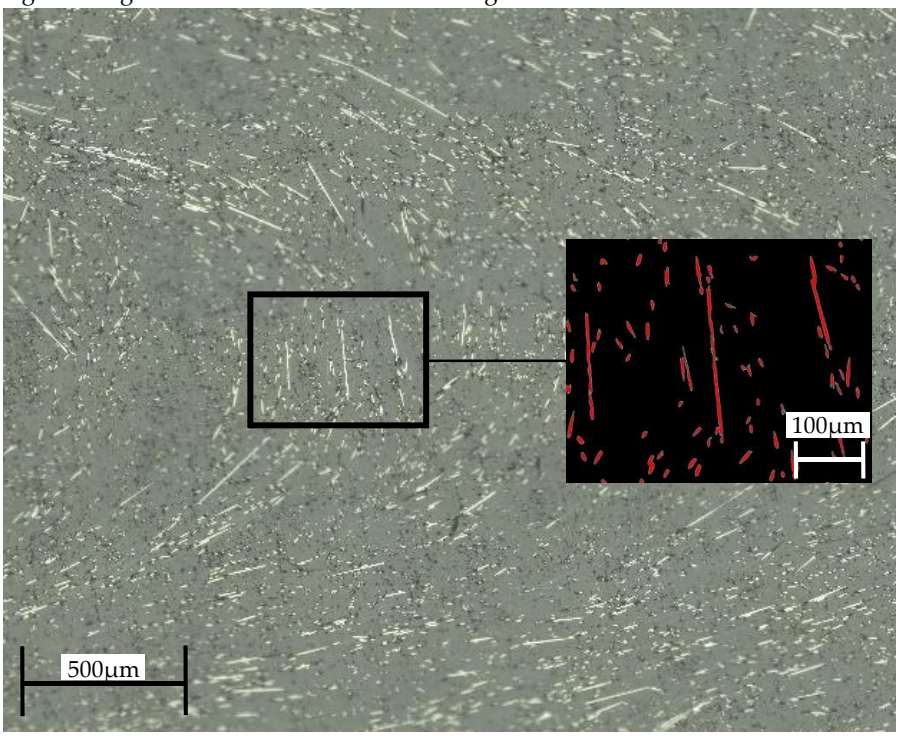

Figure 7-22: Cross section of composite material with carbon fibre content of 20 wt%

7.8 Conclusions of debonding tests

In this preliminary study on the debonding of single fibre in thermoplastic matrix, good, reproducible results were achieved. The careful preparation of samples allows to get a first impression of the visibility of debonding in 0°- and 90°-oriented fibres in a thermoplastic, transparent matrix under load. A tensile stage was designed for a common light microscope with polarising filters. The stage was constructed to be able to rotate the lenses to switch magnifications during a test and to use the x-y-movement of the table to position the sample correctly while being clamped in the tensile stage.

Along 0°, the fibre slides out of the matrix, leaving a hollow space with residual stresses. In 90°-fibre orientation, the debonding starts at the fibre tips and moves along the fibre. This effect is also visible with three fibres in parallel. A distance of 0.5 mm between the parallel fibres does not lead to an influence of the fibres on each other. To study debonding further, the addition of a numerical study can be recommended to avoid extensive trial and error. From the experimental side, this preliminary study

shows the potential for a study on debonding, the feasibility of producing single short fibre samples and provides the necessary equipment in form of a special purpose tensile stage.

7.9 Outlook of the study of debonding

From the current state of research, improvements are possible in regard of the sample quality. To avoid influences of unwillingly embedded dust particles, preparing the samples in a clean room should be considered. In addition, a press with an automatically applied pressure and a rapid controlled cooling will improve the uniformity of crystals in the matrix.

The orienting of 0.3 mm short fibres turned out significantly more difficult and time-intensive than those of 3 mm. For future studies, fibres longer than 1 mm can be recommended. Alternatively, a less brittle fibre with a smaller length to thickness ratio could improve the positioning. The distances between the fibres should be smaller to mimic realistic distributions in composites. Also, the random orientation of the fibres as single fibre and in samples with a few fibres, can be an interesting object of study. Furthermore, this method is in contrast to all other debonding methods able to study also differently shaped fillers than fibres, as flakes for example.

Better strain measurements should be achievable with 2D-DIC by applying a speckle pattern on the sample to track the displacement. A speckle pattern between the films on the same level of the fibre could be of interest to measure strain and stress concentrations around the fibre at the same time.

Since the difference in the HSV-colour spectrum represents the difference in stress concentration, a digital analysis of the images would improve the information that can be obtained. By synchronisation with the force-displacement measurement, more accurate measurements could be performed.

This research is especially valuable in combination with a simulation of the material. For accurate micromechanical modelling, there are unknown factors which experiments can help to clarify. For example, it is currently unclear, if debonding of fully embedded fibres happens only in the loading direction or fully around the fibre. Experiments at different angles to the microscopic lens could visualise the debonding area. In return, the modelling can improve the experimental work by giving advice on dimensions, like sample width, film thickness and distances for the three-fibre sample.

In the long run, this test should also be modified to allow testing at elevated temperature, since this might affect the debonding behaviour between fibre and matrix. In combination with numerical simulations, a lifetime prediction on composite

material will be possible, provided that the required experiments and models are developed.

7.9.1 Future improvements on the tensile stage

During the design, it was aimed for having the axis of the force aligned with the sample, to introduce pure tension. Due to the length of the higher magnification objectives, it was not possible. The objectives and clamps would collide. In order to avoid this, an offset of 11.5 mm was added as can be seen in Figure 7-23. This offset causes a slight bending movement in the sample due to the un-centred force introduction of force. Therefore, an in-axis design would be an improvement.

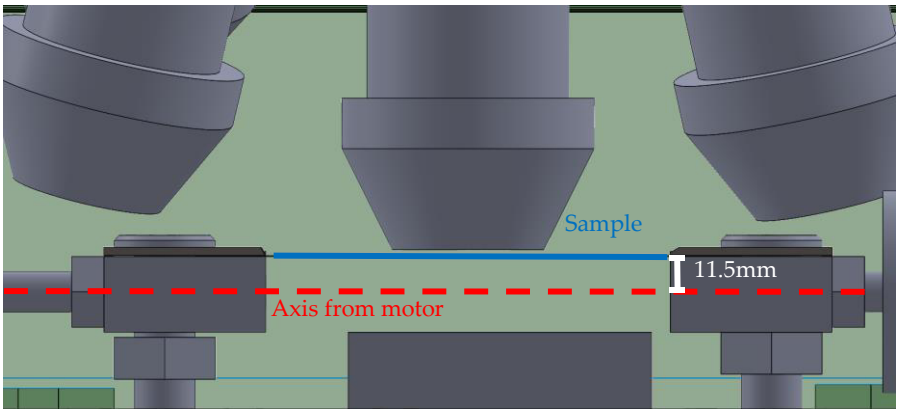

Figure 7-23: The axis of load direction and sample position are not aligned due to the needed clearance between the lens and sample

The setup was designed to keep the offset between the motor axis and the sample as small as possible. As a consequence, the revolver rotation is not always possible without moving the stage. The higher the magnification of a lens, the longer the lens. To be able to switch magnifications, a revolver revolution of all lenses is needed. This movement can cause a collision between the clamps and the rotated lenses. The further the clamps are apart, the bigger is the span length and the longer can the lens be. Every lens has a diameter of 32 mm, which is the minimum span length to be able to use every magnification at the microscope. Smaller magnifications would also be possible with a shorter span length, since the lens is further away from the sample and clamps. The revolver rotation is possible with a span length of 40 mm and magnifications below 50x, due to the thin design of the top part of the clamp (Figure 7-24). In case of a bigger magnification or smaller span length, the microscope table with the stage can be moved in one direction, the lenses rotated, and the stage sled back. The movement in pure y-direction has proven to be the best approach to find back the point of interest on the sample and still be in focus.

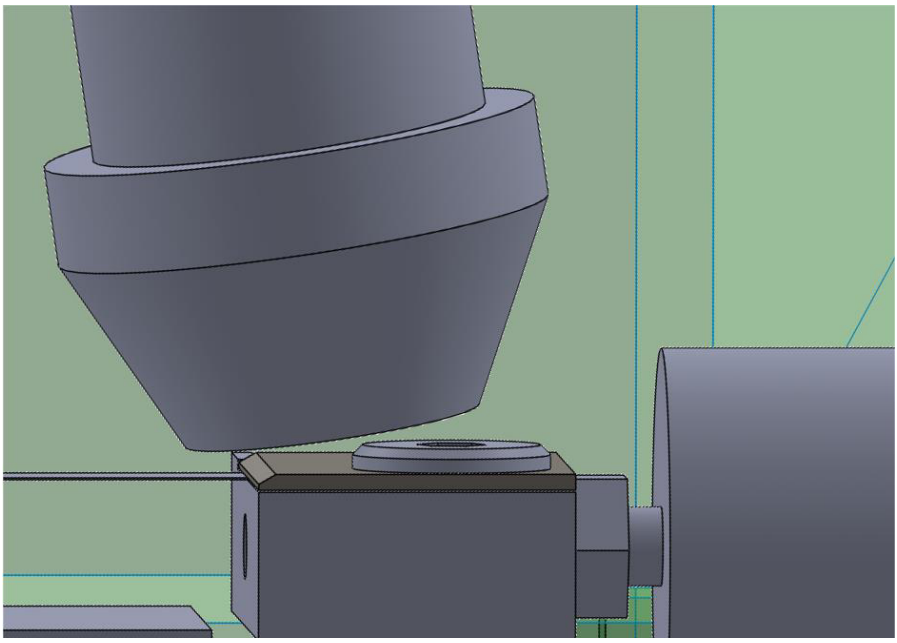

Figure 7-24: Revolver rotation of 50x lens with a span length on the sample of 40mm. Type of lens and span length influence the rotatability.

The clamps are asymmetrical with a single bolt off-centred. This does not ensure a uniform clamping over the full clamping area. However, a symmetric clamp design would increase the height of the clamp and thereby not allow for more than one installed lens. The ability to change the magnification was favoured over a symmetric clamp. To enhance the quality of clamping, the surface of the clamping plates was roughened to enhance the grip. In case of thin, smooth foils, the grip can be further enhanced with double-sided tape.

The displacement of the sample in the tensile test was measured directly from the displacement of the stepper motors. Slippage from the clamps or the mechanical connections is not accounted for. In the current design stage, the rudimentary measurement of displacement was assumed sufficient, since the accuracy could be verified with a calliper after testing. For a more refined setup, several options for the strain measurement exist. A laser displacement sensor [46] as shown in Figure 7-25 could measure the displacement of the sample more accurate.

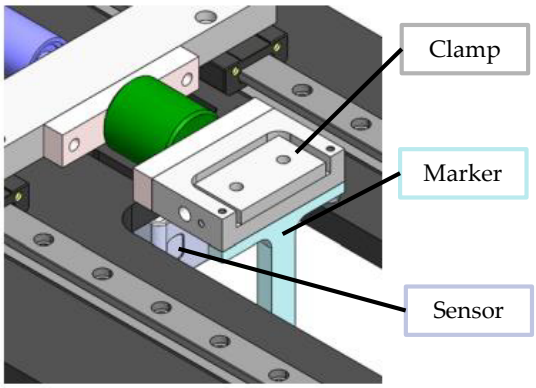

Figure 7-25: Laser displacement sensor to measure displacement of tensile clamp accurately [47]

To measure full field strain instead of pure displacement, digital image correlation (DIC) could track the movement with a speckle pattern. This pattern should be ideally applied on the same focus point as the observed object, so in case of an embedded fibre on the same depth in the sample. Another option is Raman microscopy [48]. This enables to measure the strain distribution on the fibre and is therefore a very suited method. However, it is unclear, if the geometry and weight of the designed stage can be combined with Raman spectroscopy.

Lastly, the synchronisation of data should be improved further. In the current state, load and displacement measurement are synchronised. The recording of the images is a separate procedure. By synchronising the measurement with the imaging, the accuracy of the measurement would be improved.

References

[1] N. Graupner, J. Rößler, G. Ziegmann, and J. Müssig, "Fibre/matrix adhesion of cellulose fibres in PLA, PP and MAPP: A critical review of pull-out test, microbond test and single fibre fragmentation test results," *Composites Part A: Applied Science and Manufacturing*, vol. 63, 2014, pp. 133–148.

[2] M. Piggott, "Why interface testing by single-fibre methods can be misleading," *Composites Science and Technology*, vol. 57, 1997, pp. 965–974.

[3] T. Hobbiebrunken, M. Hojo, T. Adachi, C. De Jong, and B. Fiedler, "Evaluation of interfacial strength in CF/epoxies using FEM and in-situ experiments," *Composites Part A: Applied Science and Manufacturing*, vol. 37, 2006, pp. 2248–2256.

[4] E. Gamstedt and B. Sjögren, "Micromechanisms in tension-compression fatigue of composite laminates containing transverse plies," *Composites Science and Technology*, vol. 59, 1999, pp. 167–178.

[5] S. Oller, *Numerical simulation of mechanical behavior of composite materials*, Springer, 2014.

[6] B.W. Kim and J.A. Nairn, "Experimental verification of the effects of friction and residual stress on the analysis of interfacial debonding and toughness in single fiber composites," *Journal of materials science*, vol. 37, 2002, pp. 3965–3972.

[7] P. Meurs, B. Schrauwen, P. Schreurs, and T. Peijs, "Determination of the interfacial normal strength using single fibre model composites," *Composites Part A: Applied Science and Manufacturing*, vol. 29, 1998, pp. 1027–1034.

[8] J. Thomason and L. Yang, "Temperature dependence of the interfacial shear strength in glass–fibre epoxy composites," *Composites science and technology*, vol. 96, 2014, pp. 7–12.

[9] J. Varna, R. Joffe, and L.A. Berglund, "Interfacial toughness evaluation from the single-fiber fragmentation test," *Composites science and technology*, vol. 56, 1996, pp. 1105–1109.

[10] H. Cai, M. Nakada, and Y. Miyano, "Simplified determination of long-term viscoelastic behavior of amorphous resin," *Mechanics of Time-Dependent Materials*, vol. 17, 2013, pp. 137–146.

[11] X. Wang, D. Xu, H.-Y. Liu, H. Zhou, Y.-W. Mai, J. Yang, and E. Li, "Effects of thermal residual stress on interfacial properties of polyphenylene sulphide/carbon fibre (PPS/CF) composite by microbond test," *Journal of materials science*, vol. 51, 2016, pp. 334–343.

[12] E. Correa, E.K. Gamstedt, F. Paris, and V. Mantic, "Effects of the presence of compression in transverse cyclic loading on fibre–matrix debonding in unidirectional composite plies," *Composites Part A: Applied Science and Manufacturing*, vol. 38, 2007, pp. 2260–2269.

[13] H. Zhang, M. Ericson, J. Varna, and L.A. Berglund, "Transverse single-fibre test for interfacial debonding in composites: 1. Experimental observations," *Composites Part A: Applied Science and Manufacturing*, vol. 28, 1997, pp. 309–315.

[14] "Textechno, FIMATEST Fibre-Matrix Adhesion Tester, [online: https://www.textechno.com/wp-content/uploads/2020/07/FIMATEST_Ru_Eng.pdf]," 2020.

[15] C. Rodricks, "Characterisation of interfacial properties in model fibre composites," F.S.& Conference, ed., 2019.

[16] P.W.J.V.D. Heuvel, T. Peijs, and R.J. Young, "Analysis of stress concentrations in multi-fibre microcomposites by means of Raman spectroscopy," *Journal of materials science letters*, vol. 15, 1996, pp. 1908–1911.

[17] P. Van den Heuvel, Y. Van der Bruggen, and T. Peijs, "Failure phenomena in multi-fibre model composites: Part 1. An experimental investigation into the influence of fibre spacing and fibre—matrix adhesion," *Composites Part A: Applied Science and Manufacturing*, vol. 27, 1996, pp. 855–859.

[18] V. Rao, P. Herrera-Franco, A. Ozzello, and L. Drzal, "A direct comparison of the fragmentation test and the microbond pull-out test for determining the interfacial shear strength," *The Journal of Adhesion*, vol. 34, 1991, pp. 65–77.

[19] M. Piggott, "Failure processes in the fibre-polymer interphase," *Composites science and Technology*, vol. 42, 1991, pp. 57–76.

[20] X. Ji, Y. Dai, B.-L. Zheng, L. Ye, and Y.-W. Mai, "Interface end theory and re-evaluation in interfacial strength test methods," *Composite Interfaces*, vol. 10, 2003, pp. 567–580.

[21] "Scanning Electron Microscopy, https://www.nanoscience.com/techniques/scanning-electron-microscopy/ [online: 11/10/2021]."

[22] D. Bull, L. Helfen, I. Sinclair, S. Spearing, and T. Baumbach, "A comparison of multi-scale 3D X-ray tomographic inspection techniques for assessing carbon fibre composite impact damage," *Composites Science and Technology*, vol. 75, 2013, pp. 55–61.

[23] *Instructions BX51/BX52 System Microscope*, Olympus, .

[24] "Labview [computer software], http://belgium.ni.com/labview," *National Instruments Corporation,*, 2015.

[25] ToupTek, "ToupView 3.7."

[26] "Data sheet Stepper motor, https://reprapworld.com/products/motors_fans/stepper_motors/nema17_stepper_motor_0_9_step_2_1_kg_cm/," 2019.

[27] "Mini microswitch with roller lever, https://www.gotron.be/minimicroswitch-met-rolhendel-on-on-5a-125v-3a-250v.html [online July 2020]."

[28] https://www.lcmsystems.com/DCE, "DC-100N Stainless Steel Stud Type Tension and Compression Load Cell," 2020.

[29] "Arduino Mega 2560, https://befr.rs-online.com/web/p/processor-microcontroller-development-kits/7154084/," 2019.

[30] https://www.lcmsystems.com/sga-analogue-strain-gauge-amplifier, "SGA Analogue strain gauge amplifier," 2020.

[31] "Makeblock 2h Microstep driver [online https://www.reichelt.de/de/de/makeblock-me-2h-microstep-treiber-v1-mb-2h-microstep-p202132.html?PROVID=2788&gclid=CjwKCAjwmK6IBhBqEiwAocMc8rw6A9Tswo0qBRk8W_IbNw7eCeTX57TbdVqPZO7UNTc0apwX-A3sKhoCTHEQAvD_BwE&&r=1]," 2019.

[32] "NI-9215, 4-Channel, Simultaneous Input, C Series Voltage Input Module, National Instruments," 2020.

[33] K. Claytor, "Polarized Light [online 2021: https://viva.pressbooks.pub/analyticalmethodsingeosciences/chapter/3-5-polarization-of-light/]," *Analytical methdos in geosciences*.

[34] I.M.-P. Robert A. Shanks, "Polycarbonate stress-strain mechanical analysis with polarised light visualization, video data set," *School of Science RMIT University, Melbourne, Australia*, Mar. 2016.

[35] "Theory Of Operation, [online 2021: https://help.commonvisionblox.com/Polarization/html_english_theory-of-operation.html]."

[36] "Chopped carbon fibre strands 3mm [online: https://shop1.r-g.de/en/art/210137-NA]," 2020.

[37] A. Awal, G. Cescutti, S. Ghosh, and J. Müssig, "Interfacial studies of natural fibre/polypropylene composites using single fibre fragmentation test (SFFT)," *Composites Part A: Applied Science and Manufacturing*, vol. 42, 2011, pp. 50–56.

[38] A. Paipetis, C. Galiotis, Y.C. Liu, and J.A. Nairn, "Stress transfer from the matrix to the fibre in a fragmentation test: Raman experiments and analytical modeling," *Journal of composite materials*, vol. 33, 1999, pp. 377–399.

[39] S. Feih, K. Wonsyld, D. Minzari, P. Westermann, and H. Lilholt, "Testing procedure for the single fiber fragmentation test," *Risoe National Laboratory, Roskilde, Denmark*, 2004, pp. 1–30.

[40] Q.-Q. Ni and E. Jinen, "Fracture behavior and acoustic emission in bending tests on single-fiber composites," *Engineering Fracture Mechanics*, vol. 56, 1997, pp. 779–796.

[41] A. Paipetis, "Room vs. temperature studies of model composites: modes of failure of carbon fibre/epoxy interfaces," *Composite Interfaces*, vol. 19, 2012, pp. 135–158.

[42] K. Martyniuk, B.F. Sørensen, P. Modregger, and E.M. Lauridsen, "3D in situ observations of glass fibre/matrix interfacial debonding," *Composites Part A: Applied Science and Manufacturing*, vol. 55, 2013, pp. 63–73.

[43] F. Parıs, M.L. Velasco, and E. Correa, "Micromechanical study on the influence of scale effect in the first stage of damage in composites," *Composites Science and Technology*, vol. 160, 2018, pp. 1–8.

[44] F. Parıs, E. Correa, and V. Mantic, "Kinking of transversal interface cracks between fiber and matrix," 2007.

[45] J. Koyanagi, P.D. Shah, S. Kimura, S.K. Ha, and H. Kawada, "Mixed-mode interfacial debonding simulation in single-fiber composite under a transverse load," *Journal of Solid Mechanics and Materials Engineering*, vol. 3, 2009, pp. 796–806.

[46] "Banner LM80KIQP Laser displacement sensor [online2020: https://www.bannerengineering.com/be/en/products/part.807393.html]."

[47] L. Ceulebroeck, "A micro-scale universal testing machine for the micro-mechanical analysis of composite materials," UGent. Faculteit Ingenieurswetenschappen en Architectuur, 2020.

[48] M.A. Montes-Morán and R.J. Young, "Raman spectroscopy study of high-modulus carbon fibres: effect of plasma-treatment on the interfacial properties of single-fibre–epoxy composites: Part II: Characterisation of the fibre–matrix

Chapter 8

Conclusions of this dissertation and outlook

Abstract: In this final chapter, the work of this PhD is positioned with respect to the state-of-the-art of testing methods for composite heat exchangers. Improvements on measuring accuracy and the appropriate conditions are highlighted. Furthermore, future research possibilities based on the developed setups are discussed.

8.1 Introduction to the conclusions

In the introduction to this PhD, the relevance of reliable long-term tests for composite heat exchangers was emphasised. Particular challenges were the harsh conditions a heat exchanger imposes on the material and the life-time expectancy of up to 20 years, if one considers non-accelerated testing. The state-of-the-art challenges are summarised here to introduce the improvements presented in this research. Finally, future research options are listed for further improvements in the material characterisation. This will help to develop better heat exchangers and therewith improve the economic and ecologic benefits.

8.2 State of the art

Metals are due to their high thermal conductivity, stability and durability, traditionally used as material for heat exchanger walls. However, the material costs are rising and make heat exchangers less attractive. In addition, corrosion and fouling are causing the need for expensive maintenance and cleaning. As an alternative, polymer and composite heat exchangers were introduced into the market. Especially the ones made from short-fibre reinforced thermoplastics are showing benefits over metal heat exchangers because of corrosion resistance and anti-fouling properties. Nevertheless, the long-term degradation at elevated temperature and creep are commonly posing a challenge for composites. For the specific purpose of a heat exchanger with elevated temperature, humidity, specific fluids and creep load, no long-term studies are available and no testing method existing. The schematic in Figure 8-1 illustrates the problem. With the idea of a composite heat exchanger, decisions need to be made on material and geometry. As testing method for the geometry, thermodynamic simulations of the flow and heat conductivity are available. Based on this information, the geometry is set without considering the material. For the material choice, standardised material tests are used. Since creep is the main failure, real time creep data is collected under standardised conditions. After approval, the material is shaped to the geometry and the heat exchanger is put into service without further validation. Strength and stiffness have not been tested at the accurate conditions and geometry at any point in testing. Validation purely takes place in the in-service application.

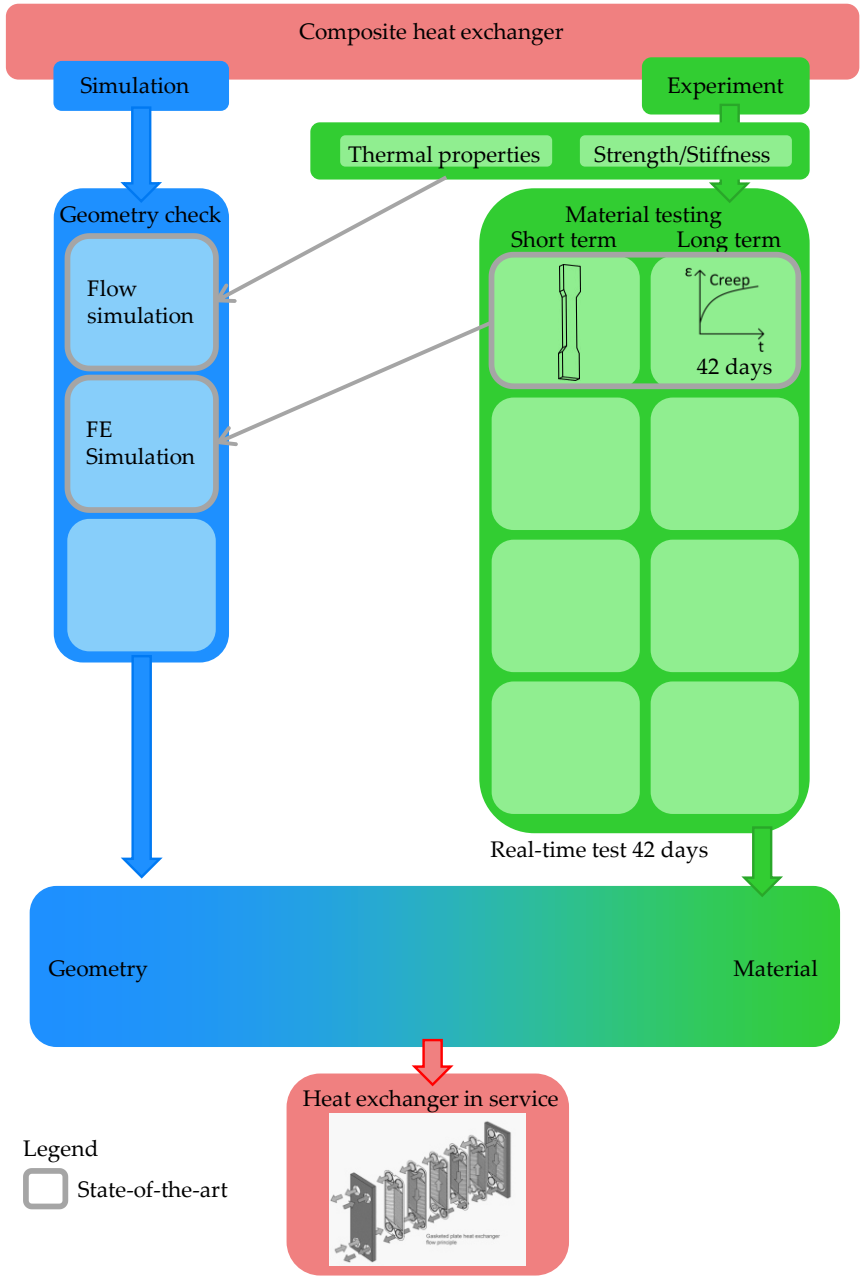

Figure 8-1: Schematic of the state-of-the-art. No sufficient methods for material testing are available

To assess the performance of a composite sufficiently, the following parameters need to be included in mechanical testing:

- Accurate environmental condition, especially temperature
- Accurate strain measurement in this specific environment
- Long-term prediction based on accurate data
- Knowledge improvement in debonding for numerical simulation

8.3 Research in this dissertation

This PhD focusses on the improvement of the experimental qualification procedure for heat exchanger materials by testing material at elevated temperature under quasi-static, dynamic and creep load. Several improvements over common test methods for heat exchanger materials were achieved. The schematic in Figure 8-2 shows the improvements over the state-of-the-art. A newly developed routine was used to confirm the material quality, which enables high quality experimental testing and numerical analysis (1).

In the original workflow, the combination of geometry and material was done by full prototypes in-service. As a validation step in between, a setup has been developed to test a small sample of the wall under realistic temperature and loading conditions (2). Furthermore, the material testing was improved by measuring strain precisely to know the temperature dependent stiffness, strength and strain rate dependency for material models. This accurate measurement is the basis for long-term predictions based on short-term tests (3). This allowed for improved knowledge of the strength of the material and can therewith positively influence the choice of geometry. Similar tests were also performed in enhanced DMA measurement to generate precise short- and long-term predictions faster (4).

As a last step, the debonding of the material was studied to obtain a better understanding of the failure mechanism (5). With these additional setups and accurate testing methods, the experimental characterisation of potential heat exchanger materials is complete.

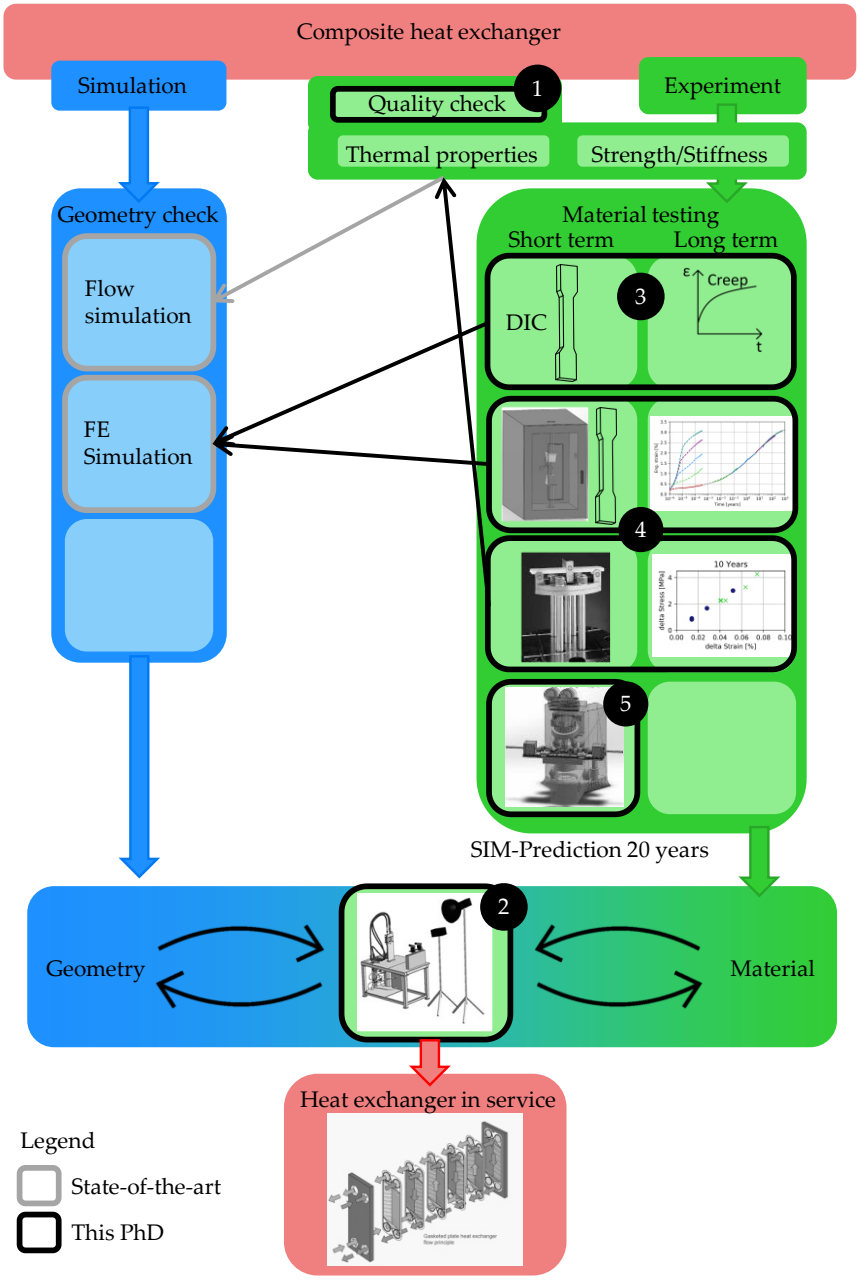

Figure 8-2: Schematic of the contribution to the state of the art by this PhD. The quality of the material (1) can be tested under environmental conditions using a realistic geometry (2). Sample deformation was measured precisely with DIC at elevated temperature for short-term results and long-term predictions using an electromechanical test bench (3) and a DMA (4). Testing of the fibre/matrix bonding was investigated using a newly developed procedure (5)

8.4 Possibilities for future research

During the research for this PhD, more possibilities of future research presented themselves, as Figure 8-3 visualises. The validation setup for the combination of geometry and material can be further used for long-term prediction considering the actual loading and environmental conditions (1), see section 8.4.1. The most important continuation of the test methods lays in the long-term validation of the SIM predictions and use of a consistent material to compare the predictions of the different test methods (2), as presented in section 8.4.2. For the numerical validation, a material model is still missing. With the help of the experimental study on debonding (3), accurate failure can hopefully be predicted in the future, shown in section 8.4.3. This would provide another validation step into the procedure to ensure safety and efficiency of the final design of a composite heat exchanger.

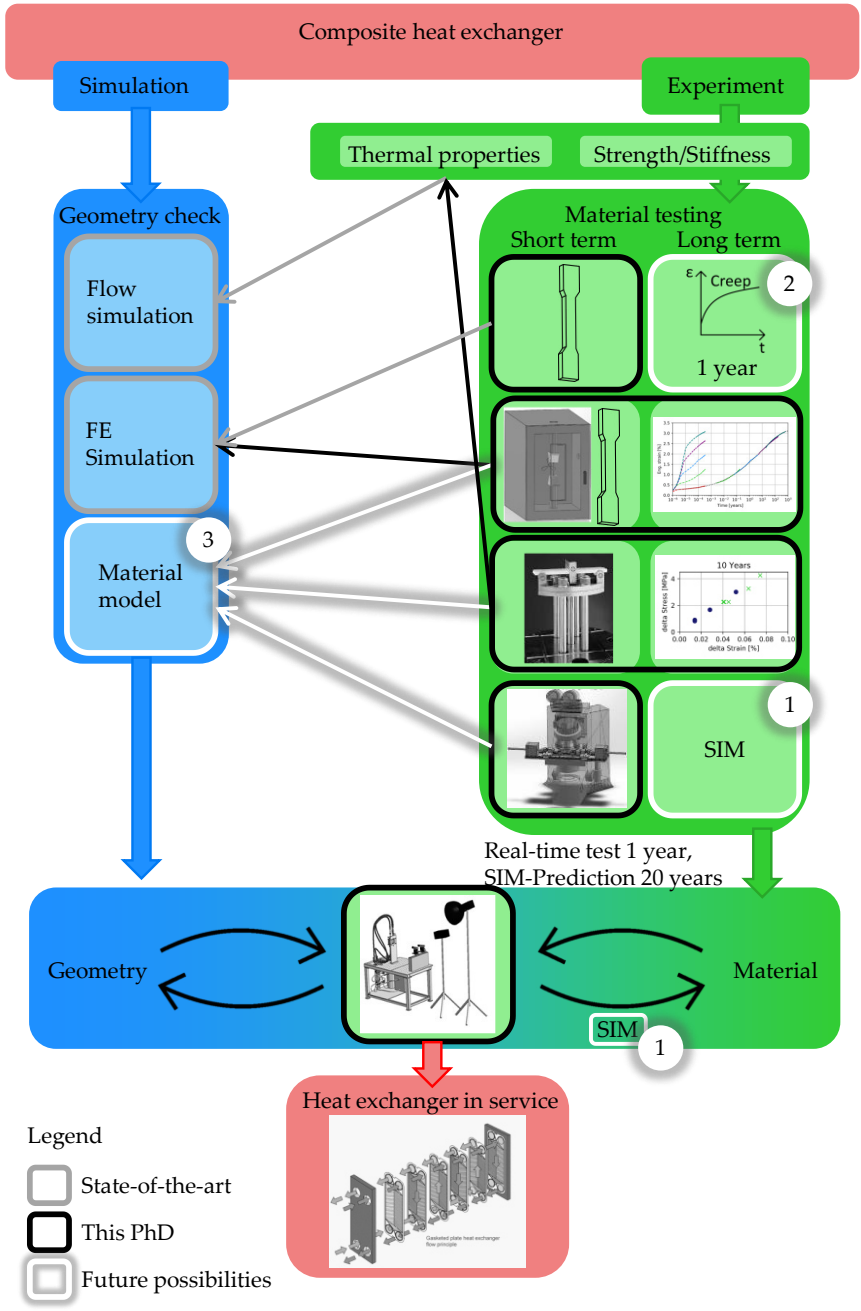

Figure 8-3: Schematic of possible future research in contribution to the state of the art and the work of this dissertation. (1) Long-term predictions based on the developed setups, (2) real-time test for sufficient comparison and (3) development of a material model for accurate stiffness prediction

8.4.1 Subcomponent-scale

The current unit cell prototype setup is designed for temperatures up to 80°C. In chapter 3, the possibility to extend the temperature range to 220°C was described. Furthermore, the setup is designed for creep tests, which offers the possibility to apply SIM on a heat exchanger wall of realistic geometry, which would allow prediction of long-term behaviour based on realistic loading and environmental conditions.

8.4.2 Coupon-scale

The test environment for the macroscopic tests is currently limited to an adjustment of temperature. In an environmental chamber with humidity control, heat exchanger material could be tested more accurately. This would allow for a better prediction of the material behaviour. Furthermore, samples could be soaked or pressurised in fluids like refrigerants and therewith improve the accuracy of the conditioning. In contrast to the prototype level, the macroscopic level allows for very comparable test results, which helps to decide on a material without taking into account the influences of geometry.

SIM was performed in tensile tests as well in DMA-bending. To validate the method with certainty, real-time creep tests over a period of at least one year are needed. Furthermore, using the same material for the different SIM tests, would allow for a comparison of the predictions made by different test methods. Also a 3-point bending setup on an electromechanical test bench would be interesting to compare to the small loads applied in a DMA machine. Together with SIM results of the prototype setup, material can be classified for long-term usage under the environmental conditions of a heat exchanger.

8.4.3 Interface-scale

To evaluate the debonding behaviour of composites, more experiments and the combination with numerical modelling is needed. The track of three fibres in parallel seems from the current stand point the most interesting one. The interaction of short fibres has not been studied much experimentally and could provide great value to numerical assumptions. For this, the fibres need to be much closer together than they were previously and the samples should be ideally produced in a clean room to avoid contamination inside the sample. As test method, creep tests are imaginable to visualise the beginning of composite failure at a very early stage. The tensile stage is designed to hold creep loads for several days, no further modification is needed.

As a step further in the future, conditioning the samples before testing or even testing at elevated temperature and humidity, would allow for a precise prediction of the debonding under these conditions. For heat exchangers, that would mean an accurate calibration of numerical models and therewith a very good chance of accurate prediction of material failure.

8.5 Final remark

With the future possibilities, researched, experimental methods and experimentally validated material models can be made available for heat exchanger producers and material suppliers. This will enable an efficient optimisation of already existing heat exchangers and the development of new material and geometry combinations for long-lasting, efficient heat transfer realised in composites.

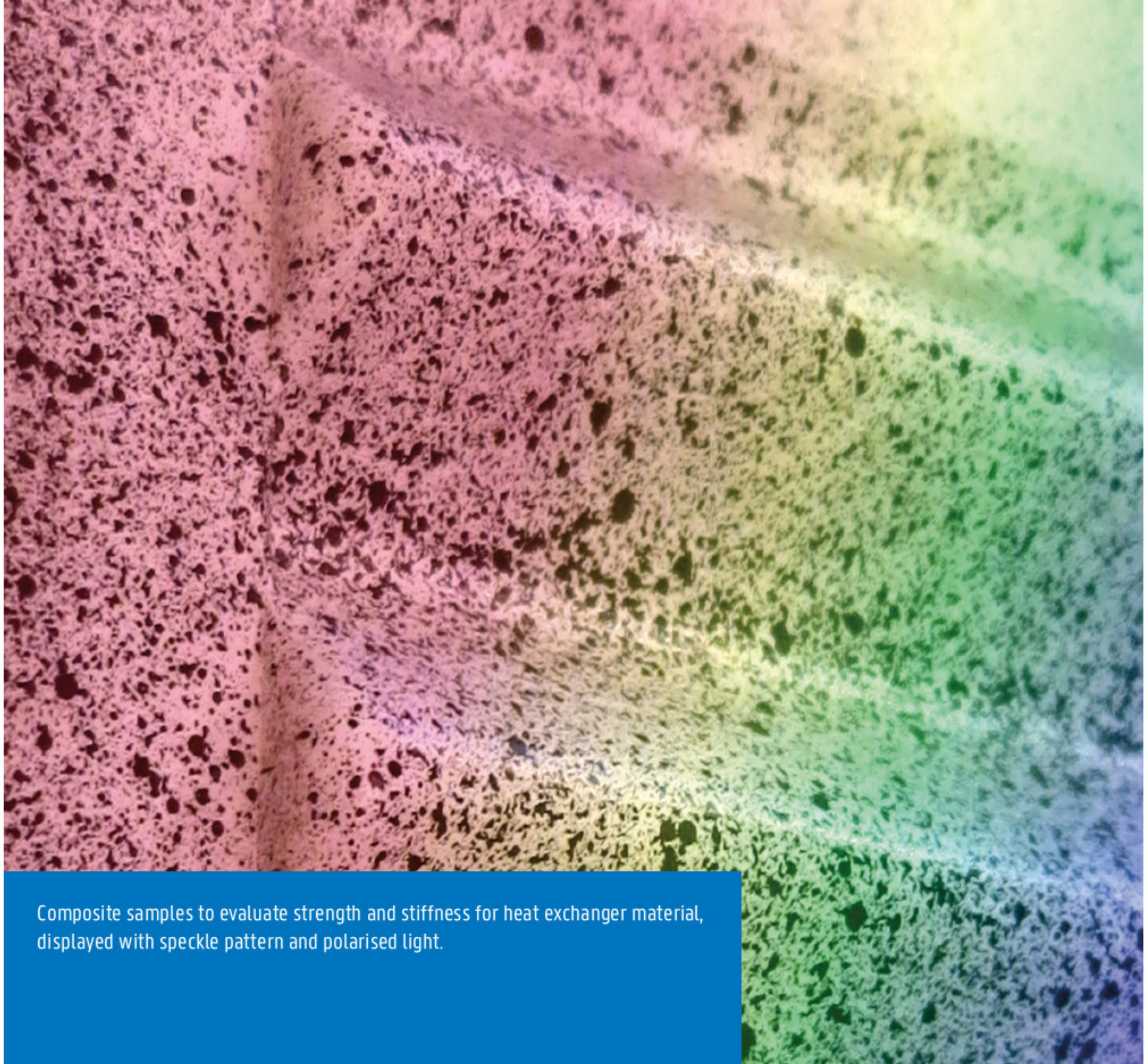

Composite samples to evaluate strength and stiffness for heat exchanger material, displayed with speckle pattern and polarised light.